UNIVERSITY OF FLORENCE
SERGIO STECCO ENERGY ENGINEERING DEPARTMENT

DOTTORATO DI RICERCA IN
INGEGNERIA ENERGETICA E TECNOLOGIE INDUSTRIALI
INNOVATIVE
DOTTORATO EUROPEO

SETTORE SCIENTIFICO DISCIPLINARE: ING-IND/08

Assessment of Advanced Numerical Methods for the Aero-Thermal Investigation of Combustor-Turbine Interactions

---

Thesis presented by Stefano Vagnoli in order to obtain the degree of Doctor of Philosophy in Engineering
Supervisors: Prof. Francesco Martelli (University of Florence, Italy) and Prof. Tom Verstraete (von Karman Institute for Fluid Dynamics, Belgium)
Director: Prof. De Lucia Maurizio (University of Florence, Italy)

To Ilaria,
for her love and support

Acknowledgements

Rhode-St-Genèse, 07/01/2016

Firstly, I would like to thank all the members of the jury for accepting to evaluate the work presented in this dissertation and taking the time to review. Their very interesting comments and discussions present an excellent basis for further improvements in the future. In particular, I wish to thank Dr. Mauro Carnevale for having revised thoroughly the first draft of the manuscript and for the interesting suggestions he gave.

I would like to express my gratitude to Prof. Francesco Martelli and Prof. Tom Verstraete for having supported my PhD activity and for their precious suggestions.
I'd like to acknowledge all the members of the TRC research group of the Department of Industrial Engineering of the University of Florence. A particular thanks to Massimiliano Insinna for all the interesting discussions we had during the last three years.
I would like to thank Simone Salvadori for his precious indications and comments, and for having believed in me three years ago when he suggested to apply for the fellowship at VKI.

During my PhD I had also the chance to spend 3 months at Turbomeca. It is a pleasure for me to thank Lorenzo Pons for welcoming me into his team and Guillaume Bonneau for following my work with great interest. It has been a great pleasure to collaborate with many valid colleagues, Jean-Loup Bourguignon, Mickael Philit, Mathieu, Nicolas Chauvet,Etienne Tang, Gilles Leroi, Christophe Favre, Charlie Koupper. A special thanks to Mickael, Etienne, Steve, Jordie for the very good time we spent together even outside the work.

I would like to thank prof. Tony Arts for having accepted me in the TU department of VKI and prof. Sieverding for his advices.
I sincerely acknowledge Fabio Bigoni for our fruitful collaboration. I really appreciated working together and I am looking forward to continuing our collaboration.
A big thanks to all people working at VKI for all technical discussions and the good times we spent together. Thank you to Sebastian, Giulia, Cis, George, Clara, Fabrizio, Alessia, Laura, Sergio, Stefano, Mohamed, Lasse, Gian Luca, Jayson, Julien , Roberto Maffulli, Roberto Tomassini and so many others.

Abstract

The individual components of modern gas turbines are optimized to such a level that any noticeable improvement of the global performance can only be the result of a significant technological effort. In this sense, one of the main strategies to increase the efficiency of new generation engines lies in the investigation of more complex but more accurate design methodologies. In particular, the different modules of a gas turbine are historically designed separately, despite the fact that a turbomachine is a fully integrated system where all components interact with each other.
In the turbomachinery community there is a growing interest in including the interfaces between different components into the design process, as it would enable to design compressors, combustors and turbines in an integrated manner by taking into account the real operating conditions of the machine.
The interface between combustion chamber and high pressure turbine is considered as the most critical one, as it directly affects the maximum temperature reached by the thermodynamic cycle. The flow field at the combustor-turbine interface is characterized by very high turbulence levels, swirl and temperature distortions, and the CFD methods currently used to design high pressure turbine (HPT) blades lack of validation for such an aggressive environment.
The aim of the present work is to develop new numerical methodologies and to analyze the accuracy of the existing ones when applied to multi-component simulations in turbomachinery. The attention is mainly focused on the interaction between combustor and turbine, as it represents the most critical interface for a modern gas turbines.
To take into account the mutual interaction between combustion chamber and HPT, in the first part of this thesis three CFD methodologies are developed to solve the flow field of the two components in an integrated framework. The procedures are validated on test cases of increasing complexity and successfully applied to a configuration representing a modern combustion chamber coupled to a nozzle guide vane.
In the second part, the advantages and limitations of RANS and LES applied to the study of the hot streak migration in HPTs are discussed. In this sense, a LES tool for the external aerodynamics of turbine blades is developed and validated, with the aim to be applied in the future to the investigation of the combustor-turbine interaction. The accuracy of LES is then exploited to validate less time-consuming RANS models in predicting the hot streak migration in a turbine stage.
The current investigations indicate that integrated multi-component studies

are necessary to reproduce the actual operating conditions of the different components, as the complex interaction between hot streaks, swirl, turbulence and potential effect of the NGV cannot be reproduced without resolving the combustor and turbine at the same time. Moreover, the extreme turbulence level at the combustor-turbine interface must be modeled with care, since it plays a major role in the migration and diffusion of the hot streak in turbine.

Contents

Nomenclature **xi**

1. Introduction **1**

2. Literature Review **11**
2.1. The flow field at the combustor-turbine interface 11
2.2. Hot streak effect on the HPT stage 16
2.3. Swirl effect on the HPT stage 21
2.4. High turbulence effect on the HPT stage 23
2.5. Combined effect of temperature distortion, swirl and high turbulence on the HPT stage 25
2.6. Potential effect of the turbine on the combustors 27
2.7. Numerical challenges for the analysis of the combustor-turbine interaction 28

I. Potential effect in the combustor-turbine interaction 35

3. Multicode Coupling Theory **39**
3.1. General structure of the coupled simulation 39
3.1.1. Coupling mechanisms in space 40
3.1.2. Coupling mechanisms in time 41
3.1.3. The passage of information 43
3.2. Extended treatment of the LES-URANS coupling 45
3.2.1. Mathematical treatment of the downstream domain inlet 46
3.2.2. Mathematical treatment of the upstream domain outlet 53
3.3. The passage of turbulence for LES-URANS coupling 65
3.4. Final remarks 67

4. The Coupling Procedures **69**
4.1. LES-LES coupling procedure 69
4.2. LES-URANS coupling procedure 71
4.3. URANS-URANS coupling procedure 73
4.4. Synthesis of the developed coupling procedures 73
4.5. Coupled test cases 73
4.5.1. The backwards-moving shock wave 75
4.5.2. The vortex convected downstream 76
4.5.3. Turbulent channel flow 78

4.5.4. Turbulent cylinders in tandem 91
4.5.5. LES-LES coupling applied to the cylinders in tandem 102
4.6. Final remarks 105

5. Investigation of the combustor-turbine mutual interaction by coupled simulation 109
5.1. Design of the test case 109
5.1.1. Design of the NGV 111
5.1.2. Design of the combustion chamber 113
5.2. CFD validation for the NGV 115
5.3. CFD analysis of the combustion chamber 119
5.4. Coupled combustor-turbine simulation 127
5.4.1. Set-up of the coupled simulation 130
5.4.2. Results of the coupled simulation 133
5.4.3. Potential Effect of the NGV on the Combustor 138
5.5. Final remarks 140

II. LES for the analysis of the hot streak migration 143

6. Application of LES to a LPT test case 147
6.1. Background of the test case 147
6.2. Limitations of RANS and advantages of LES 148
6.3. The experimental set-up 148
6.4. Numerics 149
6.5. Time Average Quantities 152
6.6. Time Dependent Results 156
6.7. Final remarks 159

7. Application of LES to a HPT test case 161
7.1. Background of the test case 162
7.2. Limitations of RANS and advantages of LES 163
7.3. Experimental Arrangement 164
7.4. Numerics 166
7.5. Results of the Investigation 167
7.6. Final remarks 177

8. Assessment of RANS against LES for the Hot Streak Propagation in Turbine 179
8.1. The Combustor-Turbine Configuration 180
8.2. LES set-up 181
8.3. RANS set-up 183
8.4. RANS for Realistic Flows in Turbine 184
8.4.1. Effect of the inlet turbulence decay 185
8.5. Effect of the Turbulence Model 187

8.6. The Combustion-Turbine Aerothermal Interaction 194
8.6.1. Migration of the Hot Streak within the passage 195
8.6.2. Adiabatic Wall Temperature Evolution 195
8.6.3. Aerodynamic performance 199
8.7. Effect of the Solid on the Rotor Blade Temperature 200
8.8. Final remarks 205

9. Conclusions **209**

III. Appendix **215**

A. Advanced Methods for the Interaction Between Compressor and Inlet Ducts **217**
A.1. Introduction 217
A.2. The Flow Solver and Numerical Model 219
A.2.1. Analyzed Geometry 219
A.2.2. The Flow solver 219
A.2.3. Boundary Conditions for the Unsteady Analysis . . . 220
A.3. Validation of the Numerical Approach: the NASA Rotor 37. . 221
A.4. Analysis of the Stability Limit for the Centrifugal Compressor with Straight and Bent Pipe at the Inlet 224
A.4.1. Numerical Setup 224
A.4.2. The Numerical Computations 226
A.4.3. Centrifugal Compressor With Straight Inlet 226
A.4.4. Centrifugal Compressor With Bent Pipe 232
A.5. Final remarks 238

B. Validation of the NSCBC implemented in OpenFOAM **241**
B.1. The shock tube 241
B.2. Euler vortex convected across the outlet 242
B.3. High Reynolds vortex shedding test case 244

Bibliography **261**

Nomenclature

Roman Symbols

c	speed of sound
C	chord
c_v	specific heat at constant volume
c_p	specific heat at constant pressure
f	frequency
g	pitch
h	span / heat transfer coefficient
hr	hour
l	length of flow structures
L	length
$\dot{m}$	massflow
M	Mach
Nu	Nusselt number
P_r	Prandl number
q	heat transfer
Re	Reynolds number
Sn	Swirl number
St	Strouhal number
T	temperature
tb	blade thickness
TKE	Turbulent kinetic energy
TT	total-to-total
TS	total-to-static
TU	turbulence level
U	velocity
W	power

Greek Symbols

β	overall pressure ratio
Δ	cell volume
η	Effectiveness
θ	tangential direction
K	Kelvin
μ	viscosity

ν	viscosity
Π	pressure ratio
ρ	density
τ	Reynolds stress tensor
ϕ	equivalence ratio
Φ	temperature distortion parameter
ω	specific turbulence dissipation rate

Subscripts and superscripts

1	related to upstream of the airfoil
2	related to downstream of the airfoil
ad	adiabatic condition
ave	averaged
ax	axial direction
d	relative to the subdomain downstream
dom	referred to the domain
in	relative to the inlet
Inf	relative to the far-field
is	isentropic condition
max	maximum value
o	relative to the overlapping region
out	relative to the outlet
r	relative reference system
ref	reference value
rms	root mean square
t	relative to turbulence
te	relative to the TE
tot	total
u	relative to the subdomain upstream
w	relative to the solid wall

Acronyms

CFL	Courant Friedrichs Lewy
CHT	Conjugate heat transfer
CS	Cold streak
DNS	Direct numerical simulation
FT	Flow-Through
HPT	high pressure turbine
HS	Hot streak
LBC	Lean Burn Combustor

LE	leading edge
LES	Large Eddy Simulation
LPT	low pressure turbine
NGV	Nozzle guide vane
NSCBC	Navier Stokes Characteristic Boundary Conditions
RANS	Reynolds-averaged Navier Stokes
RQL	Rich-Quench-Lean
SGS	subgrid scale
TE	trailing edge
TUMDF	transonicUnsteadyMDFDYMFoam
VKI	von Karman Institute for Fluid Dynamics
WALE	wall-adapting local eddy-viscosity

Chapter 1.

Introduction

The gas turbine is a device dedicated to the conversion of chemical energy into mechanical energy. Its main advantage with respect to other common engines lies in the production of a very large amount of mechanical power with respect to its size. Because of this feature, in the last 60 years the gas turbines have became the most common machine in use for power generation and for the aviation industry.
Irrespective of their application or technological level, the main components and thermodynamic steps are unchanged since the introduction of the first modern gas turbine engine by Whittle in 1930. The main components characterizing a turbine are shown in Fig. 1.

- The air is compressed by one or more compressor stages. Several axial compressor stages are employed for large machines, while smaller machines are usually characterized by a limited number of radial compressors.

- The compressed air is burnt in a combustion chamber. The chemical process taking place during the combustion generates thermal energy which increases the gas temperature.

- The hot gas is expanded in one or more successive turbine stages. In this phase, the thermal energy of the gas is converted into mechanical energy by the turbine rotors.

A large part of the mechanical energy extracted by the turbine is directly transferred to the compressor, while only a small fraction can be actually extracted and used for other purposes.
The aforementioned thermodynamic steps describe a Brayton cycle. This is depicted in detail in Fig. 2 in an entropy-temperature (T-S) diagram.
Focusing the attention on the ideal cycle (in black), along the line 1-2 the temperature and pressure of the gas are increased by an isentropic transformation into the compressor stages. The phase 2-3 depicts instead an increase of temperature at constant pressure which takes place within the

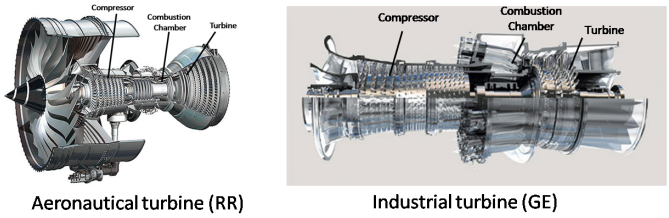

Figure 1.: Main components of a turboengine.

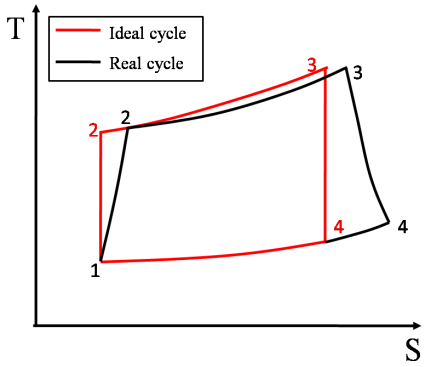

Figure 2.: T-S diagram of the Brayton cycle.

combustor. Between points 3 and 4 the flow pressure is decreasd by an isentropic expansion in turbine.
The real Brayton cycle deviates from the ideal one because of the energy losses taking place in the different components of the engines, which lead to an entropy increase for each thermodynamic transformation. If one neglects the auxiliary air injections within the machine (cooling, seal gas etc..) the efficiency of the real Brayton cycle can then be calculated as:

$$\eta_{TH} = 1 - \frac{\left(1 - \eta_T \left(1 - \frac{1}{\beta_T^{(\gamma-1)/\gamma}}\right)\right)\frac{T_3}{T_1} - 1}{\frac{T_3}{T_1} - \frac{\beta_C^{(\gamma-1)/\gamma} - 1}{\eta_C} - 1} \tag{1.1}$$

Where η_T and η_C represent the isentropic efficiency of turbine and compressor, while β_T and β_C are their respective pressure ratios. If one neglects the pressure loss in the combustion chamber and considers $P_4 = P_1$, then $\beta_T = \beta_C = \beta$.

The two factors that mostly influence the efficiency of the cycle are the overall pressure ratio β and the turbine entry temperature T_3 (usually defined as TET) [1]. The effect of these two parameters on η_{TH} is shown in

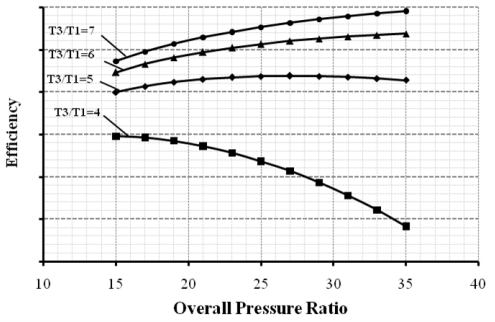

Figure 3.: Efficiency η_{TH} of the real Brayton cycle.

Fig.3, where Eq. 1.1 is directly applied. One can observe that an optimum β can always be identified by keeping the TET fixed. On the other hand, the efficiency of the machine always increases by increasing the TET.
The maximum temperature of the cycle has therefore the predominant effect on the engine efficiency. For 50K of increase in TET, one can observe an increase of work output of about 10% together with a $0.5-1\%$ improvement in the global efficiency [2].
The request of increasing the TET copes with the technological limits of the high pressure turbine (HPT) to operate at high temperature. In this sense, important progresses have been made in the last 40 years thanks to the development of advanced cooling techniques, which permit to reach a TET which is even higher than the melting temperature of the HPT blades.
Another method to increase the global efficiency of the cycle comes from a separate improvement of the compressor and turbine efficiencies (η_T and η_C in Eq. 1.1). For modern engines, it is commonly accepted that each module is optimized at a point that any further efficiency gain can only be obtained at the cost of a significant technological breakthrough.

At industrial level, compressors, combustors and turbines are normally designed separately by different offices which have little interactions between each other (often limited to the passage of massflow averaged boundary conditions at the interface between different components). It is well known, on the other hand, that a turbine is a very complex machine in which the different components heavily interact between each others.
In the optics of an increase of the overall performance of the machine, the turbomachinery community constantly seeks for more accurate design methods. In this sense, an effort has been done in the last years to include the interfaces between inlet duct/compressor, compressor/combustor and combustor/turbine directly into the design and optimization process [3]. In fact, the compressor performance and the overall pressure ratio are affected by the non-uniform field at the outlet of the intake ducts [4, 5]. At the compressor-

combustor interface, the heterogeneities exiting the compressor alter the flow distribution in combustion chamber (affecting the fuel-air mixing and therefore the TET), while on the other hand the aerothermal fluctuation in combustion chamber affects the compressor performance [6–8].
Among the interfaces which can be individuated in a turboengine, the one between combustor and turbine is probably the most critical, since it directly affects the TET and the design of the HPT cooling system. As it will be explained in more detail in the following chapter, the flow field at the combustor-turbine interface is described by four main features:

- A very high turbulence level (up to 25%);
- A non uniform total temperature profile, characterized by the presence of hot streaks (HS) and cold streaks (CS);
- A non uniform total pressure profile;
- A swirling and highly unsteady velocity field;

Considering this, one can clearly understand that the imposition of a uniform flow field at the turbine inlet is a critical approximation of the real flow physics. In this sense, the application of realistic non uniform inlet conditions during the design phase could constitute a significant improvement both for the aerodynamic and the cooling system performance of modern HPTs. Nevertheless, to be able to do so, it is mandatory in a first phase to develop robust numerical tools which are able to solve accurately such a complex flow field.
The assessment of numerical approaches for the analysis of the combustor-turbine interface constitutes the main topic of this thesis. In the appendix, another problematic interface will also be briefly discussed: the one between compressor and inlet duct.

CFD for combustor-turbine Interaction

The rapid increase of the available computational power contributes to a fast development of the Computational Fluid Dynamics (CFD). Nowadays, CFD is an essential tool for the industrial everyday's work and for the research community. The use of advanced numerical software during the design phase represents one of the main reasons for the improvement of the state of the art of turbomachinery components in the last 40 years. Nevertheless, the application of classical numerical techniques to the combustor-turbine interaction presents major problematics requiring further investigation.

The flow field within a gas turbine is intrinsically unsteady because of the

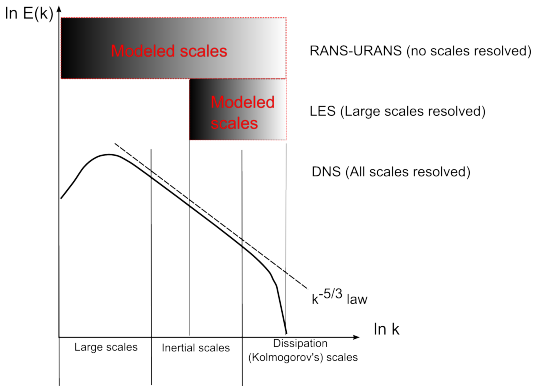

Figure 4.: Turbulent scales resolved and modeled by each approach (elaborated from [9].

interaction between static and rotating parts (i.e. stator and rotor blades) and because of the turbulent fluctuations characterizing the flow field.
Turbulent fluctuations are characterized by a wide range of frequencies and are intrinsically present into the Navier-Stokes (NS) equations [10]. Three main numerical approaches exists for their resolution: Direct Numerical Simulation (DNS), Large-Eddy Simulation (LES) and Reynolds-Averaged Navier-Stokes (RANS). The part of turbulent spectrum which is directly resolved by each approach is shown in Fig. 4.

- From a conceptual point of view, the **Direct Numerical Simulation** (DNS) constitutes the easiest approach possible. It is based in fact on the direct resolution of all turbulent structures generated by the flow field [9, 11]. Historically, this approach has been very useful for the study of the turbulent flow physics. Its main limitation, on the other hand lies in the high-order schemes required to avoid numerical dissipation and in the fact that the number of grid cells to be used is proportional to $Re^{37/14}$ [12] while the computational cost scales like Re^3 [13]. For these reasons, the application of DNS to engineering-type problems is limited to low-Reynolds cases.

- The principle of **Large Eddy Simulation** (LES) is to directly resolve the most energetic structures while modeling only the effect of the smallest scale (Kolmogorow's scale). The smallest turbulent scales drive the energy decay and are more isotropic and universal, therefore limited adjustements of the turbulence model (subgrid scales models, sgs) are required when passing from one test case to another. The transition between resolved and modelled scales is obtained by the filtering operation of the NS equation, which is in most cases linked

to the mesh size. According to the Pope's criterion [9], independently from the sgs model used, the grid must be sufficiently refined to permit the direct resolution of 80% of TKE. This can be formulated as follows:

$$\frac{TKE_{solved}}{TKE_{solved} + TKE_{sgs}} \geq 0.8 \tag{1.2}$$

An estimate of the computational requirement for wall-bounded LES was given by Chapman [14] and recently revised by Choi et al. [12]. A wall modeled LES requires a number of grid points which is proportional to Re while it scales like $Re^{13/7}$ for wall resolved LES.
Nowadays, the computational cost of LES is becoming acceptable for flows in which a detailed resolution of the wall is not required. This explains the rapid diffusion of this method to simulate the flow in industrial combustion chambers [15–17]. On the other hand, despite the increased popularity of LES applied to HPT airfoils [18–21], its computational cost remains prohibitive for the current industrial practice.

- To limit the computational costs, **Reynolds-Averaged Navier Stokes** (RANS) approaches are introduced. These are based on the application of a time-average to the NS equations to eliminate the unsteady terms. The effect of the turbulence on the mean flow field (which explicitly appears into the system because of the non-linear nature of the NS equations) is reproduced by turbulence models [22]. Because of its limited computational cost, RANS is by far the most popular numerical method in use during the design phase, despite the fact that the different turbulence models suffer from a lack of universality.
A time dependent solution of the flow field using classical RANS models is defined as Unsteady-RANS (URANS).

The application of typical CFD methods to the combustor-turbine interaction presents several issues, which are discussed in detail in the next chapter. In this part, a preliminary overview is given:

Issue I: The combustor-turbine interaction is not limited to the aerothermal effect of the flow field at the combustor outlet on the turbine blade. Some recent works (Klapdor [23], Roux et al. [24]) demonstrated that the NGV blade has a potential effect on the combustor flow field.
Considering this, the best way of investigating the combustor-turbine interaction would be to solve both components at the same time in an integrated framework. From a numerical point of view, the combined resolution of a low-Mach flow (for the combustor) and a transonic flow (for the turbine) with a unique solver is problematic and requires the development of ad-hoc codes, to guarantee the stability and the accuracy of the solution [23].
To overtake this problem, recently an approach is proposed, which is based

on the use of two different codes for the combustor and HPT communicating with each other to get a unique converged solution (defined as coupled approach). This idea is rather new and very promising, due to the possibility of using solvers which are optimized for a particular component.

Issue II: a less elaborated but more practical way of reproducing the effect of the combustion chamber on the gas turbine aerothermal field is to solve the HPT flow field only, by imposing non-uniform realistic boundary conditions at the inlet. The main drawback of this approach can be individuated in a lack of validation for classical RANS methods when applied to the extreme conditions observed at the combustor-turbine interface. In fact, classical test cases in use for the validation of CFD for turbomachinery (such as [25, 26]) normally consider axial and uniform flows with no more than 5% of turbulence at the inlet, which is about 1/5 of what is normally expected in recent engines.
Before including the combustor-turbine interface into the design process, it is therefore necessary to have a better understanding in the actual capabilities and limitations of RANS in reproducing the flow field of HPTs operating with realistic inlet conditions.

Context and outline of this thesis

The present PhD thesis was launched in the framework of the European project COPA-GT (Coupled Parallel Simulations of Gas Turbines). The aim of the present work is to develop new methodologies and to analyze the accuracy of the existing ones when applied to multicomponent simulations in turbomachinery. The attention is mainly focused on the combustor-turbine interaction, which represents the most critical interface of modern turboengines.
To do so, the thesis is divided in two main parts, which are representative of the two major problematics previously introduced. Its structure is presented below:

- **Chapter II** Presents a detailed literature review of the main numerical methods employed for the combustor-turbine interaction.

Part I To take into account the mutual interaction between combustor and turbine, an integrated framework is developed to allow the resolution of the two components at the same time by using multi-code techniques.

- **Chapter III.** The theory behind a multi-code coupled procedure is discussed in detail. To simulate the interaction between different components, the two codes solving the domain upstream (i.e. the combus-

tor) and the one downstream (i.e. the turbine) must exchange some information. The information to be passed depends on the approach used to solve the upstream and downstream domains. The coupling methodologies are thus initially presented for URANS-URANS and LES-LES approaches for the upstream and downstream domains respectively, and then generalized to LES-URANS.

- **Chapter IV.** Three different coupling procedures are developed. These are suited to LES-LES, LES-URANS and URANS-URANS applications. All methods are validated on test cases with increasing difficulty.

- **Chapter V.** One of the coupling techniques previously developed and validated is applied to a realistic combustor-turbine test case. The aim is to have a detailed comprehension on the aerothermal interaction between the two components. The test case is designed in the framework of this thesis and described in detail.

Part II. The strong and weak points of RANS and LES applied to the study of the hot streak migration in HPTs are discussed. In this sense, a LES tool for the external aerodynamics of turbine blades is developed and validated for the first time at the Von Karman Institute (VKI), with the aim to be applied in the future to the investigation of the HS migration in turbine. In the last chapter, LES and RANS results obtained for a HPT stage with realistic inlet conditions are compared.

- **Chapter VI.** In the optics of the development of a LES tool for turbomachinery, a first test case is investigated. This consists of a low pressure turbine (LPT) operating at a relatively low Re. The complex flow field characterizing the airfoil is examined in detail.

- **Chapter VII.** A second test case to validate the LES tool for turbomachinery is identified in a prismatic HPT profile, characterized by high Re. The airfoil was the object of a large experimental campaign at VKI to study the pressure distribution at the trailing edge of HPT profiles under different outlet conditions. The strong and weak point of the tools emerged during the validation process are discussed, together with the future works necessary to complete their development.

- **Chapter VIII.** To conclude, an experimental test case designed to study the combustor-turbine interaction is analyzed by LES [27] and RANS. In particular, the accuracy of RANS for realistic flow fields in

turbine is investigated by employing the most common two equations models used during the design phase.

- **Chapter IX.** The final conclusions of the thesis and the future works are discussed.

In appendix A, the unsteady investigation of the mutual effect between an inlet duct and a compressor is presented. This part, which is not directly linked to the rest of this thesis, aims at discussing the unsteady problematics which can be observed in another critical interface of turbomachines.
In appendix B the validation of the non-reflecting conditions implemented in OpenFOAM in the framework of this thesis to avoid spurious reflections at the LES outlet is presented.

Chapter 2.

Literature Review

The interaction between combustion chamber and turbine is a relatively new topic in the turbomachinery community. Even though the first pioneer facilities date from the early 80's [28] and the 90's [29], the first machine-representative experimental test rigs and numerical investigations appear only from the 00's.
Despite the fact that the real flow at the combustor outlet is characterized by non-uniform temperature, pressure and velocity distributions together with very high turbulence levels, a large majority of the works studies these aspects separately. The first part of this literature survey follows the same "segregated" approach; the flow at the interface between combustion chamber and turbine and the most recent experimental apparatus are described in detail in section 2.1. In section 2.3, an overview on the effect of non-uniform temperature profile on the HPT aerothermal field is given. The effect of swirl and high turbulence are taken into account in section 2.3 and 2.4 respectively. To conclude, the few studies aiming at reproducing all these aspects at the same time are discussed in section 2.5.
In a second part, the very recent and almost unesplored topic of the influence of the HPT on the combustion chamber flow field is presented in section 2.6. To conclude, the attention is focused on the numerical methodologies in use to reproduce the combustor-turbine interaction, section 2.7. The complex flow at the interface poses in fact several challenges from the numerical point of view which are not yet fully clearified.

2.1. The flow field at the combustor-turbine interface

Nowadays, the requirement of low emissions brings the main manufacturers towards the design of combustion chambers based on lean premixed flames (Lean Burn combustors, LBC): this concept (schematized in Fig. 2.1-a) is characterized by much lower NO_x emissions with respect to classical Rich-Quench-Lean (RQL) geometries (Fig. 2.1-b), at the expenses of a weak flame stability. To avoid the quenching of the flame, the injection of premixed fuel-air flow is characterized by high swirl, which generates vortex breakdown at the center of the combustion chamber and prevents from the flame blow-off. For the same reason, the cooling of modern LBC is provided

by effusion plates only.
For RQL geometries, on the other hand, the fuel is injected separately in a swirling stream of air, while the cooling enters into the combustor from diluition holes and slots at the endwalls. As a consequence, for both design concepts the temperature field is highly non-uniform at the HPT inlet. Comparing the flow field at the outlet of LBC with RQL combustor, one can observe that for LBC the temperature results more uniform in the middle of the passage, while reaching lower values closer to the wall. On the other hand, the strong swirl employed to stabilize the flame, generates a more pronounced residual swirl at the combustor outlet [30].
To perform an experimental campaign at actual machine conditions is ex-

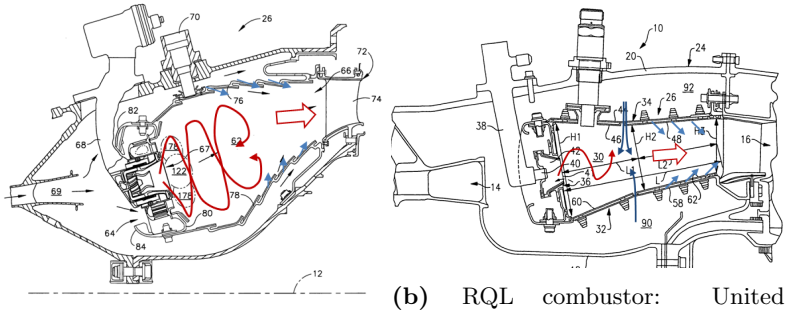

(a) Lean Burn combustor: General Electric patent US6389815

(b) RQL combustor: United Technologies Corporation patent US7954325

Figure 2.1.: Rich Quench Lean combustor scheme (a) and Dry Low NO_x combustor scheme (b). The fuel and air entering the primary zone are indicated in red, the diluition air in dark blue and the cooling flow in light blue.

tremely difficult, and therefore a very limited number of works exists in this sense. The temperature distribution measured at the outlet of a real RQL combustor of a military engine is reported by Povey et al. [31], from which Fig. 2.2 is taken. Here one can appreciate the pronounced temperature non-uniformity characterizing the flow at the combustor outlet: the peak of temperatures are in the order of 2200 K, while lower temperatures than 1500 K are obtained in regions closer to the endwall.

To simplify the measurements, the combustor-turbine interface is commonly analyzed by developing non-reacting test rigs simulating the flow of real combustors. In what follows, an overview on the most recent ones is given in more detail.
A lean burn combustor simulator has been recently designed by Hall et al. [32] to be installed in the QinetiQ Enhanced Isentropic Light Piston Facility rig in Oxford [33]. The objective of the design was to reproduce a range of realistic swirl and temperature distortion profiles, by also taking

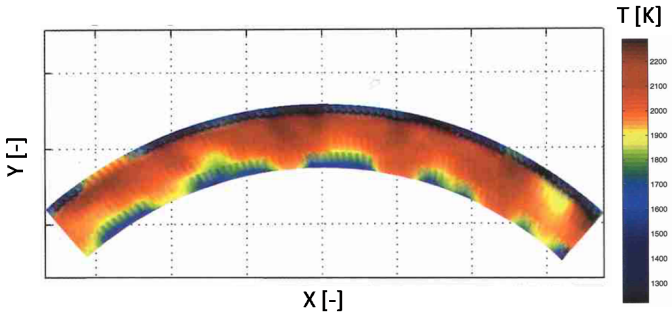

Figure 2.2.: Temperature field measured at the outlet of a military engine [31].

into account the real turbulence level and pressure distortion of real machines. The design was performed by a detailed URANS-based numerical campaign. The final geometry obtained is shown in Fig. 2.3. An axial swirler characterized by a swirl number $Sn = 0.4$ is used to inject hot air. It is known that non-reacting chambers are characterized by the formation of unstable phenomena (such as processing vortex core vortices, PVC) which are not present (or less predominant) in real reacting machines; the flow field is then stabilized in the current case by means of an additional axial injection of air from the center of the swirler. Cold air is injected by slots to simulate the endwall cooling.

The first experimental visualizations on the flow at the outlet of the com-

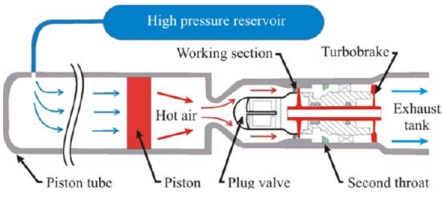

(a)

(b)

Figure 2.3.: The OTRF QinetiQ experimental facility (a) and the hot streak generator designed by Hall et al. [32] (b). Pictures from [32, 34].

bustor simulator have been published very recently by Hall et al. [34] and reported in Fig. 2.4, together with some meaningful numerical results obtained during the design process. The total temperature profile obtained for the current case is mainly radial. On top of that, the swirl remains well defined and coherent at the combustor outlet. The swirl angle is characterized by peaks of $\pm 25^o$, generating a non-negligible pressure minimum at the

passage center.

For the current test case, an experimental visualization of the turbulence

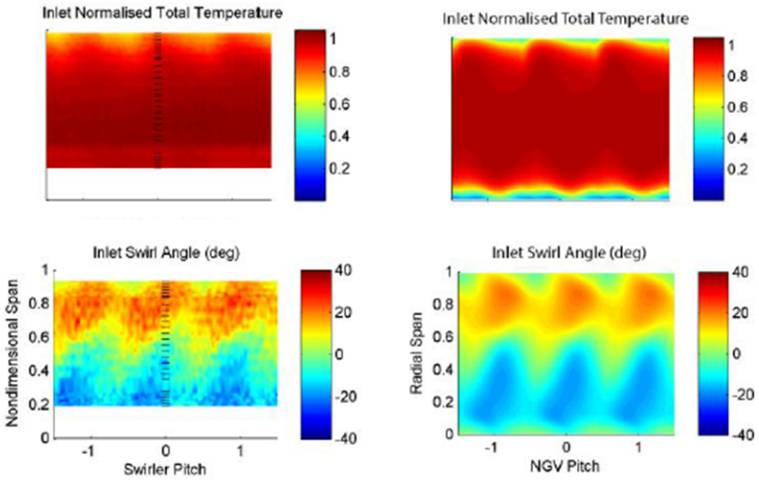

(a) **(b)**

Figure 2.4.: Experimental (a) and numerical visualization (b) of the flow field at the outlet of the QinetiQ test rig [34].

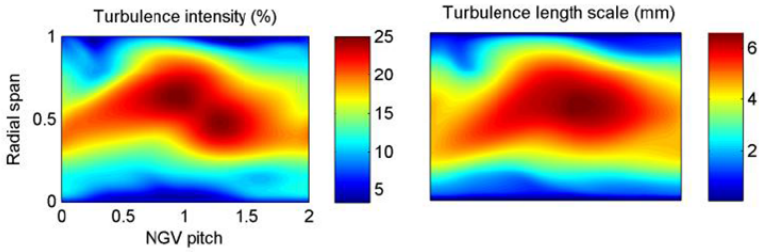

Figure 2.5.: Turbulence field at the QinetiQ test rig outlet obtained by URANS simulation [32].

field obtained is not yet available, therefore the URANS-based prediction of the turbulent intensity and lengthscale is shown in Fig. 2.5. A central high turbulence spot is numerically predicted, which reaches up to TU=25%.

Another recent engine-representative combustor simulator has been designed within the European project FACTOR, with the aim to represent a typical LBC [35]. A full annulus non-reactive combustor simulator is coupled with

a 1.5 HPT stage. Hot flow ($T_{tot,M}$=531K) is injected by a swirler characterized by a swirl number comprised between Sn=0.6-0.7 (which is typical for LBC [30]). Here it is mixed with a cold flow ($T_{tot,c}$=300K) entering from effusion plates installed along the walls. The ratio between hot and cold massflow is such that the reference total temperature at the NGV inlet is $T^{ref}_{tot,P40} = 450K$. To avoid excessive unsteadiness and to get a more representative temperature profile at the outlet, the swirler is placed inside a 55 mm long duct. The full annulus is assembled with 20 swirlers, 40 NGVs and 60 rotor blades.
The test rig is not yet operational, therefore detailed experimental results are not yet available. Nevertheless, preliminary investigations are performed on two reduced-size test rig operating at the University of Florence, which reproduce a limited sector of the whole combustor simulator including one and three swirlers respectively. The experimental observations are discussed in detail in [36–38] and briefly summarized herein.
A PIV visualization of the flow field at the center of the reduced-size com-

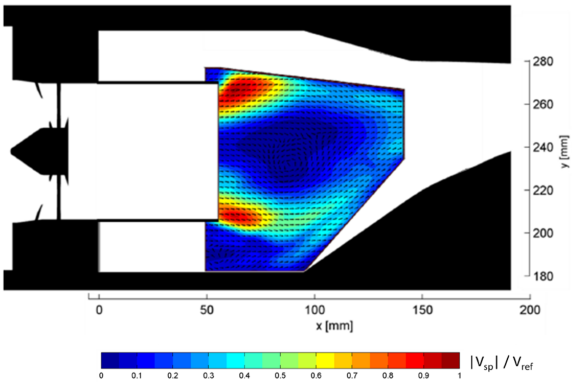

Figure 2.6.: PIV of the velocity field measured at the center of the combustor simulator [36].

bustor simulator is shown in Fig. 2.6 [36]. It can be observed here that the typical structures of a modern swirl-stabilized combustor are present. These are the corner vortex (under the inner jet) and the central recirculation zone generated by the vortex breakdown. The 55 mm pipe moves the recirculation zone closer to the outlet and enhances the stability of the swirl. As a result, the outlet swirl results more intense with respect to the QinetiQ test rig. The flow measured at the outlet is shown in Fig. 2.7. The temperature non-uniformity is characterized by the parameter T_{nd}, defined as:

$$T_{nd} = \frac{T_{tot} - T_{tot,M}}{T_{tot,M} - T_{tot,c}} \tag{2.1}$$

Where $T_{tot,M}$ and $T_{tot,c}$ were previously defined. For the current case, the presence of a marked hot spot at the passage center can be depicted. The maximum swirl angle is particularly intense, arriving up to 45^o. The turbulence distribution, reported in Fig. 2.7-c, shows that the peak of turbulence intensity is reached at the center of the vortex core, where it ranges between 28 and 30%.

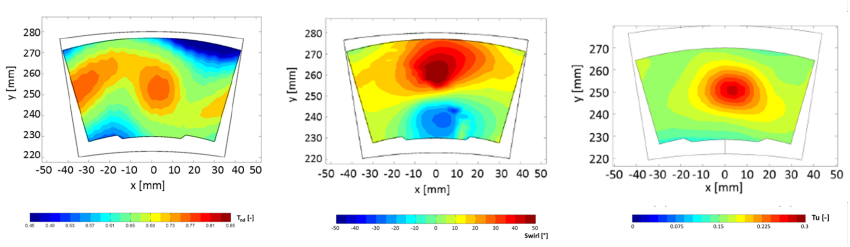

(a) **(b)** **(c)**

Figure 2.7.: Outlet temperature (a), swirl (b) and turbulence conditions (c) measured at the outlet of the FACTOR combustor simulator [36, 37].

2.2. Hot streak effect on the HPT stage

In most of the cases, the combustor-turbine interaction is studied by taking into account only the presence of a non-uniform temperature contour at the turbine inlet.

Relevant experimental as well as numerical studies were based on the QinetiQ Isentropic Light Piston Facility (ILPF); before its recent upgrade to include the swirlers [34], from 2008 to 2014 the test rig was used in the framework of the Brite-Euram Turbine Aerothermal External Flows programme (TATEF II) to study the HS migration in HPT stages. In particular, the HPT transonic stage MT1 has been largely investigated, constituting one of the most complete test cases for this topic.

The MT1 stage is composed by 32 stators and 60 rotor blades. Nevertheless, for computational reasons, several numerical studies considered a scaled geometry with 32 stators and 64 rotors, to get an exact 1-to-2 periodicity between the blades; as a drawback, Salvadori et al. [39] pointed out that the increment of the rotor blade count by 7% generates a non-negligible reduction of the aerodynamic load at midspan with respect to the original design.

Povey et al. [31] investigated the effect of a temperature non-uniformity on the MT1 nozzle aero-thermal field considering a 1-to-1 periodicity between blades and HS. The authors measured the heat transfer by using thin film

gauges installed along the blades. A Nusselt number distribution was then obtained by scaling the measured heat transfer with respect to a reference adiabatic wall temperature (estimated for uniform inlet conditions). The Nu distribution at 50% of span is shown in Fig. 2.8-a for the uniform and non-uniform cases with two different clocking conditions: hot streak aligned with the passage center (OTDF1) and with the blade LE (OTDF2). For the OTDF2 configuration, a higher Nu on the suction side is depicted with respect to the other operating conditions. As schematized in Fig. 2.8, this was attributed to the fact that the limiting steamline (marked in black) is not exactly aligned with the LE. As a consequence, the cold flow migrates along the SS for OTDF1, while for OTDF2 the hot streak directly impacts the SS of the vane.
An et al. [40] analyzed the HS migration within the NGV passage of an heavy duty HPT by means of URANS simulations. The hot streak at the NGV inlet is simply generated by an analytical function to get an elliptic shape, resulting in a more marked hot spot with respect to realistic machine profiles. Differently from Povey et al. [31] a 1-to-2 periodicity is considered between HS and blades.
The HS propagation obtained for different clocking positions is shown in Fig. 2.9. For $RPLE = -2\%$ (HS aligned with blade 1) the HS entering into the passage is divided in two by the vane. Along the blade PS, the HS is squeezed towards the wall while expanding in radial direction. The elliptoid shape remains instead evident along the SS.
For the opposite clocking configuration (RPLE=81%, HS aligned with blade

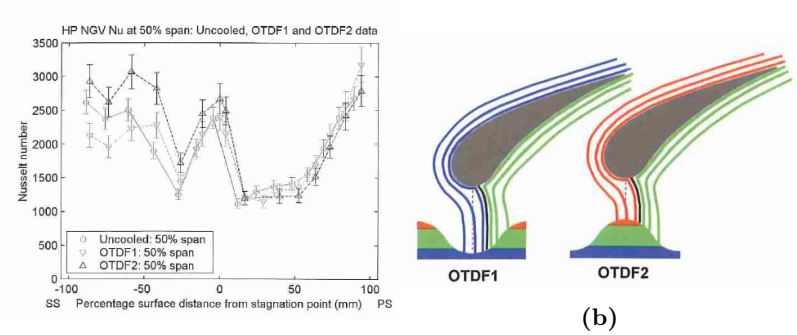

Figure 2.8.: Nu distribution at 50% span of a NGV blade with and without HS imposed at the inlet (a) and schematization of the HS propagation for different clocking positions [31].

2) the HS is squeezed along the circumferential direction in the first part of the passage, while it is elongated again closer to the trailing edge. This is respectively due to the acceleration and deceleration of the flow in the front and rear suction side. As a main result, the HS at the NGV outlet still

keeps its elliptoid shape. When the HS is aligned with the passage center ($RPLE = 31 - 48\%$) it results attracted towards the pressure side of the adjacent blade.

From the aerodynamic point of view, one can conclude that the HS does

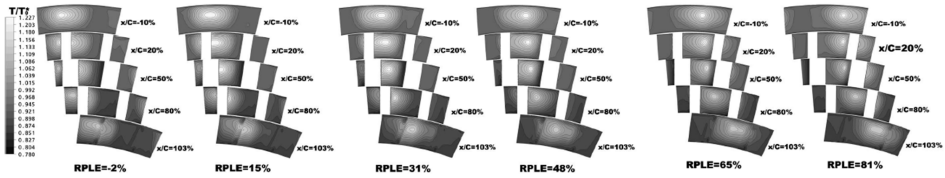

Figure 2.9.: Migration of the HS in a stator passage for different clocking configurations [40].

not have any effect on the NGV if not accompanied by a non-uniform inlet total pressure distribution [31, 41].
On the other hand, it is demonstrated that a HS imposed at the HPT stage inlet strongly affects the flow incidence on the rotor. The driving mechanism determining the change of incidence is analogous to the migration of a wake in the relative frame of reference, described for the first time by Kerrebrock et al. [42]; at the outlet of a NGV operating with a non-uniform inlet temperature field, the fluid is characterized by an approximately constant total pressure and a non-uniform density. As a consequence, the higher temperature (and lower density) flow has a higher absolute velocity with respect to the flow at lower temperature. The corresponding velocity triangles in the relative frame of reference are shown in Fig. 2.10-a. The HS is then characterized by higher incidence, and migrates towards the pressure side of the blade, while the cold flow (with low incidence) tends to migrate towards the suction side. This mechanism, known as segregation effect, is confirmed by the studies of Dorney et al. [43] and more recently by other authors [44–46].

Beard et al. [45] quantified the influence of the HS on the rotor relative inlet angle by experimental measurements at the MT1 stator row outlet. In Fig. 2.10-b the difference in relative angle between two tests with uniform and non-uniform inlet conditions is reported. The non-uniform results are limited to the OTFD2 clocking configuration. The high temperature flow at the passage center causes a $+5^o$ increase of incidence, while it decreases to -10^o closer to the endwalls, where the cold flow generated by the cooling of the combustion chamber is present. Butler et al. [47] and Ong et al. [44] also evidence the fact that the hot streak promotes additional secondary flows within the rotor, characterized by two contra-rotating vortices formed in proximity of the PS having the same sign as the endwall secondary flows, Fig. 2.11. The global effect of the HS on the stage aerodynamics is quanti-

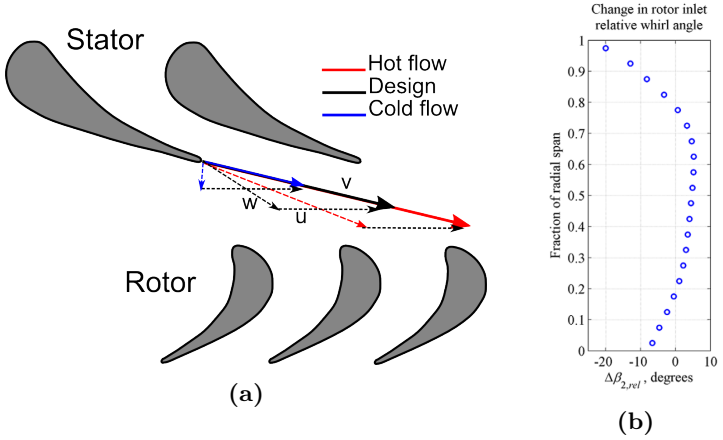

Figure 2.10.: Segregation effect for cold and hot streaks: scheme of the incidence variation elaborated from [46] (a). Experimental measurement of the relative inlet angle to the rotor of the MT1 stage, from Beard et al. [45].

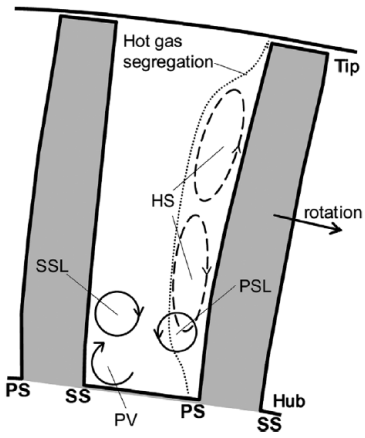

Figure 2.11.: Secondary flows generated by the HS in the rotor passage [**?**].

fied by Beard et al. [45]: the author measured a -0.88% variation in mixed out turbine efficiency with respect to uniform inlet conditions. The variation in incidence taken singularly is estimated to cause a decrease of -0.07% with respect to nominal incidence conditions.
The incidence variation and secondary flows formed in the relative frame of reference have an evident effect on the rotor heat transfer. This was investigated in detail by Qureshi et al. [48], by performing a numerical and

experimental campaign on the MT1 test case. Figure 2.12 depicts a visualization of the $T_{ad,w}$ obtained by URANS simulations on the MT1 scaled geometry. The segregation of the hot streak on the PS can be pointed out, together with a migration of the cold flow towards the SS. The HS is spread along the PS by the aforementioned contra-rotating vortex pair induced by the temperature gradient. The change in driving temperature leads to a significant variation in heat transfer along the blade, which is doubled or

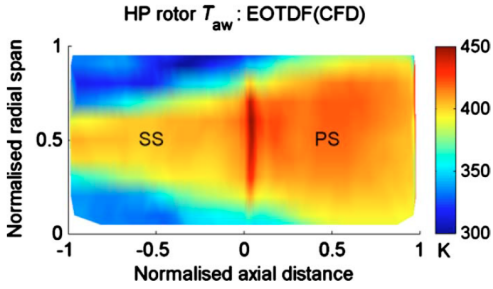

Figure 2.12.: Temperature distribution calculated for the MT1 rotor blade [48].

halved in different areas with respect to uniform conditions. The HS effect on the heat transfer coefficient appears instead to be less significant.
Qureshi et al [48] characterized the heat transfer along the endwalls of the MT1 rotor. The heat transfer measurements were obtained by using a series of thin film gauges [49] installed in discrete points along hub and shroud; the discrete values were then interpolated to get a continuous mapping on the whole surface. Starting from the heat transfer, $T_{ad,w}$ was evaluated assuming an equivalent Nu distribution between the cases with uniform and non-unifom inlet temperature. The results on the rotor casing demonstrate that a realistic inlet temperature profile determines a marked reduction in $T_{ad,w}$ with respect to uniform conditions, expecially close to the rotor leading edge. According to these results and to further numerical investigations, Salvadori et al. [39] suggest the possibility of using the coolant from the combustion chamber to protect the high pressure turbine casing.
The effect of the clocking between NGV and HS on the rotor heat transfer was studied in detail by He et al. [50]. The authors carried out an extensive numerical campaign employing both RANS (mixing plane) and URANS on the real MT1 configuration with 32 NGVs and 60 rotors (8 NGVs and 15 rotors were modeled for the unsteady computation). Two different temperature profiles were considered, representing 8 and 32 HS for the whole annulus (i.e. a 1-to-4 and a 1-to-1 periodicity with respect to the stator blades). The temperature profiles are rather simplified and not representative of real machine conditions, nevertheless the conclusions obtained can

be considered of general interest. When the number of HS and NGV blades is the same, the rotor heat load appears influenced by the HS-NGV relative position. The effect of the clocking on the rotor can be quantified in fact in a 8% variation in heat load. On the other hand, for the case with 8 HS, the heat load on the rotor appears independent from the HS-NGV clocking, and the time averaged temperature on the PS appears 5% lower than the previous case.

2.3. Swirl effect on the HPT stage

The effect of realistic swirl levels typically found at the outlet of modern LBCs were investigated in detail at the Technishe Universität Darmstadt [51, 52] by using a low speed cascade wind tunnel equipped with a swirl generator and two dimensional vanes. The periodicity between swirlers and NGV blades was 1-to-2. Results reported in the current review are limited to the case with $Sn = 0.8$, swirlers placed at $2.5 \cdot h$ distance from the vane LE and aligned with the passage [51]. To quantify the losses caused by the swirl, the flow visualizations at NGV outlet are reported in Fig. 2.13. The plane downstream is colored by the loss coefficient ζ, defined as:

$$\zeta = \frac{p_{tot,ave,in} - p_{tot,out}}{p_{tot,ave,in} - p_{out}} \tag{2.2}$$

Where subscripts *in* and *out* are referred to the NGV inlet and outlet. With respect to axial inflow conditions, the imposition of a swirl at the inlet significantly changes the NGV behavior. The revolving flow upstream from the passage, characterized by pronounced inlet angles (well over 30^o), leads to a variable incidence at the vane LE in spanwise direction. A negative incidence occurs in the upper region, while a positive incidence is generated closer to the hub. The positive incidence provokes a separation bubble close to the hub, which causes the extended loss area indicated as L2 in Fig. 2.13.

In terms of losses, a well defined area L3 can also be identified. This is generated by the shear stresses of the vortex V1, whose position and intensity suggests that the swirl imposed upstream continue to exist through the passage.

The mutual interaction of hot streak and swirl at the inlet of a HPT stage is discussed by Khanal et al [53]. The authors performed a series of numerical investigation on the MT1 stage imposing 2D nonuniform profiles of temperature and velocity at the stator inlet. Four different configurations were studied, considering a vane-aligned or passage-aligned swirl, combined with positive or negative swirl directions (corresponding respectively to decreasing and increasing aerodynamic load at the NGV tip).

Isosurfaces of the HS migrating within the passage are depicted in Fig. 2.14. The swirl influences the HS shape considerably, which appears twisted

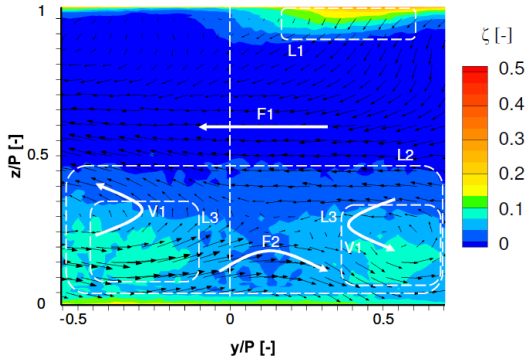

Figure 2.13.: PIV visualization of the vortices formed downstream from a NGV passage with swiril imposed at the inlet [51].

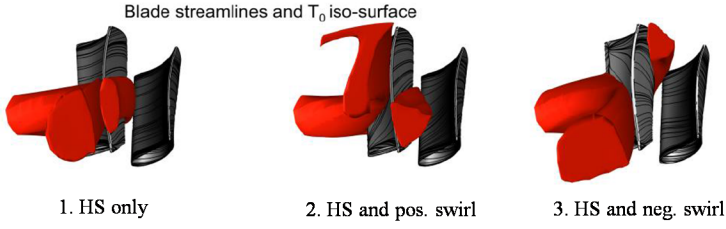

(a) Vane aligned conf.

(b) Passage aligned conf.

Figure 2.14.: Swirl effect on the HS migration from Khanal et al. [53].

and deformed at the NGV outlet; in particular, when swirl and vane are aligned, a positive swirl unloads the NGV tip, but it also transports the hot fluid towards the tip region of the PS, increasing the local heat transfer. A negative swirl, on the other hand, determines the migration of the hot flow towards the hub along the PS and towards the tip along the SS. For the configuration with swirl aligned to the passage center, on the other hand, a positive swirl tends to redistribute the HS closer to the casing, which results

instead less thermally loaded when a negative swirl direction is applied. The swirl effect on the rotor blade is also important; a positive swirl determines a mild migration of the flow towards the PS-tip region, while a more decise migration towards the hub can be observed for a negative swirl direction. The effect of the swirl-vane alignment on the rotor appears instead to be almost negligible. From the investigation, the authors conclude that the passage aligned configuration with negative swirl presents the most interesting features from the aero-thermal point of view, being characterized by the lowest thermal load at the rotor tip together with low pressure losses for the NGV.

2.4. High turbulence effect on the HPT stage

Even though it is well known that very high turbulence intensity is reached at the combustor-turbine interface, the actual value of TU has been quantified only by recent studies. Cha et al. [54] measured the turbulence level and lengthscales at the interface between a RQL combustor and a NGV operating in "cold" conditions. The results, reported in Fig. 2.16, show that the surface-averaged turbulence intensity is higher than 20%, while it reaches peaks of 35% at the center of the passage. The lengthscale is instead comprised between 15% and 25% of the blade chord.

Very few experimental and numerical investigations can be found in liter-

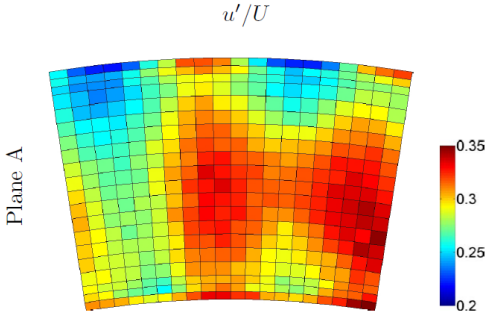

Figure 2.15.: Turbulence level measure at the outlet of a RQL combustor operating in "cold" conditions [54].

ature aiming at investigating how such a high turbulence level affects the HPT performance. Radomsky et al. [55] studied from the experimental point of view a scaled-up turbine vane geometry placed in a low speed with tunnel. An active grid placed at about $2C$ upstream from the vane leading edge generates up to TU=20% at the passage inlet. The effect of the

high turbulence level on the blade aerodynamics is depicted in Fig. 2.16, where the total velocity contours obtained for a highly turbulent flow are compared to a laminar inlet case. The differences between the two cases appear almost negligible, even though the authors point out the presence of a larger region of high-speed fluid for the highly turbulent flow field, which is due to an anticipated transition of the boundary layer along the blade SS. The impact of the turbulence on the heat transfer is instead more evident: high turbulence levels anticipate the laminar-to-turbulent transition of the boundary layer along the suction side, and increase the global heat transfer along the PS. These effects are well documented by several authors, such as Arts et al. [56].

Jenkins et al. [57, 58] experimentally investigate the attenuation of the hot

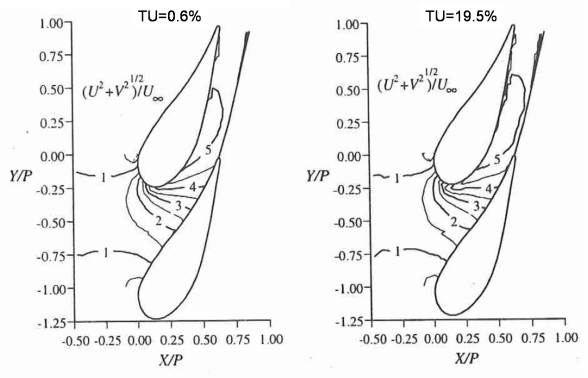

Figure 2.16.: Total velocity isolines for low and high free-stream turbulence levels. Experimental investigation from Radomsky et al. [55].

streak within the stator passage due to a high inlet turbulence level. The study was performed on the test rig shown in Fig. 2.17-a. Two vane passages are installed in a closed-loop low speed wind tunnel. The hot streak generator consists of a metal duct with electrical resistances, designed to give a temperature ratio of $T/T_{\text{inf}} = 1.1$ at high turbulence. Different turbulence intensities can be generated by using different grids, installed halfway between the HS generator and the vanes.

Figure 2.17-b shows the HS close to the NGV outlet (position B in Fig. 2.17-a) for Tu=3.5% and Tu=20%. For the high turbulence case, the hot spot at the NGV outlet appears much more spread and attenuated in intensity, leading to conclude that the mainstream turbulence level can have a significant effect on the aerothermal behavior of the HPT stage. The same conclusions are also in line with similar numerical investigation conducted by Wang et al. [59] on an industrial HPT stage.

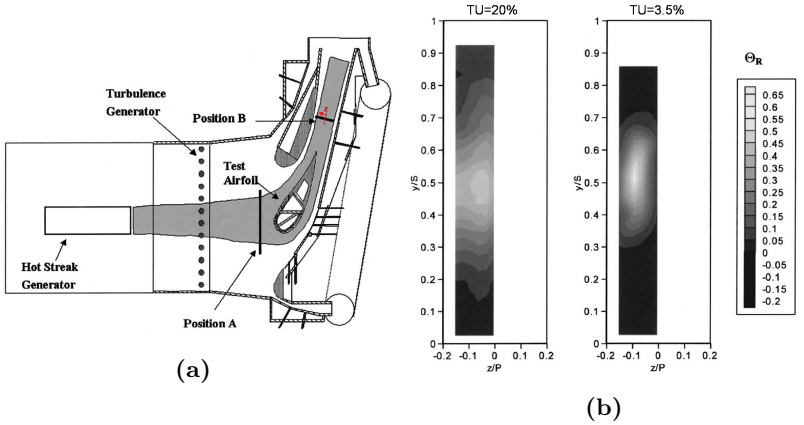

Figure 2.17.: Experimental test rig used by Jenkins et al. [57, 58]. to investigate the interaction between HS and turbulence level (a). HS visualization on plane B for two different turbulence levels, results are shown for negative Z only (b).

2.5. Combined effect of temperature distortion, swirl and high turbulence on the HPT stage

Historically, the different features of the flow at the outlet of a combustion chamber have been investigated separately, as it clearly emerges from this review. At this purpose, in 2013 Khanal et al. [53] pointed out how "there appears to be hardly any published work investigating the combined effect (of swirl, temperature distortions and turbulence) on HPT performance". In reality, swirl, total temperature distortion and high turbulence influence each other and a realistic reproduction of the HPT aerothermal field cannot be obtained without considering all these elements at the same time. An interesting discussion in this sense is given by Khanal et al. [53], whose work is described in more detail in section 2.3. The authors pose the question wether the combined effect of swirl and non-uniform inlet temperature at the HPT inlet can be reproduced by simply superimposing the results obtained by two different simulations, modelling respectively the isolated effect of non uniform temperature and swirl.
At this scope, the heat flux on the rotor blade for a uniform inlet case was subtracted from the swirl-only, the hot streak-only, and the combined swirl-hot streak simulation to derive the corresponding "perturbed heat flux". The distributions obtained for the two cases including swirl and HS separately were then superimposed. The superimposed results are then compared with the ones from combined swirl-hot streak simulation in Fig. 2.19. The differences between the two fields are marked. In particular, a simple

superposition of the single effects leads for the current geometry to a much cooler tip area. This demonstrates that the impact of swirl and hot-streak in the aerothermal solution is clearly non-linear and must be both modeled at the same time.

Dyson et al. [60] performed a set of large scale URANS simulation of

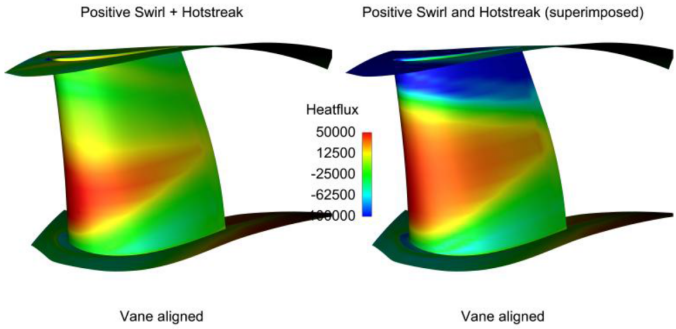

Figure 2.18.: Rotor blade surface heat fluxes. Solution of the HS-swirl combined case (left). Superimposed solution of two separated simulations (right) [53].

an industrial two-stages HPT by modeling non uniform fields of T_{tot}, p_{tot}, flow angles and turbulence quantities at same time. The interest in such a comparison lies in the fact that the use of 1D profiles at the HPT inlet is a classical method employed in industry to study in more detail the aerothermal behavior of the turbine stage.

Figure 2.19 shows the temperature distribution at the outlet of the first stage NGV for the cases with 1D and 2D inlet conditions. For the second case, the HS was aligned with the passage center. Even if the mean average temperature is the same, 2D inlet profiles cause a marked radial migration of the HS, which cannot be reproduced with 1D conditions.

Based on similar observations, Shahpar et al. [3] optimized for the first

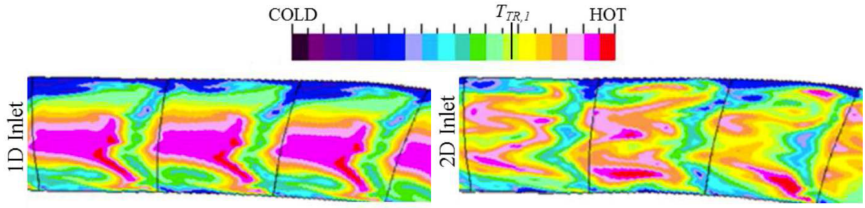

Figure 2.19.: Total temperature outlet at the high pressure NGV outlet computed with 2D inlet boundary conditions (left) and 1D inlet boundary conditions (right) [60].

time a cooled high pressure NGV by imposing realistic 2D non-uniform inlet profiles: the automatically-optimized airfoil leads to a 1% improvement in efficiency with respect to the original hand-designed configuration. This work evidences that there is room for improvement of the state of the art by including the real combustor-turbine interface in the design procedure.

2.6. Potential effect of the turbine on the combustors

The potential effect of the turbine on the flow field of the combustion chamber is a rather unexplored topic. As for the author's knowledge, only two research groups in europe investigated the problem in more detail.
A first publication in this sense is due to Roux et al. [24]. The authors applied LES to reproduce the flow field within an industrial RQL combustion chamber. Two simulations were performed and compared between each other: in the first one, only the combustion chamber is modeled, while for the second one the NGV downstream is also included into the numerical domain. The potential effect of the NGV on the combustor can then be quantified by comparing the results obtained. A view of the full domain is shown in Fig. 2.20-a, while the mean and RMS temperature profiles detected in different positions within the combustor are reported in Fig. 2.20-b.
The influence of the NGV is evident in the downstream region of the combustion chamber, both in terms of mean and fluctuating quantities. The authors also detected the main resonance modes of the combustion chamber from the pressure signals. These appears to be highly affected by the presence of the NGV. Without the blades downstream, a single mode at 790 Hz is observed, while two modes (at 440 and 600 Hz) appear when the stator is included into the analysis.
Klapdor et al. [23, 61] developed a steady RANS solver (recently generalized to handle unsteady simulations [62]) which is able to solve at the same time the reacting low-Mach flow in combustion chamber and the transonic flow in turbine. The solver has been employed for two different simulations of an industrial RQL combustion chamber with and without NGV downstream. A comparison of the velocity distribution at different distances from the NGV LE is reported in Fig. 2.21 [23]. The potential effect of the NGV is marked between $25 - 50\%$ of the NGV axial chord, while it appears attenuated farther upstream.

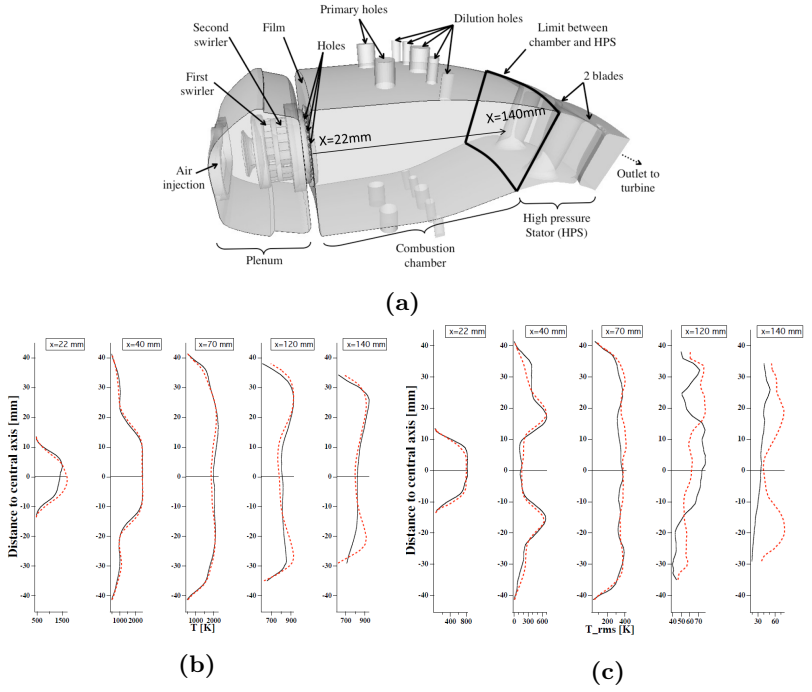

Figure 2.20.: Potentiale effect of the NGV on the time averaged and rms temperature field within a combustion chamber from Roux et al. [24]: geometry investigated (a), time averaged (b) and RMS (c) temperature distribution.

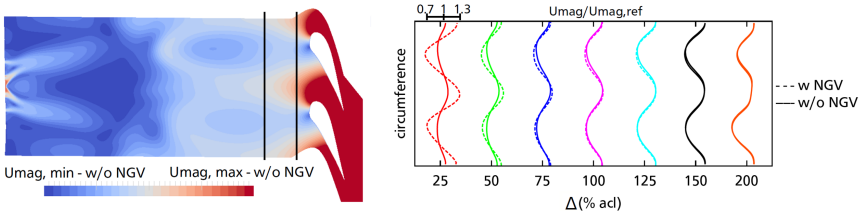

Figure 2.21.: Comparison of the velocity profile in different axial positions within a combustor: simulations with and without NGV downstream [23].

2.7. Numerical challenges for the analysis of the combustor-turbine interaction

As previously pointed out, experimental investigations of the combustor-turbine interaction are difficult from the technical standpoint and economi-

cally expensive. Mordern aeronautical engines employs in fact annular combustion chambers which cannot be reproduced by simply isolating a limited sector of the chamber, since lateral fixed walls in the experimental set-up alter the periodicity of the flow [35]; to study the flow of real machines, the test rig must then include a reproduction of the full annulus, whose construction and set-up requires very important investments.
Moreover, it must be pointed out that the design and operation of large-scale reactive test rigs present several additional problems, which are usually bypassed by using cold experimental configurations. Cold set-ups cannot reproduce in an exact way the flow field of a real combustion chambers, since the combustion plays an essential role in the flow dynamics.
With these considerations in mind, one can conclude that the development of accurate CFD tools is essential to get a better and complete understanding of the physics involved in the combustor-turbine interaction at real-machine conditions. From the numerical works which can be found in the open literature, it can be evidenced that the use of the state-of-the-art numerical tools to study the problem present some technical limitation. Because of that, CFD is used in most of the cases with simplified conditions, which are not fully representative of real working conditions of the machine.
In particular, two main problematics requiring further investigation are individuated and investigated in the framework of this thesis, as explained in the following.

CFD of the potential effect of the NGV on the upstream flow

As previously discussed in section 2.6, the turbine can have a non-negligible effect on the combustor flow field. To take it into account into the analysis, both combustor and turbine should be simulated at the same time in an integrated framework.
It must be pointed out that the flow field within combustion chamber and turbine are very different from each other, requiring very specific numerical features for the solver. The most important ones are listed herein:

- **Solution algorithm:** A low-Mach (quasi-incompressible) reactive flow is present in the combustion chamber, while the HPT usually operates with transonic flows. The resolution of a low-Mach and a transonic flow requires different algorithms to assure the stability and accuracy of the solution. In most of the cases, the combustor is solved by a pseudo-incompressible low-Mach approach or a p-based compressible solver, while ρ-based solvers are generally used in turbine. Nowadays, this trend is still maintained, despite the fact that modern compressible solvers have generally a larger range of applicability.

- **Specific features of the solver:** to cope with the rotor-stator inter-

face, turbomachinery solvers must include sliding mesh, mixing plane and frozen rotor interfaces, while the presence of shocks require the implementation of specific shock capturing techniques. For the combustion chamber, on the other hand, additional equations for the reactive flow must be solved.

- **Grid requirements:** the combustion chamber is a very heterogeneous component, including cooling holes, swirlers and other complex geometrical features. To simplify the meshing procedure, non-structured grids are usually preferred. On the other hand, the airfoils are most of the times modeled with structured grids, to improve the quality of the boundary layer solution.

- **Resolution of turbulence:** it is well known that the complex flow field in combustion chamber is characterized by the formation of unsteady and fluctuating structures (PVC vortices etc.). The use of URANS and LES rather than steady RANS leads in general to considerable improvements in terms of quality of the solution.
  The features of the flow field in combustion chamber (presence of big vortical structures, no particular accuracy required for the boundary layer resolution) are particularly favorable for the application of LES, which has become nowadays the state of the art in industry. On the other hand, despite the increasingly interest in developing LES tools for high pressure turbines [63], its computational cost remains prohibitive for the current industrial practice.

To reproduce combustor and turbine at the same time, two main methodologies can be pointed out in the open literature.

1. A **monolithic approach** has been proposed by Klapdor [23] and Klapdor et al. [61]. The authors developed an in-house ad-hoc code to handle both the low-Mach reactive flow in combustion chamber and the transonic flow in turbine. This was achieved in two steps: (I) extending an incompressible SIMPLE solver to all Mach number flows. (II) Modifying the SIMPLE algorithm to deal with combustion. As previously discussed, the solver has been successfully employed to simulate the combustor-turbine interaction for an industrial configuration [62].

2. Standard commercial and in-house codes are normally optimized for a certain application. To avoid developing a new ad-hoc solver for the combustor-turbine interaction, a **coupled approach** can be employed. This method was firstly proposed during a long-term research program in Stanford whose aim was to simulate all components of a turboengine at the same time [64]. The approach proposed consisted in coupling a LES-based pseudo-incompressible low-Mach solver used for the combustion chamber to

a compressible URANS ρ-based solver for compressor and turbine. A common converged solution for all components was then obtained by exchanging information between the solvers during the simulation;

1. At the compressor-combustor interface RANS outlet conditions were obtained by time-averaging the pressure coming from the LES domain. At the LES inlet, velocity and temperature fields coming from the upstream RANS were imposed. The TKE level resolved by RANS was then used to characterize the synthetic turbulence injected [64–66].

2. At the combustor-turbine interface, body forces were used to drive the mean flow fields at the LES outlet to the solution obtained by the steady RANS downstream, while the inlet conditions for the steady RANS were obtained by time averaging the LES solution [66, 67].

Alternative techniques to exchange information between an incompressible LES solver coupled to a compressible RANS downstream were also presented by Von Terzi et al. [68].
Collado-Morata [69] developed a coupled approach between the compressible LES p-based code AVBP and the compressible URANS ρ-based solver ElsA with the aim to study in the future the combustor-turbine interaction. A common convergence is obtained by exchanging all time-averaged characteristic variables from the LES to the URANS solver, while transferring backwards the pressure from URANS to LES.
The approach was validated for laminar test cases and a turbulent duct; as it will be explained in more detail in chapter 3, such a methodology can result unstable if applied to more complex test cases.
In very recent times, Insinna et al. [70] proposed a coupling procedure between two RANS simulations of combustor and turbine, based on the Ansys p-based SIMPLE solver and a ρ-based in-house code. The procedure was successfully applied to a realistic combustor-turbine test case, while its extension to the use of SAS into the combustion chamber and URANS in turbine is currently ongoing [71].

Despite the increase of complexity due to the necessity of an exchange of information between two distinct solvers, the coupled approach appears more versatile and more suitable to be used at industrial level. With this in mind, the coupled methodology has been further investigated in this work.

CFD for very high-turbulence flows

In section 2.4, it has been shown that the very high turbulence level observed at the combustor outlet (up to 25%) must be carefully taken into account to adequately model the HS migration in turbine. To the author's

knowledge, the actual capability of RANS to handle the complex flow at the turbine inlet (including turbulence) has never been fully assessed. In particular, very few CFD investigations of the HPT with realistic inlet TU levels can be found in literature, and in most of the cases the numerical approach appears questionable and lacks of validation.
Wang et al. [59] performed a numerical study on the effect of the turbulence intensity and HS on the aerothermal behavior of a HPT stage. All simulations were performed on a single-stage turbine by using the $\gamma - Re_\theta$ model coupled with the $k-\omega$ SST, and considering different values of TU at the inlet (this discussion will be focused on the case at TU=20%), together with a simplified non-uniform temperature distribution. The inlet value of ω was computed by considering a reasonable turbulence lengthscale (13% of the span). The distribution of TU obtained within the NGV passage is shown in Fig. 2.22. It can be observed that the turbulence intensity drops significantly between the domain inlet and the passage inlet. This behavior, which is clearly non-physical and only linked to the arbitrary choice of ω, leads to the conclusion that the inlet turbulent boundary conditions should be tuned with care to keep a more uniform and realistic TU level upstream from the blade.

Dyson et al. [60] performed URANS simulations of HPT stages with re-

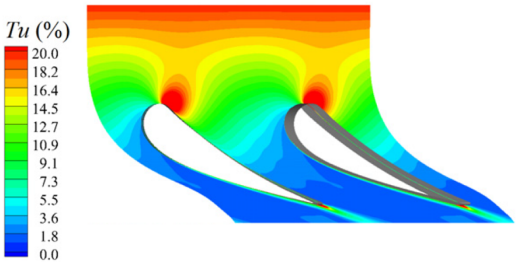

Figure 2.22.: Numerical decay of the inlet turbulence level upstream the NGV LE obtained by RANS. It clearly shows that for high inlet TU the turbulent decay must be tuned with care to avoid a quasi-laminar free-stream flow at the NGV LE. Results from Wang et al. [59].

alistic inlet turbulence levels (see section 2.5 for further details), employing the $k-\omega$ Wilcox model. Even though the effect of TU on the aerothermal field is not directly discussed by the authors, the choice of the $k-\omega$ Wilcox for this kind of computations appears questionable; this model, in fact, is known to be very sensitive to the turbulence variables imposed at the inlet. In particular, high free-stream turbulence levels cause a non-physical production of TKE in the boundary layer interacting with negative pressure gradients [72]. This leads to a dramatic overestimate of the skin friction, which compromises the aerodynamic results. To avoid this behavior, the $k-\omega$ SST model was developed by Menter et al. [73] by limiting the maxi-

mum TKE production of the original $k-\omega$ Wilcox to a maximum value. Other shortcomings in the application of some common RANS models to flows with high free-stream turbulence are discussed by Tucker et al. [74]. The Spalart-Allmaras model, for example, has no explicit free-stream TKE destruction term, meaning that the turbulent viscosity cannot decay. As a consequence, a high turbulence level imposed at the inlet of a muti-stage turbine would remain high (and even increase) all along the domain.

The main difficulties in developing RANS models to accurately reproduce very high free-shear turbulence effects are due to a general lack of experimental test cases. In this sense, more accurate techniques based on a direct resolution of the turbulent structures (DNS and LES) can help in better understanding the physics behind the extreme flow conditions at the combustor-turbine interface and to develop more suitable RANS models for those conditions.

Cha et al. [54] performed both RANS (employing the Realizable $k-\epsilon$

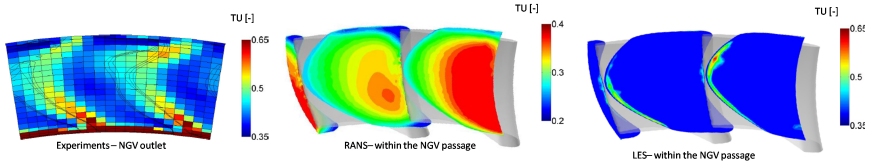

Figure 2.23.: LES and RANS TU distribution resolved within the NGV passage, compared to experimental visualizations at the NGV outlet. Results from Cha et al. [54].

model) and LES investigations on their test rig including a cold RQL combustor simulator with NGVs upstream. Both the combustor-simulator and the high pressure stator were modeled into the numerical domain. The TU distribution obtained by CFD within the NGV passage is shown in Fig. 2.23, together with the experimental visualization at the NGV outlet. When RANS is employed, a high turbulence level which is uniformly distributed along the pitch is observed. The LES prediction, on the other hand, is in a better agreement with the experiments, depicting high turbulence only close to the blade SS. A good agreement of LES and experimental results at the combustor-turbine interface is also depicted by Koupper et al. [75].

In this work, the most common two equations models will be applied to solve the real flow field in HPT stages, including at the same time temperature distortions, swirl and high turbulence levels. RANS results will be assessed against more accurate LES computations performed with a well estabilished in-house solver developed at CERFACS [76].
Moreover, the validation of a LES tool suitable for turbomachinery application is also discussed. In the future, the aim is to employ the tool for the

study of the combustor-turbine interaction.

Part I.

Potential effect in the combustor-turbine interaction

Introduction to part I

As consistently discussed in section 2.6 the HPT stage can have a non-negligible potential effect on the flow field of the combustion chamber. From the numerical point of view, this can be reproduced only by modeling combustor and turbine in an integrated framework. The development of an integrated technique which can be easily implemented at industrial level imposes several requirements:

- **Different codes for the combustion chamber and the turbine have to be used**. In industry, the combustion and turbine department are usually two distinct entities, using different tools that have been extensively validated for their specific purposes.
- **Different approaches to solve the combustor and the turbine are required**. For stability reasons, the low-Mach flow of the combustor is solved with low-Mach quasi-incompressible or compressible pressure based codes, while the transonic flow of the turbine is generally solved with ρ-based codes. Furthermore, the state of the art of CFD in the combustion chamber is moving towards LES, while RANS is still widely used for turbines.
- **The methods have to be non-intrusive**. Solvers employed are optimized for every component, and cannot be heavily modified for this particular application.
- **The methods have to be versatile**. A solver can be replaced without any modification in the methodology.

Among all possible approaches presented in section 2.7, the "coupled" approach seems to be the most suitable one to fulfill these requests. This is based on the use of two different codes for the combustor and the HPT, which are are modeled as two different subdomains. The solvers communicate with each other by exchanging the necessary information to get a coupled solution.

In this part of the thesis, the possible strategies to include the potential effect of the NGV into the analysis are analyzed. Chapter 3 presents an extended theoretical analysis of the coupling between two "segregated" simulations. Based on that, three procedures are discussed and validated in chapter 4. These are suitable for LES-LES, LES-URANS and URANS-URANS applications.
To conclude, the mutual combustor-turbine interaction is studied in chapter 5 for a realistic test case.

Chapter 3.

Multicode Coupling Theory

The motivation leading to the development of a methodology to couple different codes for the contemporary resolution of combustor and turbine is discussed in detail in section 2.7.
Considering the better quality of the solution in combustion chambe when unsteady approaches are used, the aim of the current chapter is to discuss a tool to perform **zonal coupled simulations between two different compressible unsteady solvers** for the application to the combustor turbine interaction.
For stability reasons, a p-based solver for the combustor is coupled with a ρ-based solver in turbine.

The code XiFOAM is chosen to solve the flow field in the combustion chamber. This solver is based on the OpenFOAM platform and is developed for premixed and partially premixed flames. To handle the low-Mach flow field in the combustion chamber, the compressible NS equations are solved by the unsteady p-based algorithm PIMPLE. The solver supports both URANS and LES.
To test the coupling methods proposed, rhoPimpleFoam is employed. This is equivalent to XiFOAM, with the exception of the reactive equations which are not solved.
The flow field in turbine will be computed by the solver TUMDF. This is an unsteady fully-coupled ρ-based solver, from the OpenFOAM-ext platform. The NS equations are solved with a dual TS technique, which demonstrated to be accurate and stable for transonic flows.

3.1. General structure of the coupled simulation

A coupled approach is based on the resolution of a mathematical problem by dividing the whole domain in subdomains. Each subdomain is handled by a different solver, and an unique solution is obtained by exchanging information at the interfaces.
In the combustor-turbine interaction framework, two subdomains are typically used (i.e. two solvers) reproducing combustor (which can be referred as subdomain upstream) and turbine (the subdomain downstream) respec-

tively. A two-way couplig technique aims at reproducing the mutual interaction between the subdomains, while a one-way coupling takes into account only the effect of one subdomain on the other.

As specified by Morata [69] three points shall be defined to set-up a two-way coupling technique:

- The area of the domain where the passage of information between the two solvers takes place.
- The synchronization of the passage of information in time.
- The information shared between one code and the other.

All these issues will be discussed in the current section.

3.1.1. Coupling mechanisms in space

From the study of the state of the art, two different approaches in space can be defined to allow the passage of information between two simulations:

- The upstream outlet and the downstream inlet boundaries collapse in a common patch.
- Part of the domain, located between the upstream subdomain outlet and the downstream inlet, is modeled by both solvers (overlapping region).

A sketch of the two approaches is shown in Fig. 3.1. A coupling with a common patch is used by [77, 78], while the overlapping region is used by [67, 69, 70].

In this work, the passage of information between the subdomains is obtained by interpolating the physical quantities at the upstream outlet and downstream inlet by an inverse distance weighting (IDW) method. This guarantees the possibility of using non-conformal meshes between the domains.
The IDW procedure can be explained considering as example the interpolation of the information coming from the downstream subdomain to the upstream outlet. The IDW method can be mathematically expressed as:

$$u_{x_{j,d}} = \begin{cases} \dfrac{\sum_{i=1}^{N} \omega\left(x_{i,u}, x_{j,d}\right) u_{x_{i,u}}}{\sum_{i=1}^{N} \omega\left(x_{i,u}, x_{j,d}\right)} & \text{if } d\left(x_{i,u}, x_{j,d}\right) \neq 0 \\ u_{x_{i,u}} & \text{if } d\left(x_{i,u}, x_{j,d}\right) = 0 \end{cases} \tag{3.1}$$

where $u_{x_{j,d}}$ and $u_{x_{i,u}}$ are values defined on respectively the downstream grid in point $x_{j,d}$ and upstream grid in point $x_{i,u}$. The weighting factor

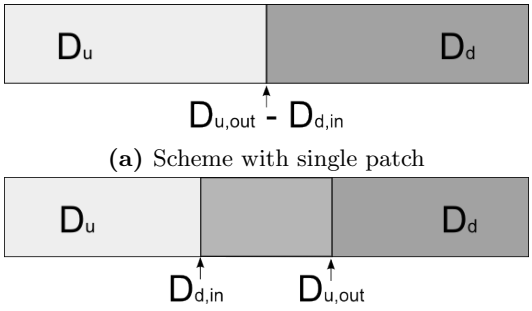

(a) Scheme with single patch

(b) Scheme with overlapping

Figure 3.1.: Scheme of the two possible approaches in space for coupled simulations. The solver applied to the domain upstream (D_u) is coupled to the one for the domain downstream (D_d).

$\omega\left(x_{i,u}, x_{j,d}\right)$ is expressed as:

$$\omega\left(x_{i,u}, x_{j,d}\right) = \frac{1}{d\left(x_{i,u}, x_{j,d}\right)} \tag{3.2}$$

Where d is the distance between the two points $x_{i,u}$ and $x_{j,d}$, defined as:

$$d\left(x_{i,u}, x_{j,d}\right) = || \; x_{i,u} - x_{j,d} \; || \tag{3.3}$$

The weighted sum to define $u_{x_{j,d}}$ is limited to the cell of the downstream grid including $x_{j,d}$ and to all its neighbours.
It is worth noticing that Wang et al. [19] proposed an alternative method to exchange information between two different solvers. This is based on the overset grid approach Chimera [79]. In a full Chimera grid system, a domain is decomposed by a set of two or more overlapping grids. The information are interpolated from one grid to another on a number of fringe points (ghost cells), which are then used to compute the solution of the inner cells. This kind of approach is not investigated in the present work.

3.1.2. Coupling mechanisms in time

When dealing with unsteady computations, the passage of information (defined as "communication") between the solvers must be properly coordinated in time. From this point of view, Duchaine et al. [80] propose an interesting classification in the optics of the coupling between a flow and a solid solver for Conjugate Heat Transfer (CHT) problems, which can be easily extended to the current coupling problem.
In general, the syncronization of unsteady solvers has to cope with two main issues.

- **Synchronization in physical time:** the physical time computed by the two codes between two subsequent communications may be the same or not. It is clear that the time simulated by the two solvers between two communications must be consistent for an accurate exchange of unsteady structures between the subdomains. On the other hand, the convergence of unsteady simulations is dependent on the characteristic time of the domain t_{ref}, which is related (in fluid dynamics) to the time employed by a particle to cross the domain from the inlet to the outlet. It is worth to notice that the characteristic time of a combustor and a turbine are very different from each other, being typically of the order of 1ms for the turbine and 10ms for the combustor [30, 81].
  A more convenient approach for a quick solution of the coupled simulation would be to exchange information every $\alpha_u t_{ref,u}$ for the upstream subdomain and $\alpha_d t_{ref,d}$ for the downstream one, where $\alpha_u = \alpha_d$. This would assure the convergence of the two simulations in the same computational time, but on the other hand the two solutions would be decoupled in physical time.

- **Synchronization in CPU time:** on a parallel machine, the two solvers could run at the same time or sequentially. For machines with a sufficiently large number of processors, the first approach could lead to a significant computational time saving: for simulations running in parallel, in fact, the computational time is ideally proportional to $max(\alpha_u t_{ref,u}, \alpha_d t_{ref,d})$, while it is proportional to $t_{ref,u} + t_{ref,d}$ for a sequential approach.

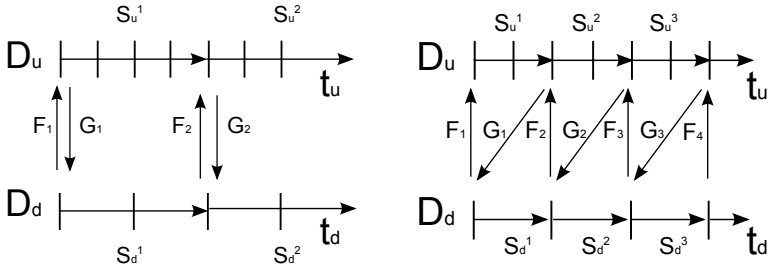

(a) Weak structure in time.

(b) Strong structure in time.

Figure 3.2.: Scheme of the two possible approaches in time for coupled simulations. The solver applied to the domain upstream (D_u) is coupled to the one for the domain downstream (D_d).

According to the previous discussion, two different coupling procedures in time have been developed for this work. These two procedures are schemat-

ically shown in Fig. 3.2. The weak structure in time (Fig. 3.2-a) is characterized by communications which are not syncronized in physical time. The algorithm followed is described below:

- when the simulation starts, the two solvers applied to the upstream domain (D_u) and the downstream domain (D_d) communicate the information F_i and G_i between each other.
- After the communication, the upstream and downstream simulations (S_u and S_d) run in parallel for a respective physical time $\alpha_u t_{ref,u} \neq \alpha_d t_{ref,d}$.
- The two solvers communicate again.

The same procedure is repeated until convergence.

According to the strong coupling in time, Fig. 3.2-b, the two solvers run and share the information in a time-accurate way. The following algorithm is applied:

- when the simulation starts, the solver applied to the downstream domain communicates the information to the upstream one.
- The upstream solver can then iterate for a certain physical time.
- The upstream solver transfers the information to the downstream one.
- After this second communication, the downstream solver starts to iterate for the same physical time.

The same procedure is repeated until convergence.
In general, it is always convenient to employ a weak approach in time for the first part of the simulation, while switching to a strong coupling only in a second time. The use of a weak approach leads to a faster statistical convergence of the unsteady fields, since the two solvers can be run in parallel and for a completely independent physical time. The use of the strong coupling in time for the second part of the analysis assures instead an accurate passage of the unsteady signals at the interface.

3.1.3. The passage of information

In the previous sections, the possible mechanisms in time and space to couple two different solvers are discussed. It is now important to discuss which is the information to be exchanged. To do that, the nature of the NS equations must be taken into account.

An inviscid subsonic flow is driven by a system of hyperbolic equations. The

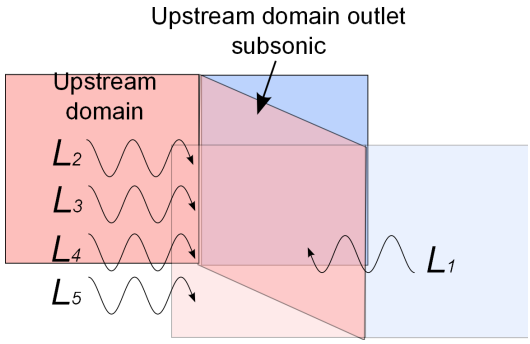

Figure 3.3.: Scheme of the upstream subdomain outlet with characteristic waves.

boundary conditions of hyperbolic systems can be specified by analyzing the different waves crossing the boundary. Figure 3.3 represents the subsonic interface between an upstream and a downstream domain. According to the characteristic formulation, five characteristic waves can be identified:

- Four forward-moving waves: a pressure wave L_5, an entropy wave L_2 and two vorticity waves L_3 and L_4.

- One backward-moving pressure wave L_1.

For a well-posed problem based on hyperbolic equations, the information related to the waves entering into the domain from the boundary must be specified, while the outwards moving waves must be calculated from the internal solution, since they are not influenced by the external environment [82]. The same conclusion is given for the Navier-Stokes equations, despite the fact that they cannot be strictly considered as hyperbolic [83] because of the viscous term.
As a direct consequence, the NS equations for a subsonic flow require only four information on the inlet patch (in turbomachinery, usually one imposes total temperature, total pressure, u_{ax}/u and u_t/u) while only one information shall be defined at the outlet (usually the static pressure).
In literature, there is an open discussion whether more than four variables can be transferred from the upstream to the downstream subdomains during the coupling [18, 70]. According to the characteristic waves theory, the passage of more than four variables from the upstream to the downstream domain can lead to a well posed problem only if the backwards-traveling wave calculated within D_u in correspondence of the downstream subdomain inlet is exactly the same as the one calculated within D_d, i.e. if $L_{1,u} = L_{1,d}$ in correspondence of the downstream inlet. If this condition is not respected, the problem is ill-posed and only four variables must be transferred onwards. During the coupling, $L_{1,u} \neq L_{1,d}$ if one of these conditions is present:

- The transfer of information from the downstream to the upstream domain is relaxed (this is typical, for example, for LES-URANS coupling).
- The time steps of the simulations are very different (in general, if $dt_u \ll dt_d$).
- The grids at the interface are non-matching.
- When the overlapping region is used, the numerical dissipation of the upstream and downstream simulations along the overlapping can be different. This leads to $L_{1,u} \neq L_{1,d}$ in correspondence of the downstream inlet.

According to these considerations, two possible structures for the passage of information are proposed in this work:

1. The pressure wave $L_{1,d}$ is transferred directly from the upstream to the downstream domain, this is used to compute all variables at the upstream outlet. The domain upstream passes all characteristic variables to the downstream inlet.
2. The pressure is passed from the upstream to the downstream domain, this is used to compute all variables at the upstream outlet. The domain upstream passes only four characteristic variables to the downstream one, while one variable will be free to change according to the flow field within the downstream domain.

If the condition $L_{1,u} = L_{1,d}$ must be respected, the first strategy to pass the information is stable only if a short (or no) overlapping region is used, the grids at the interface are similar and if $dt_u \sim dt_d$. This will be demonstrated in section 4.5.2.
The second passage of information, on the other hand, will be unconditionally stable.

3.2. Extended treatment of the LES-URANS coupling

When the coupling is applied to a LES for the domain upstream and an URANS simulation for the one downstream, the following additional requirements shall be taken into account:

- Differently from URANS simulations, LES is able to resolve a large spectra of fluctuations, therefore the information coming from the upstream to the downstream domain must be properly filtered.

- The potential effect of the downstream domain on the upstream one shall be imposed without introducing spurious deformations of the vortical structures approaching the upstream outlet.
- Despite the different approaches applied by RANS and LES for the resolution of turbulence, a continuity of the turbulent variables shall be guaranteed at the interface.

All these aspects will be discussed in the next sections.

3.2.1. Mathematical treatment of the downstream domain inlet

The flow field resolved by LES is characterized by a broadband frequency spectrum. According to the Nyquist's theorem, the frequencies characterizing the solution are comprised between :

$$\begin{aligned} 0 \leq f \leq \frac{f_{dt,LES}}{2} \\ f_{dt,LES} = \frac{1}{dt_{LES}} \end{aligned} \tag{3.4}$$

Where dt_{LES} is the physical time step resolved by the upstream simulation, whose corresponding frequency is $f_{dt,LES}$. In general, for a LES-URANS zonal coupling, the signal should not be completely filtered at the interface, but it has to be partly transferred from the upstream to the downstream subdomains. In particular, all fluctuations related to the direct resolution of turbulence (resolved by LES) must be filtered out at the interface, while the main coherent structures must be passed to the URANS solution. A typical example of flow field with coherent structures is a flow interacting with a cylinder at high Re, which gives rise to the vortex shedding phenomenon (i.e. a regular formation of vortices which are convected downstream).
These "coherent structures" are in many cases characterized by a well defined frequency content, which can be approximated by a single-frequency signal:

$$m_{c,LES} = M_{c,LES} e^{2\pi f_{c,LES} t} \tag{3.5}$$

Where the subscript c defines the coherent signal. An ideal filter applied to the LES-URANS coupling should then let the signal $m_{c,LES}$ pass without affecting its amplitude, while filtering the high frequency broad-band component representing the turbulence.
The most straightforward procedure to deal with the unsteady fields is to apply a moving average filter to the signal obtained from LES. This kind

of filter is commonly employed for digital signals [84], mainly because it is very easy to implement and to use. According to the theory, the signal obtained at the downstream subdomain inlet (m_{URANS}) can be defined from the signal of the domain upstream (m_{LES}) as follows:

$$m_{URANS}(i) = \frac{1}{N}\sum_{j=0}^{N-1} m_{LES}(i-j) \tag{3.6}$$

Where N refers to the number of snapshots averaged from the LES solution. It should be noticed that the way in which Eq. 3.6 is written leads to a slight phase shift between m_{LES} and m_{URANS}, since the signal at the URANS inlet is defined from the N previous LES snapshots. To avoid the phase shift, the average should be done over $N/2$ samples before and after snapshot i.
The moving average filter is known to behave very well in the time domain (being the best filter to cut off the white noise from a signal), but not in separating one band of frequencies from another. The frequency response of the filter is described by the following Fourier transform [84]:

$$\alpha_f = \frac{m_{URANS}}{m_{LES}}(f) = \frac{sin\left(\pi \dfrac{f}{f_{dt,LES}} N\right)}{N sin\left(\pi \dfrac{f}{f_{dt,LES}}\right)} \tag{3.7}$$

Its evolution is represented in Fig. 3.4 in function of the parameter N, which is the number of LES snapshots used to compute m_{URANS}. It is clear that

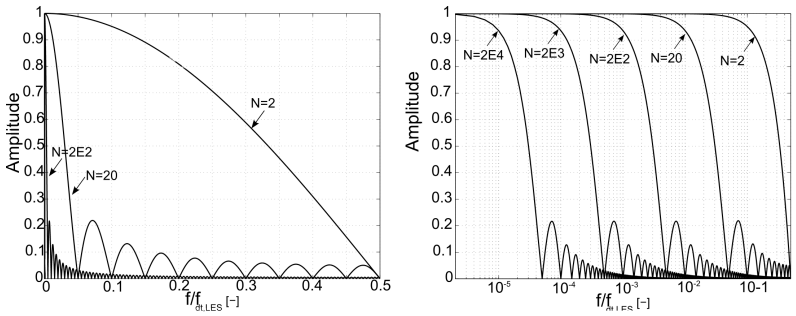

Figure 3.4.: Frequency response of the time marching average filter. The time is defined in linear scale on the left, while it is defined in logaritmic scale on the right.

the frequencies which will be filtered out at the LES-URANS interface, as well as the accuracy in transferring $m_{c,LES}$ depends on the parameter N, which shall be properly chosen by the user. In general $N \cdot dt_{LES} \geq dt_{URANS}$.

For a better insight into the use of the filter, Eq. 3.7 is applied in this section to the signal obtained by the LES of a high-Reynolds flow interacting with a cylinder. The numerical test case will be described more in detail in section 3.2.2.5. For the current analysis, it is important to point out that the solution is characterized by turbulent fluctuations and vortex shedding (which represents te coherent structures $m_{c,LES}$).
The time marching average filter is directly applied to the signal registered by a probe placed along the wake of the cylinder, where a LES-URANS interface could be located during a coupled simulation.
Results in function of N are shown in Fig. 3.5 in the time domain and in Fig. 3.6 in the frequency domain.
The vortex shedding can be identified within the spectrum by the relative

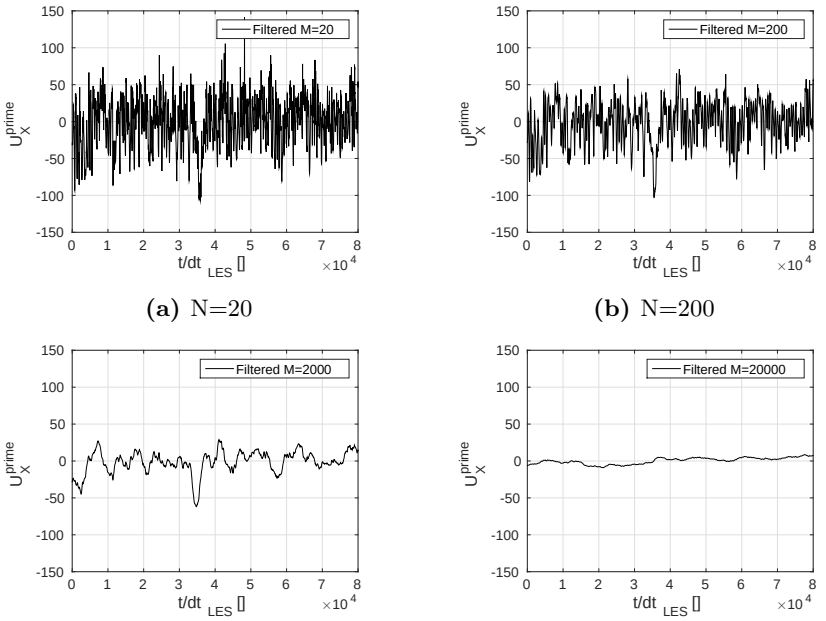

(a) N=20 **(b)** N=200

(c) N=2000 **(d)** N=20000

Figure 3.5.: Filtering of the signal obtained along the wake of a cylinder at $X/d = 3.5$. The flow is solved by LES. $Re = 400000$. Time domain.

peak at $f_{c,LES} = 1350Hz$. For this particular case, a clear action of the filter on the signal in time is not observed for $N < 2000$ (Fig. 3.5 a and b). Observing Fig. 3.6-c, it clearly appears that for N=2000 the solution is largely smoothed and the vortex shedding signal is almost completely damped out, which is not acceptable for an accurate transmission of the coherent structures between the upstream and the downstream domains. For the current test case, N=200 seems then to be the best trade-off to get a significant

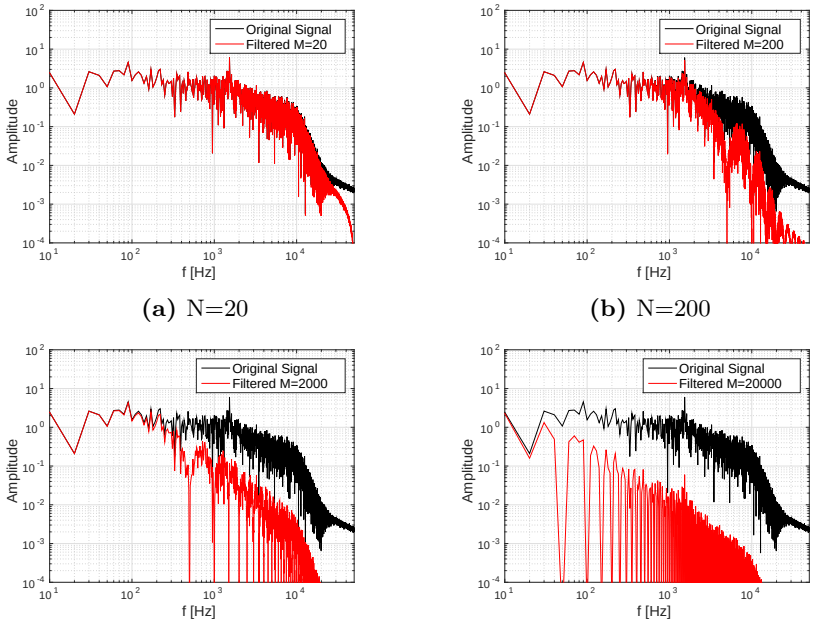

(a) N=20 **(b)** N=200

(c) N=2000 **(d)** N=20000

Figure 3.6.: Filtering of the signal obtained along the wake of a cylinder at $X/d = 3.5$. The flow is solved by LES. $Re = 400000$. Frequency domain.

damping of the turbulence leaving the domain with a limited impact on the transfer of the vortex shedding.

To develop a simple procedure to set-up the filter for the coupling, $f_s = 1/dt_s = 1/(Ndt_{LES})$ is defined as the sampling frequency to perform the time average. Eq. 3.7 can then be recast as:

$$\begin{aligned} \alpha_f^* &= \frac{sin\left(\pi \frac{f}{f_{dt,LES}} N\right)}{N sin\left(\pi \frac{f}{f_{dt,LES}}\right)} \\ &= \frac{sin\left(\pi \frac{f}{f_s}\right)}{\frac{f_{dt,LES}}{f_s sin\left(\pi \frac{f}{f_{dt,LES}}\right)}} \end{aligned} \tag{3.8}$$

Focusing the attention on the passage of $m_{c,LES}$, $f = f_{c,LES}$ can be imposed. It is easy to observe that in general $f_{dt,LES} \gg f_{c,LES}$, since the physical time

step resolved dt_{LES} is linked to the request of $CFL = 1$ to get an accurate resolution of the smallest turbulent structures [13] (the reason for that will be better explained in chapter 6). If this condition is respected, the expression of the filter can then be simplified to eliminate $f_{dt,LES}$: considering $x = \pi f / f_{dt,LES} \to 0$ one can write the following:

$$\alpha_f = \lim_{x \to 0} \frac{\frac{sin(\pi \frac{f}{f_s})}{\pi f}}{f_s \frac{sin(x)}{x}} \tag{3.9}$$

Leading to:

$$\alpha_f^* = \frac{sin\left(\pi \frac{f}{f_s}\right)}{\frac{\pi f}{f_s}} \tag{3.10}$$

Equation 3.10 can be used to determine how f_s affects the transfer of the signal in a completely independent way from the time step dt_{LES} chosen for the simulation.

A correct value of f_s to damp the turbulent spectrum can instead be estimated by defining the smallest frequency which shall be filtered $f_{t,LES}$. This frequency is related to the biggest turbulent structures solved by LES. Considering that $dt_s > dt_{t,LES}$ to effectively filter out the signal, $f_{t,LES}$ can be mathematically expressed in function of f_s as follows:

$$f_{t,LES} = \kappa f_s + f_x \tag{3.11}$$

where $\kappa = int(f_{t,LES}/f_s)$ and $0 \leq f_x < f_s$. Hypothesizing $f_{t,LES} \gg f_{dt,LES}$, Eq. 3.10 remains valid and can be further elaborated as:

$$\alpha_f^* = \frac{sin\left(\kappa\pi + \frac{f_x}{f_s}\pi\right)}{\kappa + \frac{f_x}{f_s}} \tag{3.12}$$

Expanding Eq. 3.12 and considering that $sin(2\pi\kappa) = 0$ one obtains:

$$\alpha_f^* = \frac{sin\left(\pi \frac{f_x}{f_s}\right)}{\kappa + \frac{f_x}{f_s}} \tag{3.13}$$

Since the turbulence is characterized by a broadband signal, a conservative estimate of the accuracy of the filter can be obtained considering the worst

case for f_x/f_s. Observing Fig. 3.4, we can deduce that $f_x/f_s = 0.5$ is very close to the relative maxima of the transfer function for each value of κ. The filter can then be approximated as:

$$\alpha_f^* = \frac{1}{\pi(\kappa + 0.5)} \tag{3.14}$$

Merging Eq. 3.10 and 3.14, one obtains:

$$\alpha_f^* = \begin{cases} \dfrac{sin\left(\pi \dfrac{f}{f_s}\right)}{\dfrac{\pi f}{f_s}}, & \text{if } f < f_s/2 \\ \\ \dfrac{1}{\pi(\kappa + 0.5)}, & \text{if } f > f_s/2 \end{cases} \tag{3.15}$$

The main advantage in using the simplified Eq. 3.15 rather than the original transfer function in Eq. 3.7 is that Eq. 3.15 is completely independent from any parameter linked to the numerical setup of the simulation: in this sense, the equation can be used to compute f_s a priori, whose estimate will only be based on the definition of $f_{c,LES}$ (signal to be transferred to the downstream domain) and $f_{t,LES}$ (signal to be filtered out). The trend of Eq. 3.15 is shown in Fig. 3.7 and compared to the original Eq. 3.7. The hypothesis of $f_{dt,LES} \gg f_{c,LES}$ and $f_{dt,LES} \gg f_{t,LES}$, which are necessary to eliminate $f_{dt,LES}$ from the transfer function of the filter, is well respected in particular for the cases with higher N. Eq. 3.10 and 3.14 can be combined together

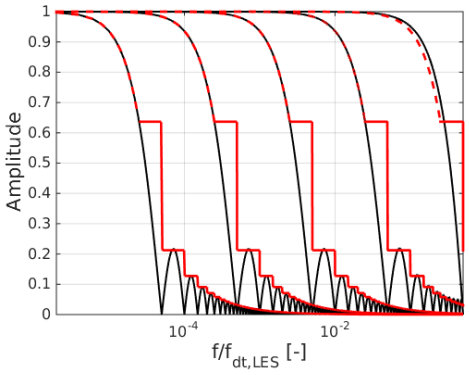

Figure 3.7.: Frequency response of the time marching average filter (in black) compared to the simplified expression 3.15 (in red), to estimate the damping of f_c and $f_{t,LES}$.

to obtain the graphs in Fig. 3.8. This represents the main outcome of the

analysis, and can be directly used to select a proper value of f_s based on $f_{c,LES}$ and $f_{t,LES}$.
The procedure recommended in this work to impose f_s is then the following:

- Compute $f_{c,LES}/f_{t,LES}$, where $f_{c,LES}$ is the frequency of the coherent structure to be transferred to the downstream domain, and $f_{t,LES}$ can be defined as the smallest frequency to be filtered out.
- Use graphs 3.8-a and 3.8-b, imposing the value of the ordinate.
- Choose the value of the abscissa, based on the acceptable error $M_{c,URANS}/M_{c,LES}$ (Fig. 3.8-a).
- Based on that, calculate the expected noise $M_{t,URANS}/M_{t,LES}$ which will be produced at the URANS inlet by the non perfect filtering of the turbulent signal.

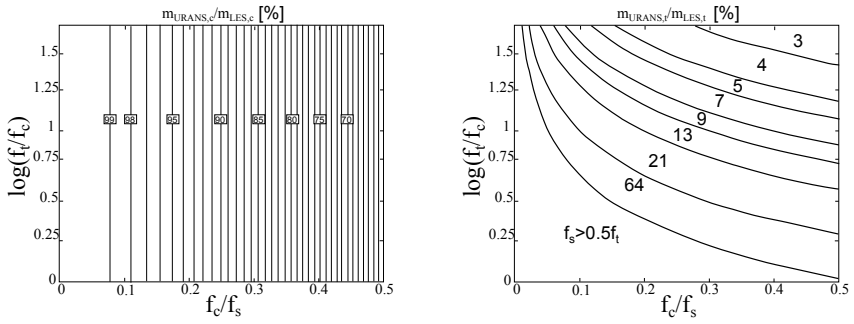

Figure 3.8.: Damping of the signal $m_{c,LES}$ (a) and $m_{t,LES}$ (b) in function of the sampling frequency.

It is important to observe that, depending on $f_{t,LES}$ and $f_{c,LES}$, the choice of a sufficiently low f_s to effectively damp the turbulent fluctuations is not always possible, therefore in most of the cases spurious fluctuations are generated at the inlet of the URANS simulation, by the non perfect filtering of the turbulence resolved by LES. In general, these fluctuations will then be damped within the downstream domain by the numerical diffusion of the solution.
For a LES-URANS coupling, it is a good practice to include an overlapping region between the domains. This allows to discard the solution close to the inlet for the URANS simulation, where spurious fluctuations due to the turbulence of the upstream LES are generated. Indeed, in the overlapping region, the more accurate solution coming from the LES can be used.

3.2.2. Mathematical treatment of the upstream domain outlet

The application of compressible LES codes to high Reynolds flows permits the direct resolution of the turbulent structures and acoustic waves propagating within the domain. The interaction of such a complex unsteady flow with the domain boundaries is generally critical, requiring the development of ad-hoc boundary conditions.
At the upstream domain outlet, two main requirements must be satisfied:

1. The fluctuations coming from the upstream domain should cross the outlet patch without being reflected.

2. The potential effect coming from the domain downstream shall be effectively imposed at the LES outlet.

To get a non-reflecting outlet for the upstream domain, the Navier Stokes Characteristic Boundary Conditions (NSCBC) developed by Poinsot and Lele [83] and including the improved approach proposed by Lodato [85] are chosen in this thesis.

3.2.2.1. The Navier Stokes Characteristic Boundary Conditions

The boundary conditions of hyperbolic systems can be specified by analyzing the different waves crossing the boundary. The subsonic outlet of the upstream subdomain during the coupling is shown in Fig. 3.3 . As previously discussed in section 3.1.3, five characteristic lines cross the upstream outlet: four outward-moving waves (a pressure wave L_5, an entropy wave L_2 and two vorticity waves L_3 and L_4) and one inward-moving pressure wave L_1.
In an attempt to identifying appropriate boundary conditions for hyperbolic systems, Thompson [82] proposed a treatment to put the Euler equations in characteristic form at boundaries. The treatment was then applied to the hyperbolic part of the Navier-Stokes equations by Poinsot and Lele [83]. According to the authors, the Navier Stokes system of equations can be recast

as:

$$\begin{aligned}
&\frac{\delta\rho}{\delta t} + \frac{1}{c^2}\left[L_2 + \frac{1}{2}(L_5 + L_1)\right] + \frac{\delta\rho u_t}{\delta x_t} = 0 \\
&\frac{\delta u_1}{\delta t} + \frac{1}{2\rho c}[L_5 - L_1] + \frac{\delta u_1}{\delta x_t}u_t = \frac{1}{\rho}\frac{\tau_{1j}}{\delta x_j} \\
&\frac{\delta u_2}{\delta t} + L_3 + \frac{\delta u_2}{\delta x_t}u_t + \frac{1}{\rho}\frac{\delta p}{\delta x_2} = \frac{1}{\rho}\frac{\tau_{2j}}{\delta x_j} \\
&\frac{\delta u_3}{\delta t} + L_4 + \frac{\delta u_3}{\delta x_t}u_t + \frac{1}{\rho}\frac{\delta p}{\delta x_3} = \frac{1}{\rho}\frac{\tau_{3j}}{\delta x_j} \\
&\frac{\delta p}{\delta t} + \frac{1}{2}(L_5 + L_1) + \frac{\delta u_t}{\delta x_t}\gamma p + \frac{\delta p}{\delta x_t}u_t = \\
&= (\gamma - 1)\left(\tau_{ij}\frac{\delta u_i}{\delta x_j} + \frac{\delta}{\delta x_i}\left(\frac{\mu c_p}{P_r}\frac{\delta T}{\delta x_i}\right)\right)
\end{aligned} \tag{3.16}$$

Where the subscript t refers to the tangential directions 2 and 3 while 1 is the direction perpendicular to the boundary. The Einstein's summation is used.

The characteristic waves appearing into the system of equations can be mathematically defined as:

$$\begin{aligned}
L_1 &= \lambda_1\left(\frac{\delta p}{\delta x_1} - \rho c\frac{\delta u_1}{\delta x_1}\right) \\
L_2 &= \lambda_2\left(c^2\frac{\delta\rho}{\delta x_1} - \frac{\delta p}{\delta x_1}\right) \\
L_3 &= \lambda_3\frac{\delta u_2}{\delta x_2} \\
L_4 &= \lambda_4\frac{\delta u_3}{\delta x_3} \\
L_5 &= \lambda_5\left(\frac{\delta p}{\delta x_1} + \rho c\frac{\delta u_1}{\delta x_1}\right)
\end{aligned} \tag{3.17}$$

Where λ_i represents the characteristic velocity related to the wave i, given by:

$$\begin{aligned}
\lambda_1 &= u_1 - c \\
\lambda_2 = \lambda_3 = \lambda_4 &= u_1 \\
\lambda_5 &= u_1 + c
\end{aligned} \tag{3.18}$$

The system of Eq. 3.16 may be directly used to advance the solution in time on the boundary. For a subsonic outlet, in particular, the information propagating from the inside to the outside of the domain (corresponding to waves $L_{2,3,4,5}$) may be directly calculated from the solution obtained at the previous time step, using one sided differences.

The incoming wave L_1, on the other hand, shall be estimated in function of the boundary condition which must be imposed.

At this scope, Poinsot and Lele [83] propose to examine the local one dimensional inviscid problem (LODI), which is obtained neglecting the trans-

verse and viscous terms from Eq. 3.16. The LODI equations are:

$$\begin{aligned}
\frac{\delta\rho}{\delta t} + \frac{1}{c^2}\left[L_2 + \frac{1}{2}\left(L_5 + L_1\right)\right] &= 0 \\
\frac{\delta u_1}{\delta t} + \frac{1}{2\rho c}\left[L_5 - L_1\right] &= 0 \\
\frac{\delta u_2}{\delta t} + L_3 &= 0 \\
\frac{\delta u_3}{\delta t} + L_4 &= 0 \\
\frac{\delta p}{\delta t} + \frac{1}{2}\left(L_5 + L_1\right) &= 0
\end{aligned} \tag{3.19}$$

Equations 3.19 permit an easy interpretation of the physics, allowing to properly choose the value L_1 in function of the outlet boundary to be reproduced.
For example, a constant pressure outlet condition could be specified by imposing $\delta p/\delta t = 0$ in Eq. 3.19-e, leading to $L_1 = -L_5$. Once the value L_1 is computed, the other fields at the boundary can be advanced in time by using the system of equations 3.16. To be coherent with the imposition of the constant outlet pressure, Eq. 3.16-e must be neglected during the time integration.
A new version of the NSCBC, proposed by Lodato et al. in 2008, completely avoids the LODI approximation using the 3D Navier-Stokes viscous equations also to compute L_1. For the detail of the treatment proposed by the authors, the reader is referred to [85].
During the LES-URANS coupling, a non-reflecting condition shall be imposed at the outlet of the upstream subdomain. According to the theory, for a uniform free shear flow at the outlet this means that no backwards-moving pressure waves can enter inside the domain, leading to [82]:

$$L_1 = 0 \tag{3.20}$$

From the numerical point of view, Poinsot and Lele point out that the problem with a perfectly non reflecting boundary condition is ill-posed; the reason can be easily understood considering a free shear layer simulated imposing constant velocity and temperature at the inlet and a non reflecting outlet for all the other boundaries. In this case, no information on the averaged pressure is given to the numerical domain, and a unique solution of the Navier Stokes system cannot be obtained.
To solve this issue, a modified formulation of L_1 is proposed by the authors, in which L_1 is expressed as:

$$\begin{aligned}
L_1 &= \kappa\left(p - p_{Inf}\right) \\
\kappa &= \sigma\frac{c\left(1 - M^2\right)}{\lambda_{Inf}}
\end{aligned} \tag{3.21}$$

Where p_{Inf} represents the pressure ideally imposed at a distance λ_{Inf} from the domain outlet. λ_{Inf} is the parameter controlling how "hard" the impo-

sition of p_{Inf} at the outlet is. The larger is λ_{Inf} the more the outlet behaves as an ideal anechoic patch. Rudy and Strikwerda [86] recommend the use of $\sigma = 0.28$ and λ_{Inf} of the same order of magnitude of the domain length. The formulation was then improved by Lodato et al. including the transverse terms [85] as follows:

$$L_1 = \kappa\left(p - p_{Inf}\right) + (1-\beta)\left(\rho c u_t \frac{\delta u_1}{\delta x_t} - u_t \frac{\delta p}{\delta x_t} - \gamma p \frac{\delta u_t}{\delta x_t}\right) \tag{3.22}$$

Where β is a transverse damping parameter comprised between 0 and 1. In particular, $\beta = 1$ neglects the transverse terms into the equation, leading to the simplified formulation of Poinsot and Lele in Eq. 3.21.

3.2.2.2. Implementation of the NSCBC in OpenFOAM

The NSCBC formulation is not present in the official OpenFOAM release, therefore it was implemented into the OpenFOAM platform in the framework of this thesis. Several examples of implementations of the NSCBC in OpenFOAM can be found in literature (two examples are [87, 88]).
The approach followed in this work is based on the integration of the NSCBC algorithm within the original p-based PIMPLE solvers. The scheme of the modified algorithm can then be described as follows:

- The resolution of the time t_i starts.
- L_1 is computed using equation 3.22.
- $L_{2,3,4,5}$ are computed from the internal field of the time step t_{i-1}, using equation 3.17.
- The Navier Stokes characteristic equations in Eq. 3.16 are solved.
- p, T, U obtained from the Navier-Stokes equations (together with the perfect gas law) are imposed as outlet conditions for pressure, temperature and velocity.
- The internal field is solved by the classical pimple algorithm.
- The resolution of the time t_i ends.

The implementation of the NSCBC were validated on different test cases with increasing difficulty. For the sake of brevity, the most significant ones are discussed in Appendix B:

3.2.2.3. Analysis of the NSCBC set-up for the coupling

A correct use of the non reflecting characteristic boundary conditions at the interface of a coupled simulation requires further considerations:

- During a coupled LES-URANS simulations, a numerical distortion of the coherent structures crossing the interface would be transmitted to the downstream domain. Therefore, the ideal set-up of the NSCBC for the coupling should **limit as much as possible the numerical deformation of the vortices approaching the LES outlet**.

- A zonal multi-code combustor-turbine simulation is meaningful only if **the potential effect of the turbine is transferred at the combustor outlet**. If this is not achieved, the simulation is equivalent to a one-way coupling in which the boundary conditions are simply passed from the upstream to the downstream domain.

These two points will be the object of discussion of the next sections.

3.2.2.4. The passage of vortical structures from LES to URANS

To avoid numerical deformation of the big coherent structures crossing the interface (which must be transferred to the URANS domain), the NSCBC formulation can be mathematically analyzed to detect an optimum value for the parameter β (defined in Eq. 3.22 and which can be tuned by the user) to be used during the coupled simulations.
A coherent vortical structure approaching the LES-URANS interface is modeled analytically by considering an Euler vortex convected across the outlet. The Euler vortex at $t = 0$ can be described by the following mathematical formulation:

$$\begin{aligned} \Phi &= C_v exp\left(-\frac{r^2}{2R_v^2}\right) + U_0 y \\ u_1 &= \frac{\delta\Phi}{\delta x} \\ u_2 &= -\frac{\delta\Phi}{\delta y} \\ p(r) &= p_0 exp\left[-\frac{\gamma}{2}\left(\frac{C_v}{cR_v}\right)^2 exp\left(-\frac{r^2}{R_v^2}\right)\right] \end{aligned} \tag{3.23}$$

where p_0 is the ambient pressure, C_v represents the vortex intensity, R_v is the vortex radius and $r = \sqrt{x^2 + y^2}$ is the radial coordinate from the vortex center. Starting from $t = 0$, the vortex will be convected towards the domain outlet in x direction.
The evolution of the pressure in time for a vortex convected at a velocity U_0 can be expressed as.

$$\frac{\delta p}{\delta t} + U_0 \frac{\delta p}{\delta x} = 0 \tag{3.24}$$

While on the other hand, the NSCBC for anechoic surfaces implies that the outlet pressure is solved by Eq.3.16-e.
Therefore, the mathematical error introduced by the NSCBC can be expressed as:

$$\frac{\delta p}{\delta t}_{err} = \frac{\delta p}{\delta t}_{calc} - \frac{\delta p}{\delta t}_{exact} \tag{3.25}$$

Where the index *calc* refers to the value calculated by Eq.3.16-e and *exact* is referred to Eq. 3.24. Neglecting the effect of viscosity, the following exact mathematical formulation of the error for a vortex crossing the outlet can be obtained:

$$\begin{aligned}\frac{\delta p}{\delta t}_{err} = -(\frac{1}{2}(U_0 + c)(\frac{\delta p}{\delta x} + \rho c\frac{\delta u_1}{\delta x}) - U_0\frac{\delta p}{\delta x} + \frac{1}{2}(1+\beta)(u_2\frac{\delta p}{\delta y} + \\ +\gamma p\frac{\delta u_2}{\delta y}) + \frac{1}{2}\rho c(1-\beta)u_2\frac{\delta u_2}{\delta y})\end{aligned} \tag{3.26}$$

The effect of the NSCBC formulation is analyzed applying Eq.3.23 to 3.26.

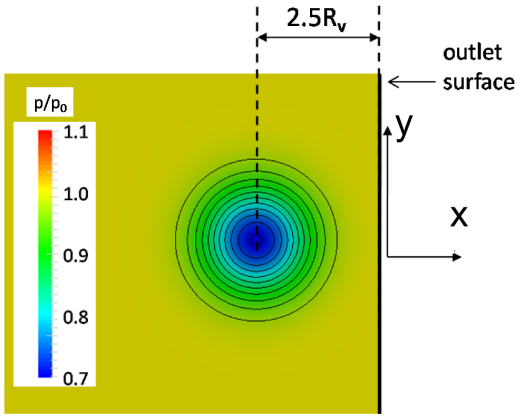

Figure 3.9.: Visualization of an ideal vortex approaching the outlet of the computational domain: $C_v = 2.5m^2/s$.

The ideal vortex approaching the LES-URANS interface is represented considering the LES outlet at $x = 2.5R_v$, as shown in Fig. 3.9. Equation 3.23 is written in such a way that the y axis is directed towards the part of domain with negative values of $u_1 - U_0$ (in other words, considering x aligned with U_0, z is directed as vorticity vector).
The following values are considered in Eq. 3.23: $U_0 = 100m/s$, $T_0 = 1500K$, $C_v = 2.5m^2/s$, $R_v = 0.01$, $p_0 = 100000$. These data indicate a high energy vortex convected by a low-Mach and high-temperature flow, similar to the one observed at the outlet of a combustion chamber.
Figure 3.10-a shows the mathematical development of $\delta p/\delta t_{err}$ along y at the outlet for different values of β. To point out the distortions at which

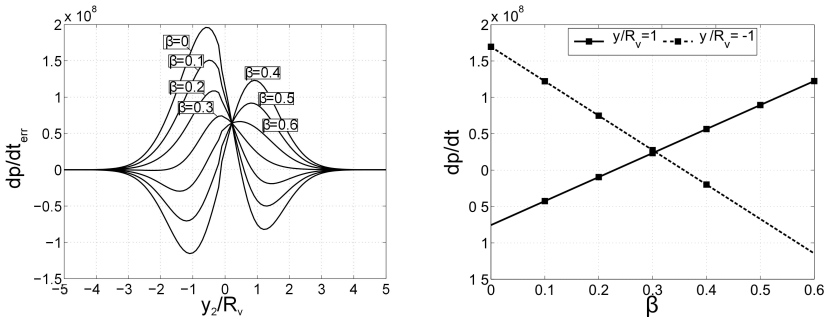

Figure 3.10.: $\delta p/\delta t_{err}$ along y for different values of β (a). $\delta p/\delta t_{err}$ with respect to β at $y = \pm/R_v$ (b).

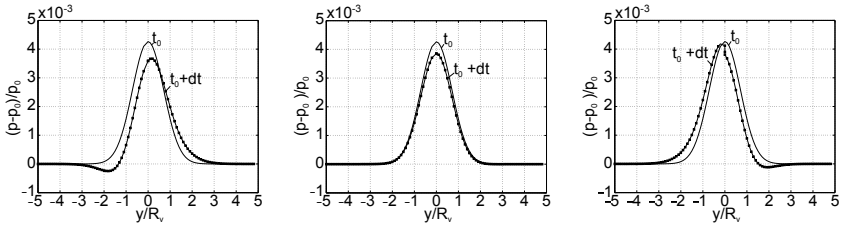

Figure 3.11.: Evolution of the outlet pressure between two consecutive time instants for different values of β. $\beta = 0$ (a), $\beta = 0.3$ (b), $\beta = 0.6$ (c). $dt = 10^{-6}s$. At t_0 the LES outlet is at $x = 2.5R_v$.

the vortex is subject, Fig. 3.10-b shows the development of the error for $y/R_v = \pm 1$ with β. For low values of β one obtains a spurious numerical increase of p towards $y < 0$ and a decrease towards $y > 0$, while the opposite trend can be observed for too high β. These conditions represent a deformation of the vortex, whose low-pressure center moves towards positive values of y when a too low β is used, and towards negative y for too high values of β.

To better explain this concept, Fig. 3.11 shows the effect of the numerical error on the outlet pressure distribution for two consecutive time instants. This is obtained computing the evolution of the initial pressure distribution as $\delta p/\delta t_{calc} \cdot dt$, with $dt = 10^{-6}s$. No deformation of the vortex is observed for $\beta = 0.3$, even though in general a numerical increase of p along y can be depicted. $\beta = 0.3$ can then be defined as an optimal value for the coupling in this particular condition, since the vortex crossing the outlet is only attenuated in intensity but its shape is not affected by the outlet boundary.

To verify how the optimum set-up changes for different vortices and flow

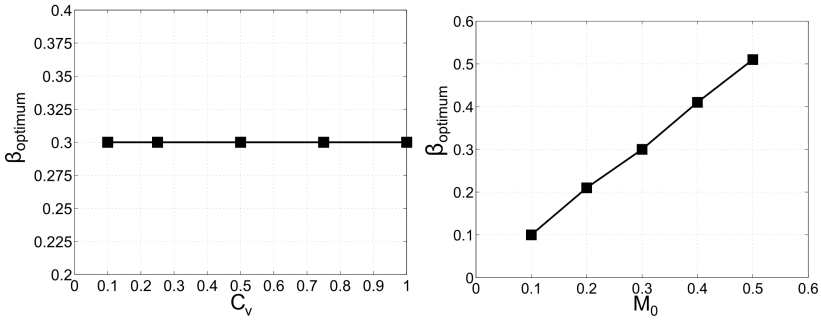

(a) (b)

Figure 3.12.: Optimum β in function of the vortex intensity C_v (a) and of the freestream Mach number (b).

conditions, mathematical tests were performed using Eq. 3.26, and modifying independently U_0 and C_v. The "optimum" β (defined as the one avoiding deformations of the vortex) following for each condition is reported in Fig. 3.12. It can be observed that this value does not depend on the vortex intensity, while it increases linearly with the convective Mach number. In particular, $\beta = M_0$ can be individuated as "optimum" for every flow condition.
This value, arising from the mathematical treatment proposed, is also in line with what is suggested by Lodato et al. [85] to limit the numerical reflections of the outlet.

The ideal set-up mathematically obtained for $\beta = M_0$ is numerically validated by directly simulating the test case of the Euler cylinder crossing the outlet. This is done by using the OpenFOAM solver rhoPimpleFoam on a 100x100 2D grid. The initial solution is described by Eq. 3.23, using the values introduced in the present section for U_0, T_0, C_v, R_v, p_0 and U_0. For further details on the numerical set-up, the reader is referred to appendix B.
Three computations were performed on the $C_v = 2.5$ configuration, setting three different values of β, namely $\beta = M_0/2$, $\beta = M_0$ and $\beta = 2M_0$. The pressure field obtained at $C_v = 2.5$ is shown in Fig. 3.13 for the three cases at $t/t_{ref} = 0.375$ (vortex approaching the outlet), where $t_{ref} = L_{dom}/U_0$. A numerical deformation of the pressure field towards positive values of u_1 (corresponding to $y < 0$) can be observed for the highest value of β. The field is instead deformed in the opposite direction for the lowest β, while it crosses the outlet without being deformed for $\beta = M_0$.
This observation is in agreement with the mathematical analysis proposed in the previous paragraph, therefore the "optimum" value $\beta = M_0$ can be confirmed.

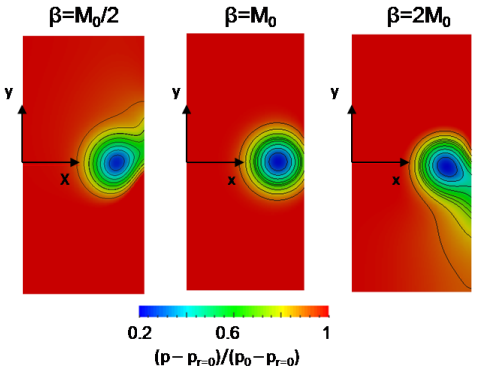

Figure 3.13.: Vortex approaching the domain outlet. $C_v = 2.5m^2/s$. Effect of the parameter β. The z axis is directed as the vorticity vector.

3.2.2.5. The passage of potential effect from URANS to LES

One of the main drawbacks of using non-reflecting boundary conditions is linked to the imposition of the outlet pressure, which is relaxed according to Eq. 3.21. For coupled simulations, the continuity of the pressure fields at the interface must be as accurate as possible to transfer the potential effect of the HPT to the combustor. At this purpose, the imposition of the outlet pressure for the anechoic NSCBC formulation must be discussed in detail. The discrepancy between p_{Inf} in Eq. 3.21 and 3.22 and the time-averaged outlet pressure can be easily explained considering that the anechoic condition introduced by Poinsot et al. [83] is strictly valid only for free shear flows, and further considerations are necessary when more complex flows crossing the outlet are simulated.

For example, Fig. 3.14 shows a sketch of an hypothetical numerical domain to represent a fully developed Pouiseuille flow. The flow is characterized by a zero velocity gradient in axial direction, accompanied by a decrease of pressure. Considering the definition of L_1 in Eq. 3.17-1, one can clearly understand that $L_1 = L_{Inf} \neq 0$ even for a steady anechoic outlet:

$$\begin{aligned} L_1 &= \lambda_1 \left(\frac{\delta p}{\delta x} - \rho c \frac{\delta \cancel{u_x}}{\cancel{\delta x}} \right) \\ L_1 &= \lambda_1 \frac{\delta p}{\delta x} \neq 0 \end{aligned} \tag{3.27}$$

As a consequence, the imposition of $L_1 = \kappa \left(p - p_{Inf} \right)$ leads to $p \neq p_{Inf}$:

$$\begin{aligned} L_1 &= \kappa \left(p - p_{Inf} \right) = L_{Inf} \\ p &= p_{Inf} + \frac{L_{Inf}}{k} \end{aligned} \tag{3.28}$$

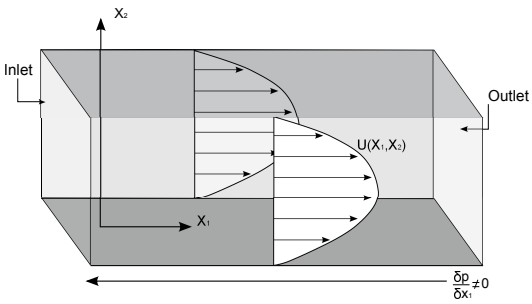

Figure 3.14.: Pouiseuille flow developing between two planar surfaces. $x_1 = x$ and $x_2 = y$.

Observing Eq. 3.28, two main different techniques can be individuated to decrease the difference between p and p_{Inf}.

Technique 1: The classical method is based on increasing κ by decreasing λ_{Inf} in Eq. 3.21. This permits to reduce the relative weight of L_{Inf} in Eq. 3.28, but at the expense of an increase of spurious reflections at the outlet. This can be explained by considering the steady state flow in Fig. 3.14. If a sharp pressure wave L_5 crosses the domain outlet at the time t_i, the non-reflecting outlet will be perturbed by a pressure increase Δp_i. In this case, the backwards-moving pressure wave at the time t_i, indicated as $L_{1,i}$, can be computed as:

$$\begin{aligned} L_{1,i-1} &= \kappa\left(p_{i-1} - p_{Inf}\right) = L_{Inf} \\ L_{1,i} &= \kappa\left(p_{i-1} + \Delta p_i - p_{Inf}\right) = L_{inf} + \kappa\Delta p_i \end{aligned} \tag{3.29}$$

The term $\kappa\Delta p_i$ represents then a spurious backwards-moving pressure wave which is generated by the NSCBC formulation. Its magnitude increases linearly with κ.

Technique 2: A further technique can be individuated considering that the ideal imposition of p_{Inf} at the outlet (without increasing the spurious reflections) is obtained only by directly including L_{Inf} into the definition of L_1:

$$L_1 = \kappa\left(p - p_{Inf}\right) + L_{Inf} \tag{3.30}$$

The main drawback of this formulation is that L_{Inf} should be known a priori.
As alternative, L_{Inf} can be iteratively computed during the simulation until an accurate matching $p_{out,ave} = p_{Inf}$ is obtained. This technique was tested in this work without obtaining a significant improvement with respect to technique 1, therefore it won't be further discussed.

Testing of technique 1

The effect of k on the outlet pressure distribution is tested on a cylinder in crossflow. The test case, shown in Fig. 3.15-a, is chosen as it includes both turbulent structures and coherent vortices crossing the outlet patch. The dimension of the cylinder and the inlet conditions are chosen to get $Re = 400000$ (based on the cylinder diameter) and $M = 0.3$. These values are in line with the ones typically observed at the outlet of industrial combustion chambers.
The test case is solved by the p-based code rhoPimpleFoam. A 3D domain is reproduced, whose dimensions are 12.5 d_{cyl}, 20 d_{cyl} and $2d_{cyl}$ in x, y and z directions. The domain is modeled by a structured mesh with $1.3 \cdot 10^6$ cells. $Y+$ lower than 10 is kept at walls, while $X+/Z+$ are limited to 150. The NS equations are discretized by a second order central scheme in space and the explicit Euler scheme in time. The subgrid scales are modeled by the Smagorinsky model, using the Van Driest formulation at wall. Uniform fixed velocity and temperature inlet conditions are imposed, while the NSCBC are used at the outlet. For all the other patches, periodic conditions are considered. To enhance the unsteadiness interacting with the outlet patch, the cylinder is placed very close to the outlet (at a distance $\Delta x/d_{cyl} = 3.5$).
To simulate the potential effect which can be obtained during a coupled

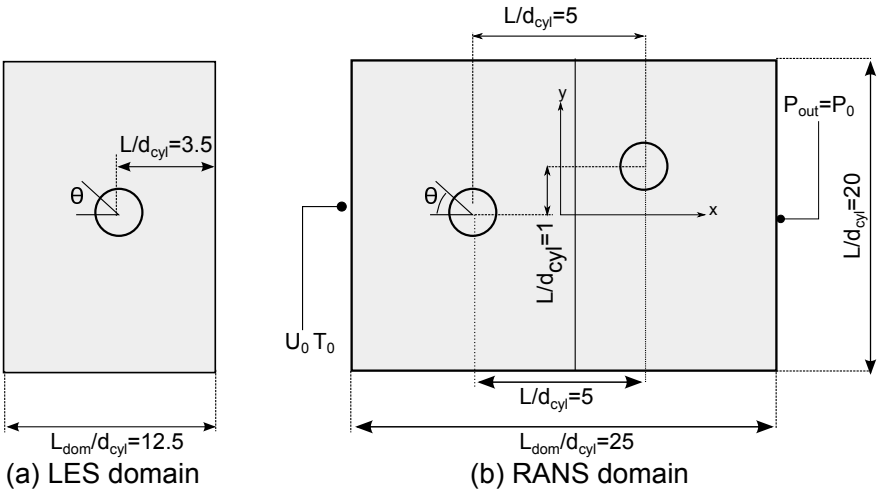

Figure 3.15.: Domain including one single cylinder (a). Cylinders in tandem simulated to reproduce the potential effect (b).

combustor-HPT simulation, a non-uniform distribution of p_{Inf} is obtained by a preliminary RANS simulation on the test case shown in Fig. 3.15-b. This represents two cylinders at a distance $L/d_{cyl} = 5.5$ and shifted of

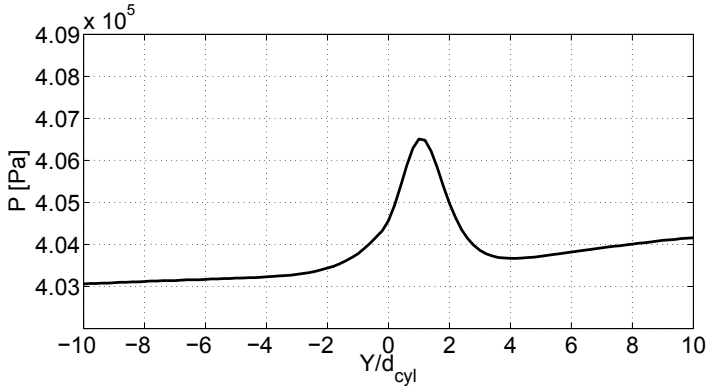

Figure 3.16.: Pressure distribution obtained at $\Delta x/d_{cyl} = -1.5$ from the downstream cylinder.

$\Delta y/d_{cyl} = 1$ in tangential direction, simulated imposing exactly the same inlet conditions of the single cylinder domain and $p = 400000Pa$ at the outlet. The pressure distribution obtained at $\Delta x/d_{cyl} = -1.5$ from the center of the cylinder downstream is shown in Fig. 3.16-a. As expected, this shows a localized peak of pressure located between $y/d_{cyl} = 0 - 2$, due to the potential effect of the cylinder downstream on the flow.
The domain representing one single cylinder is analyzed by three LES, imposing $\lambda_{Inf} = 10 \cdot L_{dom}$ (which is relatively high with respect to what recommended in literature, to enforce the anechoic condition), $\lambda_{Inf} = L_{dom}$ and $\lambda_{Inf} = 0.01 \cdot L_{dom}$.
The simulation is run for $0.5s$, corrisponding to about 100 flow-through (where the flow through is based on the domain length and U_0). A time step $dt = 10^{-8}s$ is employed to keep $CFL < 1$ everywhere.
Figure 3.17 shows the time averaged outlet pressure obtained. The NSCBC formulation with a very large λ_{Inf} appears too weak to accurately impose the 1D distribution of the time-averaged outlet pressure field at the outlet. On the other hand, the non-uniform outlet pressure profile can be accurately imposed by decreasing λ_{Inf} to L_{dom}.
To quantify whether the outlet behaves as an anechoic patch, the massflow averaged pressure fluctuations calculated over $\Delta t = 20$ flow through are shown in Fig. 3.18, plotted in function of λ_{Inf}.
From the analysis, it appears that a decrease of λ_{Inf} leads to a decrease of pressure fluctuations at the outlet; this means that the surface tends more and more to become non-anechoic and similar to imposing a fixed pressure condition.

In conclusion, for the current case the choice of $\lambda_{Inf} \sim L_{dom}$ can be considered as the best compromise between the requests to impose the outlet

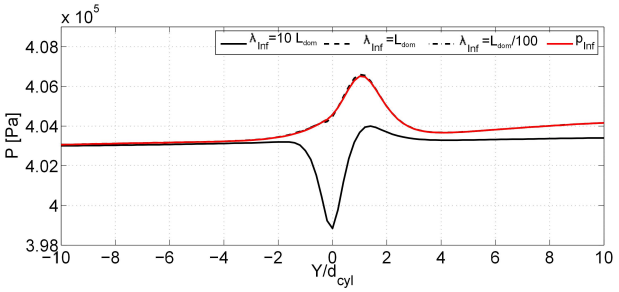

Figure 3.17.: $P_{out,ave}$ distribution at the anechoic outlet for different values of λ_{Inf}.

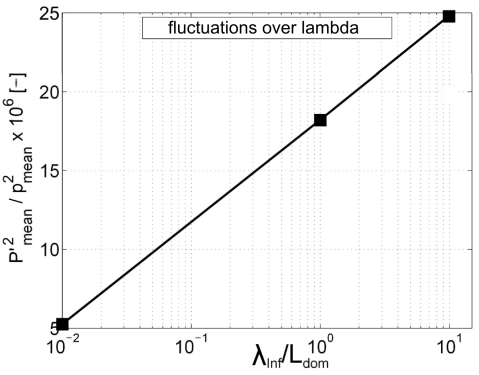

Figure 3.18.: Surface averaged pressure fluctuations at the anechoic outlet for the computations performed to test the p_{Inf} imposition at the outlet.

pressure and to get an anechoic outlet patch.

3.3. The passage of turbulence for LES-URANS coupling

When a LES-URANS coupling is performed, the passage of TKE and ω to the downstream domain needs further considerations. In particular, the TKE profile to be transferred at the RANS inlet can be directly computed from the solution of the upstream LES as:

$$TKE = \frac{1}{2}(u\prime^2_{X,rms} + u\prime^2_{Y,rms} + u\prime^2_{Z,rms}) \tag{3.31}$$

The expression is exact when no coherent structures shall be passed from the LES to the URANS solution. In case only part of the LES signal is

filtered at the interface, the passage of TKE requires further attention (as discussed in section 4.5.4).
The estimate of ω from the LES shall be considered with care as well. The importance of a correct estimate of the turbulent decay to simulate the HS migration in turbine was already observed in section 2.7 and will be discussed in more detail in chapter 8. One of the main conclusions of the study is that a too high (or too low) turbulent decay leads to a wrong prediction of the turbulent mixing, which affects the accuracy in predicting the hot streak migration in turbine.
To propose a physical estimate of ω from the LES, the classical transport equation for the TKE can be considered:

$$\frac{\delta TKE}{\delta t} + u_j \frac{\delta TKE}{\delta x_j} = \tau_{ii} \frac{\delta u_j}{\delta x_j} - \beta^* k\omega + \frac{\delta}{\delta x_j}\left[(\nu + \sigma^* \nu_T)\frac{\delta k}{\delta x_j}\right] \tag{3.32}$$

where the Einstein's notation is used. It is worth to notice that the interface between combustor and turbine is normally placed upstream from the blade leading edge in a region where the flow passage is straight. In this part of the domain, one can hypothesize that the convection and destruction terms are the most important ones within the equation. Therefore, the unsteady and the diffusive terms can be neglected. This leads to the following formulation:

$$u_j \frac{\delta TKE}{\delta x_j} = -\beta^* TKE\omega \tag{3.33}$$

To simplify the equation for ω a further hypothesis is considered, imposing that the transverse contribution of the velocity vectors are negligible with respect to the axial one. In these cases, an inlet value of ω for the RANS domain can be estimated from the TKE decay of LES at the interface in the following way:

$$\omega = -\frac{1}{TKE\beta^*} u_x \frac{\Delta TKE}{\Delta x} \tag{3.34}$$

The hypothesis of 1D flow is a strong assumption at the combustor-turbine interface, which is on the other hand caracterized by high swirl. Nevertheless, this makes the estimate of ω very practical and extremely simple. In fact, the following procedure can be applied:

- The surface averaged TKE is evaluated for two surfaces within the overlapping region of the upstream domain.
- An estimate of ω can be calculated from Eq. 3.34.
- The uniform value of ω is imposed to the downstream subdomain inlet.

In section 8.4.1 it is demonstrated that Eq. 3.34 remains a valid method to estimate ω for the combustor-turbine interface by applying the equation to the FACTOR test case [35], which is characterized by high-swirl flow at the combustor outlet.

3.4. Final remarks

In this section, the development of a coupling approach to be applied to the combustor-turbine interaction study is discussed. The whole combustor-turbine domain is solved by using two different compressible codes, applied to the combustion chamber and the turbine separately. The two simulations communicate some information to each other to get a common stabilized solution. Considering the better quality of the solution in combustion chamber when unsteady approaches are used, coupling procedures are studied for URANS-URANS, LES-URANS and LES-LES applied to combustor and the turbine respectively.
The exchange of information takes place at the outlet patch of the subdomain upstream and at the inlet of the subdomain downstream. These patches can collapse in one single patch or can be placed at a certain distance between each other, with one region of the domain (overlapping region) which is modeled by both subdomains. According to the theory of characteristics, only one information is transferred from the subdomain downstream to the one upstream. This can be used to define a Dirichlet or a non-reflecting condition at the upstream subdomain outlet. On the other hand, four or five characteristic variables can be transferred from the subdomain upstream to the downstream inlet. The passage of all five characteristic variables to the domain downstream assures a better continuity of the solution at the interface, but in this case the problem is well-posed only under strict conditions.
During the unsteady simulation, the exchange of information takes place regularly in time. For an accurate transfer of the unsteady structures between the subdomains it is required that the physical time simulated by the two solvers between two communications is consistent. On the other hand, in a first phase of the coupled analysis it is suggested to run the two simulations independently in time, employing a "weak" synchronization for the communications (Fig. 3.1-a). This permits a quicker convergence of the unsteady fields for the two subdomains.
The application of a coupling procedure to LES-URANS requires further considerations.

1. The turbulent fluctuations resolved by LES must be filtered out at the URANS inlet. This can be done by using a time-marching filter. The set-up of the filter is based on the estimate of the signals to be transferred from the upstream to the downstream domain f_c and the

minimum frequency to filter out f_t. The use of the simplified transfer function in Fig. 3.8 is suggested in this work.

2. All LES fluctuations approaching the interface must cross the upstream subdomain outlet without being substantially deformed by the numerical boundary. This is achieved by using non-reflecting conditions, such as the NSCBC by Poinsot and Lele [83]. The set-up of the non-reflecting outlet is optimized in this chapter to be applied to the coupled simulation. At this purpose, the use of $\beta = M$ and $\lambda_{inf} = L_{dom}$ in Eq. 3.22 is recommended.

3. The continuity of the turbulent variables at the interface is obtained by using Eq. 3.33 and 3.34.

Chapter 4.

The Coupling Procedures

The aim of the present chapter is to develop optimal and stable coupling procedures for LES-LES, LES-URANS and URANS-URANS for combustor and turbine respectively. This is achieved by taking into account the theoretical discussion in chapter 3.
Two different methods are proposed:

- A coupling without overlapping region for LES-LES is discussed in section 4.1.
- A coupling with overlapping region is proposed in section 4.2 for LES-URANS and generalized to URANS-URANS in section 4.3.

The procedures will be validated in section 4.5.
Part of the results discussed in the present chapter were published in:

S.Vagnoli, T.Verstraete: A new method for zonal LES URANS computations with exchange of information between different codes. Proceedings of the ECCOMAS conference, 2014, Barcelona (Spain).

4.1. LES-LES coupling procedure

The procedure aiming at coupling two compressible LES is developed without employing any overlapping region, with the upstream outlet connecting directly to the downstream inlet. A scketch of the coupling is shown in Fig. 4.1. For clarity, the upstream and downstream domain are plotted as shifted in tangential direction. During the communication i, the domain upstream transfers the vector G_i to the downstream one, while vector F_i is exchanged from the upstream to the downstream solver. The two vectors are defined as:

$$F_i = \begin{pmatrix} (U_x - c)\left(\frac{\delta p}{\delta x} - \rho c \frac{\delta U_x}{\delta x}\right) \end{pmatrix} \qquad G_i = \begin{pmatrix} \rho \\ \rho U_x \\ \rho U_y \\ \rho U_z \\ p \end{pmatrix} \tag{4.1}$$

One can clearly recognize that F_i represents the backwards-moving charac-

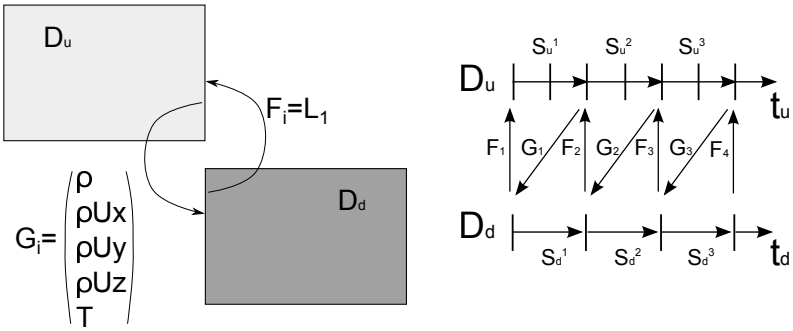

Figure 4.1.: Method 1: structure of the LES-LES coupling procedure in space (right) and synchronization in time (left).

teristic wave L_1, defined in Eq. 3.17. For the classical NSCBC formulation, L_1 represents the information passed from the external environment to the outlet patch, and must be specified by imposing a proper boundary condition. During a coupled simulation, L_1 can instead be directly computed from the solution downstream.
On the other hand, the upstream domain transfers all flow quantities to the downstream one. These are then used to impose Dirichlet conditions for all the characteristic values at the inlet. Such a coupling procedure can then be defined as "hard", since it assures an exact continuity of all fields at the interface between the two solutions. This is an essential advantage for an accurate LES-LES coupling, since it guarantees that all turbulent structures, as well as the pressure waves, are accurately transferred between the two simulations.
The synchronization in time of the two solvers is based on the strong coupling procedure, already shown in Fig. 3.2-a and repeated in Fig. 4.1 as a reference. It is characterized by the following steps:

- When the simulation starts, the downstream solver communicates F_i to the upstream one.

- F_i is used to solve Eq. 3.16 at the upstream outlet. In this case, the forward-moving characteristic waves L_2, L_3, L_4 and L_5 are evaluated from the solution within the upstream domain, while L_1 is obtained directly from F_i.

- After the integration of S_u for a time interval $\Delta t = dt_d$, the vector G_i is passed to the solver downstream and is used to impose Dirichlet conditions for all characteristic variables at the inlet.

- The solved downstream S_d integrates one time step

- The algorithm continues until convergence.

In case $dt_u < dt_d$, G_i can be averaged over N snapshots, where $N = dt_d/dt_u$ is an integer. As previously discussed in section 3.1.3, the passage of all five unknowns from the upstream to the downstream domain leads to well posed problems only if certain conditions are respected. In particular, the current application can be stable only if $dt_u \sim dt_d$ and the grids of the upstream and the downstream subdomains are similar on the common patch.

4.2. LES-URANS coupling procedure

For LES-URANS applications, the use of non-reflecting conditions at the LES outlet and of a filter in transferring the quantities from LES to URANS causes two main issues:

- The vortical structures transferred from LES to URANS will be affected by the non-reflecting boundary at the LES outlet. This leads to a decrease of the vortices intensity and eventually to distortions, which can be only partly limited by an appropriate set-up of the NSCBC (section 3.2.2.4).

- The filtering procedure introduces numerical fluctuations at the URANS inlet, due to the non-perfect filtering of the turbulence at the LES outlet. This will affect the solution in the first part of the domain.

According to these considerations, it is convenient to include an **overlapping region** between the LES outlet and the URANS inlet. In this way, two beneficial effects can be achieved:

- The vortical structures transferred from LES to URANS are taken at a certain distance from the LES outlet, therefore the numerical impact of the outlet patch on the solution is more limited.

- Due to the numerical diffusion, the spurious fluctuations generated at the URANS inlet can be observed only in proximity of the inlet patch. In this region, the LES solution then can be used to describe the flow.

The structure of the coupling in space with overlapping is shown in Fig. 4.2. For clarity, the upstream and downstream domains are shifted in the picture, while in reality they are overlapping. During the communication i,

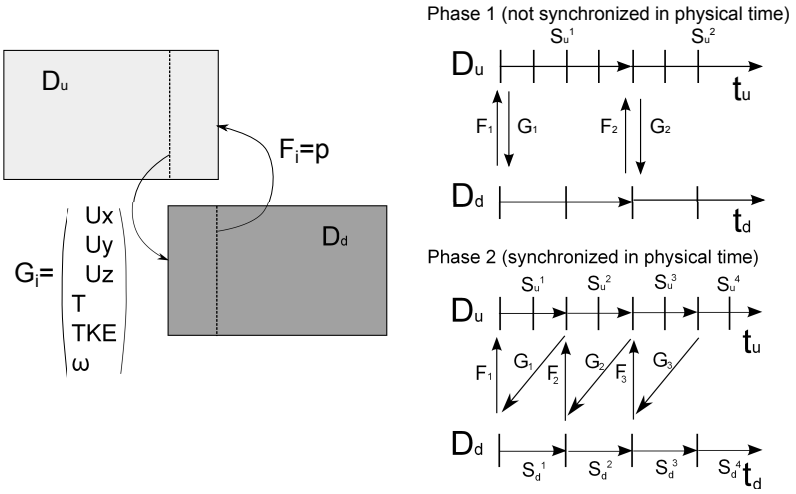

Figure 4.2.: Method 2: structure of the LES-URANS coupling procedure in space (right) and synchronization in time (left).

G_i is interpolated from the internal field upstream to the downstream inlet, while F_i is interpolated from the downstream subdomain to the upstream outlet. The two vectors are defined as:

$$F_i = (p_i) \qquad G_i = \begin{pmatrix} \rho U_x \\ \rho U_y \\ \rho U_z \\ T_i \\ TKE \\ \omega \end{pmatrix} \tag{4.2}$$

Differently from the previous procedure, p_i is transferred from the URANS to the LES domain. This is used to define p_{Inf} within Eq. 3.22 following the indications in section 3.2.2.5 to improve the continuity of the solution at the interface.
At the inlet of the downstream subdomain, a Dirichlet condition is imposed for ρU and T. TKE and ω can be calculated from the LES domain by Eq. 3.31 and 3.34 respectively. According to the RANS turbulence model, ω can then be converted to ϵ before being imposed as Dirichlet condition.
The sincronization in time of the two solvers is based on the alternance between "weak" coupling in the first part of the simulation and strong coupling in the second part. For a more detailed description of the corresponding algorithm, the reader is referred to section 3.1.
Since only four information are transferred from the upstream subdomain to the downstream one, the stability issues described for the previous method don't apply to this technique, therefore $dt_u \neq dt_d$ can be imposed.

4.3. URANS-URANS coupling procedure

The coupling procedure introduced for LES-URANS applications can easily be extended to URANS-URANS. In this case, TKE and ω appearing in G_i can be directly obtained from the variables solved by the RANS model. Moreover, for some configurations in which URANS is used for the simulation upstream, no unsteady structures cross the interface between the subdomains. In these cases, the pressure coming from F_i can be directly imposed at the upstream outlet by a Dirichlet condition, improving the continuity of the solution at the interface.

Method \ Application	LES - LES	LES - URANS	URANS - URANS
Method 1: no overlapping	hard approach	N.A.	N.A.
Method 2: with overlapping	N.A.	mild approach	mild approach

Table 4.1.: Range of applicability of the two coupling methods developed.

4.4. Synthesis of the developed coupling procedures

The coupling procedures developed in this chapter and their range of applicability are synthesized in Tab. 4.1.

- The first coupling (method 1) does not include the overlapping region. It is developed in particular for LES-LES.
- The second coupling (method 2) includes the overlapping region. It is suitable for LES-URANS and URANS-URANS and can be defined as a “mild” coupling.

Starting from the next section, the validation of all the procedures is presented.

4.5. Coupled test cases

The coupling procedures presented are validated on a series of test cases with increasing complexity, listed in Tab. 4.2. In a first step, the stability and accuracy of methods 1 and 2 are assessed on simple laminar condition:

Approach	Methods	Test case	Reynolds number
Laminar	method 1	Shock wave	N.A.
Laminar	method 2	Shock wave	N.A.
Laminar	method 1	Euler vortex	N.A.
Laminar	method 2	Euler vortex	N.A.
LES-URANS	method 2	Turbulent channel	24000
URANS-URANS	method 2	Turbulent channel	6900
LES-URANS	method 2	Cylinders in tandem	400000
LES-LES	method 1	Cylinders in tandem	400000

Table 4.2.: List of test cases presented in this chapter.

- **The backwards-moving shock wave**. This is a fully laminar test case permitting to assess the capability of the methods to transfer unsteady pressure wakes from the downstream to the upstream domains.

- **Euler vortex convected downstream**. This is a second laminar unsteady case, which can be used to assess the capability of the methods to transfer vortical structures from the upstream to the downstream domain.

In a second step, high-Reynolds flows are analyzed to verify the coupling methods for URANS-URANS, LES-URANS and LES-LES. The test cases are chosen to be representative of some typical aspects characterizing the flow field at the combustor-turbine interface:

- **High-Reynolds turbulent channel**. For the current test, the turbulence developed close to the wall is the only unsteadiness detected at the interface. This flow is chosen to be representative of the outlet of a combustion chamber characterized by low swirl and big dimensions. The simulation will be resolved by LES-URANS and URANS-URANS.

- **High-Reynolds flow over two cylinders in tandem**. This is a very challenging test case, since both turbulent and big structures cross the interface. This test case is chosen to be representative of the outlet of a compact combustion chamber characterized by a highly turbulent and unsteady flow field. It will be used to verify the LES-URANS and the LES-LES approaches.

4.5.1. The backwards-moving shock wave

The first test case discussed is very effective in clarifying one of the main differences between methods 1 and 2. A domain of length L_{dom}=0.4m in axial and 0.2m in tangential direction is employed to simulate a flow with constant inlet velocity U_0=100m/s. The initial solution is a uniform field characterized by P_0=100000Pa and T_0=300K. At t=0, P_{out}=105000Pa is imposed. This generates a backwards moving pressure wave which migrates across the whole domain.
To set-up the coupled simulations, the domain is divided in two subdomains, identical to each other. When used, the overlapping region extends for $L_o/L_{dom} = 0.05$. Each domain is meshed by a 200x200 2D grid and solved by the p-based solved rhoPimpleFoam. For both simulations, the integration in time is performed by an explicit Euler scheme with $dt = 10^{-7}s$, while second order central schemes are used in space. For method 2, NSCBC are employed at the upstream subdomain outlet. A sketch of the numerical set-up is shown in Fig. 4.4.
The evolution of the wave in time is monitored by plotting the pressure along the axis perpendicular to the interface. Figure 4.5 shows the pressure distribution for three different time instants, representing the pressure wave approaching and crossing the upstream outlet.
As expected, method 2 is not able to transfer a pressure unsteadiness from the downstream to the upstream domain. This is due to the use of the Lodato's formulation [85] for the anechoic downstream outlet.
As a matter of fact, the "weak imposition" of p_{Inf} for the anechoic outlet, specified by Eq. 3.22, only gives the possibility of imposing the potential effect of the downstream domain on the upstream one in a time-averaged sense.
This limitation does not lead to a loss in accuracy when URANS simulations are performed for the subdomain downstream; for the combustor-turbine test case only aeroacoustic pressure waves are expected to cross the interface from the turbine to the combustor [80]. These waves cannot be reproduced in detail by URANS because of the high numerical dissipation. On the other hand, it is worthwhile to note that LES is able to solve in detail the propagation of aeroacoustic waves within the domain [20], therefore a similar approximation cannot be accepted for a LES-LES coupling.
Method 1, on the other hand, is able to transfer the pressure wave between the two domains in a very accurate way. This is due to the fact that the backwards moving information L_1 is directly calculated into the downstream domain and imposed at the upstream outlet. This test, although very simple, confirms that method 1 is well suited for LES-LES applications, whilst method 2 presents evident limitations in this sense.

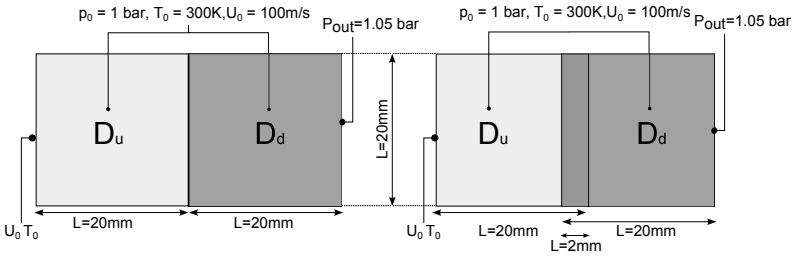

Figure 4.3.

Figure 4.4.: Scheme of the backwards-moving shock wave test case. On the left: method 1. On the right: method 2.

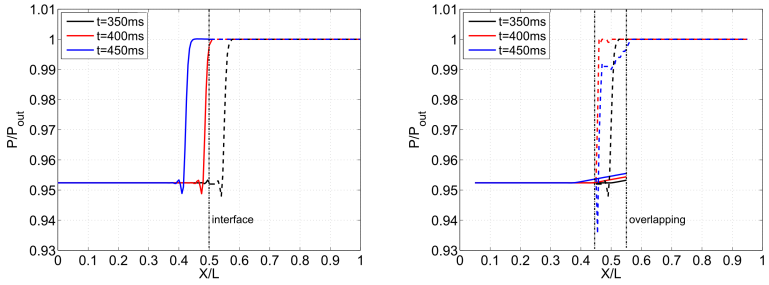

(a) Method 1 **(b)** Method 2

Figure 4.5.: Shock propagation between the domains.

4.5.2. The vortex convected downstream

The accuracy in transferring the main vortical structures between the upstream and downstream domains is tested by applying the two methods to the classical test case of the Euler vortex. An empty domain of length L_{dom}=0.4m in axial and 0.2m in tangential direction is employed. At t=0 an Euler vortex is mapped in the first half of the domain, applying Eq. 3.23 with the following parameters: $C_v = 2.5m^2/s$, $R_v = 0.01$, $U_0 = 100m/s$, $T_0 = 300K$, $p_0 = 100000Pa$.
The computation is performed by dividing the domain in two parts and using two instances of rhoPimpleFoam. The two subdomains are meshed by a 200x200 2D grid. A constant velocity $U_0 = 100m/s$ and temperature $T_0 = 300K$ are imposed at the upstream domain inlet, $P_{Inf} = 100000Pa$ is imposed by means of the anechoic NSCBC formulation at the outlet of the domain downstream. The integration in time is performed by an explicit Euler scheme with $dt = 10^{-7}s$, while second order central schemes are used in space. A sketch of the numerical set-up is shown in Fig. 4.7.
Methods 1 and 2 are both tested. In the second case, the overlapping region

extends for $L_o/L_{dom} = 0.05$.

Figures 4.9 and 4.10 show three snapshots representing the vortex ap-

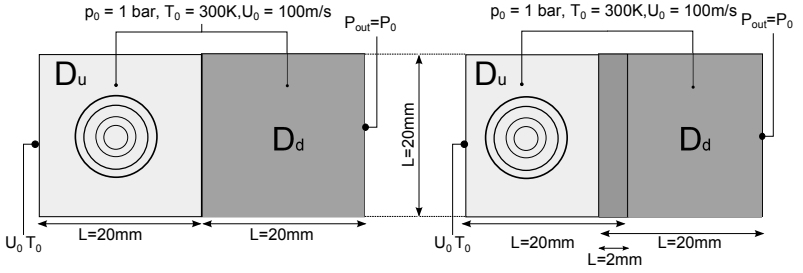

Figure 4.6.

Figure 4.7.: Scheme of the convected Euler vortex test case. On the left: method 1. On the right: method 2.

proaching and crossing the interface between the domains, applying method 1 and 2 respectively. For both approaches, no evident distortions of the vortex transferred downstream are observed: considering in particular the very high vortex intensity, the transfer of the structure appears very accurate for both cases.

To quantify the accuracy of the exchange of information for methods 1 and 2, the pressure distribution is evaluated at the center of the overlapping region for method 2 and on the common patch for method 1. Fig. 4.8 shows the error $\epsilon_{\Delta p}$ for the three time instants shown in Fig. 4.9 and 4.10. The error is defined as:

$$\epsilon_{\Delta p} = \frac{p_{CFD} - p_{exact}}{p_{Inf} - p_{exact,r=0}} \tag{4.3}$$

For both methods, higher errors are observed for $t/t_{ref} = 0.5$ and $t/t_{ref} = 0.625$ (where $t_{ref} = L_{dom}/U_0$), since the error cumulates during the interaction of the vortex with the outlet surface. As a general consideration, the error is very low for both methods (compared for example to [83]), although one can notice that method 1 performs slightly better than method 2: this seems to be linked to the "hard" imposition of the inlet pressure, which is calculated both from the backwards and the onwards moving information. Moreover, method 2 is more affected by interpolation errors, since the grids are compenetrating each other at the interface.

It is interesting to observe that method 1 is even more accurate than the original NSCBC applied without coupling. The error distribution obtained for the classical NSCBC expression without coupling is represented in Fig. B.3. This improvement is clearly due to the fact that L_1 is computed directly from the solution downstream, and not imposed by Eq. 3.22.

As previously discussed, stability issues can be observed when a "hard"

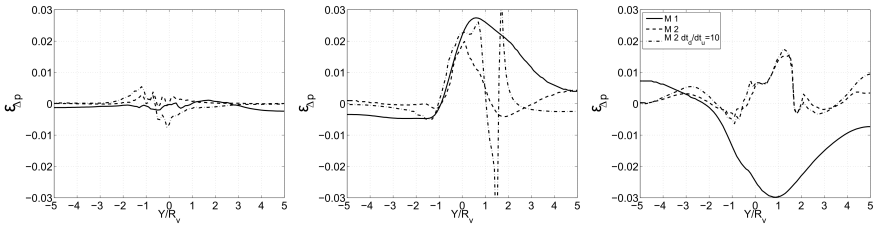

(a) **(b)** **(c)**

Figure 4.8.: Error $\epsilon_{\Delta p}$ in function of the Y coordinate at the outlet for the two coupling procedures.

coupling procedure is used in cases where the backwards-moving pressure waves calculated within D_u and D_d in correspondence of the downstream subdomain inlet are not exactly the same. This happens for example when overlapping regions or $dt_u \neq dt_d$ are used (see section 3.1.3). To verify this observation, Fig. 4.11 shows the result obtained on the same test case by employing method 2, modified to include the variable p into G_i in Eq. 4.2. The pressure is then used to define a Dirichlet condition at the downstream domain inlet. An analogous methodology is proposed by Morata [69].

For this case, when the vortex crosses the interface, spurious pressure fluctuations are generated at the downstream inlet. The nature of these wiggles is clearly numerical, being generated by the boundary condition which is not "in agreement" with the information coming from the inner solution. This is a clear indication of an intrinsic instability of the method, which can only be solved by passing to a "mild" approach (i.e. reducing the number of information exchanged from the upstream subdomain to the downstream one).

To assess the effect of different upstream and downstream time steps on the stability of method 1, tests were performed increasing dt_d while using method 1. As expected, starting from $dt_d/dt_u = 10$ the simulation shows similar instability issues as the ones observed in Fig. 4.11. The coupling becomes completely unstable for $dt_d/dt_u > 10$. It is worth noticing that the error at the interface results lower than the one calculated for a classical NSCBC outlet (i.e. without coupling) even for the extreme case of $dt_d/dt_u = 10$.

4.5.3. Turbulent channel flow

All laminar tests performed gave essential information about the stability and the accuracy of the coupling methods. Nevertheless, before performing coupled simulations of combustors and turbines, it is essential to assess the

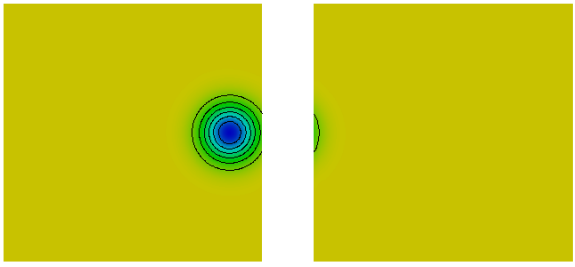

(a) t/t_{ref}=0.375

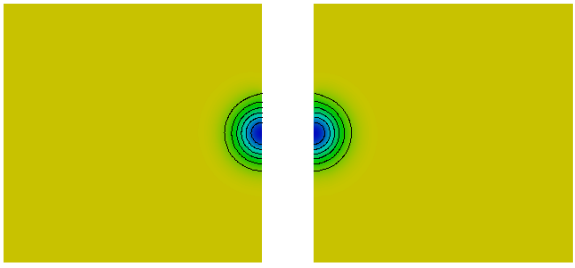

(b) t/t_{ref}=0.5

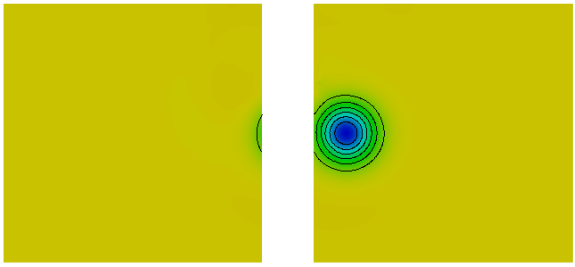

(c) t/t_{ref}=0.625

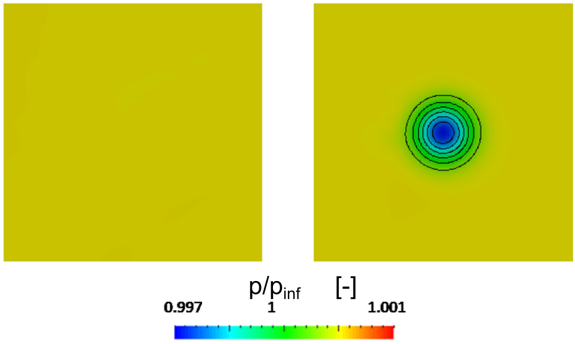

(d) t/t_{ref}=1

Figure 4.9.: Vortex convection between the domains. Method 1 is applied.

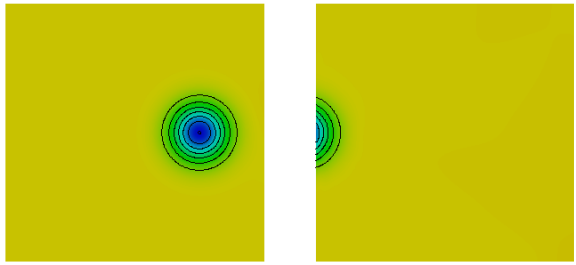

(a) t/t_{ref}=0.25

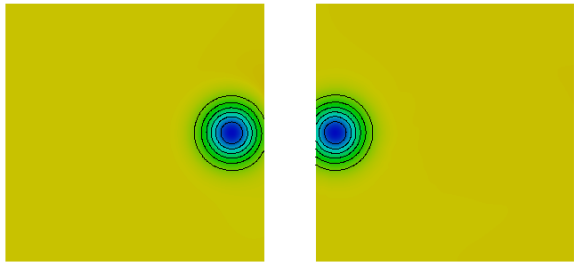

(b) t/t_{ref}=0.375

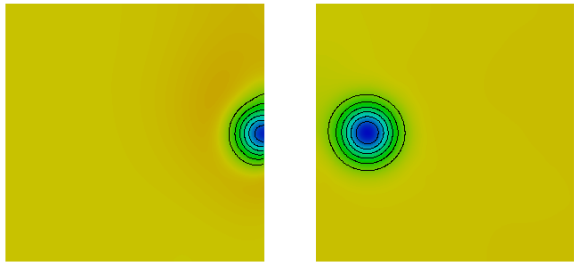

(c) t/t_{ref}=0.5

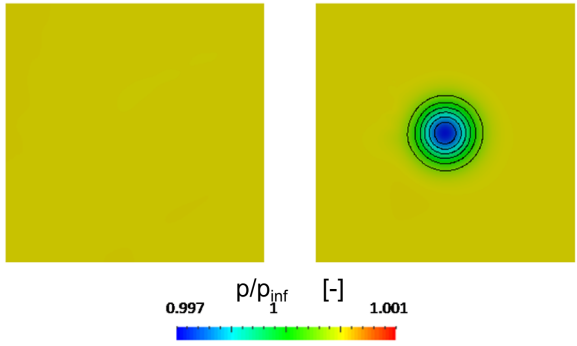

(d) t/t_{ref}=0.8

Figure 4.10.: Vortex convection between the domains. Method 2 is applied.

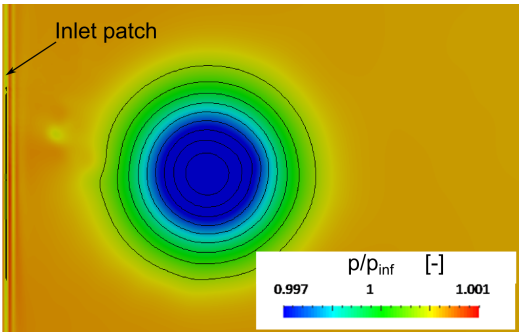

Figure 4.11.: Wiggles generated at the inlet of the upstream domain when method 2 with strong coupling is applied.

methods on academic turbulent test cases.
The first turbulent test case proposed is a flow between two parallel walls. The scheme of the case is shown in Fig. 4.12. The flow is limited by solid planes placed at a distance h between each others. As a reference, x represents the coordinate parallel to the flow, while y is the direction perpendicular to the walls. To complicate a bit the test case, a uniform velocity is imposed at the inlet of the computational domain, in such a way that the boundary layer will develop directly within the channel. The channel length is set to $L = 40h$ to make sure that one portion of the domain will be characterized by a fully developed flow. This facilitates the comparison of the numerical results with the large amount of experimental data which can be found in literature (an exaustive list of experiments can be found in Kim et al. [89]).
The channel flow can be characterized by a Reynolds Number based on the bulk velocity:

$$Re_b = \frac{\rho U_b h}{\mu} \tag{4.4}$$

where the bulk velocity U_b is defined as:

$$U_b = \frac{1}{h}\int_0^h u_x dy \tag{4.5}$$

For the current test case, the inlet conditions are set to get $M = 0.3$ within the channel, which is representative of the low-Mach condition at the outlet of industrial combustors. In terms of Reynolds number, Re_b=6900 and 24000 are imposed. These value are lower than the one expected for typical combustor-turbine test cases (for which the Reynolds number based on the passage height reaches $\sim 10^5$) but permits to use the experimental results of Kim et al. [89] as a reference.
The turbulent channel will be used to test the quality of the LES-URANS

and URANS-URANS coupling methods. In this sense, the present discussion will be splitted in three parts.

- The full domain at Re_b=6900 is simulated by URANS, to validate the CFD with respect to the experimental data.
- The URANS-URANS procedure will be validated by coupling the ρ-based and p-based codes for the case at Re_b=6900.
- The LES-URANS method will then be applied to the case at Re_b=24000.

It is important to point out that for the current test case the unsteady signal depicted at the interface between the subdomains is generated only by turbulence. This situation is representative of a combustor-turbine configuration in which the unsteady vortices due to the flow injected from the swirlers remain confined into the primary zone of the chamber; such a flow field could be generated for example by a combustion chamber characterized by low swirl and big dimensions.
When the URANS is used for the domain upstream, an unsteady signal at the interface can be obtained only during the transient from the initial to the stabilized solution.
A further test case with coherent unsteady vortices crossing the interface will be presented in section 4.5.4.

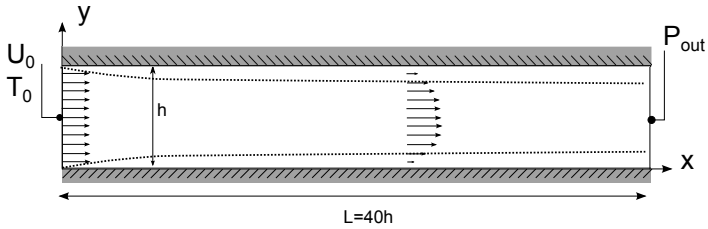

Figure 4.12.: The turbulent channel geometry with boundary conditions.

4.5.3.1. Validation of CFD

As a first step, URANS is used to simulate the whole domain, and validated with respect to the experimental results of Eckelmann et al. [90] and Kreplin et al. [91], which are characterized by a similar Re_b.
The URANS is carried out both with the p-based code rhoPimpleFoam and the ρ-based $TUMDF$. No particular differences were observed in terms of stability and quality of results, therefore only the flow field obtained with rhoPimpleFoam is presented in the following.
The simulation is performed using an explicit Euler scheme in time and a

second order central scheme in space with a small amount of upwind filtering (filteredLinear scheme in OpenFOAM). The steady solution is obtained imposing $dt = 10^{-6}s$ and 50 outer corrector loops to guarantee stability during the transient from the initial solution.

Figure 4.13 shows the grid obtained after a mesh convergence study. This

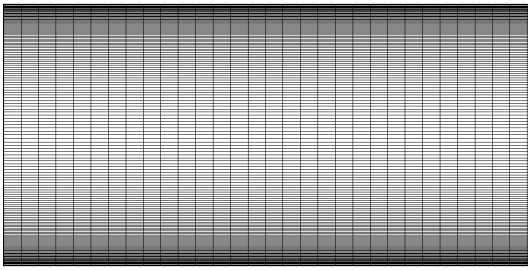

Figure 4.13.: Detail of the 2D grid used for the RANS simulations of the turbulent channel: passage center.

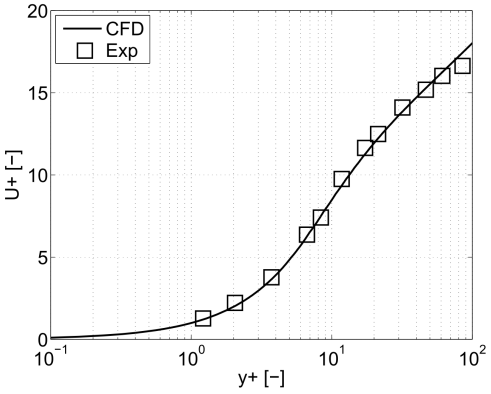

Figure 4.14.: Velocity distribution close to the wall computed by CFD and compared to the results of Eckelmann [90].

is a 2D structured mesh with 70000 cells, characterized by $Y+ \sim 0.8$ all along the wall. The simulation is run with the $k-\omega$ SST low-Re model. Figure 4.14 shows the boundary layer profiles obtained at $x/h = 30$ (where a fully developed flow is expected) and compared to the experimental trend measured by Eckelmann et al. [90]. It can be clearly observed that the RANS model is able to reproduce accurately the turbulent boundary layer shape.

In terms of skin friction coefficient at $x/h = 30$, defined as $C_f = \tau_w / \frac{1}{2}\rho U_b^2$, the local results is $6.89 \cdot 10^{-3}$ which is in very good agreement with Dan's

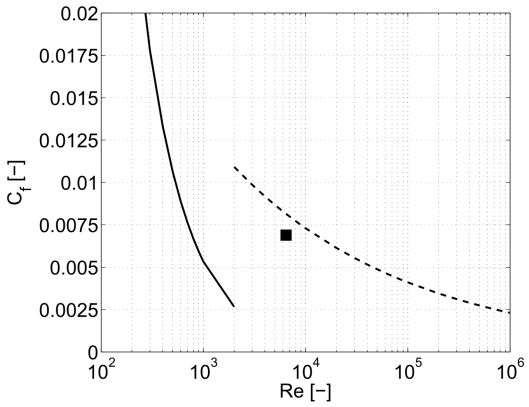

Figure 4.15.: Friction coefficient computed by CFD and compared with the correlation of Dean [92].

correlation for fully developed turbulent channels, as shown in Fig. 4.15. Fig. 4.16 shows the $u\prime_{rms}$ obtained by RANS, which can be calculated as:

$$u\prime_{rms} = \sqrt{\frac{2}{3}TKE} \tag{4.6}$$

This is compared to the $u\prime_{rms}$ components obtained by the experiments of Kreplin et al. [91]. Based on the experimental results, it is interesting to point out that the real turbulent field developed within the channel is not isotropic. The $u\prime_{rms}$ calculated by the $k-\omega$ SST model (which is based on the assumption of isotropic turbulence) is of the same order of magnitude as the fluctuating components experimentally obtained. In particular, CFD presents the classical features of a turbulent bounded flow, presenting a peak of turbulence at $Y+ = 20$ which approaches zero close to the wall.

4.5.3.2. URANS-URANS coupling

The second step of the analysis consists of an investigation of the channel by using the URANS-URANS coupling technique (method 2) previously described.
For this purpose, the domain is splitted in two subdomains equal to each other, including an overlapping region which extends for $L = 4h$, as shown in Fig. 4.17.

For the subdomain upstream (D_u) the pressure based solver rhoPimpleFoam is employed. The flow evolution in time is solved by imposing $dt = 10^{-6}s$ and 50 outer corrector loops for the PIMPLE algorithm. The explicit Euler scheme is used to discretize in time the NS equations. The

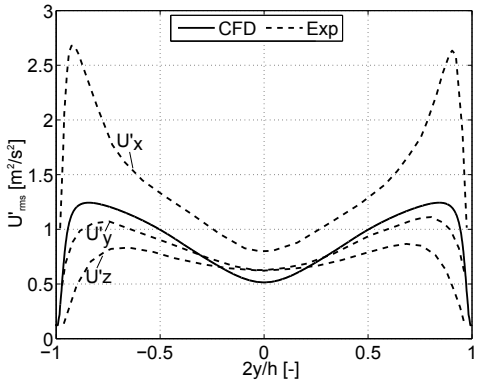

Figure 4.16.: RMS velocity fluctuations computed by the experiments of Kreplin et al. [91] and the current simulation.

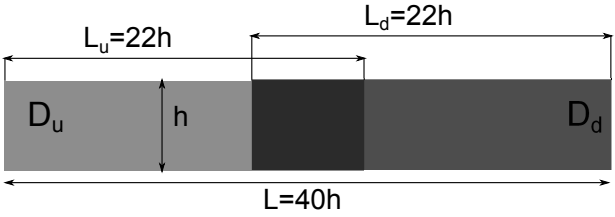

Figure 4.17.: Upstream and downstream subdomains for the URANS-URANS coupled simulation of the cooling channel.

subdomain is reproduced by a 3D structured grid with 0.6MLN cells, characterized by a very similar Y+ distribution as the one used for the full domain investigation. The filteredLinear scheme is employed for space discretization.The subdomain downstream (D_d) is solved using the ρ-based solved TUMDF, considering a time step $dt = 5 \cdot 10^{-7} s$ and 125 inner iterations. A second order central scheme is employed for space discretization. To enhance the non-conformity of the meshes at the interfaces between the two subdomains, a 2D grid with 26000 cells and $Y+ \sim 0.8$ is used for the upstream domain. The $k - \omega$ SST model is used for both computations.
The initial solution consists of uniform velocity, pressure and temperature fields imposed on the whole domain. The coupled evolution towards a stabilized solution is obtained by exchanging information every $dt = 10^{-4} s$ (corresponding to about 1/3 of the convective time for the full channel). To avoid reflection of the pressure waves formed during the transitory phase, non-reflecting conditions at the upstream subdomain outlet are used, while a fixed pressure is imposed at the outlet of the subdomain downstream.

The convergence of the coupling procedure is monitored by recording the

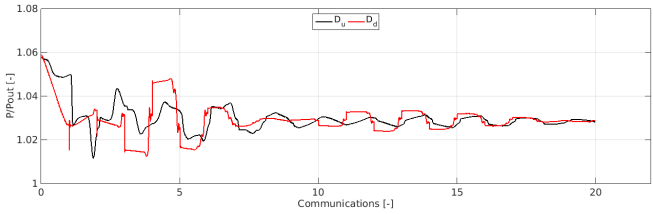

Figure 4.18.: Convergence of the URANS-URANS coupling procedure: pressure evolution at the overlapping region center.

pressure signal at the overlapping region center, as shown in Fig. 4.18. Starting from an omogeneous field, strong pressure fluctuations are formed and exchanged between the subdomains during the first communications. After about 20 exchanges of information, the pressure fluctuations at the interface have almost disappeared and the coupled procedure can be considered as converged.

The pressure and velocity distributions along the x axis are shown in Fig.

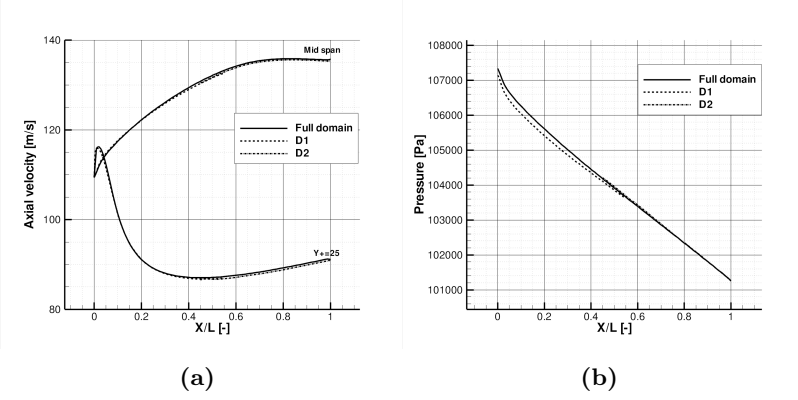

(a) **(b)**

Figure 4.19.: Axial velocity (a) and pressure (b) distribution in X direction for the URANS-URANS coupled solution.

4.19, where the coupled solution is compared to the single-solver one. The evolution of the velocity field is not influenced by the interfaces between the subdomains, and the solution is in excellent agreement with the one obtained by using an unique solver.

The pressure continuity from the inlet to the outlet patches is satisfactory, even though one observes a small jump in correspondence of the outlet upstream. This is most probably due to the use of non-reflecting conditions at upstream domain outlet. The error can be quantified in terms of pressure difference between the inlet and the outlet of the channel, which is estimated to Δp=5930 Pa for the coupled and Δp=6010 Pa for the single-code simula-

tion. This discrepancy can be considered acceptable for typical engineering purposes.

To better evaluate the effect of the interfaces on the solution quality, Fig.

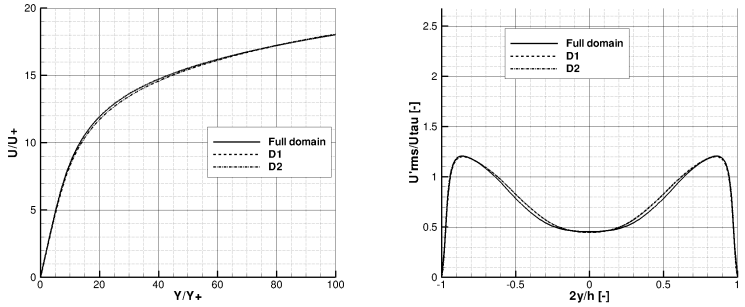

(a) **(b)**

Figure 4.20.: Axial velocity (a) and TKE profile (b) in Y direction for the URANS-URANS coupled solution. Results at the overlapping region center.

4.20 shows velocity and TKE plotted in y direction at the center of the overlapping region. The upstream and downstream solutions match each other almost exactly and are both in excelled agreement with the single code solution. This leads to the conclusion that these quantities are not influenced by the presence of the interface.

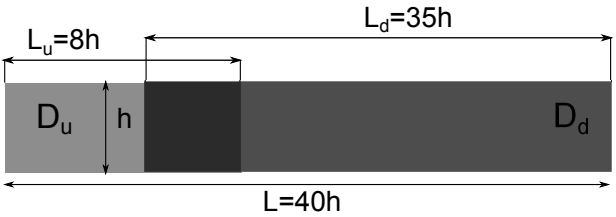

Figure 4.21.: Upstream and downstream subdomains for the LES-URANS coupled simulation of the cooling channel.

4.5.3.3. LES-URANS coupling

In a second phase, the flow between parallel walls is studied by using the LES-URANS coupling procedure (method 2). To facilitate the generation of turbulent fluctuations within the LES subdomain, it was decided to scale the channel to get $Re = 24000$ while imposing the same pressure, velocity and temperature fields at boundaries. The domain in study is shown in Fig.

4.21. The upstream LES subdomain is relatively short, extending for about $L_u = 8h$ (1/5 of the whole channel). The URANS domain, on the other hand, extends for about $L_d = 35h$. An overlapping region of about 4h is considered between the subdomains.
The development of turbulent fluctuations is enhanced by injecting a random noise at the LES inlet. At this scope, the inlet velocity formulation is modified as:

$$u_x(t) = U_x + a_x|U|r(t), u_y(t) = U_y + a_y|U|r(t), u_z = U_z + a_z|U|r(t) \quad (4.7)$$

Where r(t) is a random number comprised between 0 and 1 (changing in time) and $a_x = a_y = a_z = 0.35$. The grid employed for the upstream subdomain is characterized by 0.48MLN cells. It is refined enough to satisfy the Pope criterion everywhere (i.e. the TKE resolved shall be higher than the 80% of the global TKE, see section 1) except really close to the inlet (for the current set-up, it is important to point out that the Pope criterion becomes meaningless close to the inlet, since the random noise generated is not representative of a real turbulent spectrum).
From the numerical point of view, the same set-up employed for the URANS-URANS coupling procedure described in the previous section is used, except the fact that the LES makes use of 21 corrector loops to solve a time step $dt = 8 \cdot 10^{-8}s$ (chosen to get $CFL < 1$ everywhere). The Smagorinsky model is chosen for the subgrid scales, including the van Driest formulation at wall [13].
The exchange of information between the two domains is done every $2{\cdot}10^{-5}s$. The time interval T_s (to average the fluctuating quantities transferred from the upstream to the downstream domain, see section 3.2.1) is selected considering that it must be long enough to filter out all LES turbulent structures to get a quasi-steady solution at the URANS inlet.

The value chosen for T_s was verified testing two different coupled simulations, in which the time average of all quantities transferred from the upstream to the downstream domain is performed on two different time intervals, equal to $T_s = 2{\cdot}10^{-4}s$ (about 1 flow-through time for the LES domain) and $T_s = 2{\cdot}10^{-5}s$. The axial velocity signal obtained for the two cases at the center of the overlapping region is shown in Fig. 4.22. The smallest T_s examined is not large enough to completely filter out the unsteadiness generated within the LES domain, as the URANS solution depicts velocity fluctuations equal to about 1% of the local mean value. On the other hand, when the longest time interval is employed, the solution downstream appears smooth and can be considered steady in first approximation.
In agreement with this observation, the results discussed in the following following are related to the case with $T_s = 2 \cdot 10^{-4}s$.

The effect of the filter can be better appreciated in Fig. 4.23, where the velocity field on the x-y plane is depicted. The solution for the subdomain upstream is characterized by spots of high and low velocity, representing unsteady turbulent structures which develop within the LES subdomain.

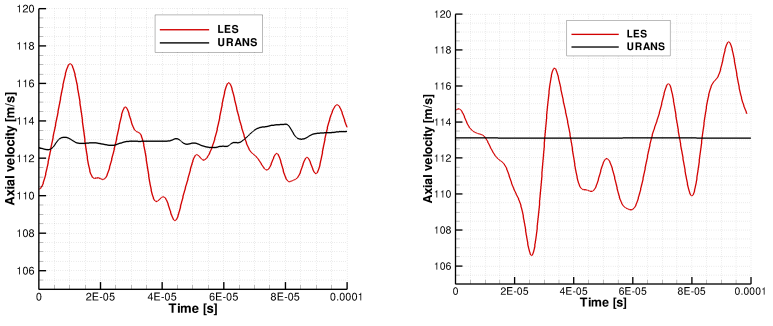

(a) $T_s \sim 0.1$ FT of the LES subdomain **(b)** $T_s \sim 1$ FT of the LES subdomain

Figure 4.22.: LES and URANS signals in correspondence of the URANS subdomain inlet section. The signal is monitored in the middle of the channel for two values of T_s

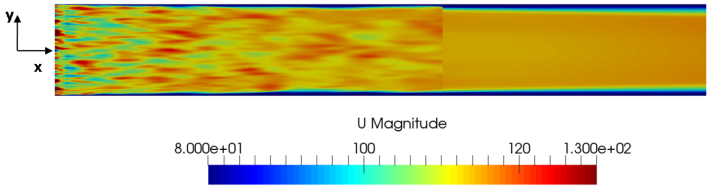

Figure 4.23.: Velocity field close to the LES-URANS interface.

These structures disappear completely at the URANS inlet, and for the subdomain downstream the velocity gradient is almost exclusively radial. Figure 4.24 shows velocity, pressure and TKE fields plotted along a line parallel to the y axis, located at $x = 4h$ (i.e. where the inlet of the URANS domain is positioned). The LES solution is depicted in terms of time averaged results, computed on 8 flow-through times. Only the upper half of the channel is shown in the graph.

In terms of velocity, the upstream and downstream solutions match each other satisfactorily. A good matching is also observed in terms of TKE, even though one can evidence the presence of wiggles at the downstream domain inlet, which completely disappear in the time averaged LES field; this is most likely due to the fact that a longer T_s would be required to better compute the TKE imposed at the downstream domain inlet. Nevertheless, the discrepancy between LES and URANS solutions is definitely acceptable for industrial applications.

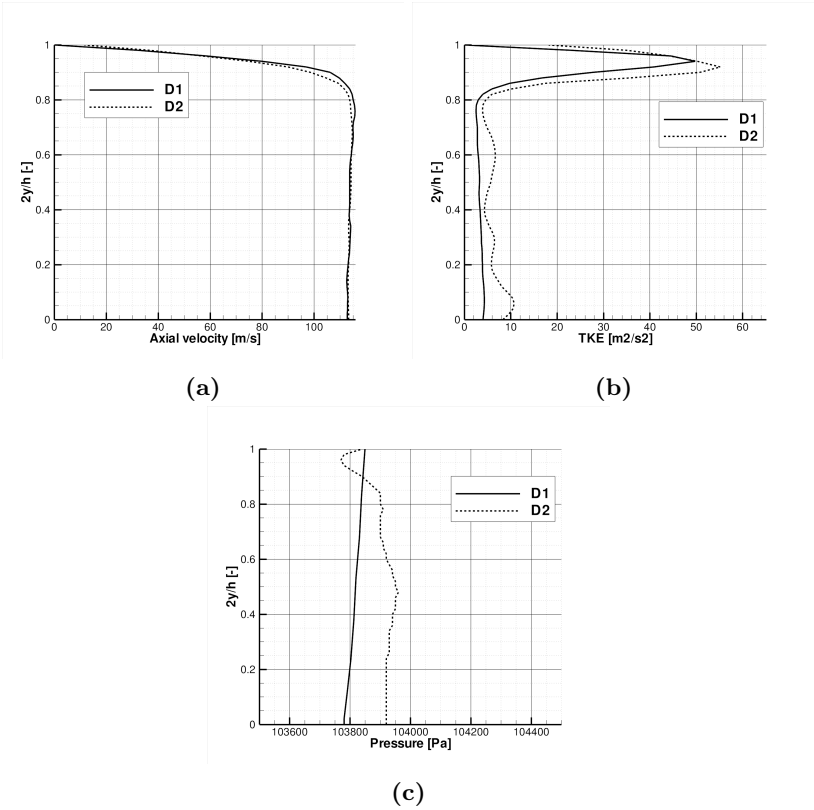

Figure 4.24.: Axial velocity (a), TKE (b) and pressure profile (c) in Y direction for the LES-URANS coupled solution. Results in correspondence of the URANS subdomain inlet section.

The pressure distribution at the interface (Fig. 4.24-c) shows a good agreement between the upstream and downstream solutions. As previously discussed, a perfect match of pressure cannot be obtained when non-reflecting conditions are used at the LES outlet.
From the graph, one can observe that the pressure discrepancy reaches its maximum at the center of the channel and reduces closer to the wall.

To conclude, it must be pointed out that the current test case is not particularly critical for the LES-URANS coupling, since all turbulent structures resolved by LES must be filtered out at the inlet of the downstream subdomain. To get a complete overview on the robustness of the coupling technique, it is necessary to investigate an additional test case, in which part of the unsteady signal coming from the upstream domain must be transferred to the downstream one. This will be discussed in the next section.

4.5.4. Turbulent cylinders in tandem

For the final step of the analysis, the flow field generated downstream of a cylinder operating at high-Reynolds is used to reproduce the outlet of an hypothetical combustor characterized by a very turbulent and unsteady internal flow field. In this sense, a test case including two cylinders in tandem is chosen, since it presents two main features which are of interest for the validation of the coupling methods;

- A remarkable influence of the downstream cylinder on the flow field upstream is expected, therefore the potential effect shall be transferred accurately.

- The LES-URANS coupling must be able to filter the turbulent structures at the interface, while keeping the passage of the main coherent structures generated by the vortex shedding.

The turbulent vortex shedding across one single cylinder or two cylinders in tandem finds many applications in engineering, therefore several experimental studies were carried out during the years. Avoiding the numerous low-Reynolds test cases, the works of Farell et al. [93], Roskho et al. [94], Jenkins et al. [95] are taken as reference for the current study.
Experimental works performed on high-Reynolds cases (such as Okajima et al. [96]) clearly showed the existence of a critical distance between two cylinders in tandem, below which no vortex shedding takes place in between the first and the second cylinder. In this case the flow separates on the surface of the first cylinder and reattaches directly on the downstream one. Above that distance, an intense vortex shedding takes place in the area between the cylinders. This critical spacing is about $L/d_{cyl} = 3.8 - 4.5$ where L is the distance between the centers.
The investigation proposed in this section is performed on two cylinders at a distance slightly above the critical one ($L/d_{cyl} = 5.5$) to permit the development of the vortex shedding while keeping the potential influence of the downstream sub-domain on the upstream one. The set-up of the test is chosen to match classical conditions which can be found at the outlet of an industrial combustor, in terms of Re (Re=400000 is chosen, based on the cylinder diameter) and Mach ($M = 0.3$ is matched within the domain). The study is performed by using the LES-URANS coupling procedure based on method 2. A brief discussion on the application of the LES-LES coupling approach (method 1) is also given in section 4.5.5.

4.5.4.1. Computational domain

The computational set-up of the LES-URANS coupled simulation is shown in Fig. 4.25. Two cylinders are considered at a distance $L/d_{cyl} = 5.5$ from each other. A 3D subdomain upstream is coupled to a 2D grid downstream, considering an overlapping region of $L_o/d_{cyl} = 1.5$. Uniform fixed temperature and velocity are imposed at the inlet. A fixed pressure is considered at the outlet of the downstream subdomain. The patches limiting the domain in transversal direction are treated by slip conditions, while the solid surfaces are treated by no-slip and adiabatic conditions.
The upstream subdomain is discretized by a structured grid composed by $6.7 \cdot 10^5$ cells. $Y+$ at walls is kept lower than 5, while $X+$ and $Z+$ are limited to 150. This subdomain is coupled to a 2D subdomain downstream discretized by 56000 cells, keeping $Y+ \sim 20$ to use wall functions. Pictures of the grids are shown in Fig. 4.26. On the subdomain downstream, a sponge layer is created close to the outlet by coarsening the grid to avoid spurious reflections of the pressure waves approaching the external patch.

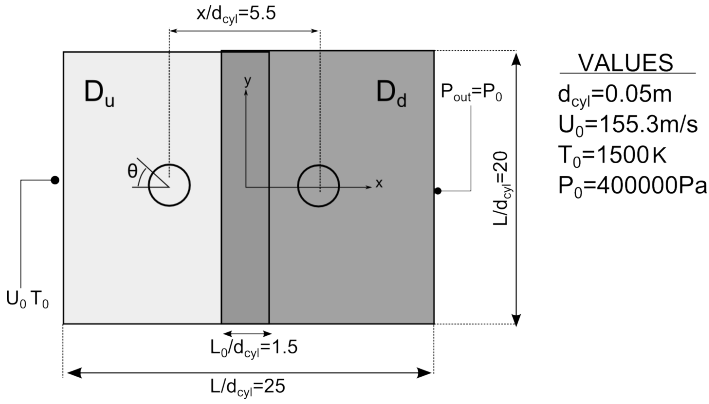

Figure 4.25.: Scheme of the cylinders in tandem test case.

The LES is performed with the p-based code rhoPimpleFoam. The domain is discretized by the second order filteredLinear scheme. A time step $dt_{LES} = 1 \cdot 10^{-6} s$ is imposed, and the advancement in time is obtained by eleven corrector loops for the PIMPLE algorithm, exploying an explicit Euler scheme. The subgrid scales are modeled by using the Smagorinsky model with Van Driest formulation at walls. No turbulence is injected at the inlet.
The URANS downstream is performed with the ρ-based code TUMDF, employing the $k - \omega$ SST model. The spatial discretization is based on a second order central (Gauss linear) scheme. A dual-time stepping technique is employed in space, with 100 inner iterations to advance the solution on

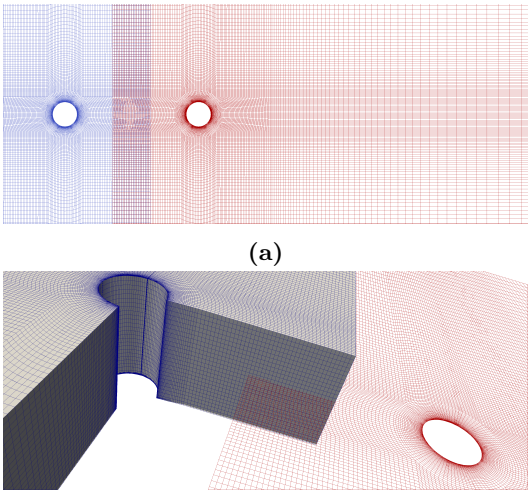

(a)

(b)

Figure 4.26.: Mesh used for the coupled computation of the cylinders in tandem: general view of the mesh (a). Detail of the overlapping region (b).

$dt_{URANS} = 2 \cdot 10^{-5} s$.
The two domains are coupled following the approach presented in section 4.2. At the LES outlet, non-reflecting conditions are applied.

To assess the results of the coupled simulation, two additional computations are performed:

- One URANS including both cylinders into the domain (indicated in the following as full URANS). The grid is obtained by keeping exactly the same set-up used for the downstream subdomain of the coupled simulation, and is characterized by $1.12 \cdot 10^5$ cells.

- One more LES including one single cylinder and a uniform p_{Inf} at the outlet according to Eq. 3.22. The same grid employed for the upstream subdomain of the coupled simulation is considered.

4.5.4.2. Effect of the filter on the coupling

The filtering time T_s for the LES-URANS coupling must be set in such a way that the turbulent structures are filtered out at the interface without affecting the coherent vortices generated by the vortex shedding, which must be transferred to the domain downstream.

The procedure followed to select the filter width was already described in section 3.1.3. Here the application of the methodology will be discussed in more detail.
Figure 3.8 shows the damping of the signals in function of the frequency to be transferred and the minimum turbulent frequency. For a high-Re flow interacting with a cylinder, the signal to transfer is clearly represented by the vortex shedding. Its frequency can be characterized by $St \sim 0.21$, which means f_c ∼700Hz for the current case. On the other hand, a first guess of the minimum turbulent frequency can be obtained considering that the biggest turbulent structures have a characteristic dimension equal to d_{cyl}, and they are convected with the free stream velocity. By approximating $f_t = U_0/d_{cyl}$ one obtains $f_t \leq 3000Hz$. The graph in Fig. 3.8 can then be employed considering $log(f_t/f_c) = log(3000/700) \sim 0.65$ in the ordinate, as shown in Fig. 4.27.

Considering these conditions, the best compromise between an accurate

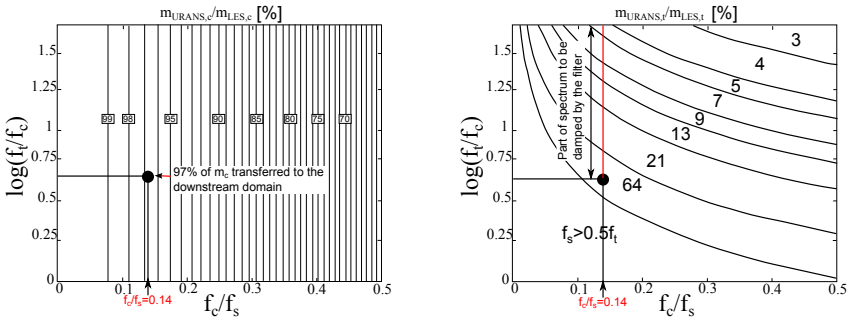

Figure 4.27.: Procedure to evaluate T_s considering the attenuation error of signal $m_{c,LES}$ (a) and the spurious propagation of the signal $m_{t,LES}$ (b).

passage of the coherent structures from the subdomain upstream to the one downstream while filtering the turbulent signal is obtained by imposing $f_c/f_s = 0.14$ (see Fig. 4.27). This means that 200 LES snapshots are considered for the time-marching average. For such a value, the 97% in amplitude of the fluctuating signal related to the coherent structures is passed to the downstream domain, while the turbulent spectrum will be damped by the filter to less than the 64% of its original amplitude.

Figure 4.28 represents the axial velocity signals obtained during the coupled simulation within the downstream inlet, in function of the number of LES snapshots N used for the filter. The signal is registered at the center of the overlapping region. Two tests are performed, using 20 and 200 snapshots. The signals are compared to the one observed at the same position by the full URANS including both cylinders. It can be clearly observed that $N = 20$ leads to high spurious fluctuations at the downstream domain inlet

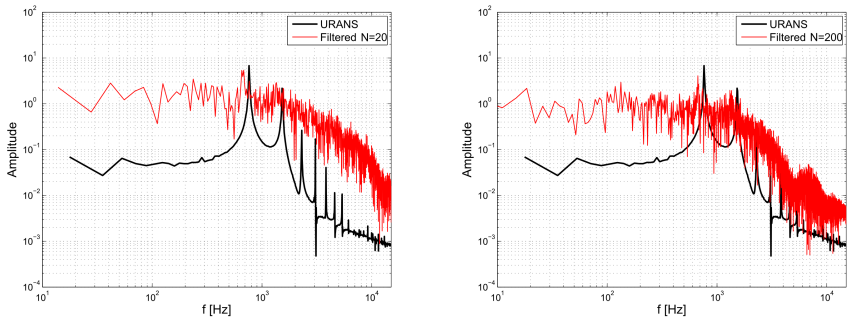

(a) N=20 **(b)** N=200

Figure 4.28.: FFT of u_x evaluated on the upstream and downstream solution in the position where the downstream inlet is located for two coupled simulations, including 20 (a) and 200 (b) LES snapshots for the average.

with respect to the full URANS. On the other hand, the signal obtained for $N = 200$ is much closer to the one of reference. Obviously, undesired high-frequency fluctuations are still observed at the downstream domain inlet, even though limited in amplitude. In this sense, the presence of the overlapping helps in numerically attenuating the spurious signal.
According to these observations, the results presented in this paragraph are related to $N = 200$ in Eq. 3.7.

4.5.4.3. Passage of turbulent kinetic energy

Another point to be discussed for the current test case is the passage of TKE from LES to URANS. In section 3.3 it was suggested to compute the TKE by directly averaging the velocity fluctuations from the LES domain (Eq. 3.31). This procedure is suited for cases in which all fluctuations must be filtered out at the interface between the subdomains (as it is for turbulent channels, section 4.5.4). For the current test, on the other hand, additional considerations must be made, since the biggest vortices (which represent the most energetic structures) are directly transferred from the LES to the URANS domain.
Fig. 4.29-a shows the TKE distribution across the two domains. Along the overlapping, the LES solution is pointed out. This is compared to the TKE obtained by the URANS on the full domain, Fig. 4.29-c. It clearly appears that for the current case the application of method 2 as it is leads to an overestimate of the turbulence at the downstream subdomain inlet: in between the cylinders, in fact, the TKE of the coupled simulation results about three times higher with respect to the full URANS results. This overestimate leads to a higher value of μ_T for the coupled simulation, which

affects the development and convection of the vortices downstream.

To avoid this overestimate, it was empirically decided to transfer a value $TKE/3$ from LES to URANS (where TKE for the LES domain is still computed by Eq. 3.31). The corresponding turbulent kinetic energy development across the interface is depicted in Fig. 4.29-b. The TKE distribution in the subdomain downstream appears more in line with the full URANS, with respect to the original method.
The influence of TKE on the migration of the vortices downstream from the second cylinder is quantified in Fig. 4.30. Here the local velocity fluctuation $u\prime_{RMS}$ resolved by URANS is plotted along the x axis from the wall of the downstream cylinder (x=0) until the beginning of the sponge layer ($x = 12.5d$). The original method leads to an evident decrease of the unsteadiness immediately downstream from the cylinder, where the intensity of the vortices is about half of the full URANS results. For the approach based on the transfer of TKE/3, on the other hand, the fluctuations downstream are in a better agreement with the full URANS results.
According to the current discussion, in the following dissertatio the results discussed are the ones obtained by exchanging $TKE/3$ from the upstream to the downstream domain.

4.5.4.4. Results of the coupled simulation

Figure 4.31 shows the vorticity field obtained during the coupled simulation, compared to the full URANS results. In the overlapping region, the LES field is shown. The smallest turbulent structures are mostly filtered out at the LES-URANS interface by the time-marching filter, and in the subdomain downstream the vortical structures are coherent in dimension and shape to the ones obtained with the full URANS. As already discussed, a spurious signal due to the filter is generated at the URANS inlet, but it is immediately damped within the overlapping region by the numerical dissipation of the RANS model.
One can better characterize the passage of information by plotting the instantaneous distribution of velocity, pressure and turbulent kinetic energy in y direction, at the center of the overlapping region. The velocity field, Fig. 4.32-a, shows an excellent agreement between the upstream and downstream solutions. In particular, it is important to point out that the vortex released by the first cylinder (depicted by the areas of low and high velocity) is not deformed by the presence of the interface.
The continuity of the pressure field at the interface, Fig. 4.32-b is also very satisfactory; as already discussed, the use of the NSCBC does not allow to transmit the potential effect from the downstream to the upstream domain in a time-accurate sense. Nevertheless, the pressure continuity is well respected in a time average sense.

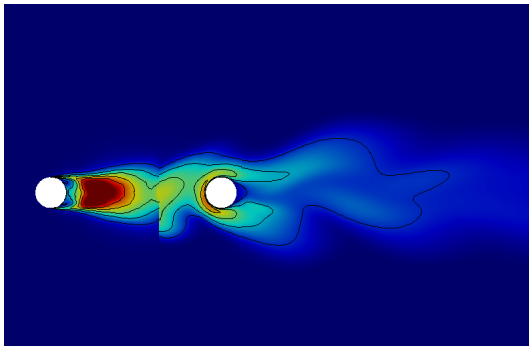

(a) Coupled: TKE transferred

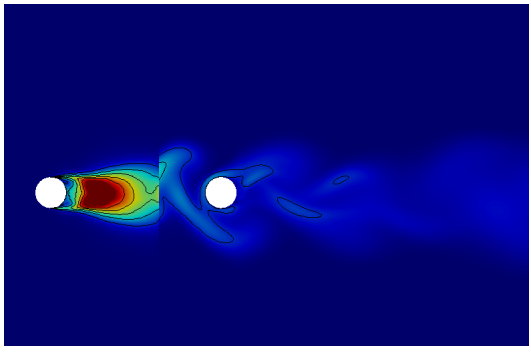

(b) Coupled: TKE/3 transferred

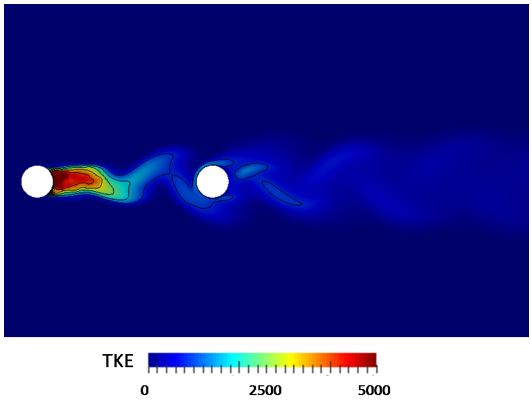

(c) URANS full domain

Figure 4.29.: TKE field resolved by the coupled procedure with passage of TKE from LES to RANS (a), passage of TKE/3 from LES to RANS (b), full URANS (c).

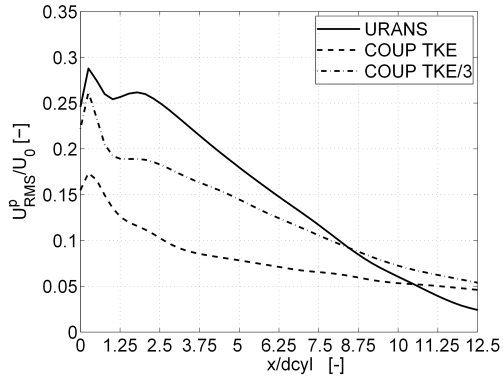

Figure 4.30.: Decay of the resolved velocity fluctuations by URANS. The coordinate x goes from the downstream cylinder wall to the domain outlet (x=1).

Figure 4.32-c shows the TKE field along the same axis, also compared to the full-URANS results. In this case, the local peak and the amplitude of the wake results accurately reproduced at the URANS inlet by exchanging TKE/3 from the LES solution.
The time averaged fields of pressure and axial velocity are shown in Fig. 4.33. The continuity at the interface is excellent for both cases. One can also notice that the effect of the wake generated by the cylinder upstream, depicted by a local pressure decrease, is correctly transmitted to the downstream domain. The errors in terms of continuity at the interface are quantified in Tab. 4.3, where the time averaged fields are integrated on a surface at the center of the overlapping, perpendicular to x. For each variable u, the relative error $\epsilon_{\Delta u}$ is evaluated as:

$$\epsilon_{\Delta u} = \frac{u_u - u_d}{u_u} \tag{4.8}$$

and it remains always lower than 0.5%, being acceptable for engineering purposes. A relatively high discrepancy is observed for ρU. This was unexpected since ρU is one of the information which is directly passed between the domains. The cause seems to be the high vorticity of the flow, which plays a role in increasing the inaccuracy of the interpolation between the two domains.

The aerodynamic behavior of the cylinders is evaluated by plotting the pressure coefficient C_p, defined as:

$$C_p = \frac{p - P_0}{\frac{1}{2}\rho U_0^2} \tag{4.9}$$

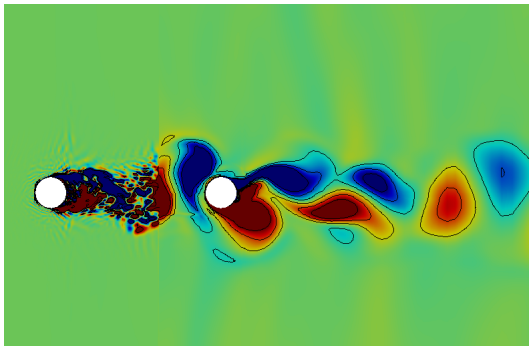

(a) Coupled

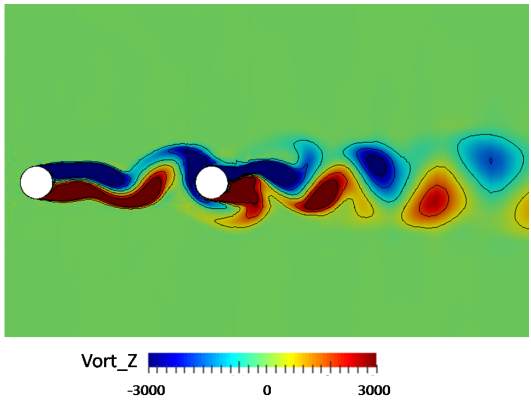

(b) URANS full domain

Figure 4.31.: Vorticity field resolved by the coupled procedure (a), and full URANS (b).

The C_p distribution for the cylinder upstream is represented in Fig. 4.34. Results are compared to the experiments of Farell et al. [93] performed on a single cylinder at the same Reynolds number. For the cylinder upstream, a pronounced pressure minimum is observed at $\theta = \pm 90°$ (θ is indicated in Fig. 4.34-a), followed by an isobaric region due to separation. The base pressure value obtained by LES appears underestimated. Comparing the coupled simulation results to the ones obtained by the single domain LES, which includes only the subdomain upstream with uniform p_{Inf} imposed, the same discrepancy is depicted. From this observation, it can be stated that this discrepancy is mainly due to the LES modeling rather than to the coupling procedure itself.
Figure 4.34-b shows the pressure distribution along the cylinder downstream. Numerical results are compared to the experiments performed by Jenkins et al. [95] on two cylinders in tandem. The experimental configuration is

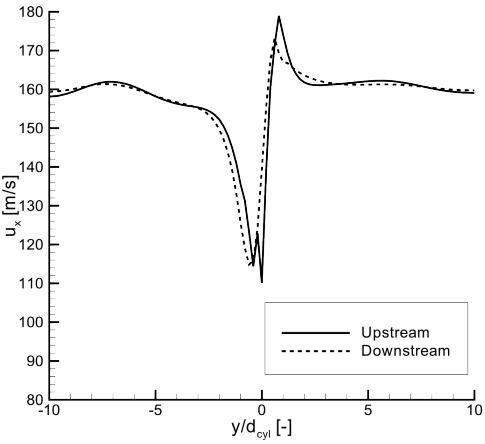

(a)

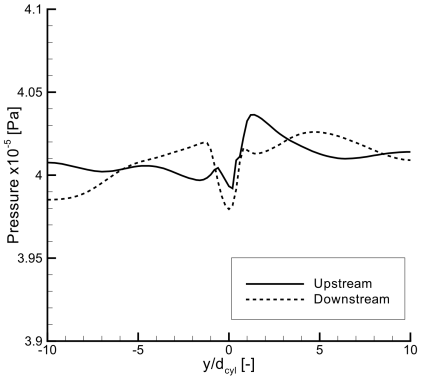

(b)

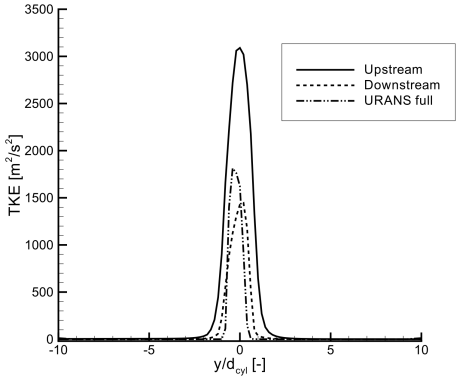

(c)

Figure 4.32.: Continuity of u_x (a), pressure (b) and TKE (c) in y direction at the overlapping center.

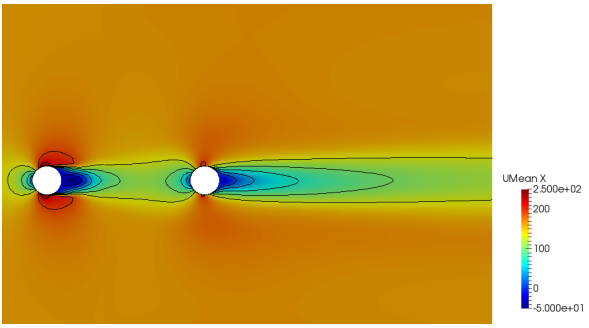

(a)

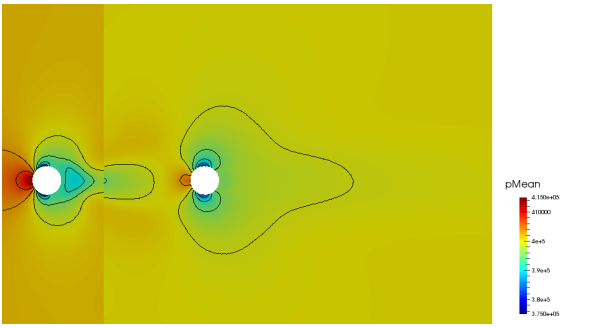

(b)

Figure 4.33.: Time averaged field obtained by the coupled simulation: mean axial velocity (a) mean pressure field (b).

operated at a lower Reynolds number than the one considered for the present study, therefore the experimental data can only give a qualitative idea of the effect of the upstream cylinder on the downstream one.

All distributions demonstrate that the interaction of the flow with the wake generated by the cylinder upstream causes a less pronounced pressure minimum before the separation.

In particular the agreement between the coupled simulation and the full-URANSis excellent, if one excludes a slight discrepancy at $\theta = 0°$. One can then conclude that coupled simulation is able to transmit the effect of the upstream cylinder to the downstream one.

The Strouhal number evaluated for the different simulations performed is shown in Fig. 4.35 and compared to several experimental works performed on single cylinders at different Reynolds numbers. For completeness, the values obtained by all simulations are also listed in Tab. 4.4.

As previously explained, when the distance between the cylinders is higher than a threshold, the vortex shedding takes place in the region between them. In such a configuration, the Strouhal number is expected to be very

Variable	Error
ρU	-0.47%
T_{tot}	-0.02%
p_{tot}	-0.43%
p	-0.46%

Table 4.3.: Continuity error at the interface for the LES-URANS coupling. High Reynolds cylinders in tandem.

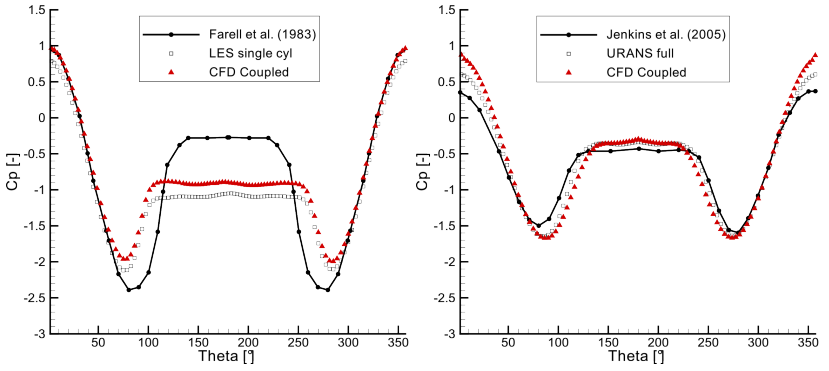

(a) **(b)**

Figure 4.34.: C_p distribution for the cylinder upstream (a) and downstream (b). Experimental data for the cylinder downstream are at lower Reynolds number than the one considered in this work, therefore it can be used as reference only.

similar to the one obtained by a single cylinder [97]. For all simulations, the frequency of the vortex shedding is in good agreement with the experimental investigations.

4.5.5. LES-LES coupling applied to the cylinders in tandem

A first validation of the LES-LES coupling procedure described in section 4.1 is performed on the same test case reproducing two cylinders in tandem. As it will be better discussed in part II, the ρ-based LES code still needs further development before being ready for 3D LES simulations of HPT, therefore at this stage the coupling procedure is tested on two instances of rhoPimpleFoam.
The set-up in Fig. 4.37 is splitted in two separated domains without including the overlapping region. The 3D grid upstream is characterized by 0.63MLN structured cells. To take into account possible approximations due

Variable	Coupled upst.	Coupled downs.	URANS 2 cyl	LES 1 cyl
St	0.221	0.219	0.239	0.245

Table 4.4.: Strouhal number evaluated by the simulations performed.

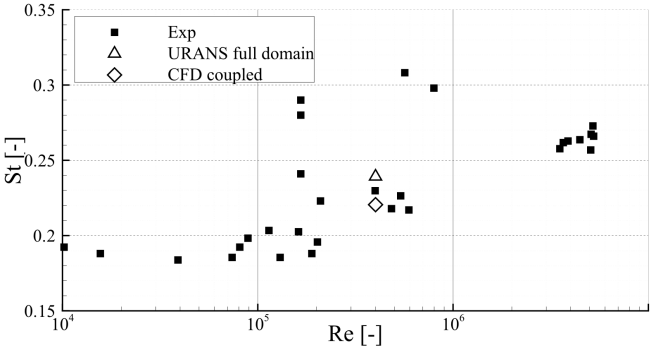

Figure 4.35.: Strouhal number evolution with respect to the Reynolds number: experimental values for single cylinders and present computations of two cylinders in tandem.

to the interpolation, two grids were tested for the downstream subdomain: the first one is generated to get a fully coincident interface with the subdomain upstream, while the second one is a coarser mesh characterized by $4 \cdot 10^5$ cells and non matching patches at the interface between the domains. The computational domain is shown in Fig. 4.36, with focus on the common patch region. The set-up with non-matching interface is shown.

In general, it is important to point out that stability issues are observed

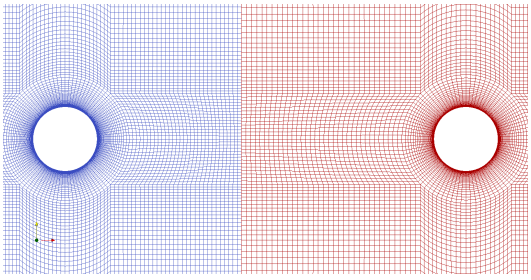

Figure 4.36.: Interface of the non-coincident grid used for the LES-LES coupling.

when this method is applied on two grids characterized by an excessive

discrepancy at the interface. As previously observed, in fact, the "hard" coupling method leads to an ill-posed problem when large interpolation errors are present.

From the numerical point of view, both LES are performed employing the

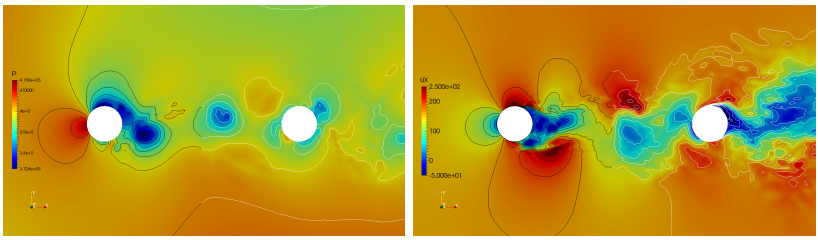

(a) **(b)**

Figure 4.37.: Instantaneous pressure (a) and velocity (b) fields obtained for the coupled simulation. Isolines for the upstream computation are pointed out in black, the ones for the downstream are in white.

second order filteredLinear scheme in space and a first order Euler scheme in time. $dt_{LES,u} = dt_{LES,d} = 1 \cdot 10^{-8} s$ is considered.

The accuracy of the coupling method can be appreciated by observing the instantaneous flow field at the interface. Figure 4.37 shows two snapshots of the vorticity field and the pressure field, for the case with non matching grids at the interface. The continuity of the solution appears excellent.

In particular, it is interesting to point out the added value obtained by the LES-LES "hard" coupling technique in comparison to the LES-URANS "mild" method. When the hard approach is used, the continuity of the pressure field at the interface is guaranteed for every time instant.

To better quantify the continuity of the solution across the domain, surface averaged integral quantities obtained at the interface are compared between the upstream and the downstream computations. For each variable, the error is computed according to Eq. 4.8. The discrepancy of the solution is very low, being almost exactly 0 for the mesh with coincident patches and only slightly increasing for non-coincident patches, remaining lower than 0.01% for all quantities.

Figure 4.38 shows the turbulent kinetic energy spectrum obtained for the coupled LES-LES computation, compared with the LES performed on a domain representing only the cylinder upstream. This is evaluated on the signals of two probes, placed along the wake of both cylinders, at $x/d_{cyl} = 2.75$ from their center. For the coupled case, both signals are taken from the computation downstream.

The TKE spectrum presents a very similar shape for both probes considered. A good agreement between the coupled and the non-coupled simulation can also be pointed out, leading to the conclusion that the presence of the interface for method 1 does not generate evident numerical errors on the

fluctuating flow field.

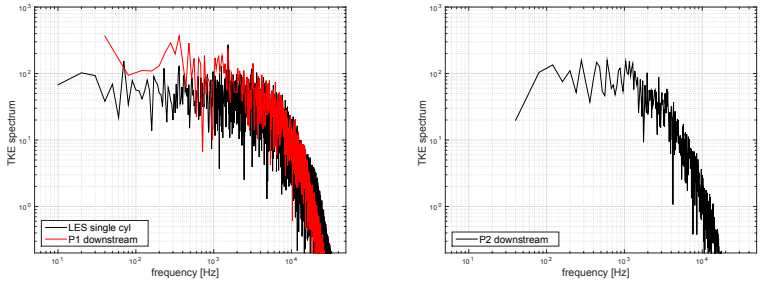

(a) **(b)**

Figure 4.38.: TKE spectrum for probes 1, placed at $x/d_{cyl} = 2.75$ from the upstream cylinder (a) and for probe 2, placed at $x/d_{cyl} = 2.75$ from the downstream cylinder (b).

4.6. Final remarks

Based on the theoretical discussion presented in chapter 3, two different coupling methods are presented in the current chapter. The first one, suited for LES-LES applications, does not employ any overlapping region (the upstream outlet is connected directly to the downstream inlet). Five characteristic variables are exchanged from the upstream to the downstream subdomain, while the pressure wave L_1 is transferred backwards.
The second method is suited for LES-URANS and URANS-URANS applications. It is based on the passage of only four characteristic variables (excluding the turbulent quantities) from the subdomain upstream to the one downstream, while pressure is transferred from the downstream subdomain to the outlet upstream. An overlapping region is modeled at the interface. The two methods are validated on series of test cases of increasing complexity, representing some typical features of the flow field of the combustor-turbine interface.
The first computations, performed on laminar test cases, show that method 1 is able to accurately transfer the backwards-moving pressure wave from the solution downstream to the one upstream, at the expense of stricter requirements to be fulfilled to guarantee the stability of the coupled computation.
To represent the flow field of an hypothetical combustor at low swirl, a turbulent duct at high-Re and low Mach was analyzed in detail. The coupled simulations are performed by means of URANS-URANS and LES-URANS coupling techniques.

In terms of velocity and TKE, the coupled simulations show a very satisfactory continuity between the upstream and downstream solutions. The pressure distribution shows instead a discontinuity at the interface between the subdomains, which is anyway limited in amplitude. This can be further reduced by decreasing the relaxation coefficient of the upstream non-reflecting outlet condition or by considering a "hard" imposition of the 2D pressure distribution coming from the downstream solution. To avoid spurious reflections, these techniques can be implemented only if the interface between the subdomain is not interested by unsteady pressure distortions.
For the LES-URANS procedure, the time-marching filter employed to define the URANS inlet from the LES solution demonstrated to be very effective in damping out all turbulent structures generated in the upstream subdomain. As a matter of fact, a quasi-steady solution can be obtained within the URANS domain (as it is expected for the current test case) by setting a sufficiently large time interval T_s for the filter.
The flow field of a combustor characterized by high unsteadiness crossing the outlet is reproduced by representing two cylinders in tandem interacting with a High-Reynolds flow. This test case has been extensively investigated by the LES-URANS and LES-LES approaches based respectively on methods 2 and 1. The test case can be employed to evaluate how the coupling performs when only part of the fluctuations coming from the domain upstream must be transfered to the URANS inlet.
For the LES-URANS method, the procedure developed to define T_s demonstrated to be effective in damping the turbulence at the interface. The passage of TKE from the upstream subdomain to the downstream one, which was discussed in section 3.3, requires some modification for the current analysis. This is due to the fact that the fluctuating energy is in part transferred to the downstream domain by the big vortices, therefore the procedure defined by Eq. 3.31 leads to an overestimation of TKE at the inlet.
The continuity of all fields at the interface between the domains is satisfactory. In general, one can conclude that the coupled simulation is able to effectively reproduce the mutual interaction between the cylinders: due to the complexity of the test case analyzed, the method can be considered validated and ready to be applied for the LES-URANS of the combustor-turbine interaction.
The LES-LES coupling procedure described in section 4.37 gives stable results for a complex turbulent flow. With respect to the "mild" LES-URANS method, a more accurate continuity of the pressure field between the domains is achieved. In particular, the method guarantees that all flow quantities at the interface are coherent in time. To obtain this, the price to pay is that the grid at the interface, as well as the time step defined, cannot change significantly between the two simulations: if these constraint are not respected, in fact, the computation is unstable.
Before getting a LES-LES coupling which is mature enough for real industrial problem, the validation must be extended to the coupling of a p-based

and ρ-based solvers. This part of the work is currently ongoing and is not discussed in this thesis.

Chapter 5.

Investigation of the combustor-turbine mutual interaction by coupled simulation

In this chapter, the coupling procedures described in chapter 4 are applied to a realistic industrial configuration involving a low-emission premixed combustion chamber and the stator of a HPT stage. The design of the test case is performed at VKI in the framework of the COPA-GT project.
The procedure followed to design the geometry is discussed in section 5.1. The CFD simulations of the NGV and the combustor separately are presented in section 5.2 and 5.3. To conclude, the coupled combustor-turbine analysis is discussed in section 5.4. Due to the high computational costs and the necessity of a preliminary validation of the tools used for LES in combustion chambers, the current study is limited to the application of the URANS-URANS approach (based on method 2). The validation of the tools to perform a LES-URANS study is currently ongoing and will not be discussed in the framework of this thesis.
For further details about the work presented in this chapter, the reader is referred to:

S.Vagnoli, T. Verstraete. *Numerical Study of the Combustor-Turbine Interaction Using Coupled Unsteady Solvers*, 22nd ISABE conference, october 25-30, 2015, Phoenix, AZ, USA.

5.1. Design of the test case

The main requirements for the design of the COPA-GT combustor-turbine geometry come from the fact that the test case should be representative of a realistic Lean Burn combustion chamber - HPT modulus for industrial machines. The following specificities are retained:

1. The combustion chamber is a Lean Burn (LBC) annular geometry. No dilution holes are present.

2. Realistic 2D surfaces of T_{tot} and velocity should be obtained at the

combustor outlet with respect to recent industrial and academic cases.

3. Since no experimental campaign will be performed on the geometry, the NGV profile should be based on an airfoil from the open literature for which an extensive aero-thermal campaign is carried out.

4. A turbulence intensity $Tu \sim 10 - 25\%$ is expected at the NGV inlet.

5. The case should be "CFD-friendly": an exact 1-to-2 periodicity is considered between injectors and NGV blades. Classical effusion cooling plates, which are typically found in real LBC, are replaced by slot cooling configurations.

6. The swirlers are aligned with the center of the NGV passage.

7. The test case should be freely open to every institution interested to use it.

As a reference, an industrial low-size machine is considered, taken from the Siemens catalog [98]. The reference parameters which are considered for the design are listed in Tab. 5.1.

The global massflow is splitted among 15 swirlers and 30 NGV. Consider-

Parameter	Value
Π_{TT}	13
W	5.7 MW
η_{TT} machine	0.29
Fuel	Natural gas
PCI	47.7 MW/kg
m_{air}	20 kg/s
$\eta_{TT,c}(compression)$	0.86

Table 5.1.: Boundary conditions for the design of the combustor-NGV test case.

ing the design parameters given, we can calculate the following values:

$$T_{tot,2} = T_{tot1} + \frac{T_{tot,is2} - T_{tot1}}{\eta_{TT,c}} \qquad (5.1)$$
$$T_{tot,is2} = T_{tot,1} \cdot \Pi_{TT}^{\frac{\gamma - 1}{\gamma}}$$

Imposing $T_{tot,1} = 293K$, $T_{tot,2} = 660K$ is expected for the air at the combustor inlet.
The total temperature at the combustor outlet $T_{tot,3}$ can then be estimated as:

$$T_{tot,3} = T_{tot,2} + \frac{W_{th}}{m_{air} c_p}$$
$$W_{th} = \frac{W}{\eta_{TT}} \tag{5.2}$$

Where W_{th} stands for thermal power. This gives $T_{tot,3} \sim 1650K$.

In what follows, the discussion is organized in two parts, describing the design procedure of the NGV and the combustion chamber separately.

5.1.1. Design of the NGV

The NGV geometry is obtained starting from the LS89 profile. The original 2D cascade was developed at VKI to have an overview of the aerodynamic and aerothermal performance of high pressure airfoils. Therefore, a very large set of experimental results can be found in the open literature [56], which are commonly used to validate numerical tools for turbomachinery. The airfoil is characterized by $C = 67.647mm$, stagger angle $\gamma = 55^o$ and $g/c = 0.85$.
The idea behind the development of the NGV is to scale the 2D LS89 geometry to get exactly the same pitch-to-chord ratio at 50% of the span. According to the similarity analysis, it is expected that the M_{is} distribution along a scaled airfoil remains the same as the original profile if the following parameters are conserved:

- Isentropic outlet Mach number $M_{2,is}$.
- Pitch to chord ratio of the profile g/c.
- The outlet Reynolds number $Re_{2,is}$ should remain similar to the original configuration.

In terms of operating point, the $MUR - 47$ testing condition [56] was considered as a reference for the scaling. The original boundary conditions are listed below:

- Inlet total temperature: $418K$.
- Inlet total pressure: $159000Pa$.
- Isentropic outlet Mach number: 1.02.

These are scaled to the operating conditions of the machine:

- Inlet total temperature: $1650K$.
- Inlet total pressure: $1310000Pa$.
- Isentropic outlet Mach number: 1.02.

Which gives an outlet pressure $p_{out} = 675000Pa$. The inlet reference total pressure is defined from the Π_{TT} of the machine, considering a total pressure loss $\Delta p_T/p_{T,in} = 0.06$ within the combustor, which is a classical value for annular geometries [30].
The original 2D profile of the LS89 was tested experimentally by varying the Reynolds number from $0.5 \cdot 10^6$ to $2 \cdot 10^6$. For the current design, it was decided to scale the profile keeping an intermediate value of $Re_{out,is} = 0.75 \cdot 10^6$, which was obtained scaling the dimensions of the airfoil for a factor 0.75. Therefore, the 3D prismatic profile obtained is characterized by $C = 50.7mm$, $C_{ax} = 29.1mm$ and $g = 43.12mm$ at 50% of span.
Once the mid-span blade-to-blade configuration is obtained, the radius of

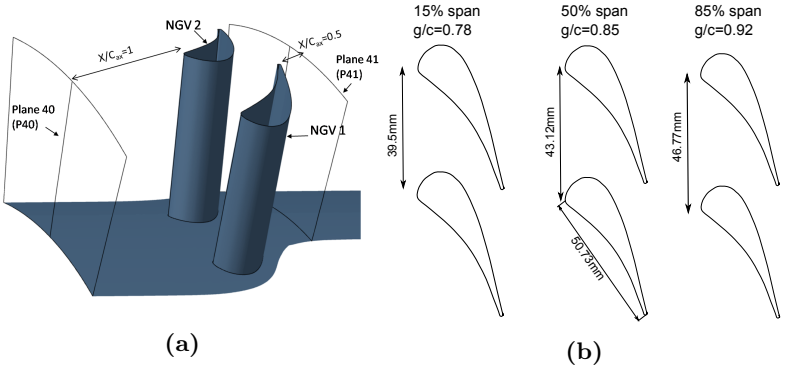

Figure 5.1.: 3D view (a) and sections of the airfoil at 15%, 50% and 85% of span (b) of the prismatic NGV designed to investigate the combustor-turbine interaction.

the machine at 50% of the span can be calculated as $r_{50} = g \cdot N_{blades}/2\pi$. Starting from that, given the mass-flow, one can directly calculate the inlet surface to the NGV as $A = \dot{m}/\rho_{P40}U_{P40}$, where P40 stands for the NGV inlet. The inlet parameters are computed considering $M_{P40} = 0.14$, which is the value obtained upstream from the blade LE during the experimental campaign on the 2D profile. The inner and outer wall radius were then obtained imposing an aspect ratio of $h/g = 0.98$.
To remain as close as possible with the experimental campaign perfomed, the original 2D profile is extruded in radial direction. This procedure is consistent with what typically found for industrial low-size machines, for which prismatic stators are used at the combustor outlet [98].
The final 3D profile is shown in Fig. 5.1. It is characterized by a maximum

difference in pitch to chord ratio with respect to the experimental configuration which is limited to 10% at the endwalls. Going from the hub to the tip, $M_{out,is}$ varies from 1.1 to 0.92. The picture also indicates the nomenclature used in this chapter: the two NGVs are distinguished between NGV 1 and NGV 2, while the inlet and the outlet surfaces are defined as P40 and P41 respectively.
The procedure used for the design, although it is far from giving an optimized geometry for the flow conditions in study, permits a reliable validation of the numerical tools employed for the analysis by studying in detail the original LS89 2D cascade and by comparing the results with the available experimental data.

5.1.2. Design of the combustion chamber

From the study of the state of the art for lean combustors, it was decided to consider the following main requirements to get a stable flame within the combustion chamber:

- $\phi = 0.57$ for the primary flow.
- The premixed fuel-air mixture is injected by a swirler, characterized by Sn higher than 0.6. This parameter is defined by Béer et al. [99] as:

$$Sn = \frac{\int_0^{R_{sw}} \rho U_x U_\theta r^2 dr}{R_{sw} \int_0^{R_{sw}} \rho U_x^2 r dr} \tag{5.3}$$

  A minimum $Sn = 0.6$ permits the generation of a recirculating flow at the center of the combustor, which is essential to get a stabilized flame [30].
- The flame stability is enhanced by employing a premixed pilot flame characterized by higher ϕ.

The final geometry is designed trying to respect reference values for the axial velocity in the primary zone (where the combustion takes place) and in the secondary zone (where the mixing is diluted by cooling air). The reference values are taken from Lefebvre et al. [30] and further adjusted by means of CFD, until acceptable profiles of velocity and total temperature are obtained at the outlet of the combustion chamber.
The final geometry of the combustor is shown in Fig. 5.2, while the main parameters characterizing the geometry are listed in Tab. 5.2. The main premixed flow is injected by a swirler, characterized by $Sn = 0.6$. The value in use is a trade-off between the requirement of a stable recirculating zone at the center of the primary volume, and a residual swirl at the combustor outlet which is in line with realistic industrial configurations.

General parameters		Cooling	
Parameter	Value	Parameter	Value
Combustor length	$240mm$	$\dot{m}_c/\dot{m}$	22%
r_{min} primary zone	$145mm$	h cooling dome	2.4 mm
r_{max} primary zone	$274mm$	h cooling liner	1.7 mm
cooling slots number	8		
Main injection		**Pilot injection**	
Sn_m	0.6	Sn_p	0
$d_{low,m}$	$9mm$	$d_{low,p}$	$0mm$
$d_{high,m}$	$46mm$	$d_{high,p}$	$9mm$
		$\dot{m}_{f,p}/\dot{m}_f$	3%

Table 5.2.: Data of the combustion chamber.

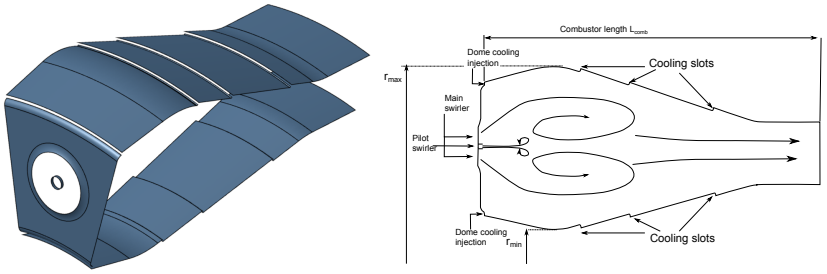

(a) **(b)**

Figure 5.2.: 3D view (a) and sketch (b) of the combustion chamber designed in the COPA-GT framework to investigate the combustor-turbine interaction.

At the center of the main swirler, the pilot mixture is injected axially. Following a technique discussed by Hall et al. [32], the main purpose of this injection to stabilize the main flame. Moreover, the axial flow pushes the flame itself sufficiently far from the injectors to avoid flash backs. $\phi = 0.65$ is employed for the premixed pilot flame.
The cooling massflow is about the 20% of the total massflow, and is injected from 8 slots disposed along the inner and outer walls. The first two slots are placed very close to the premixed flow inlet and represent the cooling of the dome.

5.2. CFD validation for the NGV

As previously stated, the NGV profile is directly obtained by the LS89 2D airfoil, which was tested in cascade configuration by Arts et al. [56]. The numerical tools employed to compute the flow field for the HPT stator vane can then be preliminarly validated by analyzing the LS89 2D profile and comparing the results with the experimental data.
The numerical study of the NGV is carried out employing two different solvers.

- The commercial code FINE/Turbo [100] is employed to verify the performance of the 3D NGV during the design.

- The open-source solver TUMDF is employed during the coupled simulation of combustor and turbine.

Considering the discussion in section 5.1.1, it was decided to validate the numerical set-up taking into account two different operating points [56]:

- The TUR-47 operating point, described in section 5.1.1, is representative of the operating condition at 50% of the span.

- The subsonic condition defined as TUR-45, is similar to the subsonic flow field expected closer to the tip. The related boundary conditions are: $p_{tot,in} = 147500Pa$, $T_{tot,in} = 418K$, $M_{out,is} = 0.875$.

All simulations are performed using the mesh shown in Fig. 5.3: this is a 2D grid, characterized by 126000 cells. $Y+$ lower than 1 is employed at wall to directly resolve the boundary layer. The two solvers FINE/Turbo and TUMDF are used to run steady RANS simulations: in both cases, 2^{nd} order central schemes in space are used (Gauss linear scheme for OpenFOAM). For the convergence, $CFL = 3$ is employed with FINE/Turbo.
Due to stability issues for TUMDF, on the other hand, $CFL = 0.1$ must be imposed in this second case. This is the main limitation in using the open-source solver TUMDF for steady simulation: due to the very low CFL imposed, the computational time for steady computation dilates, becoming comparable to performing unsteady simulations.
The analysis is limited to the aerodynamic study of the profile, therefore the fully turbulent $k-\omega$ SST model is employed. All conditions are analyzed by imposing T_{tot}, p_{tot} and velocity direction at the inlet, as well as a uniform pressure distribution at the outlet.

Figure 5.4 shows the isentropic Mach distribution obtained along the profile. The experimental data are compared with results obtained by FINE/Turbo on the left and TUMDF on the right. The first observation that clearly

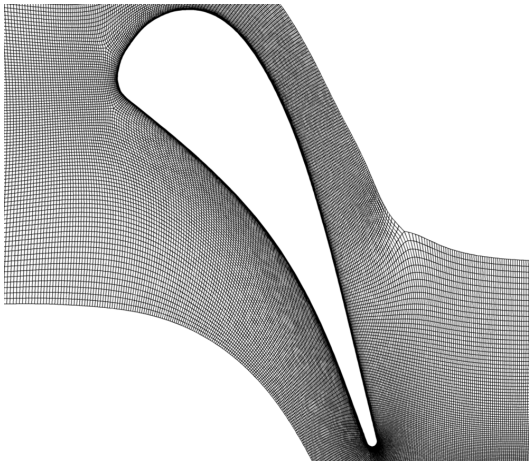

Figure 5.3.: Grid employed for the study of the LS89 2D profile.

comes out is that the numerical M_{is} distributions obtained by the two solvers are almost exactly the same. Considering that TUMDF is an open source code which is not extensively used in turbomachinery, the test case can then be considered as a validation for the equations and numerical schemes implemented.

By comparing numerical and experimental results, it can be observed that

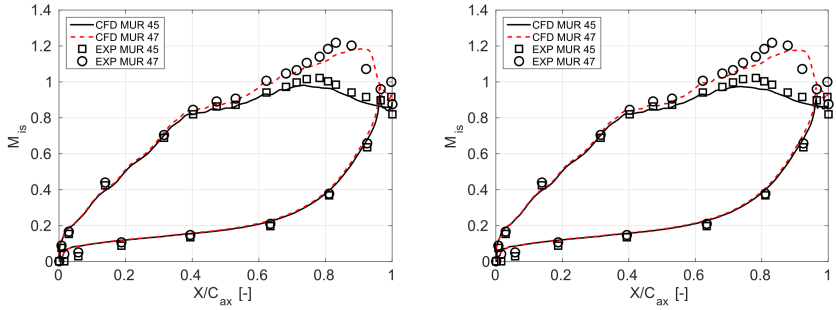

Figure 5.4.: Isentropic Mach number distribution for the LS89 profile. Conditions MUR 45 and MUR 47. Results are obtained with FINE/Turbo (a) and OpenFOAM (b) employing second order central schemes and the $k-\omega$ SST turbulence model.

a very good reproduction of the M_{is} distribution is obtained in particular for the subsonic condition. For the transonic case, the comparison is satisfactory as well, despite the fact that the shock position is slightly delayed

by CFD.
Figure 5.5 shows the absolute Mach distribution obtained by CFD, together with an experimental shlieren visualization for the transonic condition. In general, the flow field obtained with FINE/turbo and TUMDF appears almost coincident. From this picture, it can also be observed that the position of the shock is relatively well predicted by CFD.
From the discussion, it can be concluded that the set-up employed for the two solvers is successfully validated for the 2D profile and the operating conditions in study.

To make sure that the numerical set-up is accurate enough to reproduce the 3D NGV, a mesh convergence study is carried out by taking into account realistic inlet conditions to the turbine.
The 2D profiles of T_{tot}, and velocity direction imposed in this phase at the NGV inlet are shown in Fig. 5.6. These are slightly different from the final configuration, being obtained by a very preliminary design of the combustor: in particular, similar non-uniform distributions of all quantities are obtained, but the peak of temperature is located at a different tangential angle.
In terms of turbulence, a constant value of TKE is imposed to get $Tu = 16\%$ at the inlet. μ_T/μ is set to get a realistic decay before the NGV leading edge. The $k-\omega$ SST turbulence model is employed.
The grid convergence study is carried out by employing FINE/Turbo, with the numerical set-up previously described. Four meshes are considered, whose main features are listed in Tab. 5.3. For Mesh 0, wall functions are employed.
Figure 5.7 shows the M_{is} distribution at 15%, 50% and 75% of the span

Mesh name	Mesh cells	Mean Y+	Max Y+
Mesh 0	540000	62	140
Mesh 1	2000000	3	6
Mesh 2	2000000	0.8	1.8
Mesh 3	6000000	0.4	1

Table 5.3.: Grids used for the convergence study.

obtained with the four grids. Increasing the mesh size, a progressive convergence of the solution is obtained until Mesh 2. The distributions appear instead almost coincident for the two finest grids.
A similar conclusion can be obtained plotting the total pressure losses $\Delta p_{tot}/p_{tot,in}$ in function of the mesh size, Fig. 5.8-a. The losses progressively converge to a value equal to 2.8%.
To have a complete overview of the grid accuracy required to reproduce the hot streak migration in turbine, it can be interesting to analyze the effect

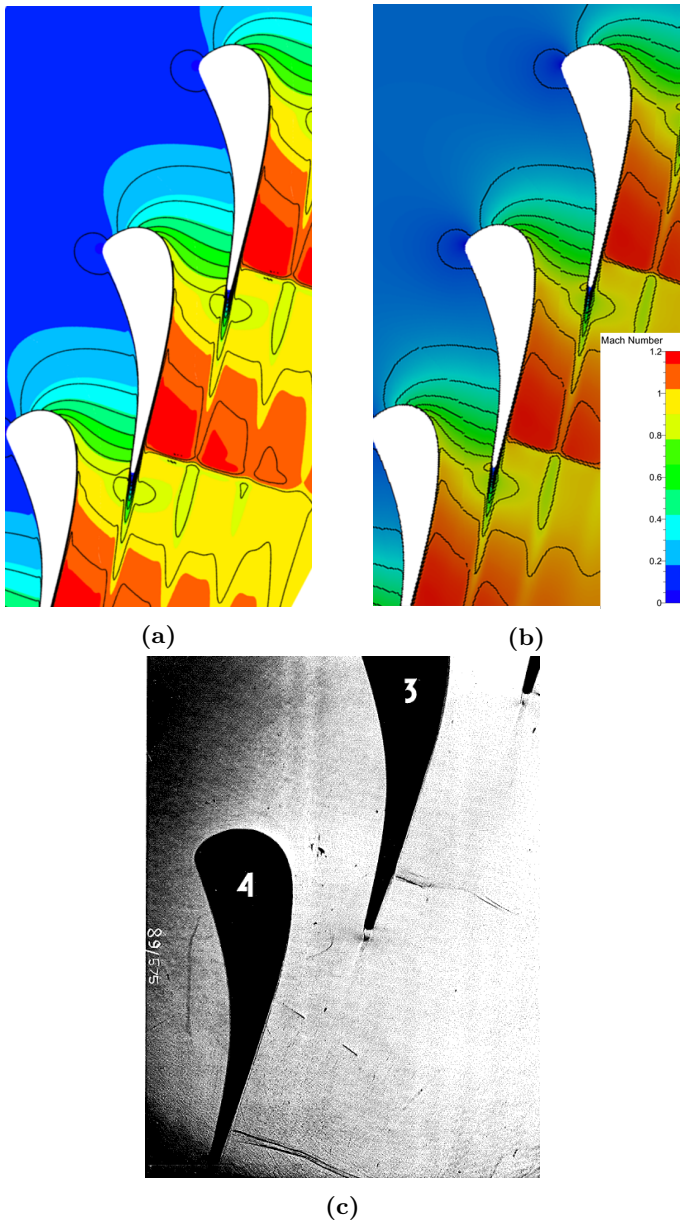

(a) **(b)**

(c)

Figure 5.5.: Absolute Mach number flow field for the LS89 profile with MUR 47 obtained with FINE/Turbo (a) and OpenFOAM (b). Experimental schlieren picture of the LS89 flow at $M_{2,is} \sim 1.02$ (c).

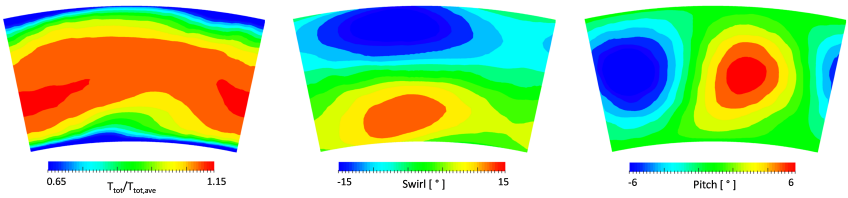

(a) **(b)** **(c)**

Figure 5.6.: Inlet conditions imposed for the mesh convergence study.

of the mesh on the development of TU and temperature within the passage. Figure 5.8-a and 5.8-b show the turbulence level and the temperature non-uniformity, massflow-averaged at the NGV outlet. The T_{tot} distribution is characterized by introducing the parameter $||\Phi_T||$, defined as:

$$||\Phi_T|| = ||\frac{T_{tot} - T^{ref}_{tot,in}}{T^{ref}_{tot,in} - T_{tot,c}}|| \tag{5.4}$$

Where $T^{ref}_{tot,in} = 1650K$ and $T_{tot,c} = 660K$.

Both for the temperature non-uniformity and the turbulence level, a progressive tendency towards a stabilized value is observed. A satisfactory convergence of the results can be depicted for Mesh 2.

Collecting all the information obtained by the analysis, one can conclude that Mesh 2 represents the best compromise between accuracy and reduction of computational time. Snapshots of the mesh are shown in Fig. 5.9.

5.3. CFD analysis of the combustion chamber

The detailed analysis of the final design of the combustion chamber is presented in this section. The analysis is divided in two steps:

- A mesh convergence analysis and study of the internal flow field is performed employing the commercial code FINE/Open.
- A comparison between the results obtained by FINE/Open and the open-source solver XiFOAM (based on the OpenFOAM platform) is carried out.

The simulations presented in this work are performed imposing a fixed massflow to all inlet patches, while a constant pressure is imposed at the outlet. Second order central schemes are employed for the space discretization. The $k - \epsilon$ model is employed, being the only turbulence model compatible with

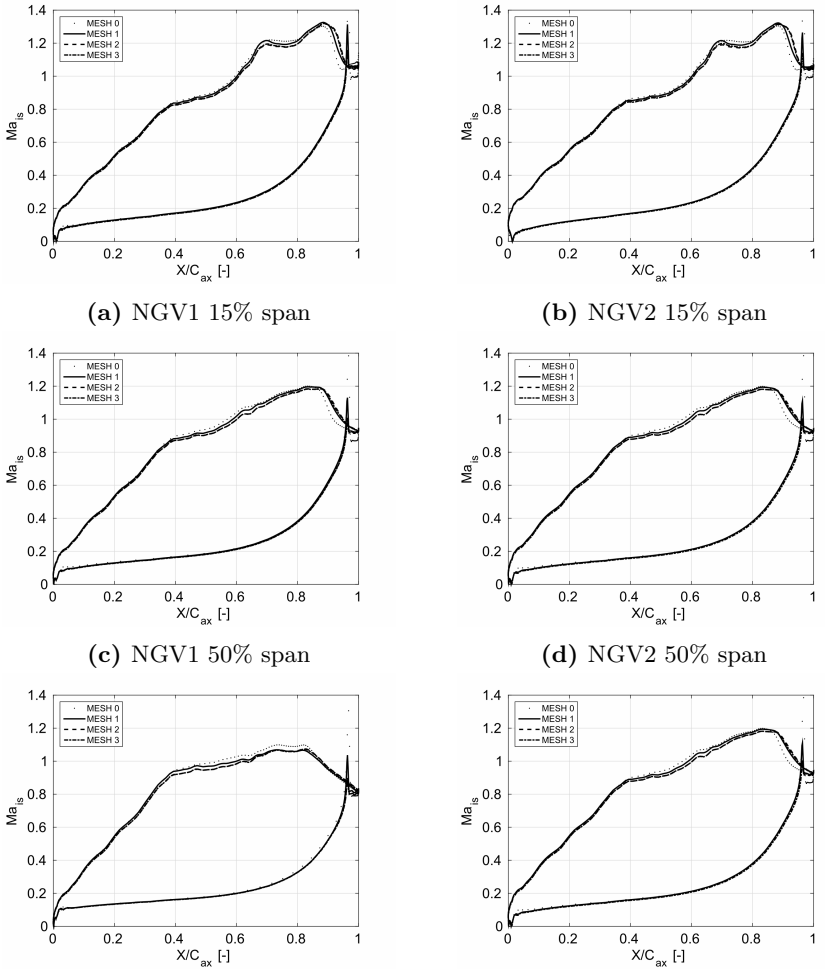

(a) NGV1 15% span

(b) NGV2 15% span

(c) NGV1 50% span

(d) NGV2 50% span

(e) NGV1 85% span

(f) NGV2 85% span

Figure 5.7.: Mesh convergence study: convergence of the blade pressure distribution.

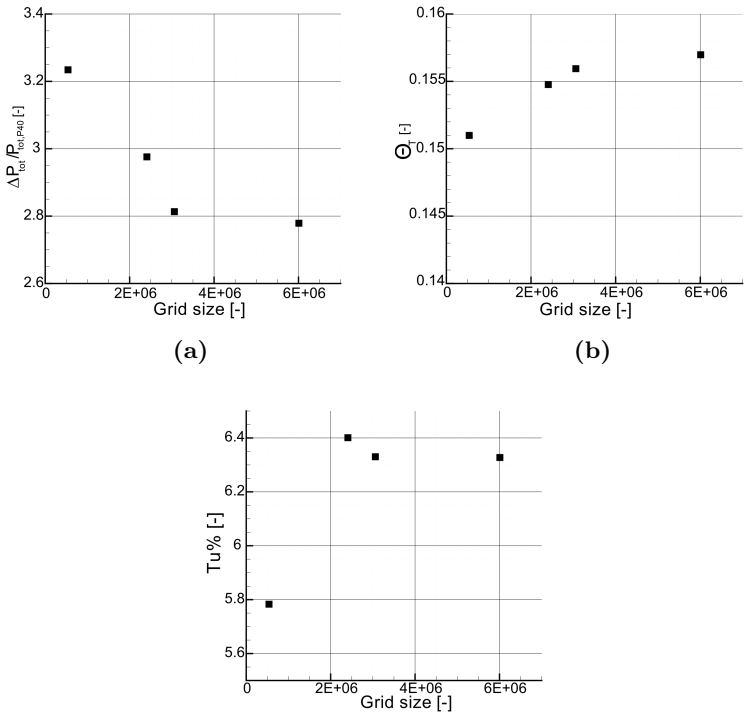

Figure 5.8.: Mesh convergence study: convergence of $\Delta p/p_{tot,in}$ (a), Φ_T (b) and turbulence on P41 (c).

the combustion modulus in FINE/Open.
To model the partially-premixed combustion, it is decided to use the hybrid BML/Flamelet partially premixed model implemented in FINE/Open. In this case, the combustion is represented by the progress variable c, defined as:

$$c = \frac{T - T_u}{T_b - T_u} \tag{5.5}$$

Where the subscript u stands for unburnt gas, and b for burnt mixture. The following equation is solved for the progress variable:

$$\frac{\delta \rho c}{\delta t} + \frac{\delta(\rho u_i c)}{\delta x_i} = \frac{\delta}{\delta x_i}\left(\frac{\mu_t}{Sc_T}\frac{\delta c}{\delta x_i}\right) - \rho S_c \tag{5.6}$$

Where Sc_T is the turbulent Schmidt number, imposed equal to 0.7. The source term ρS_c is obtained by employing the Zimont's TFC closure term

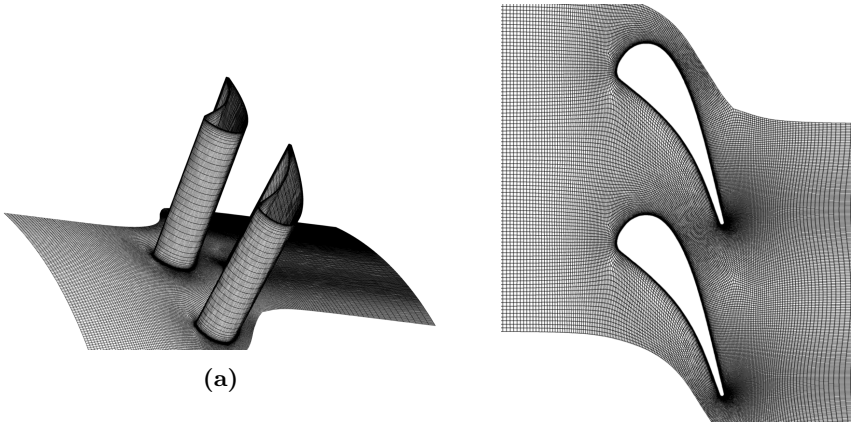

(a) **(b)**

Figure 5.9.: Snapshots of the grid used to reproduce the 3D NGV. General view (a) and blade to blade view (b).

[101] for the turbulent flame speed.

$$\rho S_c = \rho_u \mid \nabla c \mid S_t \propto \mid \nabla c \mid S_l \tag{5.7}$$

Where S_l is the laminar flame speed. The non-uniform fuel-air mixture is taken into account by solving a further equation for the mixture fraction, which will then appear in the Gülder's correlation in use to calculate the laminar flame speed [102]. To conclude, chemical tables for the burnt mixture are obtained by OpenLabs from Numeca.

A mesh convergence study for the combustor is performed as well. In particular, three different grids are employed, characterized by a progressive increase of the number of cells and described in detail in Tab. 5.4. In particular, the same grid structure is used for all cases, which are characterized by two different refinement levels for the primary region (where the combustion takes place, indicated as zone 1 in table) and the secondary region (zone 2). A further refinement is imposed close to the wall to take into account of the presence of the boundary layer. Between the two zones, a non matching interface is employed. For mesh 0, the $Y+$ imposed at wall is not sufficient for a direct resolution of the boundary layer, therefore wall models are employed.
To reduce the number of cells of the grid, the swirler is not meshed. It is rather modeled by imposing the velocity direction at the inlet patch.

The total temperature field obtained inside the combustion chamber is represented in Fig. 5.10. As expected, the combustion takes place in the first 50% of the chamber. In the secondary zone, hot and cold streaks are formed by the interaction of the burnt flow with the cooling air.

Mesh name	Mesh cells	El. size zone 1 (mm)	El. size zone 2 (mm)
Mesh 0	$1.5 \cdot 10^6$	1.5	2
Mesh 1	$4 \cdot 10^6$	0.8	1.5
Mesh 2	$5.8 \cdot 10^6$	0.6	1.1

Table 5.4.: Grids used for the convergence study of the combustor simulation.

A region of cold flow is formed between the injection of the dome cooling and the main mixture entering from the swirler. A coarser mesh in zone 1 leads to an underestimation of the temperature in this area, which is particularly evident in the bottom-left corner of the chamber, Fig. 5.10-a. By refining the grid in the primary zone, the flow field converges towards a unique solution everywhere.

In terms of vorticity, Fig. 5.11, it can be noticed that the swirl observed at

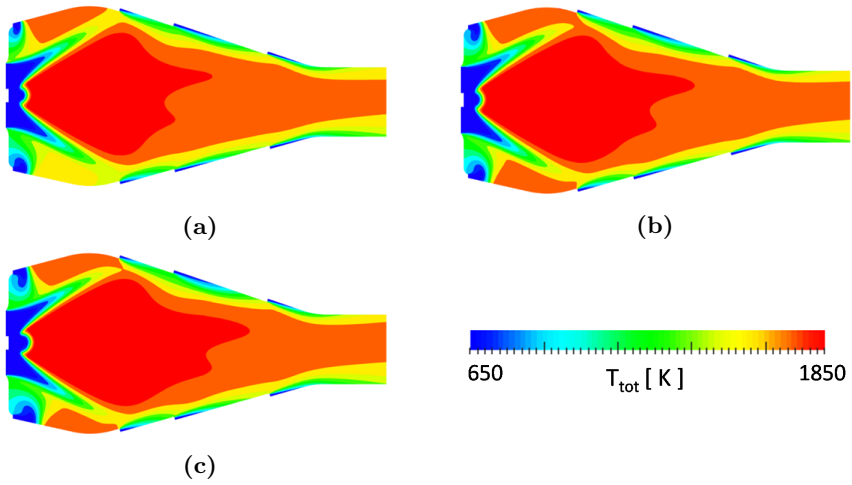

Figure 5.10.: Total temperature distribution within the passage for Mesh 0 (a), Mesh 1 (b) and Mesh 2 (c).

the combustor-turbine interface is generated just downstream of the flame, and then it migrates towards the outlet. No remarkable influence of the refinement on the solution is observed.

The total temperature and vorticity distribution on plane 40 are shown in Fig. 5.12 and 5.13 respectively. A very limited effect of the mesh is observed in terms of position and extension of the hot spot. The same conclusions can be obtained observing the vorticity field in Fig. 5.13, for which the intensity and the position of the main vortex remain the same among the three cases.

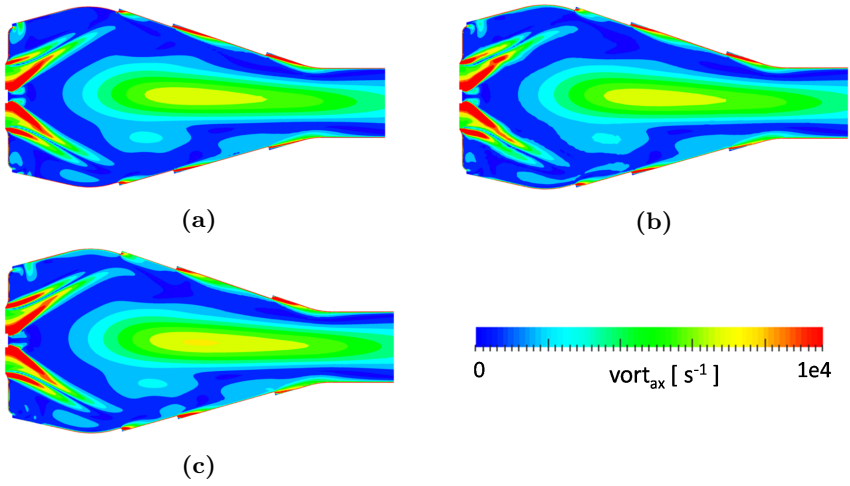

Figure 5.11.: Axial vorticity distribution within the passage for Mesh 0 (a), Mesh 1 (b) and Mesh 2 (c).

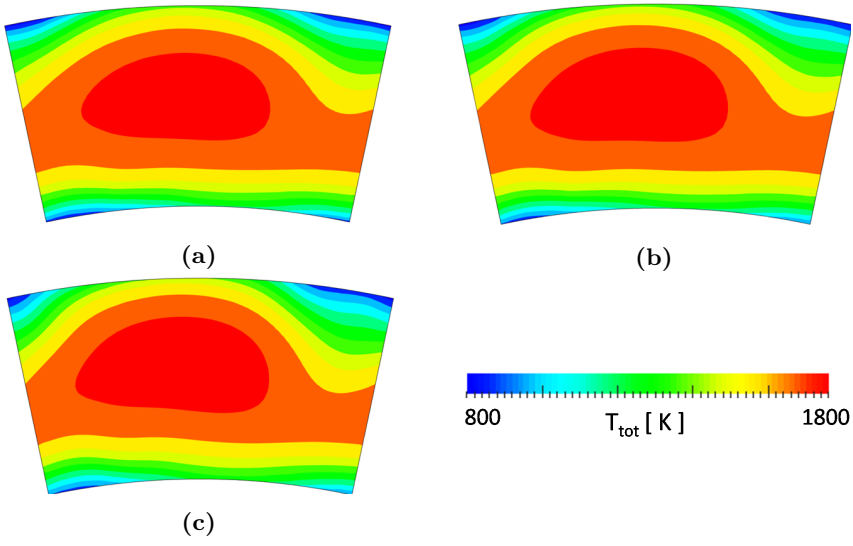

Figure 5.12.: Outlet total temperature distribution within the passage for Mesh 0 (a), Mesh 1 (b) and Mesh 2 (c).

To synthetize, the following conclusions can be obtained:

- The effect of the grid is particularly marked in the primary zone of the combustion chamber. A coarser grid underestimates the temperature

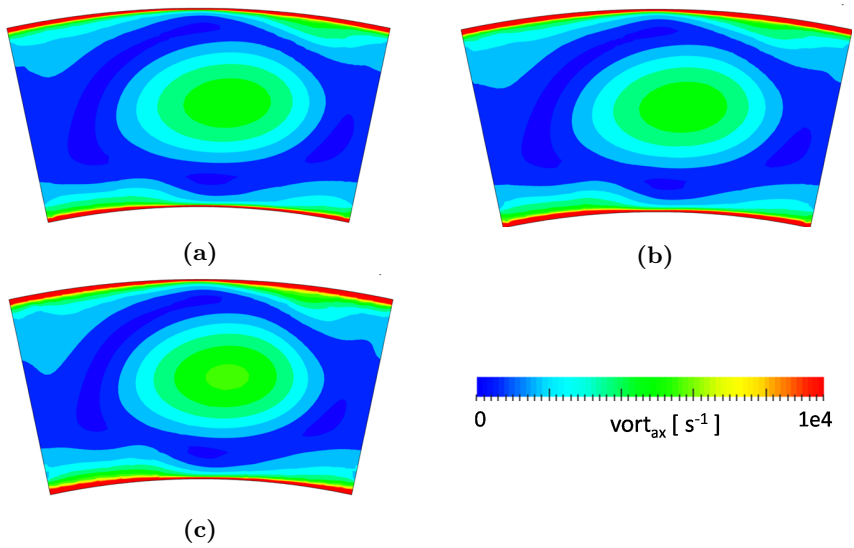

Figure 5.13.: Axial vorticity distribution at the outlet for Mesh 0 (a), Mesh 1 (b) and Mesh 2 (c).

of the cold spot region formed between the dome cooling injection and the flame itself.

- No marked influence of the mesh is observed in terms of migration of hot streak in the secondary zone of the combustor: in general, a very similar field at the combustor-HPT interface is obtained for all cases analyzed.

The flow field in the combustion chamber

As previously mentioned, the aim of this investigation is to reproduce the realistic effect of the combustion chamber on the aerothermal field of the HPT. Therefore, the main criterion followed in this work to design the combustion chamber is to obtain realistic non-uniform conditions at the NGV inlet.
Following the approach proposed by Insinna et al. [70], a comparison is proposed between different designs of modern combustion chambers in terms of radial distribution of $T_{tot}/T_{tot,ave}$ and Radial Temperature Distortion Factor (RTDF). The RTDF is defined as:

$$RTDF(r) = \frac{T_{tot,\theta} - T_{tot,ave}}{\Delta T_{tot,comb}} \tag{5.8}$$

where $T_{tot,\theta}$ is the tangentially averaged total temperature, $T_{tot,ave}$ is the local mass-averaged total temperature, and $\Delta T_{tot,comb}$ is the total temperature rise within the combustor. Figure 5.14 shows that the temperature non-uniformities generated by the current geometry are in line with other modern Lean Burn configurations published in literature (Hall et al. [32], Beard et al. [45], Cha et al. [54], Insinna et al, 2014 [70]).

Figure 5.15 shows the streamlines generated by the main swirling flow

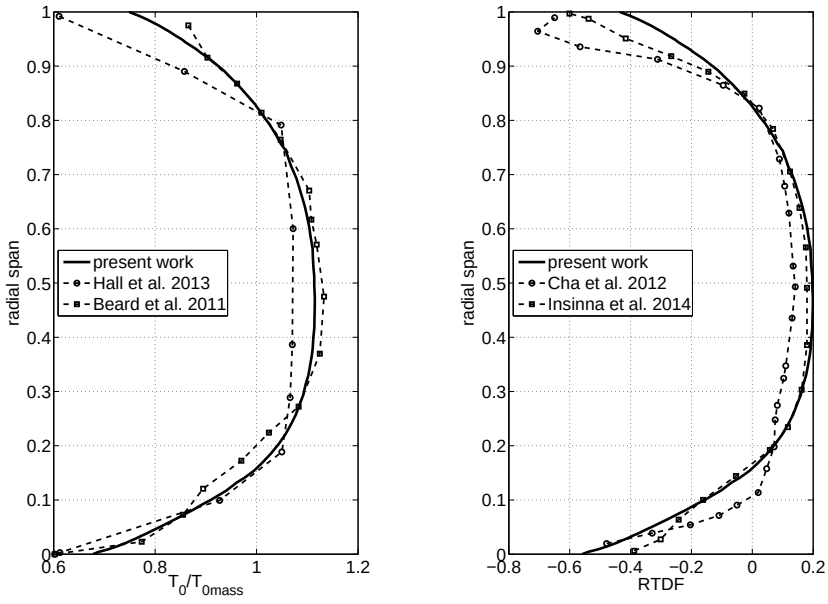

Figure 5.14.: Comparison of $T_{tot}/T_{tot,ave}$ and $RTDF$ obtained for the current geometries and for other modern geometries in literature.

and the axial premixed mixture injected into the combustion chamber. As previously mentioned, the main purpose of the pilot injection is not only to help stabilizing the flame, but also to move downstream the area where the combustion takes place. The main injection is characterized by a Sn that is sufficiently high to generate a low pressure area and a recirculation at the center of the primary zone. For classical lean combustors, this helps stabilizing the flame and to complete the combustion process in the primary zone of the combustor.

It is interesting to investigate how the non-uniform temperature flow field at the outlet, shown in figure 5.12-c, is generated. Figure 5.16 shows the streamlines arising from the cooling slots. One can clearly observe that the cooling tends to migrate in tangential direction, letting part of the wall rel-

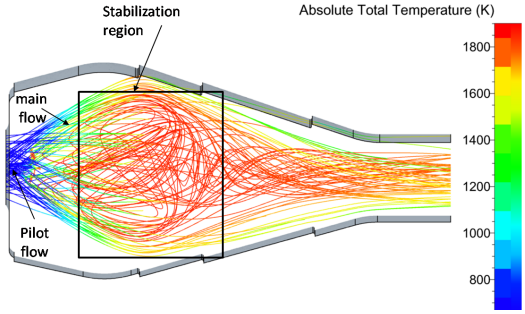

Figure 5.15.: Streamlines into the combustor colored by the total temperature.

atively uncovered. At a first analysis, this seems to be due to the hot streak generated by the flame, which tends to migrate towards the upper-right side of the chamber (in Fig. 5.16), generating blockage for the cooling. The relative migration of the cooling flow determines the position of the cold spots at the outlet, indicated as $C1$ and $C2$.

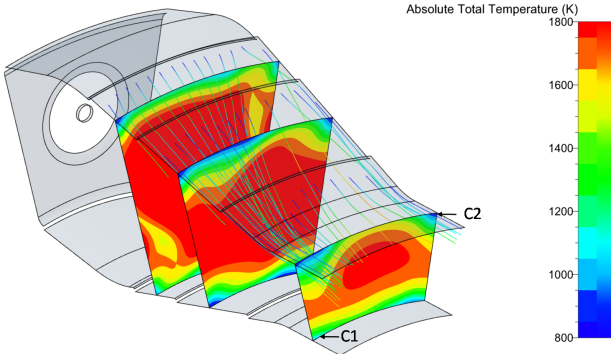

Figure 5.16.: Streamlines of the cooling and interaction with the hot streak generated by the combustion.

5.4. Coupled combustor-turbine simulation

In this section, the investigation of the mutual combustor-turbine interaction is presented The multi-code coupling procedure indicated as method 2 is applied.
As previously discussed, at the current state of the art of the tools only the URANS-URANS strategy (section 4.3) can be employed for a realistic

combustor-turbine configuration. Even though the LES-URANS and LES-LES strategies are validated and ready to be used, a further assessment of LES in turbomachinery and combustors is needed before being able to handle industrial problems.

For the coupled simulation, codes based on the OpenFOAM platform are used.
The combustion chamber is studied by using the reactive solver XiFoam: similarly to rhoPimpleFoam, employed in chapter 4 to validate the coupling methodologies, this is a pressure based PISO solver for unsteady low-Mach flows. The combustion is handled by employing a Weller flamelet combustion model [103] for premixed/partially-premixed flames. A transport equation is solved for the regress variable $b = 1 - c$.

$$\frac{\delta \rho b}{\delta t} + \frac{\delta (\rho u_i b)}{\delta x_i} = \frac{\delta}{\delta x_i} \left(\frac{\mu_t}{Sc_T} \frac{\delta b}{\delta x_i} \right) - \rho S_c \tag{5.9}$$

Where Sc_T is the turbulent Schmidt number, imposed equal to 0.7. The source term ρS_c is defined by the following (Weller) formulation.

$$\rho S_c = \rho_u \mid \nabla b \mid S_t = \mid \nabla b \mid \Xi S_l \tag{5.10}$$

Where the turbulent to laminar flame speed ratio Ξ is solved by means of a transport equation. The combustion model is completed by solving a transport equation for the mixture fraction. The Janaf tables and the Gülder's correlation for the laminar flame speed S_l are used.
The unsteady simulation of the combustor is performed with a second order central scheme (Gauss linear) in space and an implicit Euler temporal scheme, while the PISO algorithm is converged by 50 corrector loops on a time step $dt = 1.5 \cdot 10^{-6} s$. To be as consistent as possible with the simulations previously performed with FINE/Open, the $k - \epsilon$ turbulence model is chosen.
It is important to point out that the solver XiFoam presents important differences with respect to the commercial code FINE/Open. The main ones are:

- XiFoam is an unsteady solver, while only steady simulations can be performed when the combustion model is activated in FINE.
- Even though the combustion model implemented is similar, the tables and the turbulent flame speed formulation are different: the Janaf tables and the Weller's formulation are used in the OpenFOAM framework, while FINE/Open employs more advanced chemical tables generated by OpenLabs and the Zimont's TFC closure.

The discrepancies between the two codes could lead to important differences in the results. Therefore, a preliminary analysis of the combustor by OpenFOAM is required to make sure that one can obtain coherent results with

respect to FINE/Open.
To limit the computational time for the coupled analysis, it is decided to use the grid indicated as Mesh 0 in section 5.3. Figures 5.12 and 5.13 demonstrate in fact that the coarse mesh is sufficiently refined to guarantee accurate results in the secondary zone of the combustor, by keeping a relatively low computational cost.
A preliminary study of the combustor without including the turbine downstream is performed on Mesh 0 employing XiFoam, and the results at the interface are compared to what obtained with FINE/Open on the same grid. The flow field on P40 is shown in Fig. 5.17 in terms of T_{tot}, U_θ, and Tu. The comparison between OpenFOAM and FINE/Open appears excellent for all fields investigated, leading to the conclusion that the opensource code XiFoam gives sufficiently accurate results (with respect to commercial solvers) to allow the investigation of the combustor-turbine interaction.
In the end, it is important to point out that for the current case the unsteady simulation does not point out any evident unsteadiness of the flow field at the combustor-turbine interface. It was observed, in fact, that low frequency fluctuations take place only in the primary zone of the combustor, without affecting significantly the flow close to the combustor exit.

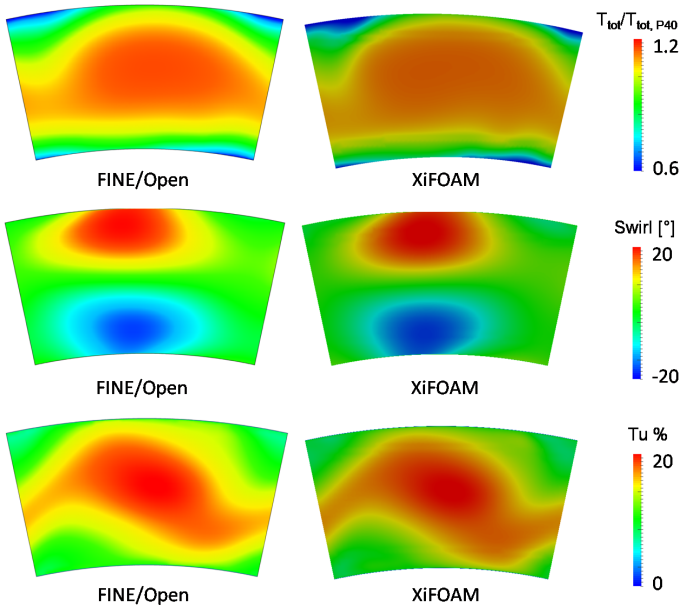

Figure 5.17.: Comparison of $T_{tot}/T_{tot,ave}$, swirl and Turbulence obtained by FINE/Open and XiFOAM on Mesh 0.

During the coupling, the turbine is solved with a second order central scheme

(Gauss linear) in space and a 4 steps Runge-Kutta approach for the time evolution. The dual time stepping algorithm is solved by 50 inner iterations, imposing $dt = 4 \cdot 10^{-6} s$. The turbulence is modeled by $k - \omega$ SST. The configuration was previously validated on the LS89 2D profile, as discussed in section 5.2.
The 3D mesh in use is the one obtained by the mesh convergence study in section 5.2. The grid is characterized by $2 \cdot 10^6$ cells, keeping the mean $Y+$ below one. Snapshots of the grid are shown in Fig. 5.18.
Figure 5.19 shows the M_{is} distribution obtained for the 3D profile when

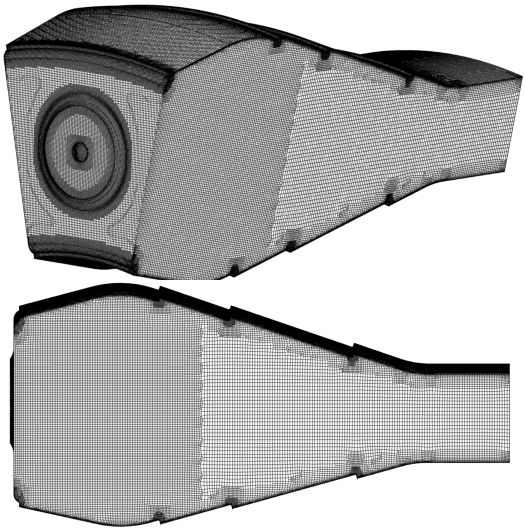

Figure 5.18.: Grid used for the to model the combustor during the analysis of the combusor-turbine interaction.

uniform inlet conditions are used. The agreement between the results at 50% of span and the experimental results for the MUR-47 operating point is excellent. The presence of shocks can be observed in the rear suction side at 15% and 50% of span.

5.4.1. Set-up of the coupled simulation

To perform the coupled simulation by using method 2, an overlapping region with an extension of 60% of span is imposed between the combustor and turbine domains. A fixed massflow is considered at the combustor inlet, while a surface averaged value of the static pressure is imposed at the NGV outlet by means of the radial equilibrium. A scketch of the coupled domain is shown in Fig. 5.20 as a reference.
To guarantee a quick convergence of the coupled simulation taking into ac-

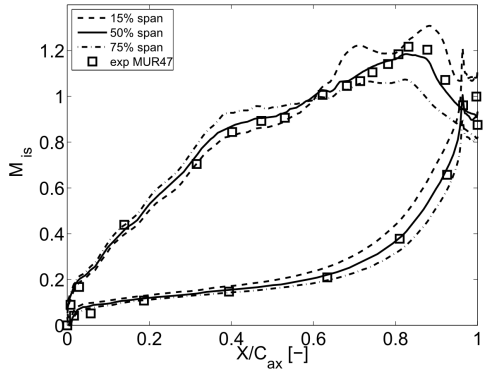

Figure 5.19.: Isentropic Mach number distribution of the 3D NGV with uniform inlet conditions.

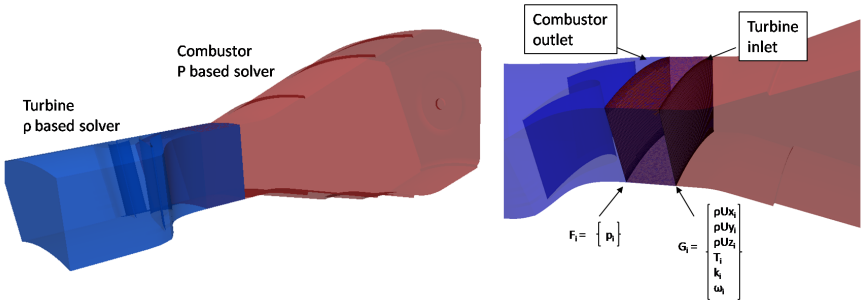

Figure 5.20.: Coupled domain for the combustor-turbine simulation. The overlapping region is shown in detail.

count the very different convective times of turbine and combustor, a weak synchronization in time (section 3.1) is used for the first part of the simulation. In this phase, communications take place every $dt_u = 1 \cdot 10^{-3} s$ resolved for the combustor and $dt_d = 4 \cdot 10^{-4} s$ for the turbine. Vectors G_i and F_i, described in sections 4.2 and 4.3 as well as in Fig. 5.20 are transferred between the domains.

Once a sufficient continuity of the time averaged flow field at the interface is obtained, a strong procedure in time is imposed. In this phase, the communication takes place every $dt_u = dt_d = 4 \cdot 10^{-6} s$. During the simulation, G_i is time averaged over dt_u.

The initial solution for the coupled simulation is obtained from two independent computations of combustor and turbine with uniform boundary conditions. The coupled domain is then solved for two flow-through after the very first communication of G_i and F_i. Hereafter, the coupling algo-

rithm is applied.
Following a practice defined during the validation presented in section 4.5.3, the convergence of the coupled simulation is monitored by imposing several pressure probes along the overlapping region. Figure 5.21 shows the pressure signals of one of these probes. After 7 communications, the convergence of the pressure field at the interface appears already very satisfactory.

Once the coupled simulation is converged, the continuity of the fields is

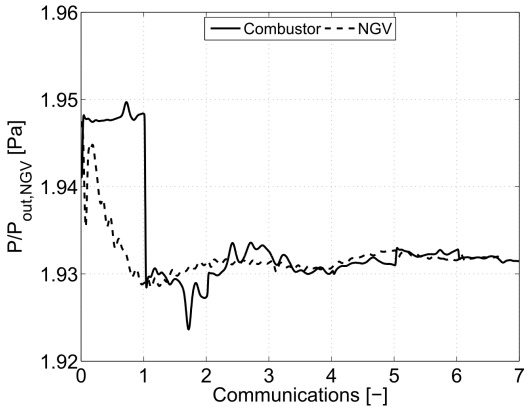

Figure 5.21.: Pressure fluctuations monitored by one of the probes in the overlapping region during the stabilization of the communication process.

verified in terms of total and static variables. The massflow-averaged values of the fields obtained at the center of the interface are shown in Tab. 5.5. The continuity between the solution upstream and the one downstream appears excellent: in particular, the error remains lower than 0.3% for all values investigated.

It is interesting to point out the perfect cohincidence of ρU at the inter-

Variable	Error
ρU	0%
p_{tot}	0.03%
T_{tot}	0.23%
p	-0.048%

Table 5.5.: Continuity error at the interface for the URANS-URANS coupling. Combustor-turbine interaction.

face. Since the exact value of mass-flow entering into the domain is known (being directly imposed as inlet condition for the combustion chamber), a correction in G_i is considered to obtain exactly the same massflow between

the upstream and downstream subdomains.
Figure 5.22 shows a picture of the Mach field along a surface at 15% of NGV

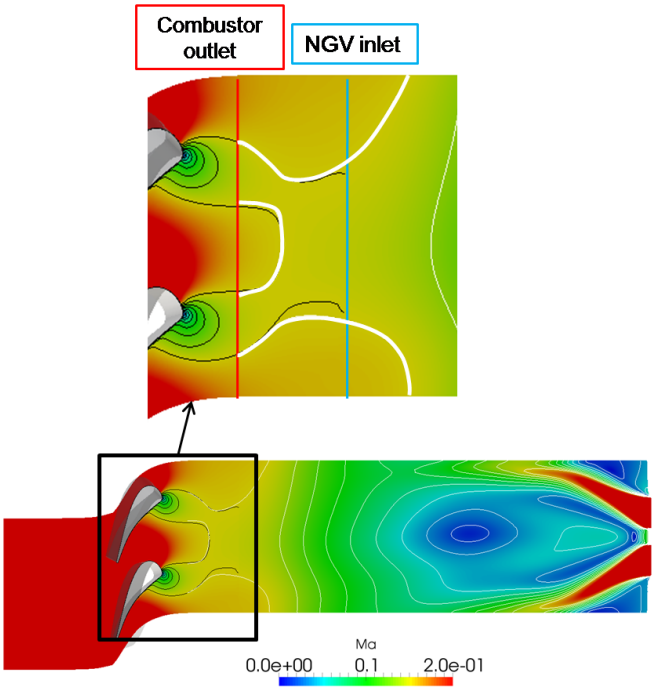

Figure 5.22.: Mach distribution at the interface between the domains. The distribution obtained for the turbine is pointed out by black isolines, while white isolines are used for the combustor.

span, pointing out again an excellent continuity in the solution between the domains. It is also interesting to observe that the Mach isolines of the combustor (in white) appear clearly influenced by the NGV downstream, since the flow is attracted towards the passage center by the pressure distortion generated at the NGV inlet. This clearly leads to the conclusion that the approach is able to transmit the potential effect of the NGV into the upstream domain.

5.4.2. Results of the coupled simulation

Figures 5.23 and 5.24 represent respectively the T_{tot} development within the passage and the adiabatic temperature distribution along the blades. At the interface between combustor and turbine, a pronounced hot spot is located

the center of the passage, while the cooling remains confined closer to hub and shroud. As previously discussed, the interaction between cooling and swirling flow within the combustion chamber generates two cold spots, defined as C1 and C2 in Fig 5.16.

When convected within the NGV, the hot streak appears deformed by the

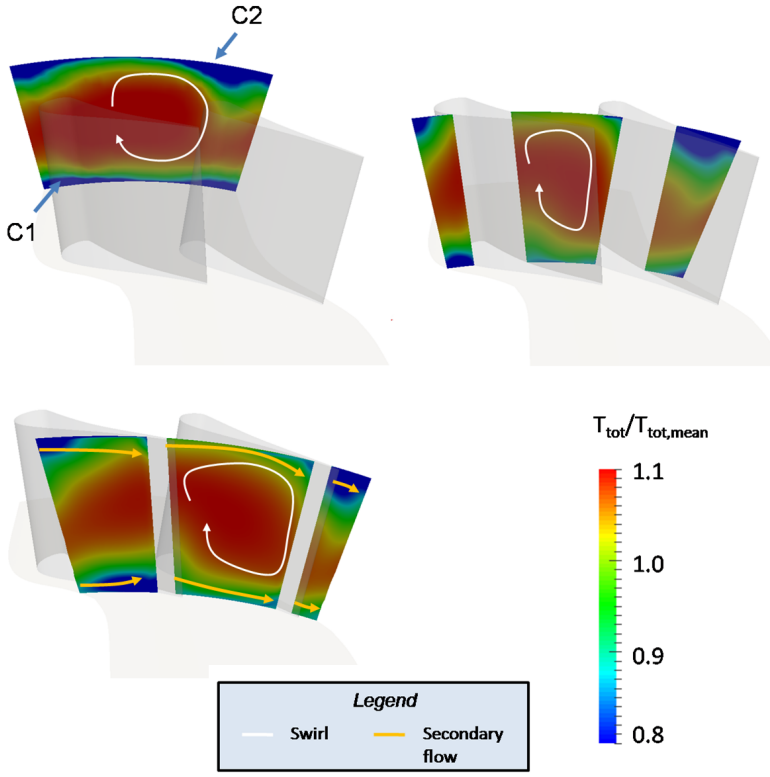

Figure 5.23.: Total temperature development within the NGV passage. The swirl and the secondary flows are indicated by arrows.

residual swirl, which is still present at the combustor outlet. This effect is schematized by a white arrow in Fig. 5.23. The hot streak deformation generates high temperature patterns towards the tip of NGV 1 and the hub of NGV 2 (NGV 1 and 2 are identified in Fig. 5.1).

Observing the adiabatic blade temperature distribution in Fig. 5.24, one can conclude that the hot spot is preferentially attracted towards the pressure side of both blades. It is interesting to point out that the same behavior is observed for the FACTOR test-case when the same clocking is considered (analyzed in chapter 8) and by other authors working on different test cases,

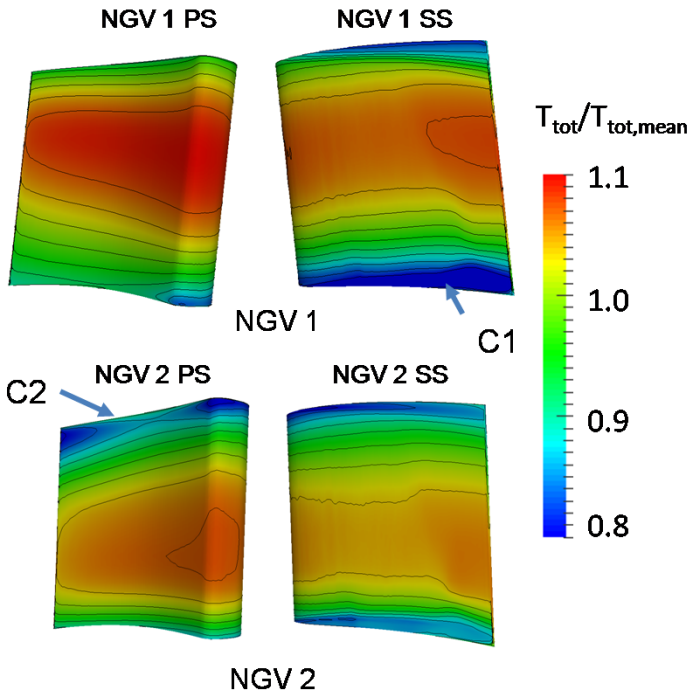

Figure 5.24.: Adiabatic wall temperature distribution on the NGV for the coupled case.

but employing a similar periodicity between NGV and swirler [53].
The cold spots mainly interact with the secondary flows generated close to the hub and the tip, indicated in yellow in Fig. 5.23. Close to the hub, the passage vortex accumulates the cold spot C1 towards the suction side of blade 1. C2 impacts instead the leading edge of blade 2, and remains close to its pressure side.
Table 5.6 shows the surface averaged values of adiabatic temperature for the two blades in study. As previously observed, the pressure side remains hotter than the suction side for both profiles.

Blade	PS	SS	Global
NGV 1	1.024	0.993	1.01
NGV 2	0.996	0.987	0.99

Table 5.6.: Surface averaged values of $T_0/T_{0,mean}$.

In terms of aerodynamic performance, Fig. 5.25 shows the M_{is} distribution

for the case with uniform boundary conditions and the coupled simulation. When the coupled case is solved, the flow incidence increases close to the hub, while on the other hand a reduction of the aerodynamic load can be depicted close to the shroud.

It is interesting to point out that the effect of the swirl on the blade

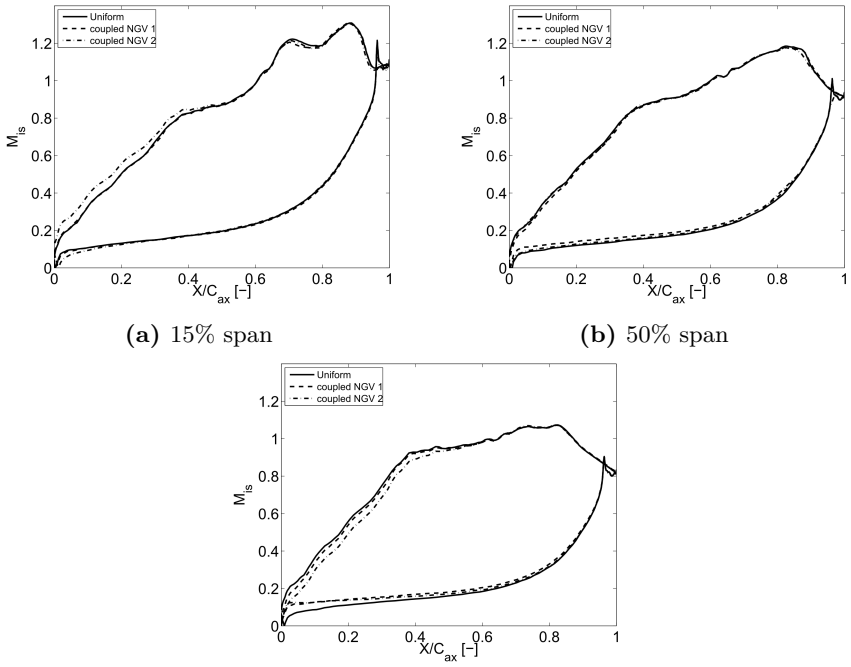

(a) 15% span **(b)** 50% span

(c) 85% span

Figure 5.25.: M_{is} at 15% of span (a) 50% of span (b) and 75% of span (c) with uniform inlet boundary conditions and for the coupled simulation.

load is more pronounced for blade 2 in comparison to blade 1. Considering that the test case was designed to have the swirler aligned with the passage center, a similar result was unexpected.

To explain this behavior, Fig. 5.26 shows the streamlines of the swirling flow within the domain. Passing from the primary zone to the outlet of the combustor, a progressive migration of the swirl towards blade 2 can be clearly observed which then influences the aerodynamics of the profiles.
A similar behavior was noticed also by Insinna et al. [70]. The authors attribute a possible explanation to a gyroscopic effect, generated by a different curvature of the inner and outer end-walls of the combustion chamber, which leads to an increase of the combustor mean line radius. For the current test case, the combustor was designed to have the same curvature between the

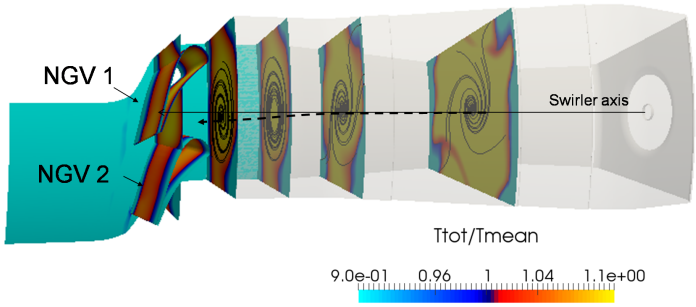

Figure 5.26.: Total temperature distribution and flow streamlines within the combustor. The swirl vortex migration is highlighted.

end-walls with the aim to keep a constant mean line radius, therefore a similar motivation is not applicable.

The reason for the migration observed is most likely linked to the annular

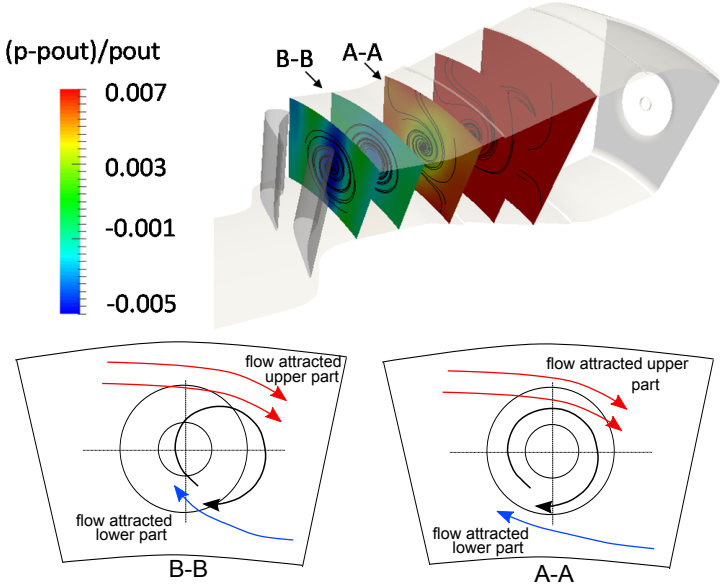

Figure 5.27.: Scheme of the swirl migration inside the combustion chamber.

shape of the chamber. A scheme of the combustor is shown in Fig. 5.27. As previously observed, the breakdown of the swirling flow injected by the main swirler generates a low pressure area at the center of the primary zone. The local low-pressure attracts flow from the external part of the combus-

tion chamber, stabilizing the flame. The centripetal flow attraction also increases the kinetic energy of the swirl, adding tangential momentum to the vortex.
Since the combustor is annular, the volume above the swirler axis is bigger than the volume below. This leads to an imbalance in the momentum of the flow attracted towards the central vortex from the upper and the lower part of the domain, in favor of the one attracted from the upper part. Such an asymmetric condition determines the migration of the vortex in the same direction of the flow closer to the external end-wall.

5.4.3. Potential Effect of the NGV on the Combustor

To evaluate the impact of the potential effect of the NGV on the combustor flow field, the coupled solution is compared to the "single domain" simulation of the combustion chamber, performed by imposing a uniform surface-averaged outlet pressure.
The potential effect is analyzed by showing plots of pressure (Fig. 5.28), ρU_x (Fig. 5.29), T_{tot} (Fig. 5.30) and turbulence level (Fig. 5.31) on transversal planes placed between $X/C_{ax} = 0.55$ and $X/C_{ax} = 0.85$ from the NGV leading edge. To quantify the potential effect in more detail, the circumferentially-averaged profiles at $X/C_{ax} = 0.55$ from the NGV leading edge are shown in Fig. 5.32.

In terms of pressure distribution, the effect of the turbine blades on the combustor flow field is visible up to 85% of C_{ax} upstream from the NGV leading edge. In particular, the stator blades cause an evident blockage, depicted by two localized areas of high pressure in correspondence of the NGV LE, accompanied by a low pressure area at the passage center.
The circumferentially averaged pressure profile at $X/C_{ax} = 0.55$ is shown in Fig. 5.32-a. The increased blockage is evident close to the endwalls, and in particular close to the hub. At 50% of span, on the other hand, the circumferentially averaged pressure is similar between the coupled and non-coupled case; in this part of the domain the pressure non-uniformity develops mainly in azimuthal direction.
The distribution of the axial momentum, shown in Fig. 5.29, is clearly linked to the pressure field, being characterized by a local minimum in front of the blades; in particular, when the NGV downstream is included into the simulation, the flow velocity in front of the vanes reduces considerably and the flow is attracted towards the passage center. The effect of the NGV on ρU_x is evident at $X/C_{ax} = 0.55$ and can be noticed up to about $X/C_{ax} = 0.75$.
The cicumferentially averaged distribution of the axial momentum in Fig. 5.32-b is in line with what already observed for the pressure field. When the NGVs are modeled, one can depict a higher blockage close to the endwall. As a consequence, more flow is attracted between 50% and 90% of span.
The presence of the NGV does not seem to have any evident effect in terms

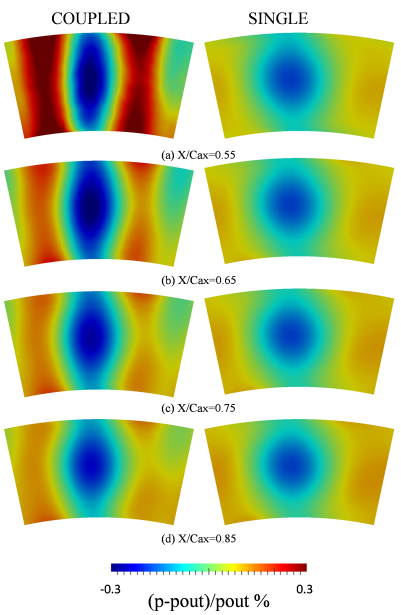

Figure 5.28.: Pressure distribution at successive axial positions upstream from the blade leading edge. The distance from the blade LE at 50% span is indicated in the graph.

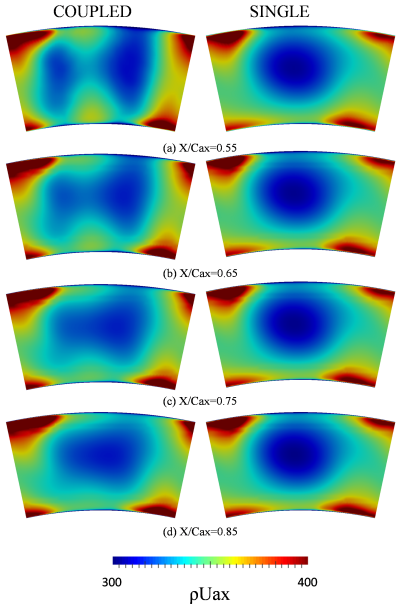

Figure 5.29.: Axial momentum distribution at successive axial positions upstream from the blade leading edge. The distance from the blade LE at 50% span is indicated in the graph.

of T_{tot} and turbulence distribution within the combustor, as confirmed by Fig.5.30 and 5.31. This is in line with what observed by Koupper [75] for the FACTOR configuration. When the NGVs are present, the only noticeable effect that can be observed is a mild migration of the high turbulent spot from the center of the passage towards the upper-right corner when approaching the combustor outlet.

In general, from the latter analysis, one can conclude that the propagation of the potential effect within the combustor is rather limited in axial direction. In particular the presence of the NGVs only affect the momentum and the pressure field within the combustion chamber, and their influence extends up to about $0.8C_{ax}$.

Nevertheless, the potential effect could have an influence on important technological details for compact modern combustors, such as the cooling of the rear part of the end-walls; as a matter of fact, the cold flow close to the end-walls could be critically deviated by the presence of the NGV downstream, and the full coverage of the wall could not be assured.

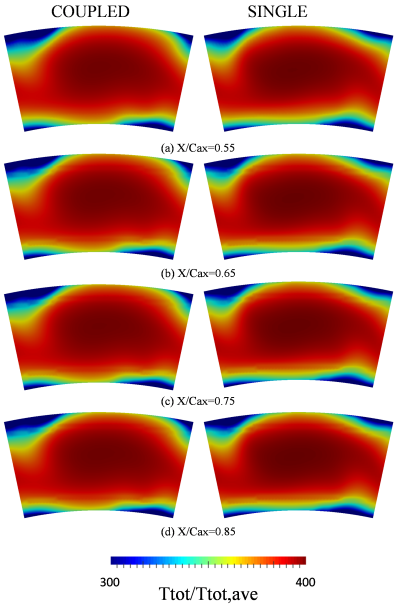

Figure 5.30.: Total temperature distribution at successive axial positions upstream from the blade leading edge. The distance from the blade LE at 50% span is indicated in the graph.

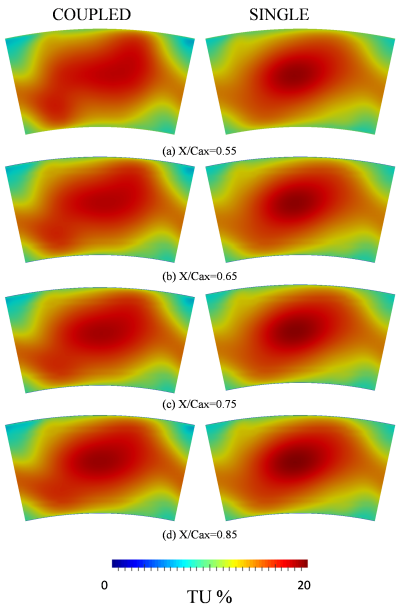

Figure 5.31.: Turbulence distribution at successive axial positions upstream from the blade leading edge. The distance from the blade LE at 50% span is indicated in the graph.

5.5. Final remarks

In this chapter, the numerical design and investigation of a combustor-turbine test case is presented. The configuration is designed to represent as close as possible a real industrial configuration equipped with a LBC.
In particular, the NGV is designed by taking into account the necessity to calibrate the numerical tools applied to investigate the hot streak propagation in turbine. In this sense, it was decided to derive the 3D aerodynamic profile from the 2D LS89 airfoil, which was extensively investigated at VKI both in terms of aerodynamic performance and aerothermal behavior.
The coupling procedure for URANS-URANS applications, described in section 4.3, is applied to study the mutual interaction between the components. The two solvers in use for combustor and turbine, both based on the OpenFOAM platform, were successfully validated by a comparison with commercial CFD solvers and experimental data.
The coupled simulation is performed starting with a weak synchronization in time and then passing to a strong approach only when the time averaged

solution is sufficiently uniform at the interface between the domains. This permits to get a quicker convergence of the flow fields.
Using this procedure, a satisfactory convergence of the solution at the interface between the two domains is obtained after only seven communications. An optimal continuity is observed between the upstream and downstream solution, and the potential effect of the NGV is correctly propagated within the combustion chamber.
The coupled simulation permits a detailed characterization of the complex interaction between the hot and cold streaks, the swirling flow generated within the combustor and the secondary flows of the NGV. In particular, the HS migration within the NGV is influenced by the residual swirl of the flow at the combustor outlet, while the cooling mainly interacts with the secondary flows developed close to the endwalls. All these phenomena have a considerable impact on the aero-thermal field of the stator, for which a very non uniform adiabatic blade temperature distribution can be observed. Moreover, it is pointed out a pronounced migration of the residual swirl within the combustor, which affects the aerodynamic performance of the airfoils. The migration is most likely linked to the geometrical structure of the chamber, and it must be taken into account for a correct estimate of the NGV performance.
To conclude, it is noticed that the presence of the NGV downstream causes an azimuthal pressure distortion at the combustor outlet, which affects the flow field in the secondary zone of the combustion chamber (in particular in terms of momentum). After employing the coupled approach it is concluded that the potential influence of the NGV extends up to $0.8C_{ax}$ upstream of its leading edge.

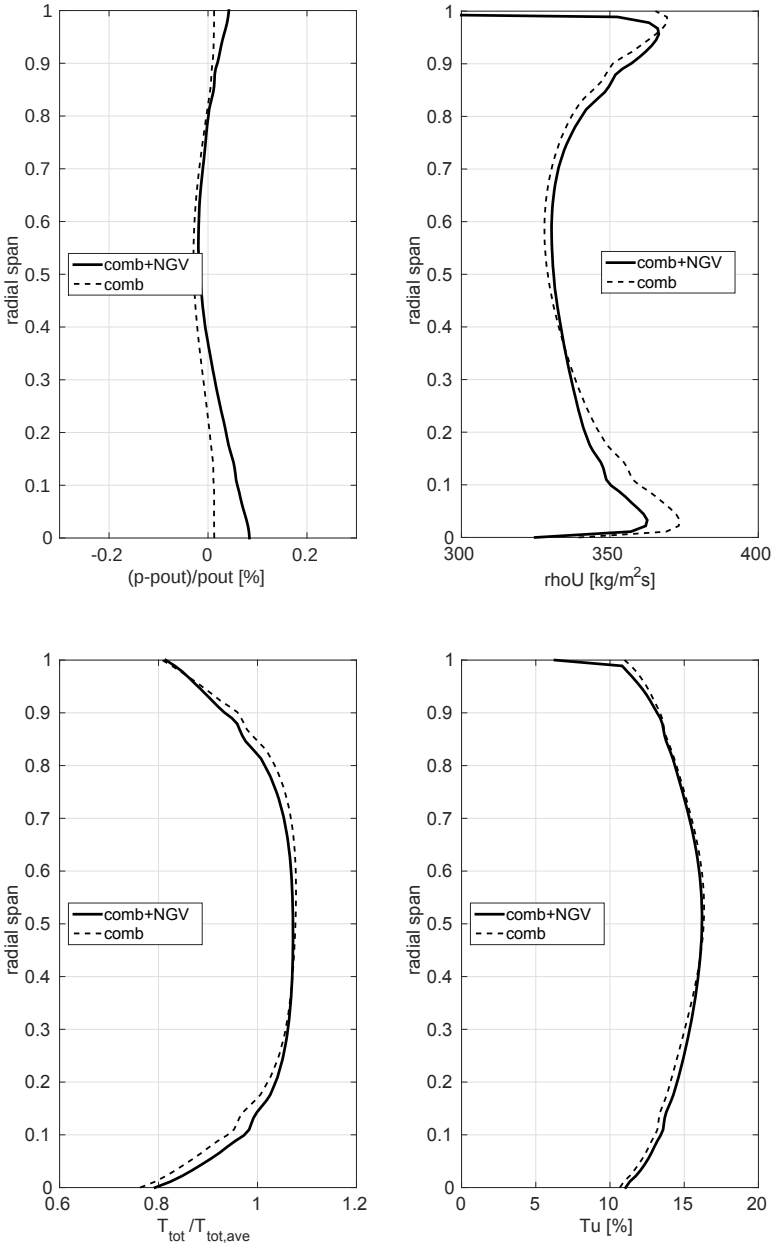

Figure 5.32.: circumferentially-averaged profiles of pressure (a), axial momentum (b), total temperature (c) and turbulence (d) on a plane at $X = 55\%C_{ax}$ upstream from the blade leading edge.

Part II.

LES for the analysis of the hot streak migration

Introduction to part II

The high turbulence level at the combustor outlet plays a major role in the combustor-turbine interaction. In chapter 2 it was pointed out a lack of experimental set-ups which are able to reproduce in detail the complex and highly turbulent flow field within real HPT stages. As a direct consequence, the RANS models commonly used have never been directly validated on cases with TU approaching 25% (as it is commonly observed at the combustor-turbine interface).
On the other hand, it has been recently observed that the use of LES to directly resolve the most energetic turbulent structures leads to a more accurate reproduction of the hot streak migration in turbine [54, 75]. Due to the high computational costs, a discussion on the feasibility of LES for 3D HPTs has taken place only recently [21], thanks to the increase of the computational power available.

The objective of this part of the thesis is to develop a LES tool to be applied to the combustor-turbine interaction. The motivation is twofold:

1. LES could help in understanding the flow dynamics and the physics of the combustor-turbine interaction.

2. LES results could be used to validate less computationally expensive RANS models.

The present work is the first attempt to apply LES to external flows in turbomachinery with the solvers available at VKI. Therefore, before studying the complex problem of the combustion-turbine interaction, a structured validation process is required, based on turbomachinery-related test cases with increasing complexity.
The validation of the solvers will be presented in detail in chapters 6 and 7, where LES is applied to a low-Reynolds LPT profile (chapter 6) and to a high-Reynolds HPT (chapter 7).
To conclude, a comparison between LES and RANS for the resolution of the combustor-turbine interaction is discussed in chapter 8. In this case, LES is performed by Koupper et al. [27] on the FACTOR test case, employing the software AVBP [76].

Chapter 6.

Application of LES to a LPT test case

In the specific context of the validation of a LES tool for turbines, the analysis of low pressure airfoils represents a first necessary step before passing to more challenging HPT profiles. The reason for that is mainly linked to the low Reynolds number at which these components operate: classical Reynolds numbers for LPTs are in fact around 100000, representing one order of magnitude less than typical HPTs. According to Tyackle [63] the computational requirement for a wall resolved LES in these operating conditons can be up to 10 times smaller than for a HPT airfoil.

For further details, the results discussed in the present chapter are also presented in a paper submitted to the ASME Turbo Expo 2016:

F. Bigoni, S. Vagnoli, T. Arts, T. Verstraete. *Detailed Numerical Characterization of the Suction Side Laminar Separation Bubble for a High-lift Low Pressure Turbine Blade by means of (U)RANS and LES*, Proceedings of ASME Turbo Expo 2016: Paper N. GT2016-56653.

6.1. Background of the test case

The pursuit for higher bypass ratios in modern commercial aircraft engines requires the low-pressure turbine (LPT) to provide an increasingly larger power output allowing to drive large diameter fans without penalizing the efficiency. At the same time, the actual design trend is oriented towards a reduction of the engine weight: since the LPT is one of the heaviest components of an aircraft engine (it can account for 20-30 % of the total engine weight [104]), the most logical solution is the reduction of its blade count. This implies, for a given stage loading, an increase of the aerodynamic load on each blade, leading to the development of the so-called high-lift airfoils, which are characterized by a higher velocity peak on the suction side, followed by a considerable diffusion.
Since the Reynolds number typical of high-altitude cruising conditions is quite low, a large part of the boundary layer developing on the suction surface of a high-lift LPT blade may be laminar; in particular, the high initial acceleration tends to keep the suction side boundary layer laminar until the

velocity peak even in presence of a significant free-stream turbulence intensity. If the subsequent diffusion is large enough, a laminar boundary layer is not able to withstand the resulting adverse pressure gradient and separates from the blade surface: a separation bubble is thus formed, causing a loss in lift and a drop in efficiency.
In his classification of the transition modes, Mayle [105] considered the laminar-to-turbulent transition which takes place in the separated shear layer, as the most important effect to determine reattachment of the separation bubble upstream from the blade TE. The author classified the separation bubbles in two different types, long or short, depending on the bubble effect on the loading distribution along the suction side. While long bubbles are associated with a greatly modified loading distribution, high losses and a relevant reduction of the exit flow angle, short bubbles have only a local displacement effect, such that before and after them the pressure distribution is close to the one predicted without any separation. Long bubbles can eventually be open, i.e. the separated shear layer does not reattach before the trailing edge of the blade. This last condition represents the worst-case scenario in terms of performance.

6.2. Limitations of RANS and advantages of LES

When the laminar boundary layer separates, the main mechanism driving the turbulent transition is the inviscid Kelvin-Helmholtz (KH) instability [106], arising in the separated shear layer. This leads to an exponential growth of local fluctuations, which eventually trigger transition and the shear layer reattachment.
To reproduce this complex mechanism by RANS, the classical turbulence models shall be coupled with further models describing the transition process. One of the most widely used transition model is the $\gamma - Re_\theta$ developed by Menter, based on the resolution of two additional equations for the intermittency γ and the transition momentum thickness Reynolds Number Re_θ [107, 108]. Several numerical works demonstrated that this model is particularly suited for cases where short bubbles are present, while it underestimates the separation length for long and open bubbles [109, 110].
On the other hand, LES can be a powerful tool for the resolution of high-lift airfoils, since the effect of the Kelvin-Helmotz instabilities arising in the separated shear layer can be reproduced without introducing any further model.

6.3. The experimental set-up

The profile chosen to apply LES is the T106-C [111], whose main features are listed in Tab. 6.1. This is classified as ultra-high-lift airfoil, and is de-

signed to get a velocity peak at $x/C_{ax} = 0.5$ along the suction side, followed by a strong deceleration (x is the axial coordinate).

The airfoil was experimentally investigated in cascade configuration at the

C	g/C	Stagger angle	Inlet flow angle
93.01 mm	0.95	30^o	33^o
Loading coefficient Ψ	Diffusion rate Dr	$M_{is,out}$	
1.24	0.58	0.65	

Table 6.1.: Details of the T106-C turbine blade in cascade configuration.

von Karman Institute in the S-1/C high-speed closed-loop wind tunnel [111]. The freestream turbulence level is equal to 0.9%, which is the natural level found in the facility. This facility allows adjusting independently the level of density and pressure ratio, to operate the profile with a wide range of Mach and Reynolds numbers.

The blade load resulting from the experimental investigations are shown in

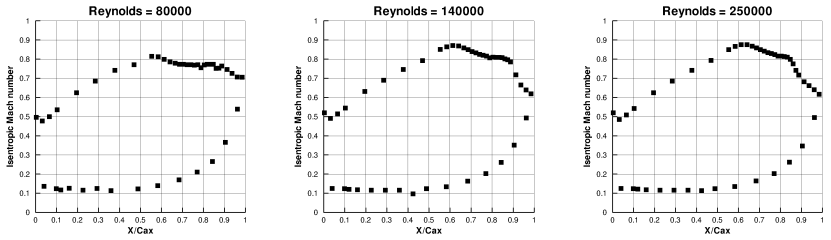

(a) **(b)** **(c)**

Figure 6.1.: Load distribution experimentally obtained for the T106-C. $Re = 80000$ (a), $Re = 140000$ (b), $Re = 250000$ (c).

Fig. 6.1 for Re (based on the blade chord) ranging from 80000 to 250000. For these operating conditions, the deceleration in the rear suction side leads to the formation of a separation bubble, which can be identified by a plateau in the isentropic Mach number distribution. In particular, for $Re = 80000$, no reattachment is observed (an open bubble is obtained).

According to the considerations discussed in section 6.2, the case at $Re = 80000$ is chosen to validate LES.

6.4. Numerics

The reproduction of the laminar-to-turbulent transition is very challenging for LES [112]. This is particularly due to the fact that the very first

turbulent vortices formed in the transition area have a very limited energy content. Several attempts to reproduce the transition of the T106 profile by LES can be found in literature [113–116] usually observing relevant discrepancies with respect to experiments for the Low-Reynolds conditions [113]. These results suggest that a very fine grid is required in the transition area, and the numerical schemes shall be chosen with care.
In this work, the code FINE/Open from NUMECA is tested, while Numeca Hexpress is used for the grid generation.
The mesh is shown in Fig. 6.2. It is an unstructured grid, obtained using Hexahedral elements and non-conformal interfaces. This permits to easily get highly localized refinements in the area of interest without penalizing the accuracy.

The spanwise extension of the computational domain is chosen equal to

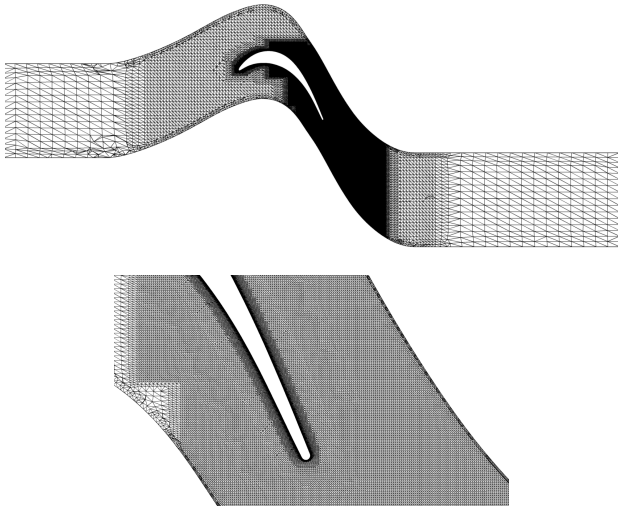

Figure 6.2.: General view of the grid (a). Zoom of the mesh close to the rear suction side (b).

10% of the blade chord. This is a classical value [116], being commonly considered sufficient to allow the development of three dimensional instabilities and turbulent structures.
The grid around the blade is characterized by $\Delta x^+ = \Delta z^+ \sim 10$, and $\Delta y^+ = 1$, reaching $\Delta x^+ = \Delta y^+ = \Delta z^+ \sim 20 - 25$ within the channel. In total, $7 \cdot 10^6$ cells are used.
For the spatial discretization, a second order central scheme [117] is used in this work. In terms of temporal discretization, an explicit 4th order Runge-Kutta with a dual time-stepping approach is adopted [118].
As already mentioned, the main requirement for the time step to get a detailed resolution of the turbulence is to satisfy the CFL condition [119]. This

request can be explained considering that the smallest turbulent structure which can be resolved by the computation has the same size of the cells Δx. Therefore, the minimum time step which has to be resolved to simulate the convection of a vortex from one cell to another can be evaluated as:

$$dt = \frac{\Delta x}{U} \tag{6.1}$$

Corresponding to $CFL < 1$. To this end, the time step is chosen equal to $1 \cdot 10^{-7}$ s, expecting a maximum Courant number lower than 0.5 all along the domain. The physical time step is solved by 5 inner iterations.

In general, compressible LES is affected by problems of spurious reflections at boundaries [83] (see section 3.2.2). For the current case, Michelassi et al. [120] observed that pressure waves are formed both upstream and downstream the blade. To obtain a uniform flow field in these regions, the authors demonstrate that non reflecting conditions are needed both at the inlet and at the outlet to avoid spurious reflections of the pressure waves.
At the current state, non-reflecting conditions are not implemented in FINE. To overcome this problem, numerical sponge layers are created upstream and downstream the blade by coarsening the grid up to $\Delta^{1/3}/C_{ax} = 0.15$, as shown in Fig. 6.2-a.
The main limitation of this approach lies in the impossibility of imposing a synthetic turbulence at the inlet, which would require a refined mesh upstream from the blade. Nevertheless, Marty [113] showed that the very low turbulence level of the experiment ($TU = 0.9\%$) has a negligible effect on the behavior of the bubble; in this sense, it is chosen to model the inlet with a simple laminar condition.
At the domain outlet, a constant pressure value is imposed, while periodic boundary conditions are used both in spanwise and pitchwise direction.
To reproduce the SGS turbulent decay, the WALE model is employed. The numerical details of the computation are shown in Tab. 6.2.

Configuration	Operating conditions	Mesh type	Cells	X+/Y+ wall	Phys. time simulated [-]
T106-C	Re=80k Laminar inlet	Unstructured hex non conformal interface	7 MLN	10/1	14FT

Table 6.2.: Details of the T106-C LES computation.

6.5. Time Average Quantities

To monitor the convergence of the LES, the following convective time has been defined:

$$CT = \frac{C}{U_1} \tag{6.2}$$

The convergence of the mean flowfield has been obtained after about ten convective times and the time average values presented hereafter are evaluated over four additional convective times.
Firstly, the criterion on the physical $CFL < 1$ introduced by Choi and Moin [119] is verified. Figure 6.3 shows the instantaneous CFL computed within the domain. Observing the CFL field, it is possible to conclude that the requirement is well satisfied over the entire flowfield.
Figure 6.4 depicts the blade load distribution. The current LES results are

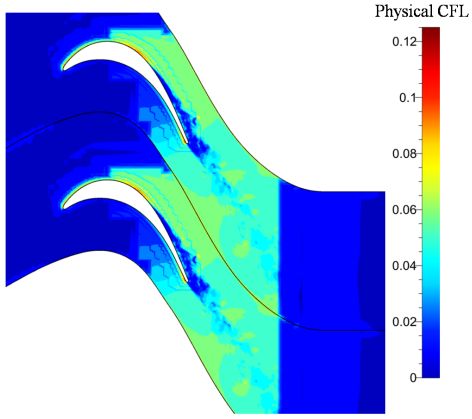

Figure 6.3.: Physical CFL field across the domain.

compared with experimental values and to RANS obtained by employing the $k-\omega$ SST coupled with the $\gamma - Re_\theta$ model, performed by Bigoni et al. [121].
As expected, the $\gamma - Re_\theta$ model fails in predicting the open bubble. In this case, the laminar separation appears delayed with respect to experiments, and the turbulent transition taking place after the separation leads to reattachment of the boundary layer at $Z/C_{ax} = 0.9$.
Apart from the slight overestimation of the peak of M_{is}, the LES prediction appears instead in very good agreement with the experiments. In particular, the massive open separation experimentally observed has been detected by LES. This is clearly indicated by the contour of negative axial velocity, which are representative of a reverse flow, in the rear part of the suction side (Fig. 6.5).
Figure 6.6 shows the experimental and numerical evaluation of ξ and the

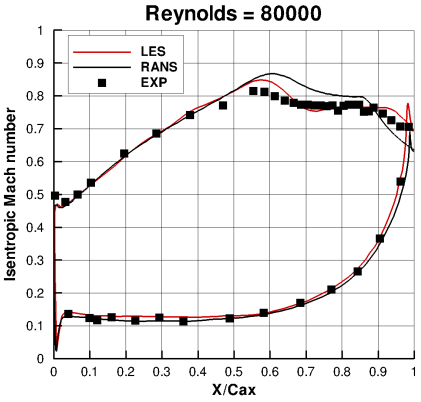

Figure 6.4.: Blade load distribution at $Re = 80000$. LES, experimental and RANS distributions are compared.

outlet angle β_2 for the blade in study over a wide range of Re, going from 80000 to 250000. ξ and β_2 are defined as:

$$\xi = 1 - \left(\frac{U_2}{U_{2,is}}\right)^2 \tag{6.3}$$

$$\beta_2 = atan(U_\theta / U_x) \tag{6.4}$$

Observing the experimental results in Fig.6.6-a, one can appreciate a sudden drop in efficiency below $Re = 100000$. This evidences the passage from short to long bubble (defined as bursting). Since RANS predicts a closed bubble for these operating conditions, a large discrepancy in ξ can be observed. On the other hand, a very satisfactory comparison is obtained by using LES.
A good agreement between LES and experiments can be also observed for the outlet angle β_2, while RANS overpredicts the outlet angle of about 2^o at the lowest Reynolds condition. For a better comparison of the results, the values of β_2 and ξ are listed in Tab. 6.3.

In Fig. 6.7 it is possible to appreciate the wake profile downstream of the

Data	ξ [%]	β_2 [deg]
EXP	8.85	58.79
LES	9.07	59.21
RANS	4.75	60.62

Table 6.3.: Results in terms of profile losses and outlet angle for $Re = 80000$.

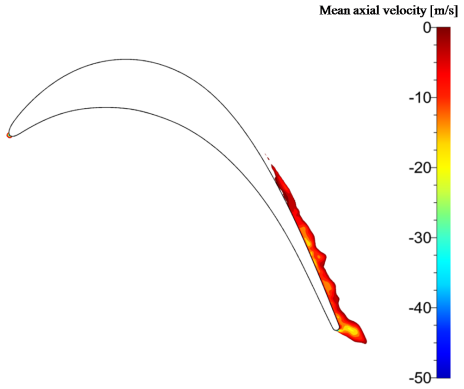

Figure 6.5.: Negative axial velocity profile in the rear suction side.

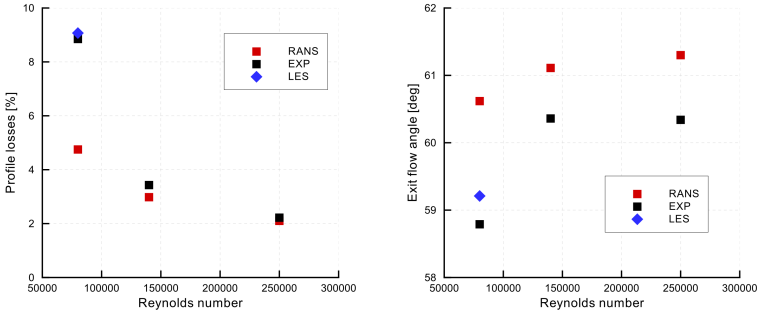

(a) Losses **(b)** Outlet angle

Figure 6.6.: Losses (a) and outlet angle (b) variation with Reynolds. Experimental and numerical results are compared.

blade. The wake profile is visualized in terms of Δp_{tot} along one pitch at $x/C_{ax} = 0.465$ downstream from the blade TE. Δp_{tot} is defined as:

$$\Delta p_{tot} = \left(p_{tot,1} - p_{tot}\right) / p_{tot,1} \tag{6.5}$$

The wake shape coming from LES is coherent with the experimental data in terms of wake width, whilst a discrepancy is observed in terms of peak of Δp_{tot}, which is overpredicted by LES. This difference explains the fact that the profile losses predicted by LES are slightly higher than the experimental value. The wake profile predicted by RANS is also reported in the graph for comparison. This appears much thinner both with respect to LES and experimental results.

In order to study the evolution of the wake shape, the total pressure distri-

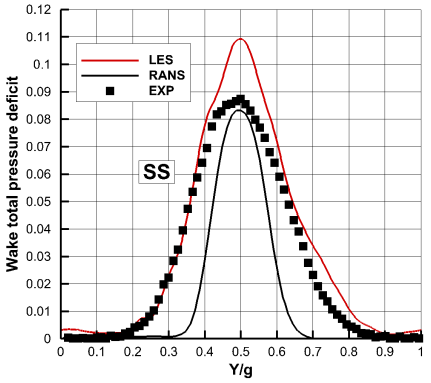

Figure 6.7.: Total pressure profile at $x/C_{ax} = 0.465$ downstream from the blade TE. Y indicates the transversal direction.

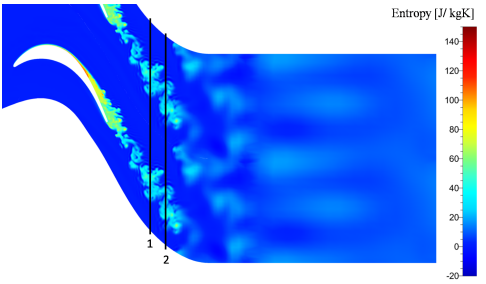

Figure 6.8.: Post processing planes used to visualized the wake profile. The entropy field in the blade to blade plane is shown.

bution extracted at $x/C_{ax} = 0.465$ is compared to the one at $x/C_{ax} = 0.625$. The planes in which Δp_{tot} is extracted are reported in Fig. 6.8 together with a contour of instantaneous entropy, while the wake shape is shown in Fig. 6.9.

From Fig. 6.8 it is first of all possible to notice that the wake is completely shifted towards the suction side because of the open separation. Moreover, by comparing the position of the planes with the vortical structures associated both to the wake and to the separation itself, it can be concluded that the wake shape significantly changes when going from plane 1 to plane 2, as also reported in Fig. 6.9.

When moving downstream, the wake becomes wider and is characterized by a smaller peak of Δp_{tot}, because of the mixing of the wake with the main flow. Consequently, ξ increase from 9.07% to 9.26% because of the increase of mixing losses.

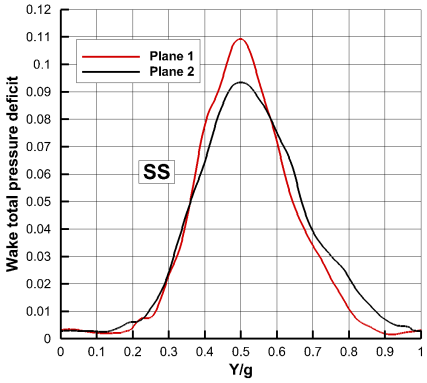

Figure 6.9.: Wake evolution on two planes at different distance from the blade TE. Y indicates the transversal direction.

From Fig. 6.8 it is also possible to observe the effect of the sponge layer (obtained by a coarse grid) on the flow field: the entropy contour close to the outlet is numerically diffused by the interaction with the sponge layer. Therefore, one can conclude that the numerical sponge layer considered appears effective in damping the unsteadiness.

6.6. Time Dependent Results

To monitor the evolution in time of the fluctuating quantities and to study the characteristic frequencies of the phenomena involved in the transition, three numerical pressure probes are placed at the midspan section close to the blade wall. Their specific positions, summarized in Tab. 6.4, are selected considering the loading distribution obtained with LES, to provide useful information in the understanding of the bubble evolution.

Probes A and B are placed at the extremities of the dead air region, which

Probe	Z/C_{ax} (from blade LE)	Local Flow Field
A	0.65	Beginning of the plateau of M_{is}
B	0.825	End of the plateau of M_{is} (the reattachment starts)
C	1.23	Wake

Table 6.4.: Location of the numerical probes imposed for the unsteady analysis of the LES results.

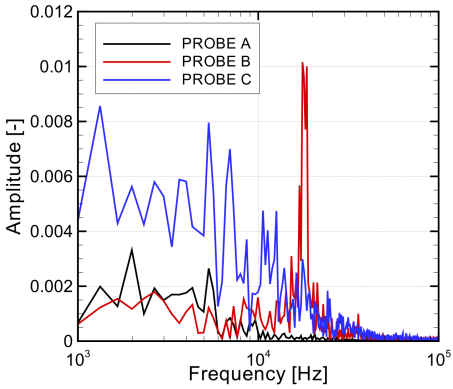

Figure 6.10.: FFT for the three probes listed in Tab. 6.4

is pointed out by the plateau in the blade loading distribution; probe A is located at the beginning of the plateau, while probe B is placed at its end. Eventually, probe C is placed further downstream from the blade TE. Its signal is representative of the vortical structures in the wake.
The statistical convergence of the fluctuating quantities is obtained after about 12 convective times. After that, the Fast Fourier Transform (FFT) of the pressure signals is performed over 3 additional convective times. The results are shown in Fig. 6.10.

Probe A

As reported in Table 6.4, probe A is located at the separation point.
Close to the separation point, small disturbances (which are inherently present in real flows) are amplified by the separated shear layer, which is unstable. The shear layer generates two-dimensional TollmienSchlichting (T-S) waves, which move in the mean flow direction [122]. In the first part of the separated shear layer, the T-S instability grows linearly.
From the FFT of probe A (black line in Fig. 6.10) a range of characteristic frequencies between 2 kHz and 5 kHz can be observed. This result is indeed coherent with the Tollmien-Schlichting frequency range detected by Marty [113]. Since in the present analysis the incoming flow is fully laminar, it is possible that the small disturbances which undergo amplification are related to the numerical noise.

Probe B

Probe B is located at the end of the plateau, where the maximum thickness of the bubble is reached.
In this area, the T-S instability is strong enough to trigger non-linear unstable phenomena. In particular, the separated shear layer rolls up and sheds big vortical structures. This process is driven by the Kelvin-Helmholtz instability mechanism, which is characterized by a well defined frequency component. From the red curve in Fig. 6.10, it can be deduced that the Kelvin-Helmholtz instability is resolved by LES, which depicts a clear frequency peak around 18 kHz.

Probe C

As a consequence of the roll up of the separated shear layer, a breakdown to turbulence occurs: large three-dimensional vortical structures are shed close to the maximum displacement position of the bubble, and the reattachment process of the separated shear layer starts (the reattachment is not completed upstream from the blade TE).
The frequency spectrum observed along the wake is reported in blue in Fig. 6.10. A low-frequency signal is depicted, being representative of big vortical structures formed by the turbulent breakdown and convected by the flow.

The phenomenology involved in the turbulent transition of the current

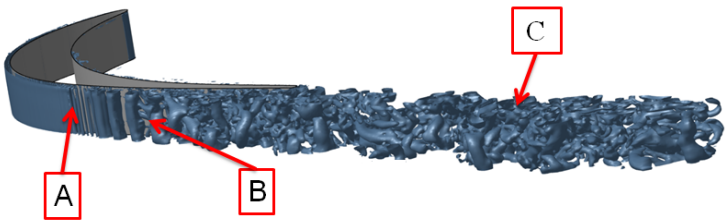

Figure 6.11.: Q criterion applied to the LES flow field.

case can be better understood by comparing the position of the probes with the instantaneous Q-criterion reported in Fig. 6.11.
The two-dimensional structures associated to the Tollmien-Schlichting instability are clearly observed in correspondence of Probe A. Moving further downstream, the wrapping of the shear layer, dominated by the Kelvin-Helmholtz instability, is visible.
Thereafter, the breakdown to turbulence occurs: three-dimensional vortical structures are shed from the bubble and they are still present at the blade trailing edge, because there is no reattachment of the separated shear layer.

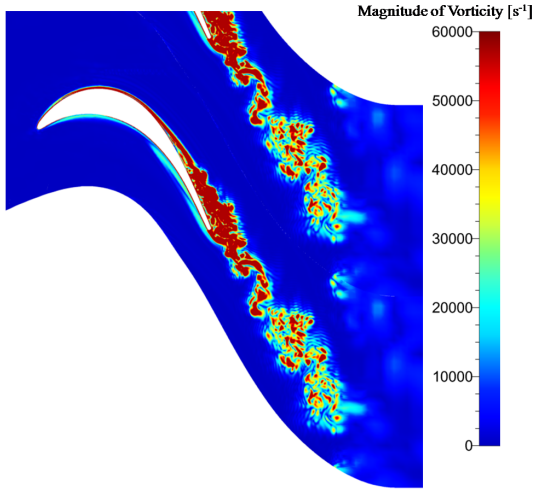

Figure 6.12.: Visualization of the vorticity field.

Consequently, the vortical structures depicted in the wake are mainly generated from the maximum displacement point of the bubble.
The breakdown to turbulence and the wake-associated vortical structures can also be clearly seen in the contour of magnitude of vorticity vector, reported for completeness in Fig. 6.12.

6.7. Final remarks

The LES approach with WALE model implemented in FINE/Open is validated in this chapter on the T106-C LPT profile at $Re = 80000$. For this condition, an open separation bubble in the rear suction side is observed. Classical RANS with the $\gamma - Re_\theta$ transition model fails in predicting the flow field; indeed, a closed separation bubble is predicted and the profile losses are underestimated.
In terms of time averaged results, LES demonstrated to be very accurate in reproducing the blade load. In particular, the presence of the open bubble is detected correctly, as well as its influence on the losses and the exit flow angle.
LES also permitted to characterize the laminar to turbulent transition observed for the separated shear layer. In this sense, it was observed that the transition is initialized by low frequency oscillations in the first part of the separation bubble, linked to the T-S instability. Closer to the maximum shear layer displacement from the wall, the Kelvin-Helmholtz instability arises, which triggers the formation of big turbulent structures.

Considering the application of the solver to the hot streak propagation in turbomachinery, the main drawback of FINE/Open is that non-reflecting conditions or "analytical" sponge layers (i.e. based on a forcing terms in the governing equations [123]) are not implemented. As observed, simple Dirichlet conditions could generate in some cases the reflection of pressure waves moving upstream and downstream the blade.
The solution used in the present chapter to damp spurious fluctuations is to include a very coarse mesh close to the inlet, to generate a numerical sponge layer. This method demonstrated to be effective in damping the waves, but it prevents from a detailed reproduction of the turbulence transferred from the combustor to the turbine, which requires a very refined grid up to the inlet.
In the last versions of the solvers, non reflecting conditions as well as synthetic turbulence generators could be implemented by the user from the tool OpenLAB. This possibility was not investigated in the framework of this thesis: in the following, it was rather preferred to test the solver TUMDF based on the OpenFOAM platform, for which non reflecting outlet conditions are already implemented and validated for the combustor-turbine coupled simulation (discussed in part I). Their generalization to inlet patches is straightforward [83]

Chapter 7.

Application of LES to a HPT test case

In the previous chapter, LES is applied to the flow field of a low-Re LPT profile. In this chapter, a second more challenging test case is considered, based on a High-Re HPT airfoil. The objectives of the current study is twofold:

- To assess the capability of LES to characterize the flow field aerodynamics of HPTs, both in terms of time averaged and unsteady quantities.

- To perform a detailed aerodynamic study of the test case, to get a first experience on the application and the advanced post-processing of LES to HPTs.

The unsteady analysis of the evolution of the trailing edge base pressure on HPTs is chosen as test case. The flow field at the trailing edge is known to play a significant role in the profile losses of turbine blades, therefore it has been extensively validated in the open literature; the steady and unsteady experimental results available can be used to validate the LES numerical approach.
Due to the limitations discussed for FINE/Open, it was decided to use the ρ-based code TUMDF (implemented for the OpenFOAM-ext library) for the current study. As for the author's knowledge, this represents the first published application of the solver for LES in turbines.

Further details of the work discussed in this chapter can be found in the following paper:

Vagnoli, S., Verstraete, T., Mateos, B., Sieverding, C. H. (2015). *Prediction of the Unsteady Turbine Trailing Edge Wake Flow Characteristics and Comparison With Experimental Data* Proceedings of the Institution of Mechanical Engineers, Part A: Journal of Power and Energy. 229(5), pp. 487-497.

7.1. Background of the test case

It is well known that the flow at the blade trailing edge can be responsible a large part of profile losses (depending on the profiles, up to 30% [124]). The losses related to the trailing edge flow can be expressed as:

$$\zeta_{bp} = C_p \cdot \frac{te}{s \sin(\beta_2)} \tag{7.1}$$

Where the blade pressure coefficient, defined as:

$$C_p = \frac{P_{s2} - P_b}{\rho_2 V_2^2 / 2} \tag{7.2}$$

Is directly linked to the base pressure value (P_b), which is defined as the pressure measured at the trailing edge center.
The von Karman Institute has a long tradition in the research of turbine blade trailing edge flows. The first important contribution was the publication of a base pressure correlation based on experimental data on a wide variety of blade profiles investigated over a period of ten years [125]. This correlation is still extensively used for the industrial design of turbine profiles.
The expected base pressure value for a blade with straight rear suction side is presented in Fig. 7.1 in function of the downstream pressure, together with schlieren photographs illustrating the different characteristic phases of the base pressure evolution. The experiments allowed to attribute the strong increase of profile losses in the transonic range to a sudden drop in the base pressure with respect to P_2 (which is clearly visible between $P_2/P_{tot,1}$=0.4-0.6 in Fig. 7.1).

One major assumption in establishing the base pressure correlation was that there exists an isobaric pressure dead air region at the trailing edge. To this end, the small size of the blades used for the correlation did not allow verifying the assumption of an isobaric region: depending on the trailing edge thickness, the pressure sensing hole to trailing edge diameter was between 15 to 50%. There was nevertheless an absolute need to verify this assumption because the separation of the boundary layers at the trailing edge was known to be a highly unsteady phenomenon leading to the formation of large coherent structures, known as the von Karman vortex street [126–128]. At that time, the influence of these structures on the trailing edge pressure distribution was still not verified.
To do that, tests on a very large scale cascade were performed, with one of the blades fitted with a rotatable trailing edge cylinder [129]. The rotatable cylinder allowed to map in detail the pressure distribution along the TE circumference. First tests run at a low downstream Mach number $M_{2,is} = 0.4$ showed that the trailing edge region was characterized indeed by an isobaric pressure distribution. In a second test series with a half scale blade tested at $M_{2,is} = 0.79$ the trailing edge pressure distribution changed drastically,

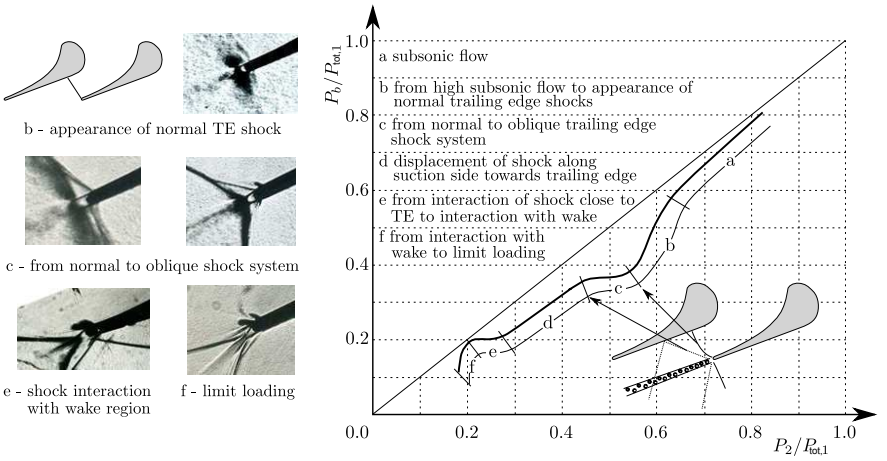

Figure 7.1.: Schematic evolution of base pressure in function of downstream pressure.

exhibiting a very pronounced pressure minimum at the center of the trailing edge circle. Shlieren visualizations showed that the enrollment of the separating shear layer into vertical motion was taking place very close to the trailing edge, influencing the base pressure distribution [130, 131].

To validate the LES solver, the same profile experimentally analyzed by Sieverding et al. [130] is studied. For a complete study of the vortex shedding-base pressure interaction, three different operating conditions are numerically analyzed in this chapter, representing three configurations of the flow and the trailing edge shock system. Results are compared to experimental data obtained during a recent experimental campaign, described in section 7.3.

7.2. Limitations of RANS and advantages of LES

The test case presented by Sieverding et al. [130] to describe the flow at the TE of a blade has been used to validate unsteady codes by several authors. Kopriva et al. [132] and Leonard et al. [133] used an URANS approach to compute the flow field for high subsonic outlet Mach number. Reliable results are obtained in terms of reproduction of the boundary layer along the blade, but the pressure minimum at the trailing edge center was clearly overestimated.
The area at the TE is in fact dominated by large turbulent structures, which are generated during the roll-up of vortices at the trailing edge. Due to its capability to directly resolve these structures, LES theoretically represents

a perfect approach for an accurate resolution of the local flow field. A preliminary LES study of the current profile was performed by Leonard et al. [133], obtaining encouraging results.

7.3. Experimental Arrangement

A recent experimental campaign is carried out at VKI to study the evolution of the base pressure distribution with the downstream Mach number [20]. The experiments are performed on the same blade used for the previous tests by Sieverding et al [130], shown in Fig. 7.2. This is a front loaded HPT profile, whose features are listed in Tab.7.1.

C	g/C	gauging angle	d_{te}/C
140 mm	0.7	19.1^o	5.3%

Table 7.1.: Details of the blade investigated for the trailing edge flow field. The gauging angle is defined as $arcsin(l_{th}/g)$, with l_{th} the throat.

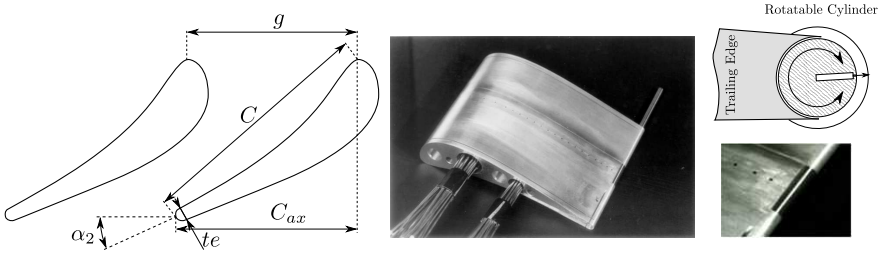

Figure 7.2.: Cascade and view of the blade with rotatable trailing edge cylinder.

The new test series is entirely focused on the investigation of the variation of the trailing edge pressure distribution with the Mach number downstream. The TE pressure distribution is investigated with a fast response sub-surface mounted pressure sensor and a conventional pneumatic pressure tap on the rotatable trailing edge cylinder, which is shown in detail in Fig. 7.2.
The tests are carried out in the VKI blow down tunnel C3 with exhaust to atmospheric pressure. The overall flow conditions used during the analysis are listed below:

- $T_{tot,1}$ = 280 K.

- $P_{tot,1}$ from 1.15 to 1.8 bar.
- $M_{2,is}$ from 0.5 to 1.05.
- TU = 1% at inlet.
- Re from $1.8 \cdot 10^6$ to $2.8 \cdot 10^6$

For all downstream Mach numbers, the pressure and suction side boundary layers at the trailing edge are turbulent; on the suction side natural transition takes place, while on the pressure side the turbulent boundary layer is triggered by a trip wire.

Figure 7.3 summarizes the P_b distribution along the TE obtained for dif-

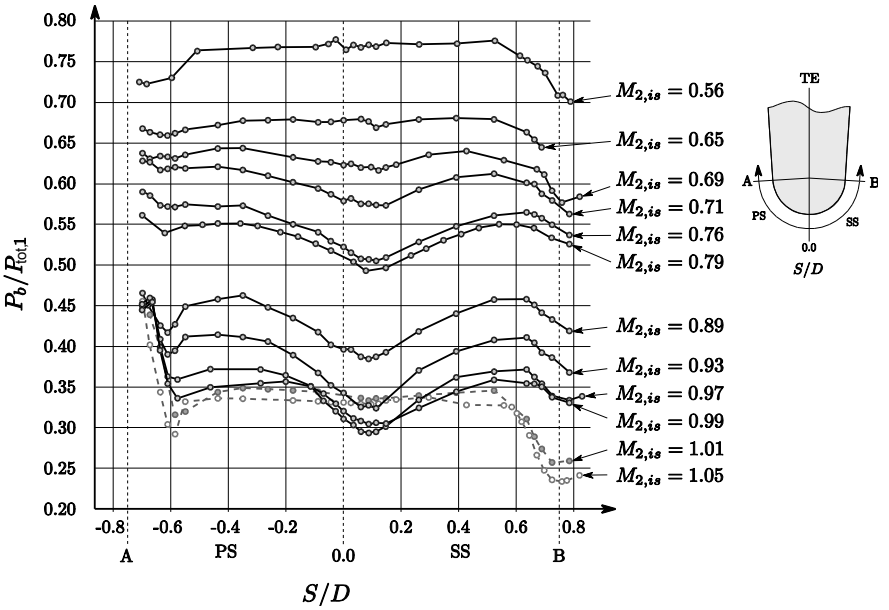

Figure 7.3.: Effect of downstream Mach number on trailing edge pressure distribution.

ferent values of $M_{2,is}$. The graph impressively demonstrates the impact of the trailing edge vortex on the pressure distribution:

- **Up to $M_{2,is} = 0.65$** the trailing edge is characterized by an extended nearly isobaric region, with the enrollment of the separating shear layers from pressure and suction side occurring sufficiently far downstream to not affect the base region.

- **From $M_{2,is} = 0.65$ up to $M_{2,is} = 0.93$** an increasing downstream Mach number leads to a faster enrollment of the shear layers. Vortices

are generated closer to the trailing edge, leading progressively to an increasingly non-uniform pressure distribution with the formation of a strong pressure minimum near the trailing edge center. The maximum difference between the minimum trailing edge pressure and the downstream Mach number is reached at $M_{2,is} = 0.93$, with $P_{b,min}/P_{tot,1} = 0.325$ for $P_2/P_{tot,1} = 0.5721$.

- **For higher values of** $M_{2,is}$ the non-uniformity decreases rapidly, The base region is completely restored for $M_{2,is} = 1.01$.

7.4. Numerics

The LES approach and the grid used are validated for the operating condition at $M_{2,is} = 0.79$, because of the large amount of steady and unsteady data available in literature [130]. The ρ-based solver TUMDF is used to perform the LES analysis [134].
Despite the fact that the profile is prismatic, a 3D numerical domain is employed. The computational span to chord ratio was set to 7.5% for all cases analyzed, based on the LES analysis of Leonard et al. [133]. Periodic conditions were used both in spanwise and in pitchwise direction to let the turbulence to develop.
The domain is discretized by an unstructured mesh, using hexahedral elements with non conformal interfaces. Prismatic layers are added at the wall to accurately reproduce the boundary layer. As already discussed, this strategy permits to get very localized mesh refinements, which are useful to contain the grid dimensions when the flow field shall be studied in detail in a limited area. Considering that LES is studied for a future application to the flow of 3D HPTs, the containment of the dimension of the grid is cosidered as a priority for the current analysis.
An accurate solution of the flow requires a very small value for Y+ and a large number of prismatic elements within the boundary layers. To contain the grid size for such a high Reynolds number, Δx^+ and Δz^+ were kept to a relatively large value.
The effect of the grid refinement was studied for the case at $M_{2,is} = 0.79$, monitoring the convergence of the time-averaged pressure distribution at the trailing edge. Three different meshes were analyzed, progressively refining the prismatic layers at the wall and in the wake region.
The final mesh used for the investigation is shown in Fig. 7.4, while its main features are listed in Tab. 7.2. The whole domain is reproduced by $2.53 \cdot 10^6$ cells.
All simulations are performed with an implicit first order Euler scheme in time and the filteredLinear scheme in space (a second order central scheme with upwind treatment of the advection terms). The time step is chosen to

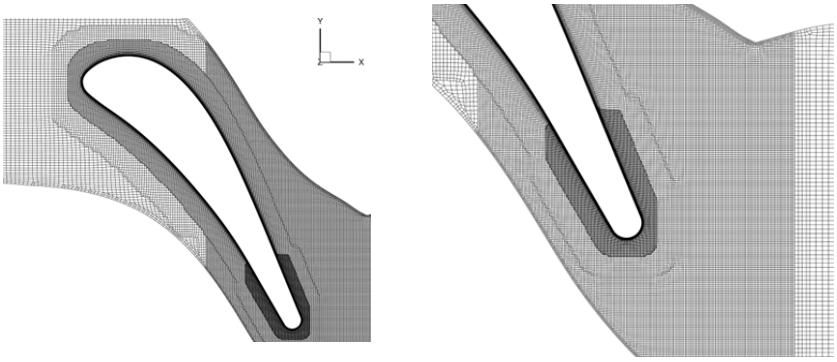

Figure 7.4.: On the left: 2D view of the final mesh around the blade. On the right: detail of the mesh at trailing edge.

Parameter	Value
Number of nodes	2.53 MLN
Average Y+	0.4
Maximum Y+	0.8
X+,Z+	48 to 105
Prism layers at wall	28

Table 7.2.: Features of the mesh.

keep the maximum CFL below 1.3 everywhere.
The Smagorinsky model is used to represent the small turbulent scales, including the van Driest formulation at the wall. The inlet is modeled by a simple laminar condition, while a convective non reflecting condition was used at the outlet. Furthermore, sponge layers were generated far from the blade by coarsening the grid.

7.5. Results of the Investigation

Validation of the LES Approach for the Reference Case $M_{2,is} = 0.79$

Figure 7.5 presents the isentropic Mach number distribution obtained by LES and experiments. The comparison between CFD and experimental results is satisfactory along the whole blade. In particular, preliminar tests performed with URANS (not shown here for brevity) showed a poor capability to reproduce the experimental behavior on the rear suction side close to the trailing edge, which are well matched when LES is employed.

The boundary layer evaluated one diameter upstream from the trailing

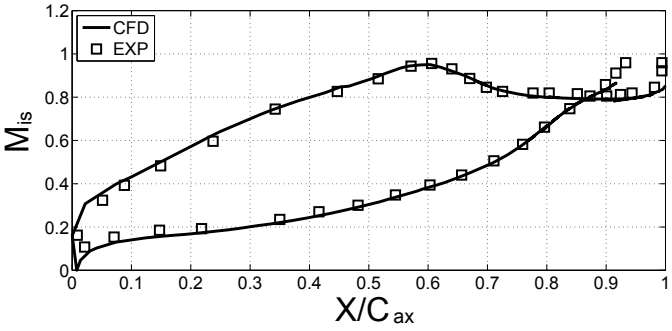

Figure 7.5.: Blade Mach number distribution.

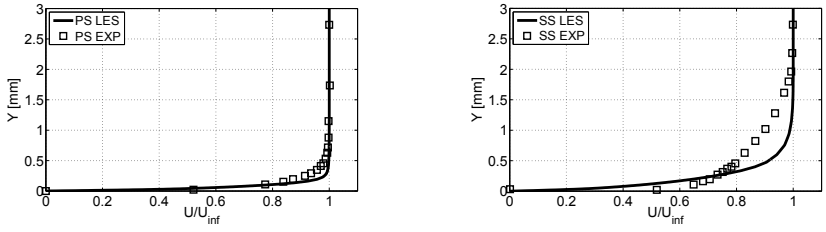

(a) Pressure side **(b)** Suction side

Figure 7.6.: Boundary layer profiles close to the trailing edge: pressure side left suction side right.

edge is shown in Fig. 7.6. The turbulent boundary layer thickness is underestimated by CFD, in particular along the suction side. The discrepancy was in this case expected, being due to the difficulty to obtain accurately resolved LES at the wall: during a laminar to turbulent natural transition, as it is the case along the suction side of the present blade, small turbulent structures are generated. Their accurate resolution would require a very refined mesh along the suction side. Considering that the final aim of the investigation is to evaluate a LES tool for future studies of the combustor-turbine interaction on 3D profiles, priority was given in this phase to the containment of the grid size with respect to the boundary layer accuracy.
Despite the discrepancy on the boundary layer, a satisfactory reproduction of the vortex shedding behavior is expected for two main reasons: (I) a high turbulent energy content is locally represented by the viscous turbulence. (II) the difference in thickness with respect to the experimental profile is limited.
Figure 7.7 represents the time averaged static pressure distribution at the

trailing edge. Experimental and LES results are also compared to RANS and URANS computations obtained by Leonard et al. [133].
The first thing that clearly comes out is that a steady simulation reproduces an unphysical isobaric region at the trailing edge, completely missing the central pressure minimum. Passing from RANS to URANS, the general match with the experimental pressure distribution improves, but a remarkable underestimation of the trailing edge pressure is still observed.

Compared to URANS, LES is in general more accurate. This is due to

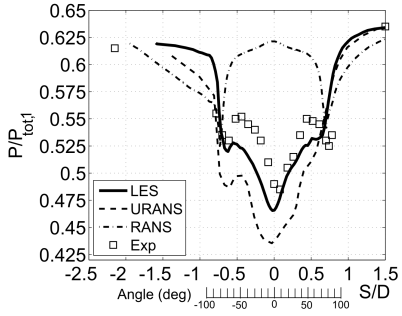

Figure 7.7.: Time averaged pressure distribution along the trailing edge. RANS and URANS results are from Leonard et al. [133].

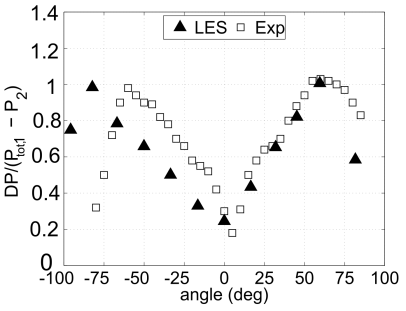

Figure 7.8.: Angular distribution along the trailing edge of the phase-lock averaged amplitude of pressure fluctuations.

the ability to directly solve the turbulent structures generated in the near wake region after separation, which are not resolved by URANS. One can therefore conclude that a LES approach, even though more computationally expensive, leads to a remarkable increase of accuracy when a highly separated flow has to be analyzed in detail.
Comparing the LES results to experiments in Fig. 7.7, a slight lateral shift of the LES curve to the left of the trailing edge center (i.e. towards the pressure side) can be observed. The maximum error in the pressure prediction is lower than 3% of $P_{tot,1}$ and is located along the compression taking place after the separation.
This shift can be linked to the under resolved suction side boundary layer, shown in Fig. 7.6. Observing the acceleration of the flow approaching the trailing edge and the position of the separation point (which is indicated by the relative pressure minimum on the suction side in Fig. 7.7 one could observe a shift of about 10^o between CFD and experiments. The narrower near wake region on the suction side, reproduced by LES, could explain the effect of a general shift towards negative S/D values of the trailing edge pressure distribution when numerical and experimental pressure profiles are compared.
Observing the phase-lock amplitude of pressure fluctuations, shown in Fig.

7.8, it can be stated that the numerical results (which are evaluated for 12 discrete points along the trailing edge) fit satisfactorily the experimental data, pointing out correctly the presence of two peaks near the boundary layer separation points. The position of the peak of fluctuations on the pressure side is predicted with a difference of 20^o with respect to the experiments, but the global trend and the absolute values of amplitude are correctly reproduced.
Figure 7.9 shows the time-averaged pressure profile compared to three instantaneous snapshots of the field, taken during one vortex shedding period. A very large pressure minimum is formed alternatively along the pressure and suction side of the trailing edge. This entrains the shear layer of the pressure and suction side during the vortex shedding. The trailing edge center doesn't appear to be particularly affected by the fluctuations, and the pressure locally remains close to the averaged value.
Observing Fig. 7.9 and Fig. 7.7, it is worth noticing that the accuracy of

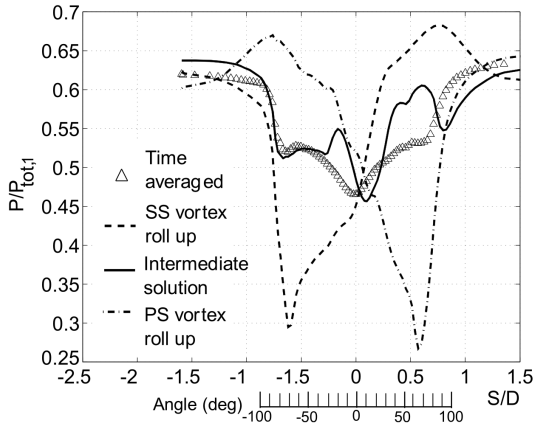

Figure 7.9.: Snapshots of the instantaneous static pressure distribution along the trailing edge.

LES in the estimate of the time averaged pressure distribution at the trailing edge is impressive, considering that the very high amplitude of the static pressure fluctuation in time makes the computation of the time averaged profile particularly problematic.

Numerical schlieren pictures corresponding to four different phase angles during one period of vortex shedding are presented in Fig. 7.10. For comparison the figure shows on the left experimental schlieren photographs corresponding to the first and third numerical picture. During the vortex shedding cycle, pressure waves are alternatively generated at the pressure and suction side (indicated as P_i and S_i respectively) by the inward and outward motion of the shear layers separating from the trailing edge. Since the flow is subsonic, the waves are moving upstream, interacting with the closest

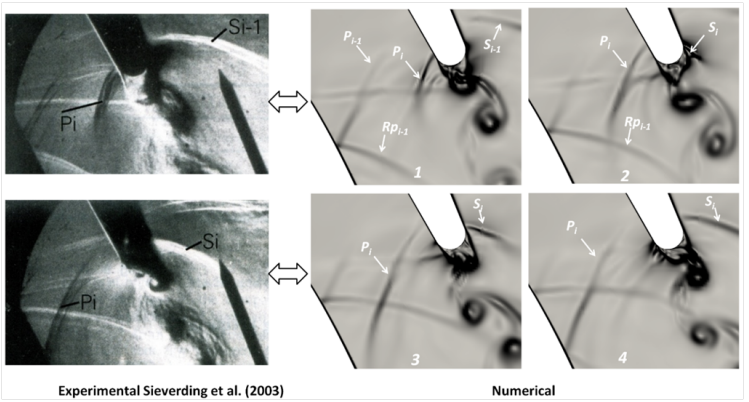

Figure 7.10.: Schlieren visualization of the flow field at $M_{2,is}$=0.79.

blades: in particular, waves generated at the pressure side interact with the suction side of the lower blade. The wave reflected, indicated with R_p in 1 and 2 is moving back interfering again with the wake of the upper blade. The reproduction of this interaction is strongly linked to the grid, which has to be fine enough in the entire rear suction side area of the domain, as it was also noticed by Leonard et al. [133].

Figure 7.11 shows the numerical and experimental unsteady pressure signals, obtained along the blade suction side from the throat region to the trailing edge. The experimental results are described in detail by Sieverding et al. [130]. The comparison between experimental and numerical appears overall very favorable. The pressure wave P_i induced by the outwards motion of the pressure side shear layer of the neighboring blade intersects the suction side between sensors 3 and 4. It moves then successively upstream across sensors 3 and 2. The migration of the wave generates an asymmetric signal, characterized by a sharp pressure rise followed by a slow decay. The amplitude of the pressure fluctuations are important, with $\Delta P = 12$ to 15% of $(P_{tot,1} \quad P_2)$ at sensor 3 and 10% at sensor 2. No unsteady signal is observed at sensor 1, situated slightly upstream of the geometric throat, where the blade Mach number reaches a maximum of M = 0.95.
Going further downstream towards the trailing edge, sensor 4, 5 and 6, the pressure fluctuations are more sinusoidal in nature and smaller in amplitude. The figure shows only sensor 5. Sieverding et al. [130] suggested that these fluctuations are likely to be caused by the downstream travelling wake vortices of the neighboring blade. The observation is confirmed by a close observation of the LES results.
The periodicity of pressure signal at position 7, located slightly upstream of the trailing edge, is rather poor and only a phase lock averaging procedure provides useful information on its periodic character. The reason is most

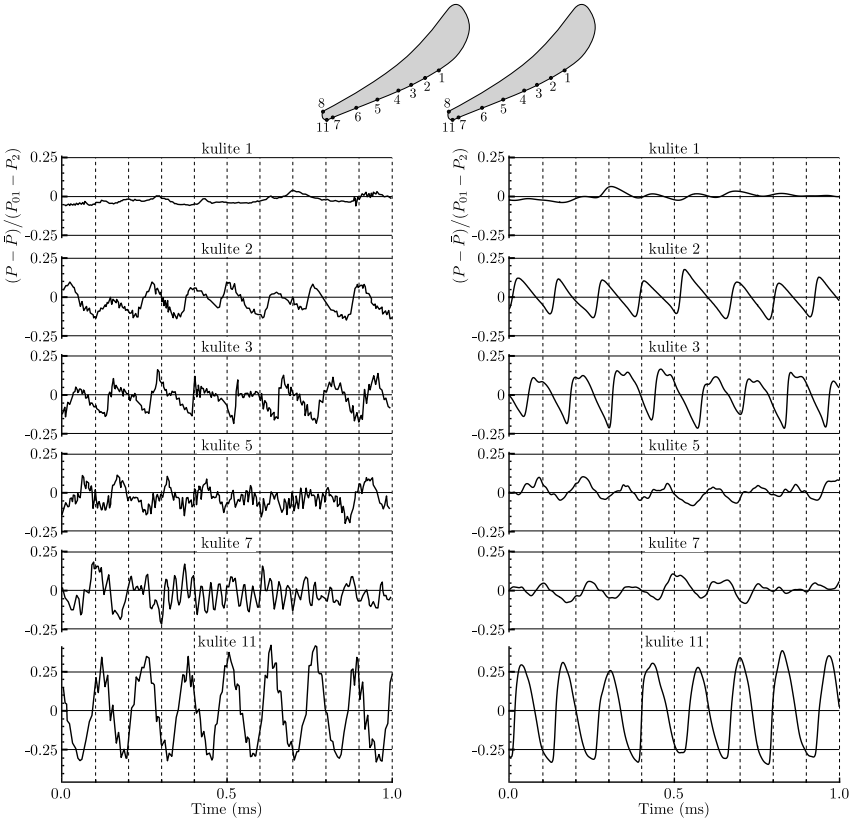

Figure 7.11.: Blade suction side unsteady pressure fluctuations: experimental-left [130]; numerical-right.

likely the result of a superposition of waves induced by the wake oscillations of the neighboring blade on one side and upstream travelling waves induced by the flapping of the suction side shear layer on the other side. Right at the trailing edge, position 11, we have as expected a strong periodic signal with good agreement between the numerical and the experimental results. In general, the only remarkable difference between numerical and experimental signals is observed for the higher frequency oscillations which are not reproduced by CFD. These could be due either to broadband noise in measurements or to the small turbulent structures close to the wall, characterized by a very low energy content. In the second case a DNS approach and a much finer grid (X+ and Z+ lower than 11 [135]) would be necessary to reproduce in detail the small vortices near to the wall, leading to a substantial increase of computational cost.

Results for the Transonic Outlet Flow Conditions

The validation of the numerical method for the test case at $M_{2,is}$=0.79 gave satisfactory results both in terms of time averaged and unsteady results. To characterize the sudden change from a non-uniform to a constant trailing edge base pressure distribution (see Fig. 7.2) two additional simulations are performed at $M_{2,is}$=0.97 and $M_{2,is}$=1.05. The computations are performed on the same grid used for the validation. For these cases, the average and maximum Y+ remain respectively lower than 0.45 and 0.9, while the Courant number increases to 1.3 for the worst case.

The TE base pressure distribution is shown in Fig. 7.12. Similar to the case

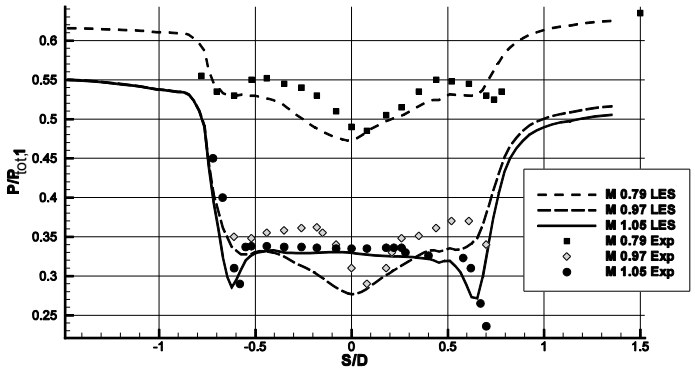

Figure 7.12.: Comparison of trailing edge base pressure variation at transonic outlet conditions.

at $M_{2,is}$=0.79, the LES at $M_{2,is}$= 0.97 agrees very well with experimental data on the right side of the trailing edge center, while the agreement is a bit less satisfactory on the pressure side between S/D = 0 and 0.5. The maximum discrepancy is anyway limited to 5% of $P_{tot,1}$. The sudden change from the non-symmetric base pressure distribution at $M_{2,is}$= 0.97 to an isobaric base pressure at $M_{2,is}$= 1.05 is well predicted. In this last condition, the agreement between experimental and numerical data is perfect. This applies also to the prediction of the over expansion of the flow before separation causing a shock, referred to in the literature also as lip shock.

Four snapshots of the vortex shedding for $M_{2,is}$=0.97 and 1.05 are shown in Fig. 7.13 in terms of density gradient and vorticity. The pictures are representative of a full period of a vortex shedding cycle. For $M_{2,is}$=0.97 (Fig. 7.13-a), in image 1 the pressure side shear layer is in its most inwards position implying that the local velocity before separation is at its maximum. The outwards motion of the pressure side shear layer in images 2 and 3 generates a pressure wave P_i. Since the local flow field is supersonic the wave P_i cannot move upstream. This is instead strongly curved

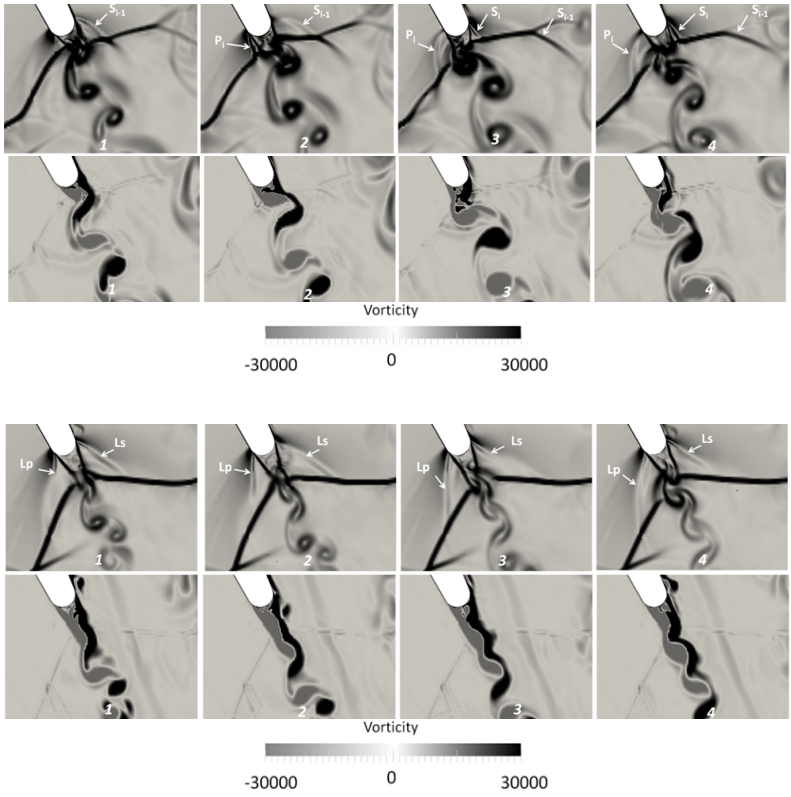

Figure 7.13.: Wake density gradients and vorticity for $M_{2,is}$=0.97 (a) and $M_{2,is}$=1.05 (b).

in streamwise direction and interacts with the right-running pressure side trailing edge shock. The interaction of P_i with this shock is particularly clear in image 3 and 4.
On the suction side the shear layer is in its maximum inwards position in image 3. In the present case, the pressure wave P_i crosses the trailing edge shock in images 1 and 2 and causes also a change of the shock angle. It is worth noting that the interaction of the suction side wave with the trailing edge shock appears more intense than for the pressure side wave. As regards the position of the trailing edge shocks, they move forwards and backwards in phase with the generation and shedding of the trailing edge vortices.
In terms of vorticity, in figure 1 the negative vorticity of the pressure side shear layer covers nearly the entire trailing edge region and starts to entrain the shear layer of the suction side with opposite vorticity. The entrainment effect increases in images 2 and 3. In image 3 the positive vorticity of the suction side shear layer becomes predominant, cutting off the supply of the pressure side vorticity. The shedding of the pressure side vortex is then

completed in image 4.

Figure 7.14 shows the fluctuations observed by probes installed along the

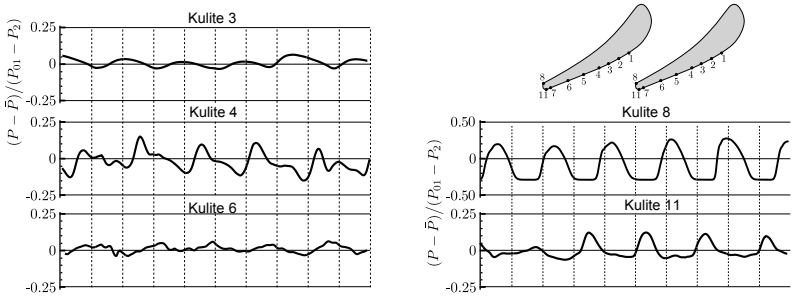

Figure 7.14.: Unsteady pressure fluctuations for $M_{2,is}$=0.97.

rear suction side. For the present condition, the upstream propagation of the pressure wave is avoided by the presence of the supersonic area at the trailing edge. Because of that, probe 2 does not detect any unsteadiness.
The right-running pressure side trailing edge shock coming from the closest blade impacts on the suction side of the current blade, between probes 2 and 3. The periodic fluctuations visualized by probes 3 and 4 are due to the oscillations of the trailing edge shock of the closest blade interacting with the vortex shedding. Further downstream, the unsteadiness of probe 6 is mainly due to the high turbulence level generated by the interaction of the trailing edge shock of the closest blade and the suction side boundary layer. The situation changes at the beginning of the trailing edge circle, where the influence of the vortex shedding is depicted by the high amplitude fluctuations of the signal for probes 8 and 11. The regular passage from a sinusoidal to a flat signal (particularly visible for probe 8) is linked to the oscillation of the trailing edge shock, which brings regularly the probes from a subsonic to a supersonic region.
Passing from $M_{2,is}$=0.97 to $M_{2,is}$=1.05 (Fig. 7.13-b) the normal trailing edge shocks have developed into an oblique shock system, which originates from the zone of confluence of the pressure and suction side shear layers. Both shlieren and vorticity pictures show that the roll-up of the shear layers into vortices is delayed to the region of their confluence, leaving an isobaric region close to the blade trailing edge, as shown in Fig. 7.12. It is interesting to observe that, due to the overexpansion around the trailing edge, the shear layers do not separate tangentially from the trailing edge surface but at a small angle. This leads to the generation of weak separation shocks known as lip shocks interacting with the trailing edge shocks as indicated on the pictures.

The fluctuations observed by some of the probes are shown in Fig. 7.15. With respect to $M_{2,is}$= 0.97, the interaction between the trailing edge shock of the closest blade and the current blade suction side moves further down-

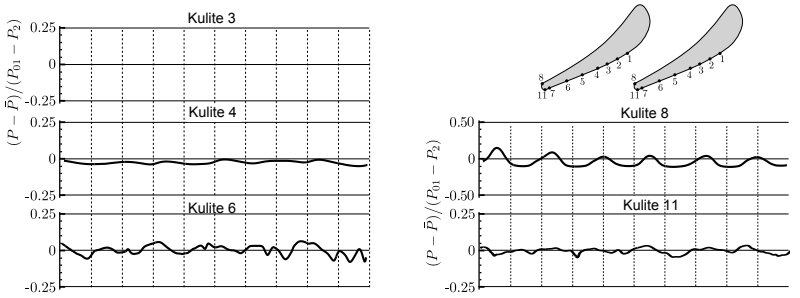

Figure 7.15.: Unsteady pressure fluctuations for $M_{2,is}$=1.05.

stream, as depicted by the fact that probe 3 does not detect any fluctuation. The limited amplitude of fluctuations observed for probes 8 and 11 indicates that the waves P_i and S_i have little effect on the unsteady pressure field at the trailing edge.
Figure 7.16 shows the peak to peak amplitude of the phase lock averaged pressure signal for all Mach numbers investigated. It is interesting to note that the most intense pressure fluctuations are obtained for the case at $M_{2,is}$= 0.79. On the other hand, the signal remains almost steady for $M_{2,is}$= 1.05, confirming that the vortex shedding has a limited influence on the trailing edge base pressure in this operating condition.
It is expected that the trailing edge shocks will further stabilize with a further increase of the downstream Mach number.

The comparison between the numerical and the experimental Strouhal

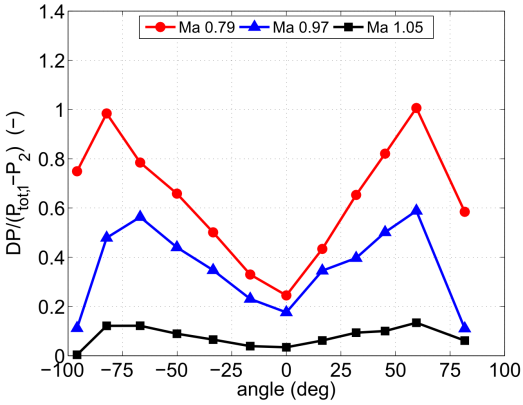

Figure 7.16.: Angular distribution along the trailing edge of the phase-lock averaged amplitude of pressure fluctuations for all cases investigated.

number characterizing the vortex shedding (calculated with respect to the

outlet velocity and trailing edge diameter) is shown in Fig. 7.17. As shown by [136], the Strouhal number is influenced by the shape factor of the pressure and suction side boundary layers. The decrease of the Strouhal number in the Mach range $M_{2,is}$=0.4 to 0.7 indicates that the transition is not yet fully completed. The value of S=0.22 between $M_{2,is}$= 0.7 to 0.9 is in line with data from other turbine blades with fully developed turbulent boundary layers [136, 137]) and is close to that for flows across cylinders. The increase of the Strouhal number to higher Mach numbers is related to the fact that in the transonic regime it is not the physical thickness of the trailing edge which determines the vortex shedding frequency but rather the distance between the separating shear boundary layers. As observed, the distance decreases for supersonic trailing edge flows due to the strong Prandtl-Meyer expansion from both the pressure and suction sides around the trailing edge.

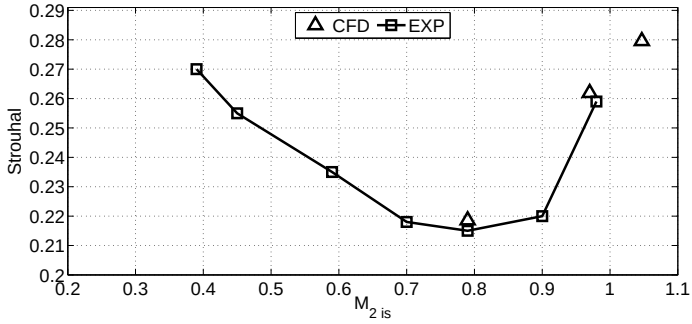

Figure 7.17.: Strouhal number for different outlet conditions obtained with CFD and experiments.

7.6. Final remarks

The trailing edge pressure distribution is strongly dependant on the outlet Mach number. When passing from subsonic to transonic Mach numbers, it varies from an isobaric to an increasingly non-uniform distribution, because of the increasing proximity of the vortex formation at the trailing edge. It suddenly returns back to an isobaric base region once an oblique shock develops at the confluence of the pressure and suction side shear layers, shifting the roll-up of the vortices to this zone of confluence.

For all the aforementioned conditions, LES seems to be the most appropriate approach to reproduce the unsteady flow field. A satisfactory matching between CFD and experiments is in fact observed both in terms of averaged and fluctuating quantities. The tool is also able to reproduce the unsteady

pressure waves moving along the rear suction side, caused by the oscillation of the separating shear layers at the trailing edge.
The requirement of a containment of the grid size, which is important for the application to 3D HPT profiles, leads to a poor reproduction of the suction side boundary layer. From the analysis performed, it is observed that results obtained using Δx^+ and Δz^+=50-100 together with $\Delta y^+ < 1$ are sufficiently accurate to reproduce correctly both the pressure distribution along the blade and the unsteady flow field.
As a main outcome of the study, we can conclude that the OpenFOAM solver TUMDF is mature enough to reproduce the aerodynamic flow field of a high pressure turbine, both in terms of time averaged and fluctuating quantities. Nevertheless, before applying the LES tool to the investigation of the combustor-turbine interaction, further steps are needed to complete its development:

- **Implementation and testing of an advanced syntetic turbulence generator at the inlet**. The simulation of combustor and turbine in an integrated framework requires a relevant effort in terms of computational power, which cannot be typically afforted on classical scientific clusters. In this sense, an advanced turbulence generator permits to analyze the HS propagation in turbine by imposing the flow field coming from the combustor as inlet condition of a domain modeling only the HPT (including a realistic turbulence level).

- **Assessment of the computational effort required for 3D LES in HPT**. The analysis of 3D profiles operating at high Reynolds number can become unaffortable for classical scientific clusters [21]. In this sense, a numerical campaign is needed to point out the actual limitations and possibilities of the machines avaliable at VKI.
  The investigation of less expensive Detached Eddy Simulation (DES) approaches is also suggested to further limit the grid requirements at wall.

Chapter 8.

Assessment of RANS against LES for the Hot Streak Propagation in Turbine

Cha et al. [54] and Koupper [75] demonstrated that LES can give a coherent prediction of the HS formation and propagation in HPTs operating at realistic conditions. On the other hand, preliminary results obtained using RANS models [54] depicted a non-physical formation of TKE within the NGV passage, which affects the HS propagation.
Considering that the computational cost of LES for HPTs is prohibitive for being currently applied in industry, it is fundamental to better understand the behavior of less computationally-expensive RANS models operating with realistic inlet conditions.
In this chapter, the accuracy of LES is exploited to validate less time-consuming RANS models to study the combustor-turbine interaction. In this sense, LES results are used as a reference to discriminate the different RANS simulations in terms of turbulence modeling and aero-thermal predictions.
As observed in chapter 7, the two LES tools analyzed in this work are not mature enough to be applied to the complex problem of the combustor-turbine inteaction. The current study is therefore based on the comparison of RANS with the LES performed by Koupper in the framework of the european project FACTOR [75]. The test-case is described in detail in section 2.1 and its main features are recalled in section 8.1.
The comparison between LES and RANS results discussed in section 8.4 clearly indicate that an accurate modeling of the turbulence development within the HPT stage plays a major role for a correct reproduction of the hot streak migration. In particular, the choice of the turbulence model and the imposition of the inlet turbulent conditions have a considerable effect in predicting the temperature distribution both for the stator and the rotor blades.
In section 8.6, the RANS methods previously validated are employed to discuss in detail the effect of the relative position between hot streak and NGV on the aero-thermal performance of the whole HPT stage. Different clocking configurations have opposite effects in terms of improvement of aerodynamic performance and Heat Transfer containment, which oblige to individuate a trade-off solution during the design of HPT stages.
To conclude, section 8.7 presents a detailed study of the wall temperature

distribution on the rotor by a coupled CFD-FEM approach. This last analysis is performed to support the future experimental campaign which is planned in 2016 for the FACTOR configuration.

8.1. The Combustor-Turbine Configuration

The set-up of the FACTOR test case is schematically shown in Fig. 8.1 together with the planes which are used as reference. A full annulus non-reactive combustor simulator is coupled with a 1.5 HPT stage (only the first NGV and the rotor are considered in this work). A non-reactive chamber simulates a LBC by mixing hot flow (injected by swirlers) and cold air (injected by effusion plates along the endwalls). The ratio between hot and cold massflow is such that $T_{tot,P40}$=450K for the reference design condition.

Downstream from the mixing chamber, a high pressure turbine stage is

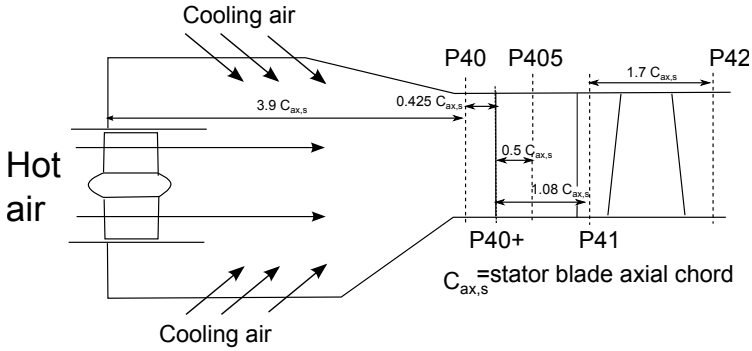

Figure 8.1.: Sketch of the test rig designed within the European project FACTOR. Dimensions are referred to the axial chord of the NGV.

installed. Furthemore, cold air is injected between the static and rotating discs at the hub (purge flow).

On the whole annulus, the swirlers are 20, while the HPT counts 40 blades for the NGV and 60 blades for the rotor. The ratio is particularly favorable for CFD, since the whole periodic test case can be represented including one swirler, two NGV and three rotor blades only.

The test rig is designed in such a way that different clocking positions can be analyzed by modifying the alignment between NGV and swirlers. The two extreme configurations are considered in this work.

- Swirler aligned with the passage center (indicated as **clocking PA** condition).

- Swirler aligned with the leading edge of a stator blade (indicated as **clocking LE** condition).

For all possible clocking conditions, temperature maps of the NGV and the rotor will be obtained during the experiments by means of thermal liquid crystal and thermal cameras. Three rotor blades out of 60 will be recovered by a thick layer of Torolon, which is a highly resistant isolating plastic commonly used to simulate adiabatic conditions. In this way, the rotor adiabatic wall temperature can also be visualized.
The complete mixing chamber - HPT full annulus test rig will be built at DLR in 2016. Despite this, simpler configurations including sectors of the combustor simulator are already operational at the University of Florence.
Fig. 8.1 shows also the nomenclature used to identify the different characteristic planes. The combustor simulator outlet is defined as plane 40 (P40) and located 17mm upstream from the stator LE. The rotor inlet defined as plane 41 (P41) and is located halfaway between the rotor leading edge and the trailing edge of the vanes. The rotor outlet is defined as P42, and located 68mm downstream P41. On top of that, the intermediate plane P405 is defined within the NGV passage.

8.2. LES set-up

An extended LES campaign was performed on the FACTOR test rig by Koupper et al. [75], reproducing a single sector of the combustor simulator with periodic boundary conditions in azimuthal direction. Results were compared to experiments performed at the University of Florence [35] on the reduced tri-sector rig without including the HPT stage.
For all quantities in study, the author evidences that results obtained by LES are close to the experimental data; in particular, LES demonstrated to be able to discriminate the presence of a pronounced hot streak and swirling flow at the passage center. Moreover, it is interesting to observe that the turbulence field is well predicted both in terms of surface-averaged value (about 25%) and non-dimensional 2D distribution [75].

According to the encouraging results, two more LES are performed by Koupper et al. [27], modeling the combustor simulator and the NGVs. Two different clocking positions are reproduced by a different alignment of the two vanes modeled with respect to the swirler, Fig. 8.2:

- **Clocking PA case:** the swirler is aligned with the passage center.
- **Clocking LE case:** the swirler is aligned with one of the two NGVs (NGV1).

The grid used for LES is similar for the two different clocking positions. Following the results obtained on the combustor simulator, the cell size is

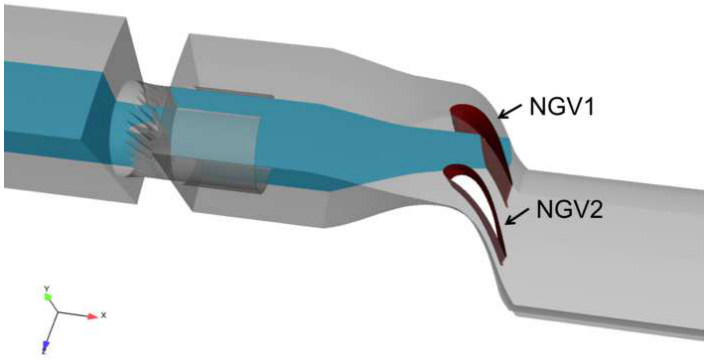

(a) Clocking PA

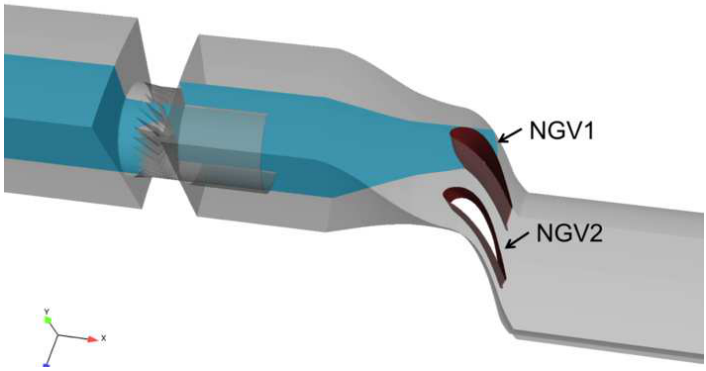

(b) Clocking LE

Figure 8.2.: Configurations reproduced by LES: clocking PA (a) and clocking LE (b).

kept to ∼0.5mm in the swirler, while it reaches ∼0.8mm in the combustor core.
For both cases in which the NGVs are included, 71M cells are used to discretize the domain. The grid size close to the wall is $Y+ <30$ everywhere, with $Y+ <15$ for most of the surface. The boundary layer shape is reproduced by wall models. The grid is not particularly refined into the wake of the NGVs, since one is not interested in the flow downstream of the vanes (the rotor is not modeled by LES). More details about the LES numerical set-up can be found in [27].
The compressible NS equations are solved by AVBP [76]. The TTG4A numerical scheme is employed, leading to fourth order accuracy in time and third order in space. The Smagorinsky model is used for the subgrid scale

structures.

8.3. RANS set-up

To assess the capability of RANS to predict the hot streak migration in turbine, the full HPT stage is modeled. The RANS inlet is placed exactly on P40, while the outlet is at 0.65 $C_{ax,r}$ downstream from the rotor TE (where the subscript r refers to the rotor blade).
To model the different alignment between vanes and combustor, the inlet boundary conditions are obtained by interpolating T_{tot}, p_{tot}, TKE and velocity direction from the LES solution on P40, for the two clocking configurations. At the rotor outlet, the nominal static pressure is imposed by including the radial equilibrium. Details of the RANS domain are listed in Table 8.1 together with the massflow averaged boundary conditions imposed. It is important to point out that the operating point analyzed does not correspont exactly to the experimental design conditions: it was in fact decided to use exactly the same massflow averaged values obtained by LES, to get a more coherent comparison between the two approaches. Moreover, the purge flow between stator and rotor is not modeled.
The RANS equations are solved by using the commercial solver FINE/Turbo

Plane 40	
Massflow rate (per sector)	0.24kg/s
T_{tot}	457K
p_{tot}	142000 Pa
TU	25%
NGVs	
$C_{ax,s}$	40mm
Re_{out} (on $C_{ax,s}$)	432000
$M_{is,out}$	1.05
ROTOR	
$C_{ax,r}$	32mm
Re_{out} (on $C_{ax,r}$)	275000
$M_{is,out}$	0.93
RPM	8500
Plane 42	
p	47562 Pa

Table 8.1.: Details of the boundary conditions and dimensions of the blades.

from NUMECA. The solver is based on a cell centered control volume approach. A 4-steps multistage explicit Runge-Kutta scheme is employed for

the steady time marching. For space discretization, a second order central scheme is used, based on a Jameson type dissipation approach with second and fourth order derivatives of the conservative variables. Acceleration techniques such as multigrid and local time stepping are employed to improve the convergence. The interface between rotor and stator is treated by a mixing plane approach based on the exchange of mass, momentum and energy fluxes [100].

Figure 8.3 shows a meridional view of the grid in use. Two NGVs and

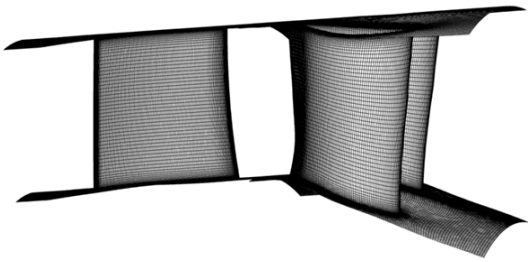

Figure 8.3.: Detail of the mesh used for the RANS analysis.

one rotor blade are included into the domain and reproduced by 5.9M cells. The mesh is a structured multiblock grid, and is obtained by a detailed grid convergence analysis. The maximum Y+ on the blades is 0.5, permitting a direct resolution of the boundary layer.

8.4. RANS for Realistic Flows in Turbine

For RANS simulations employing two equations models, it is required to impose at the domain inlet a Dirichlet condition for k and for the second turbulent variable, which defines the turbulent decay. When a LES solution of the combustion chamber is available, k can be directly mapped at the turbine inlet from the LES solution itself. The definition of the second variable is instead less straightforward.

In this work, it is proposed to use LES to tune the turbulent inlet conditions for RANS until the same k-decay is obtained upstream the NGV leading edge. At this scope, a sensitivity analysis on the second turbulent variable is carried out for the clocking PA configuration. To generalize the discussion to all possible 2-equations models, the second turbulent variable is characterized in terms of μ_T/μ, defined as:

$$\frac{\mu_T}{\mu} = \frac{\rho k}{\mu \omega} = C_\mu \frac{\rho k^2}{\mu \epsilon} \tag{8.1}$$

Where C_μ=0.09 is a constant.

8.4.1. Effect of the inlet turbulence decay

Four simulations are performed, employing the $k-\omega$ SST turbulence model [73, 138] and imposing different values for μ_T/μ at the inlet. The simulations are identified as cases 1 to 4 in Table 8.2.

Figure 8.4 shows the turbulence decay obtained for different μ_T/μ between

Case Name	Turbulence model	μ_T/μ
Case 1	$k-\omega$ SST	2000
Case 2	$k-\omega$ SST	1513
Case 3	$k-\omega$ SST	175
Case 4	$k-\omega$ SST	17
Case 5	$k-\epsilon$	1513
Case 6	$k-\omega$ Wilcox	1513

Table 8.2.: Cases run for the sensitivity analysis to μ_T/μ and to the turbulence model.

P40 and a plane placed 0.18 NGV axial chords downstream from the blade leading edge, identified as Z=0. For all cases, TKE is massflow averaged on surfaces perpendicular to the machine axis and non-dimensionalyzed by the inlet value. From the results, it can be observed that $\mu_T/\mu \sim 1500$ must be imposed to reproduce the LES results upstream the passage.

It is important to point out that numerical simulations on classical test cases to validate CFD for in turbines [139], which are characterized by relatively limited inlet turbulence levels, it is typically suggested to impose μ_T/μ ranging between 1 and 100. The application of similarμ_T/μ for a realistic combustor-turbine configuration leads on the other hand to an immediate non physical decay of the turbulent level downstream from the inlet. For the current case, TU drops from 25% measured on P40 to 1% for μ_T/μ=17 and to 5% for μ_T/μ=175 at the LE inlet.

Moreover, it shall be observed that some of the main CFD tools commonly employed in industry [100, 140] consider a threshold to $\mu_T/\mu = 3000-5000$ within the domain as default option to enhance the stability of the simulation. Considering the high μ_T/μ imposed at the inlet, such a threshold is too low for realistic flows in HPTs. For the present analysis, the aforementioned option is deactivated to let the turbulence free to develop within the passage.

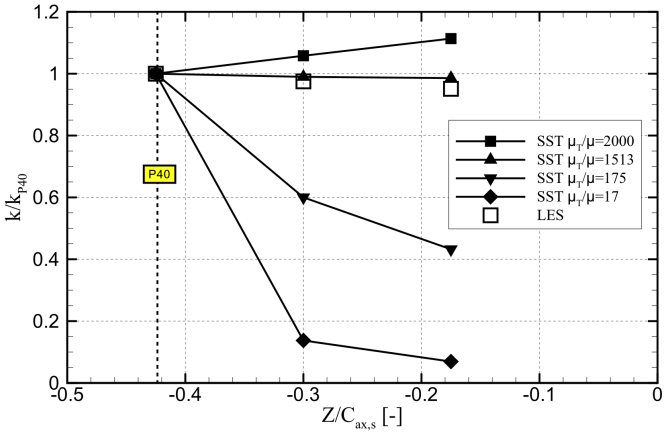

Figure 8.4.: TKE decay measured between the domain inlet and one plane placed 0.2 $C_{ax,s}$ downstream from P40. RANS results are obtained employing the SST model with different μ_T/μ at the inlet.

Validation of the passage of turbulence for LES-URANS coupled simulations

It is interesting to open a short parenthesis on the LES-URANS coupled simulations of combustor and turbine, discussed in chapter 3. In particular, in section 3.3 it is proposed to use Eq. 3.34 to calculate the turbulence decay at the RANS inlet from the LES solution.
To demonstrate that Eq. 3.34 can be effectively used at the combustor-turbine interface, the equation is used in this section to compute the corresponding value of ω which would be expected on P40 for the FACTOR test case.
In this sense, the massflow averaged TKE is computed from the LES solution on P40 and on another plane at ΔZ=10mm downstream from P40, and it is used into Eq. 3.34. According this procedure, $\omega = 9990s^{-1}$ is obtained, which corresponds to imposing $\mu_T/\mu = 1610$ at the RANS inlet. This value is very close to te one used for case 4, which gives a very satisfactory approximation of the LES decay upstream from the blade LE.
From this simple consideration, one can then conclude that the method proposed to define the turbulence decay for the LES-URANS coupling gives good results for realistic combustor-turbine configurations.

8.5. Effect of the Turbulence Model

The next step of the analysis is to evaluate the capability of the most common two equations turbulence models to face realistic inlet conditions. At this scope, the $k-\omega$ SST, $k-\omega$ Wilcox and the $k-\epsilon$ model are tested (cases 2, 5 and 6 in Table 8.2) on the clocking PA configuration. For all cases, $\mu_T/\mu = 1513$ is imposed at the inlet to avoid immediate dissipation of turbulence.

Effect of the Turbulence Model on the TKE Evolution

Figure 8.5 shows the massflow averaged TKE for different axial position within the stator passage. Cases 1,3 and 4 are added to the graph for completeness.
When μ_T/μ is correctly set at the inlet, it can be observed that the $k-\epsilon$ and the $k-\omega$ SST models give results which are comparable to each other. The turbulence development observed within the passage agrees also well with LES, although one observes that RANS slight overestimates the turbulence level within the passage at $Z/C_{ax,s}$=0.5 from the NGV leading edge. In particular, the computations show that TKE doubles when passing from P40 to P41 .The turbulence level, calculated as:

$$TU = \frac{\sqrt{\frac{2}{3}TKE}}{U} \tag{8.2}$$

decreases from 25% at P40 to 6% at P41, because of the flow acceleration within the NGV.
On the other hand, the $k-\omega$ Wilcox dramatically overestimates the turbulence production at the NGV leading edge. In this case the turbulence level remains very high within the passage, arriving up to 5-6 times the value in P40 (out of scale in Fig. 8.5). This behavior is due to the high sensitivity of the model to the turbulence decay imposed as boundary condition: Menter [72] clearly showed that the Wilcox model applied to accelerating flow gives realistic results only for quasi-laminar inlet or with very high turbulence dissipation. One can then conclude that the $k-\omega$ Wilcox model is not suited to solve the flow field in HPTs when realistic inlet conditions are applied.
The turbulent kinetic energy evolution within the passage is visualized in more detail in Fig. 8.6.
The comparison between $k-\omega$ SST, $k-\epsilon$ and LES appears to be good. The TKE level remains high all along the passage center, and is further increased by the accelerating flow along the blade suction side. A completely different behavior is observed instead for the case with high turbulence decay (case 4). In this condition, the TKE profile imposed at P40 is immediately dissipated downstream, and the turbulence is developed only by the wake of the

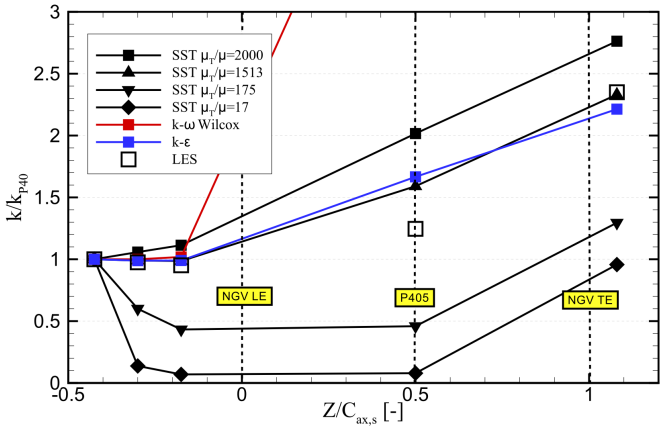

Figure 8.5.: Effect of the turbulence model on the TKE distribution within the NGV passage.

NGV. It is interesting to point out that this condition determines a much lower turbulence level also within the rotor passage, resulting about 1/3 of the one obtained for case 2.
As previously observed, the $k-\omega$ Wilcox model predicts instead a non-physical tremendous generation of turbulence at the blade LE, which compromises the TKE evolution within the passage.

Influence of the turbulence model on the HS propagation

To investigate how the turbulence modeling affects the prediction of the HS propagation, Fig. 8.7 shows the total temperature distribution obtained on P405 and P41 for RANS and LES.
From the results of case 4, one can observe that an overestimate of the turbulence decay at the NGV inlet leads to a substantial overestimate of the hot streak intensity on P405 and P41. This is due to the almost complete absence of turbulent mixing within the passage.
On the other hand, when the turbulence decay is set to a lower value (i.e. μ_T/μ is increased), the temperature distribution on P405 and P41 appears more uniform and the hot streak is less pronounced.

The agreement between RANS and LES is satisfactory for all turbulence models employed, provided that the inlet turbulence decay is correctly imposed. In general, the hot streak on P41 is more spread in azimuthal direction when predicted by RANS with respect to LES.
To conclude, it is interesting to observe that the $k-\omega$ Wilcox gives com-

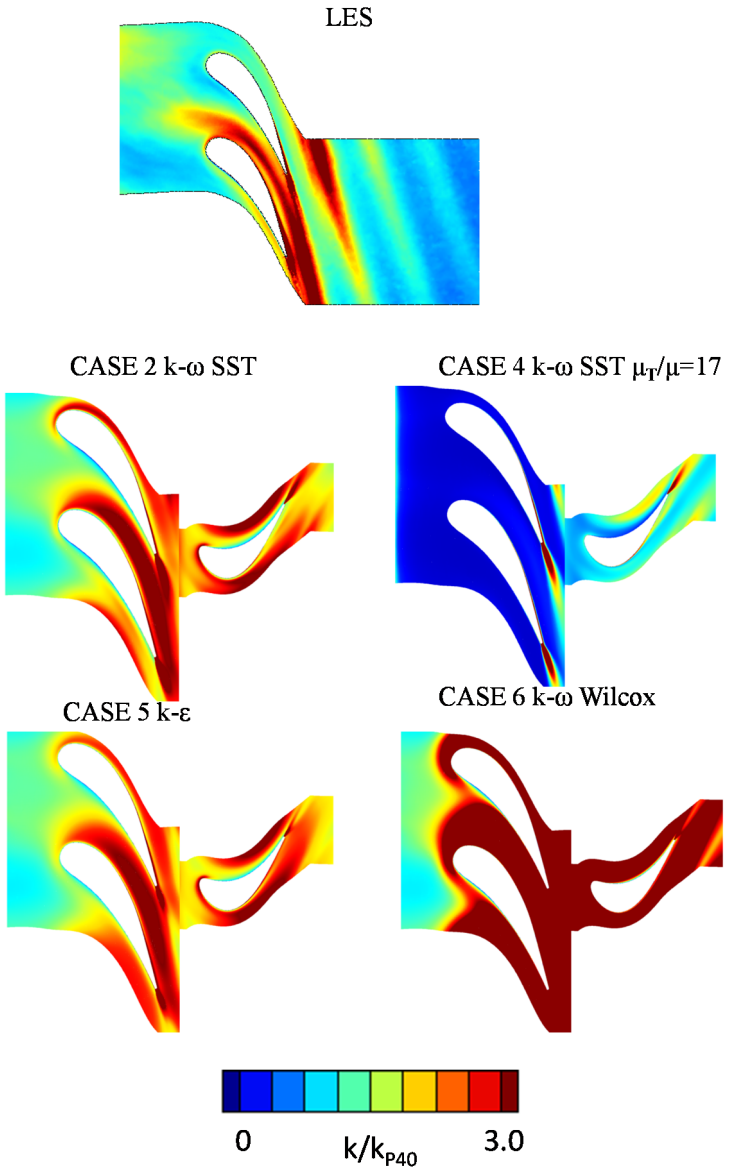

Figure 8.6.: Evolution of turbulent kinetic energy within the HPT stage-mid span evolution.

parable results to the other turbulence model in terms of total temperature distribution on P41, despite the poor reproduction of the turbulent field.

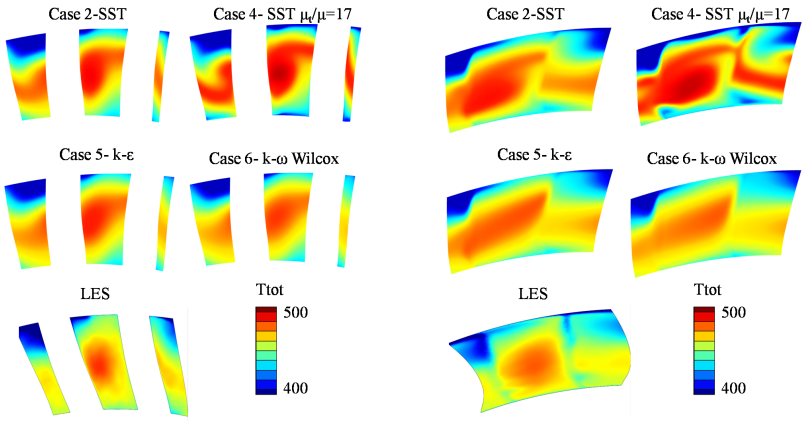

(a) P405 **(b)** P41

Figure 8.7.: Total temperature distribution on P405 and P41 for RANS and LES.

As it will be discussed later, the non-physical production of turbulence at the blade LE mainly affects the boundary layer development and the aerodynamic performance of the blade.
To quantify more precisely the effect of the turbulent mixing on the temperature field, the circumferentially averaged distributions of Φ on P40, P41 and P42 are shown in Fig. 8.8 for all cases in study. The absolute value of Φ was already defined in Eq. 5.4 and reported here for completeness.

$$\Phi = \frac{T_{tot} - T^{ref}_{tot,P40}}{T^{ref}_{tot,P40} - T_{tot,c}} \tag{8.3}$$

Where $T^{ref}_{tot,P40} = 450K$ and $T_{tot,c} = 300K$ for the current case.
Passing from P40 to P41, the temperature distribution tends to become more and more uniform for all cases except for case 4 ($\mu_T/\mu = 17$). For this last condition, the hot streak appears simply deformed between P40 and P41 without being attenuated. An overestimate of the radial temperature non-uniformity for low inlet turbulence can also be observed on P42.
On the other hand, a proper representation of the turbulence at the RANS inlet diminish the HS intensity at the NGV and rotor outlet, giving results which are closer to LES.
For all cases analyzed, one can conclude that the HS mixing taking place within the passage appears slightly underestimated by RANS with respect to LES: the difference between maximum and minimum values of T_{tot} on P41 is 153K for case 4 (k-ω SST with μ_T/μ=17), while reducing to 128K and 111K respectively for case 2 (k-ω SST with μ_T/μ=1513) and 5 (k-ϵ)

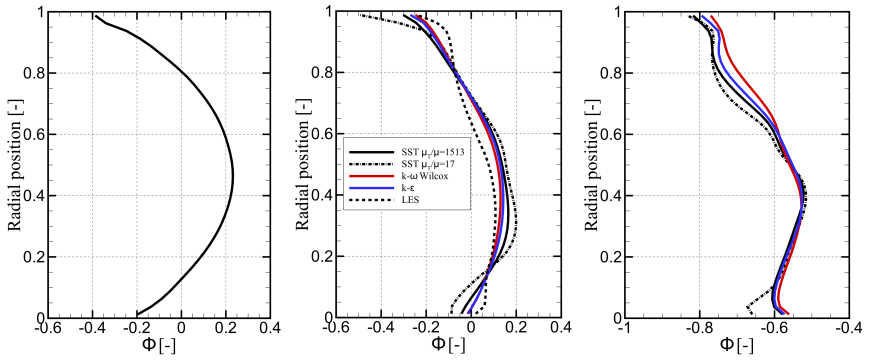

(a) P40 **(b)** P405 **(c)** P42

Figure 8.8.: Radial distributions of Φ evaluated for RANS and LES on P40, P41 and P42.

and to 94K for LES.

Behavior of the SST model with high turbulence at the inlet

It is interesting to observe that the solutions obtained with the $k-\omega$ SST and $k-\epsilon$ model for cases 2 and 5 are very close to each other in terms of k distribution, Fig. 8.5. This was expected, since the turbulence equations in the free stream are exactly the same for the two models [73]. On the other hand, when the k-ω SST is used, the mixing of the hot streak appears underestimated (Fig. 8.7).
This can be explained considering that μ_T/μ is defined differently for the two models. In particular, the classical relation between μ_T, TKE and ϵ/ω applies for the $k-\epsilon$ model, expressed by Eq. 8.1. For the $k-\omega$ SST, on the other hand, Menter [138] proposed the twofold expression in Eq.8.4:

$$\frac{\mu_T}{\mu} = \begin{cases} \dfrac{\rho TKE}{\mu\omega}, & \text{if } a_1\omega > SF_2 \text{ (a)} \\ \dfrac{\rho a_1 TKE}{\mu SF_2}, & \text{if } a_1\omega < SF_2 \text{ (b)} \end{cases} \tag{8.4}$$

Where S is the shear stress modulus and $a_1 = 0.31$ is a constant. Equation 8.4 permits to limit the production of TKE for adverse pressure gradient boundary layers in such a way that the Bradshaw's assumption is always valid for the turbulent shear stress. According to this assumption, the wall

shear stress is proportional to TKE:

$$\tau_w = \rho a_1 TKE \tag{8.5}$$

On the other hand, for classical two equations models, the wall shear stress is computed as [141]:

$$\tau_w = \rho a_1 TKE \sqrt{\frac{production}{dissipation}} \tag{8.6}$$

When the boundary layer is subject to adverse pressure gradient, the production term is normally much larger than the dissipation term ($S > a_1\omega$). In this case, Eq. 8.4-b is activated limiting the ratio between production and dissipation to 1 and respecting the Bradshaw's assumption.
For free shear layers, the Bradshaw's assumption does not necessarily hold, therefore the modification proposed by the SST model is limited by the authors to wall bounded flows by applying the blending function F_2, defined as [138]:

$$F_2 = tanh\left(max\left(2\frac{\sqrt{TKE}}{0.09\omega y}, \frac{500\nu}{y^2\omega}\right)\right) \tag{8.7}$$

The function F_2 is tuned to be 1 close to the wall while dropping to zero in the free flow.
The distribution of F_2 calculated for cases 2 and 4 is shown in Fig. 8.9. It can be observed that the imposition of a realistic decay at the inlet forces F_2 to remain equal to 1 also within the passage, and the definition expressed in Eq. 8.4-b remains active also in most part of the free shear layer, Fig. 8.9-b. When μ_T/μ at the inlet is closer to more classical academic values, on the other hand, F_2 drops to zero far from the wall, and the classical definition of μ_T/μ is activated in the free shear layer.
This behavior of F_2 for high TU limits the value of μ_T in the free shear layer for the SST model. Since the turbulent mixing is directly related to μ_T, this has a direct impact in the underestimation of the HS diffusion within the channel with respect to the other 2-equations models.

Influence of the turbulence model on the aerodynamics

In this section, the influence of the turbulence modeling on the blade aerodynamics is discussed.
According to the usual practice, it is expected that the influence of the turbulence on the blade load is rather limited [25], even though it is difficult to be quantified in more detail because of the lack of experimental set-ups operating at realistic TU levels.
Figure 8.10 shows the M_{is} distribution for NGV 1 at 50% of span for the

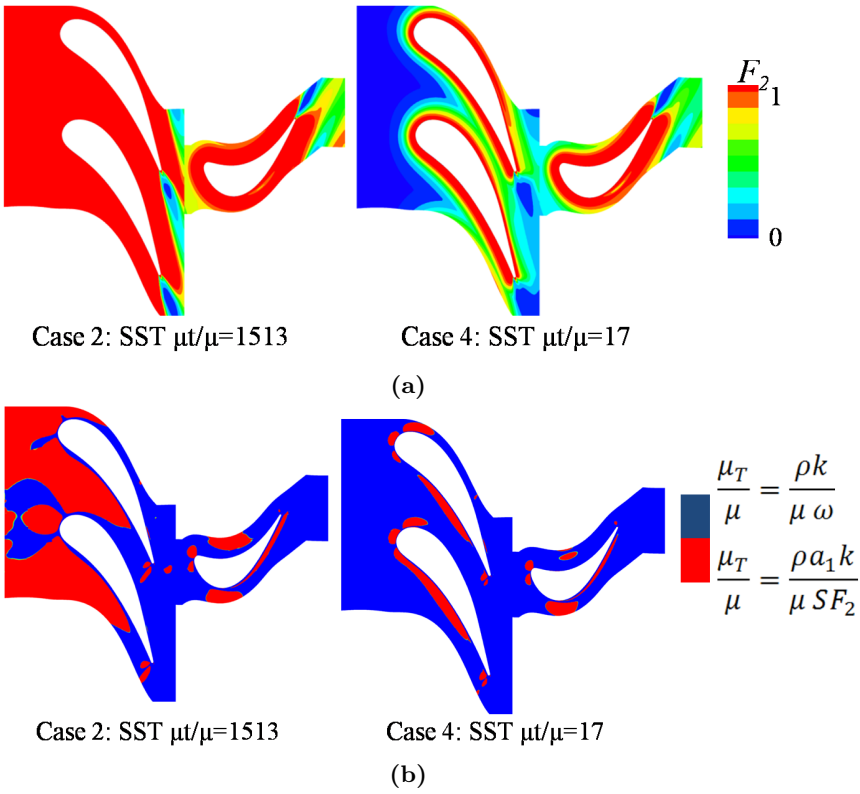

Figure 8.9.: F_2 distribution (a) and μ_T/μ definition (b) activated for the SST model within the channel for different turbulent decays imposed at the inlet.

different turbulence models employed. When the SST model is considered, no substantial differences are noticed in terms of blade load between the cases with high and low free-stream turbulence. On the other hand, the $k-\epsilon$ and the $k-\omega$ Wilcox models (for which the Bradshaw's assumption is not respected) dramatically over-predict the TKE production in the accelerating part of the leading edge. This affects the boundary layer development and the blade load in the first half of the airfoil, whose behavior appears non-physical for both cases.

The effect of the inlet turbulence on the effectiveness is quantified performing two more simulations with the k-ϵ and the k-ω Wilcox respectively, imposing high turbulent decay (μ_T/μ=17) at the inlet. The values obtained are listed in Tab. 8.3.

Passing from low to high turbulence intensity at the blade LE, the k-ω Wilcox and the k-ϵ models predict a dramatic drop in efficiency (2% and

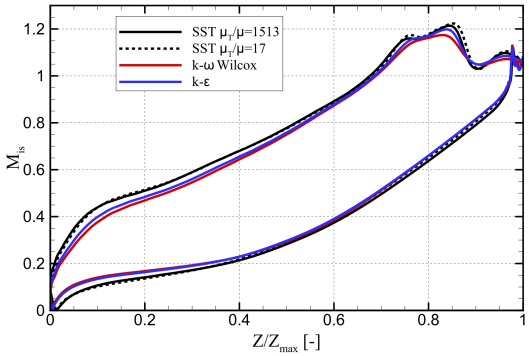

Figure 8.10.: M_{is} distribution at 50% of span for NGV 1 for different turbulence models.

3.8% respectively), while it is more limited when the SST is used (about 1%).

Model	η_{TT} High Turb. decay μ_T/μ=17	η_{TT} Realistic Turb. decay μ_T/μ=1513	Difference [%]
k-ω SST	91.17	90.14	1.03
k-ϵ	90.87	88.7	2.17
k-ω Wil.	90.96	87.13	3.83

Table 8.3.: Total to total effectiveness calculated with different turbulence models with low and high inlet turbulent decay.

8.6. The Combustion-Turbine Aerothermal Interaction

In the previous sections, the capability of RANS to reproduce the effect of realistic inlet conditions was discussed. From the analysis it clearly emerges that the reproduction of realistic flows in turbine is critical for all 2-equation models tested.
In what follows, the experience acquired is used to set-up a detailed RANS study of the combustor-turbine interaction, including swirl, non-uniform temperature field and high turbulence level at the HPT inlet. At this scope, the two clocking position previously introduced (clocking PA and LE) are

analyzed and compared.
According to the previous discussion, it was decided to use the SST model with $\mu_T/\mu = 1513$ at the inlet to simulate the HS evolution within the passage. Despite the uncertainty given by the high F_2 within the passage, which affect the μ_T definition for the free shear flow, the SST is the only model among the ones investigated which is able to reproduce the aerodynamic effect of turbulence on the blade load in a more realistic way with respect to the other models investigated.

8.6.1. Migration of the Hot Streak within the passage

The HS migration within the passage can be analyzed by plotting the total temperature field at different axial positions, Fig. 8.11. For the clocking PA configuration, the HS is attracted towards the suction side of NGV 2. The interaction between HS and residual swirl at the inlet leads to the migration of the hot flow towards the hub.
For the clocking LE case, on the other hand, the HS directly impacts the LE of NGV 2 and wraps around the blade, remaining in contact with the surface. The HS appears more evident close to the PS of the blade and migrates towards the outer endwall.
As a consequence, for both clocking configurations the HS can still be identified on P41, but its position along the surface changes; for the clocking LE, the HS remains segregated at the pressure side-shroud corner of NGV 1. On the other hand, it is more spread and closer to the SS-hub corner for clocking PA.
The migration of the cooling coming from the combustor is mainly affected by the secondary flow developed within the passage. A cold spot, indicated as CS in Fig. 8.11, can be identified on P40. For the clocking LE case, it impacts NGV 2 and is accumulated along its SS. Closer to the TE, it slightly migrates towards the passage center. For the clocking PA configuration, the CS enters into the channel and is further spread towards the SS of the adjacent blade.

8.6.2. Adiabatic Wall Temperature Evolution

Since the HS development within the passage is completely different for the two clocking, it is expected that $T_{ad,w}$ along the blades will change accordingly.
Fig. 8.12 and Fig. 8.13 show respectively the $T_{ad,w}$ distribution for clocking PA and clocking LE. RANS results are also compared with LES.
In general, the surface-averaged temperature predicted by LES will be influenced by the wall modeled approach, which affects the shape of the thermal boundary layer with respect to the wall-resolved RANS. To limit this effect,

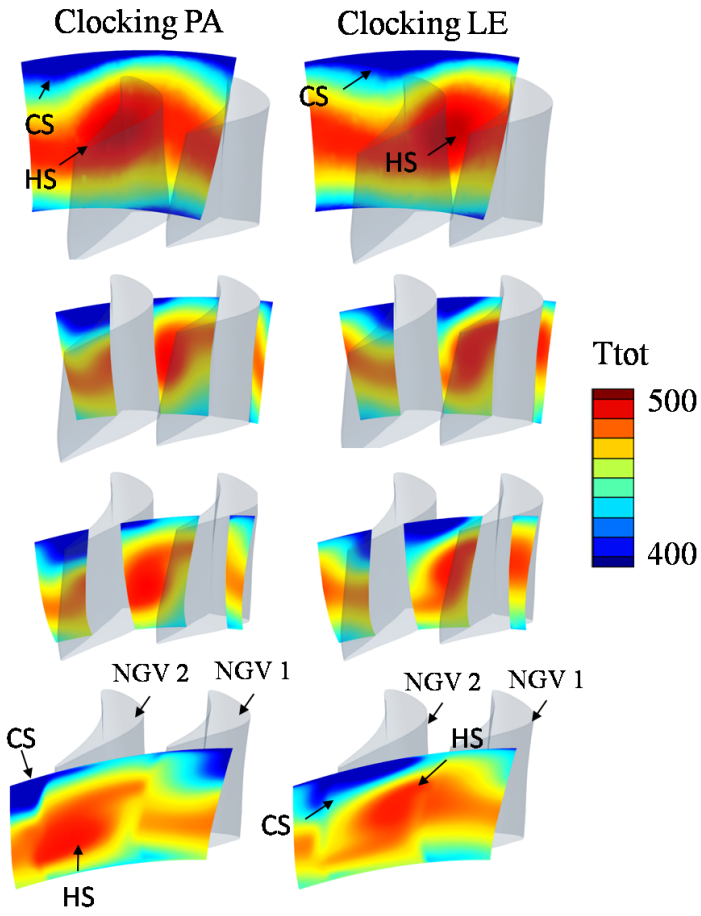

Figure 8.11.: T_{tot} distribution within the passage and visualization of the HS and CS propagation.

the RANS and LES temperature distributions are scaled with respect to the mean surface-averaged temperature computed for all blades, defined as:

$$T_{ave} = \frac{T_{NGV1}^{clockPA} + T_{NGV1}^{clockLE} + T_{NGV2}^{clockPA} + T_{NGV2}^{clockLE}}{4} \tag{8.8}$$

As expected, the worst thermal condition is obtained for NGV 1 in clocking LE configuration, Fig. 8.13-a, for which the adiabatic blade temperature is estimated to be 2.5% higher than $T_{tot,P40}$. In particular, the PS is hotter than the SS, due to the HS migration within the channel. For the same configuration, the surface averaged $T_{ad,w}$ is 2.5% lower than $T_{tot,P40}$ for the NGV which does not interact with the HS.

On the other hand, for the clocking PA configuration the surface averaged

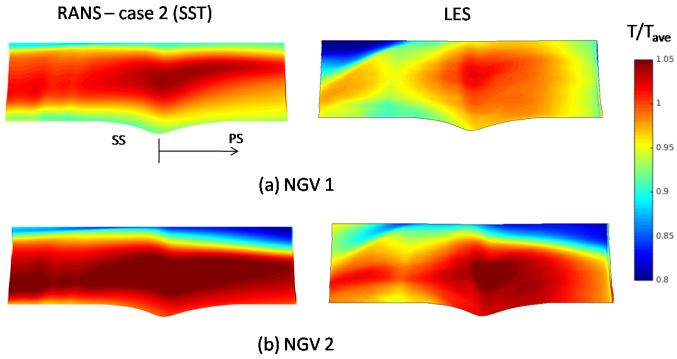

Figure 8.12.: Adiabatic wall temperature distribution on the vanes. Clocking PA case.

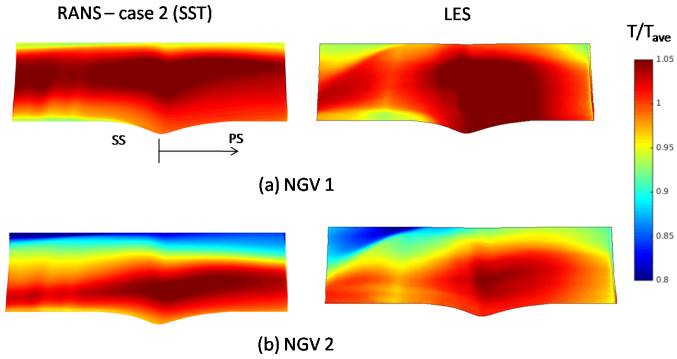

Figure 8.13.: Adiabatic wall temperature distribution on the vanes. Clocking LE case.

T_{tot} is similar to $T_{tot,P40}$ for both NGVs. The local temperature gradient however appears more pronounced for NGV 2 with respect to NGV1.
In general, the agreement between RANS and LES in terms of wall temperature distribution is satisfactory. The main discrepancy observed lies in the fact that LES reproduces a migration of the CS from the SS-tip corner towards the passage center, which is not observed by RANS. This is most probably due to the intense turbulent viscosity within the passage, which rapidly dissipates the secondary flows when RANS models are employed.

With the aim to assess how the turbulent decay applied at the inlet affects the wall temperature prediction, Fig. 8.14 shows the distribution of

$T_{ad,w}^{case2} - T_{ad,w}^{case4}$ along the blade, adimensionalized by $T_{tot,P40}$. It can be observed that the turbulent decay imposed at the inlet affects the local blade temperature up to 5% of $T_{tot,P40}$. In general, a complete dissipation of the turbulence leads to the formation of a higher local temperature peak accompanied by a more pronounced effect of the cooling.

Figure 8.15-a shows the adiabatic temperature distribution on the rotor.

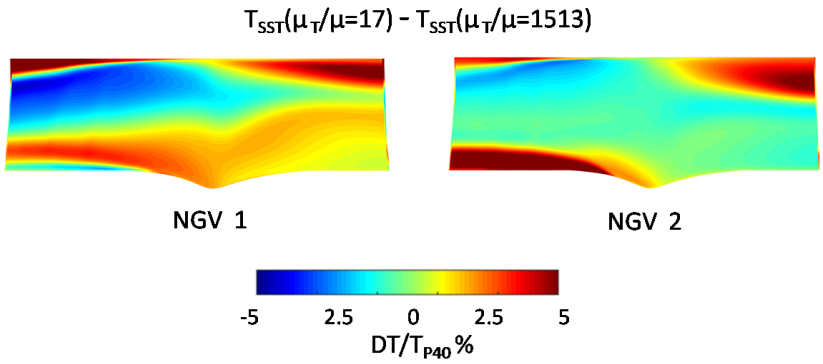

Figure 8.14.: Difference in temperature distribution on the NGV surfaces: the effect of μ_T/μ is investigated by plotting $T_{ad,w}^{case2} - T_{ad,w}^{case4}$ along the blade, adimensionalized by $T_{tot,P40}$.

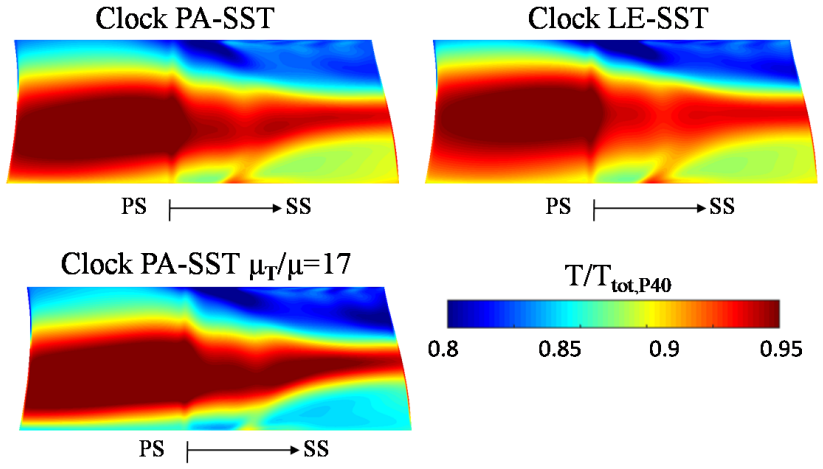

Figure 8.15.: Adiabatic temperature distribution on the rotor surface for the clocking PA and clocking LE cases. The SST model with μ_T/μ=1513 at the inlet is compared to the result with μ_T/μ=17 as well.

In this case, the adiabatic wall temperature distribution is clearly affected

by the segregation effect and the the secondary flows developed by the temperature gradient, which tend to spread the HS along the pressure side span (as discussed in detail in section 2.2).
From Fig. 8.15, it can be also noticed that the alignment between NGV and HS also affects the $T_{ad,w}$ distribution on the rotor. For the clocking LE configuration, the HS impacts the blade at an higher radius with respect to the clocking PA case. This is in line with the T_{tot} evolution within the NGV passage depicted in Fig. 8.11, which evidences a migration of the HS towards the shroud for clocking LE.
To conclude, an high turbulence decay imposed on P40 increases the temperature gradient on the rotor blade. This leads to local differences comprised between $1-2\%$ of $T_{tot,P40}$ with respect to the reference simulation.

8.6.3. Aerodynamic performance

To evaluate the impact of non-uniform conditions coming from the combustor on the aerodynamics of the profiles, a further simulation imposing uniform inlet boundary conditions is performed, using the mass-flow averaged values obtained by LES on P40 (p_{tot}, T_{tot}, k and velocity direction). In Fig. 8.16 the M_{is} distribution along the NGVs for the clocking PA configuration and for uniform inlet conditions are compared.
The incoming swirl leads to an increase of blade load at 30% of span. Close to the tip, on the other hand, a reduction of blade load can be observed. The effect of the swirl is particularly accentuated for NGV 2. This can be explained considering that the HS (and the swirl) for the clocking PA case is attracted towards the SS of NGV 2, Fig. 8.11.
The spanwise variation of the blade load with respect to uniform inlet con-

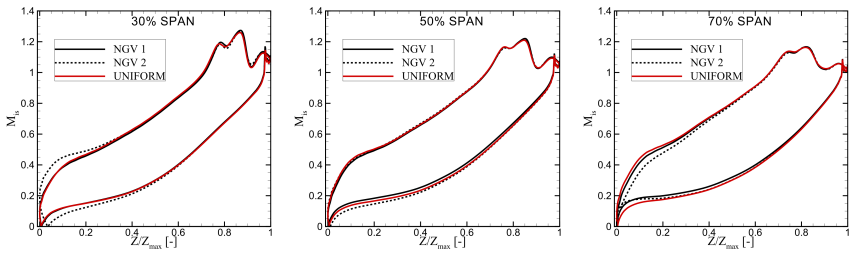

Figure 8.16.: Blade load distribution for the case with uniform inlet conditions and for the clocking PA configuration at 30%, 50% and 70% of span.

ditions is clearly due to an increase of flow incidence at 30% of span together with a decrease at 70% of span, coherently with the direction of the swirl on P40. No noticeable variation of the blade load is instead observed at 50%

of span.

The effect of the HS-NGV alignment is evidenced in Fig. 8.17, where the

Condition	1-η_{TT} [%]
Uniform	9.52%
Clocking PA	9.86%
Clocking LE	9.82%

Table 8.4.: Effect of the non-uniform flow on the aerodynamic losses.

M_{is} distribution is shown for the two NGVs at 30% and 70% of span. As expected, for the clocking LE configuration the effect of the swirl on the blade load is increased for the NGV aligned with the HS (NGV 1 in the current case).

The aerodynamic losses of the HPT stage are quantified in Table 8.4. When considering realistic inlet conditions, one can observe an increase of 0.3% of losses with respect to the case with uniform inlet. The relative position between swirler and NGVs has a lower effect on the losses, limited to a variation of about 0.05%. In general, the alignment of the combustor with one NGV has a positive effect on the performance.

8.7. Effect of the Solid on the Rotor Blade Temperature

To support the future experimental campaign for the FACTOR project, additional simulations of the HPT stage are performed. The aim of this study is to give detailed suggestions to correctly set-up the test rig, which will be experimentally analyzed in 2016.

In the framework of this thesis, only a detailed analysis of the temperature distribution on the rotor is presented. The investigation of the rotor temperature distortion can be critical for the thermal cameras if the wall temperature gradient is too weak. Considering this issue, it was decided to perform RANS with the $k-\omega$ Wilcox model, applying a conjugate heat transfer (CHT) approach to include the effect of the conduction of the solid into the analysis.

The choice of the $k-\omega$ Wilcox model could appear contradictory with respect to the previous discussion. Actually, the very high TKE developed at the NGV LE leads to overestimate the HS dissipation within the stage with respect to other RANS turbulence models, leading to more conservative results in terms of hot spot intensity on the rotor blade. Moreover, this compensates in part the trend of RANS to underestimate the HS diffusion with respect to LES, as shown in Fig. 8.8.

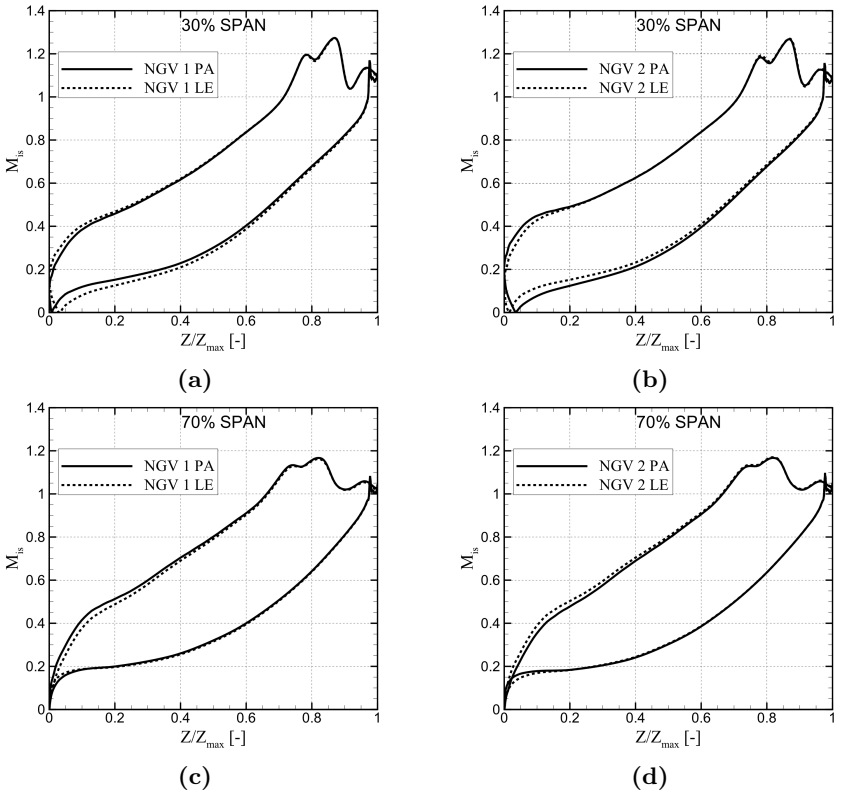

Figure 8.17.: Effect of the clocking on the aerodynamic load of the NGVs, 30% and 70% of span.

In what follows, the analysis is presented for the clocking PA configuration. With respect to the numerical set-up discussed up to now, two main modifications are pointed out:

- The inlet conditions match exactly the design point for the experimental set-up operating without cooling. In this sense, LES results are mapped at the domain inlet in terms of T_{tot}, $\dot{m}$ and TKE and scaled to get $T_{tot,P40} = 437K$ and $\dot{m} = 5.14kg/s$.
- The pruge flow injection between rotor and stator is included into the analysis. It is modeled by an additional inlet patch placed just downstream the mixing plane. The purge flow is characterized by $\dot{m} = 0.08kg/s$ and $T_{tot} = 305K$.

To solve the conjugate problem, a loosely coupled technique is used by exchanging boundary conditions between two different solvers for fluid and solid. The fluid domain is solved by using the cell centered finite-volume code ElsA, developed by Onera [140]. A second order central scheme in space is used to discretize the 3D Navier Stokes equations. The discrete equations are integrated using a 4th order multistage Runge-Kutta scheme with implicit residual smoothing. The solid is solved by a Finite Element Analysis (FEA) by using Ansys Workbench.
The coupling procedure applied is defined as Flux Forward Temperature Back (FFTB) [142] and can be synthetized in four steps, which are also outlined in Fig. 8.18:

1. The fluid domain is solved by the CFD solver (ELSA).
2. The heat transfer (q) is computed at the blade skin. Its value is interpolated on the solid mesh and passed to the FEA solver (ANSYS Workbench) as a convective boundary condition, defined by Eq. 8.9.

$$q = h_{ref}(T_w - T_{ref}) \tag{8.9}$$

3. The FEA solver calculates the blade temperature by solving the conduction equations.
4. The skin temperature along the blade is interpolated and imposed as Dirichlet condition for the fluid domain.

The iterative loop is repeated until convergence.
The convective condition for the FEA solver is defined by imposing h_{ref}

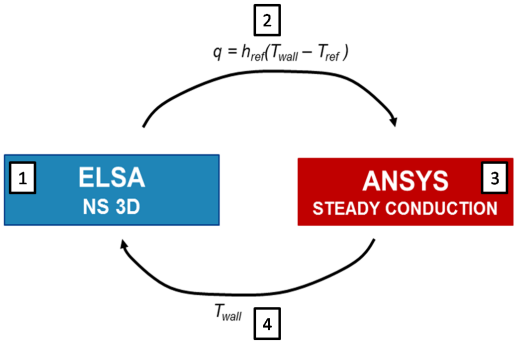

Figure 8.18.: Scheme of the FFTB algorithm used for the CHT simulation.

and T_{ref}. This can be done by defining an arbitrary value of h_{ref} and calculating T_{ref} from Eq. 8.9, where q is computed by CFD.
The arbitrary value of h_{ref} must be chosen with care. A small h_{ref} is in fact favorable to get a quick convergence of the coupled simulation. On the other

hand, Verstraete [142] showed that the FFTB approach can be stable only if $h_{ref} > h_{calc}/2$, where h_{calc} is the actual value of heat transfer coefficient for the flow.
To get a precise estimate of h_{calc}, two CFD simulatiosn of the turbine stage were performed, imposing two different uniform T_w for the rotor blade, indicated as $T_{w,b1}$ and $T_{w,b2}$. Starting from these results, the heat transfer coefficient can be calculated as:

$$h_{calc} = \frac{q_1 - q_2}{T_{w,b2} - T_{w,b1}} \tag{8.10}$$

Where q_1 and q_2 are the heat transfer distributions evaluated for $T_{w,b1}$ and $T_{w,b2}$ respectively. It is important to point out that Eq. 8.10 assumes that a different blade temperature does not affect the flow aerodynamics (i.e. h_{calc} is the same between the two cases).
In the end, a non-uniform distribution of $h_{ref} = 0.65 \cdot h_{calc}$ is chosen for the simulation. This value was considered as a good compromise to have a fast convergence and to guarantee stability.

The solid grid represents the blade and the fixing mechanism to the disk. The fluid-structure coupling takes place only along the airfoil, while a fixed temperature condition is imposed on the external surface of the fixing mechanism. This temperature condition was evaluated by a preliminary axysimmetric thermal calculation of the whole test bench, performed during its design phase.
Two different computations are carried out, considering two different materials for the rotor blade, namely the Torolon (isolating plastic) and the TA6V titanium alloy. The corresponding conduction coefficients k are $0.53W/(m \cdot K)$ for the isolating plastic and $11W/(m \cdot K)$ for the TA6V.
Figure 8.19 shows the convergence history of the coupling for the case with blade in Torolon. The simulation is considered converged when the surface averaged value of $DT/T_{CHT,i}$ is lower than 0.1% for two consecutive iterations, where $DT/T_{CHT,i}$ is defined as:

$$DT/T_{CHT,i} = \frac{T_i - T_{i-1}}{T_{i-1}} \tag{8.11}$$

for the $i - th$ iteration of the coupling. Convergence was obtained after 10 iterations for the blade in Torolon.

Figure 8.20 shows the skin temperature distribution for the blades in Torolon. Results are compared to adiabatic simulations performed at the same operating conditions. As expected, the Torolon behaves as an isolating material, leading to a temperature distribution which is very similar to the adiabatic one (the difference between the adiabatic and the coupled computation is shown in Fig. 8.20-b). The conduction effect is limited in this case to a less pronounced cold spot close to the end-walls; the cold streak is in fact convected by the passage vortex, forming a narrow area of low

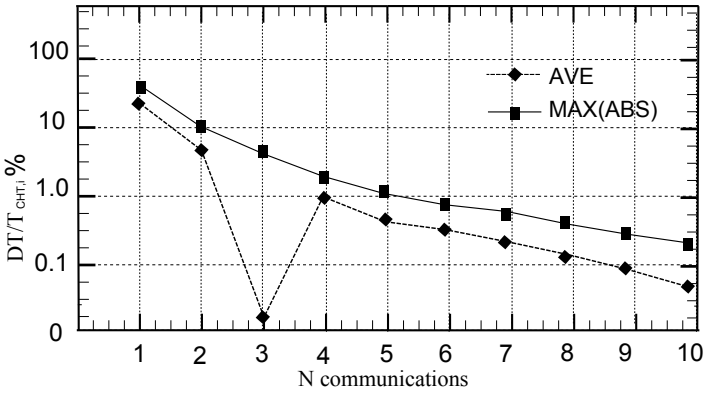

Figure 8.19.: Convergence history for the CHT simulation performed considering the blade in Torolon.

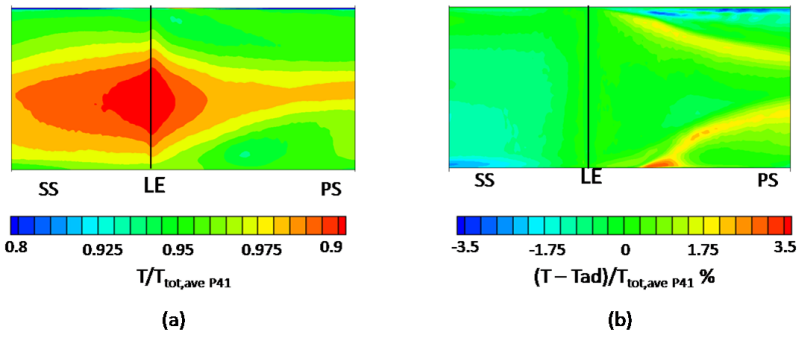

Figure 8.20.: Blade in Torolon: Wall temperature distribution on the rotor blades for the CHT computation (a). Difference between CHT and adiabatic results (b).

adiabatic temperature along the blade, which migrates from the end-walls towards the center. Notwithstanding the low conduction coefficient of the Torolon, the effect of the material is sufficient to avoid the formation of the local cold spot.

For the blade in metal, the wall temperature resulting from the CHT simulation is depicted in Fig. 8.21 together with the comparison to the adiabatic case. In this case, the blade temperature distribution is clearly affected by the solid conduction. A pronounced temperature peak is observed only at the leading edge. The temperature distribution remains instead uniform along the rear pressure and suction sides, where it reaches a maximum of $382K$ (only $4K$ higher than the surface averaged temperature of the blade). To conclude, it is interesting to point out the formation of a small hot spot localized in the rear suction side very close to the trailing edge. This is due

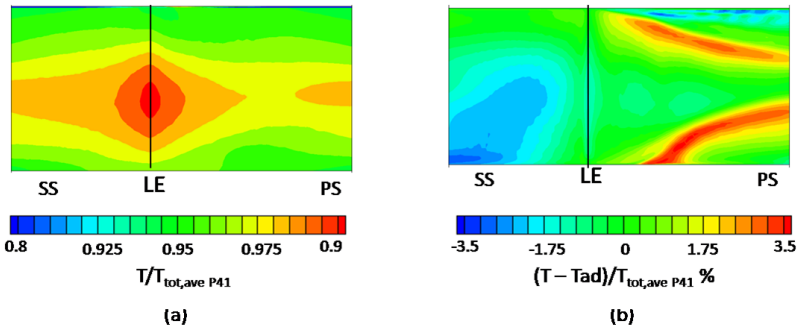

Figure 8.21.: Blade in metal: Wall temperature distribution on the rotor blades for the CHT computation (a). Difference between CHT and adiabatic results (b).

to the heat exchange from the pressure side to the suction side of the blade.

8.8. Final remarks

The present chapter investigates the actual capabilities of common RANS models used in industry to reproduce the flow field of HPTs under realistic inlet conditions. A detailed comparison of the flow evolution in HPTs with more accurate LES is proposed. According to the results, the following conclusions are given.

- When realistic turbulence levels are modeled at the turbine inlet, the turbulence decay must be tuned with care. For the specific configuration, $\mu_T/\mu \sim o^3$ shall be imposed, which is at least one order of magnitude higher than the one used for classical test cases for CFD validation.
- The $k-\omega$ Wilcox model is not able to handle the realistic turbulence level at the inlet.
- If the inlet turbulence dissipation is overestimated, the HS is not attenuated across the NGV, resulting in a very pronounced HS at its outlet. Its effect can be quantified in an increase of 5% of the $T_{ad,w}$ on the NGV and $1-2\%$ on the rotor with respect to $T_{tot,P40}$.
- If the inlet turbulence is properly modeled, RANS gives similar results to LES in terms of HS propagation.

- The $k-\omega$ SST model underestimates the HS diffusion with respect to the other 2-equation models investigated. When low turbulence dissipation is imposed at the inlet, it is observed that the alternative μ_T/μ definition introduced by Menter for the model remains active also within the passage. In standard test cases, it remains active only close to the wall to limit the production of k.

- The effect of a very high turbulence level on the aerodynamic performance is clearly overestimated when the k-ϵ and k-ω Wilcox are used. The k-ω SST predicts an increase of 1% of losses with respect to laminar cases.

In the second part of this work, the SST model is employed to study the HS propagation in turbine considering temperature distortions, swirl and high turbulence at the same time. Two different configurations are studied, indicated as clocking PA and LE.

- For the clocking PA cases, the HS is attracted towards the SS of the closest NGV. On P41 the HS is moved closer to the hub.

- For the clocking LE configuration, the HS interacts with the aligned NGV and moves towards the tip. As expected, the clocking LE configuration is the most critical one in terms of heat transfer. The surface averaged $T_{ad,w}$ of the blade aligned with the HS is 2.5% higher than $T_{tot,P40}$.

- In terms of M_{is} distribution, the swirl affects the blade load varying the flow incidence close to the hub and shroud. The losses increase of 0.3% with respect to a case with uniform boundary conditions. The clocking effect is limited to a 0.05% variation of the losses. A HS-NGV LE alignment has a slightly positive effect on the efficiency.

Generally speaking, the wall temperature distribution for the rotor is more uniform with respect to the NGV blades. In this sense, a further analysis is performed on the hot spot intensity along the rotor to support the future experimental investigation.
A more accurate estimate of the temperature distribution on the rotor is obtained by including the effect of the solid into the analysis (CHT approach). The study shows that the temperature peak is only $4K$ higher than the average temperature for the blades in titanium. For the blades in Torolon, on the other hand, the maximum difference in wall temperature is locally

limited $10K$ with respect to the adiabatic case.

Chapter 9.

Conclusions

Nowadays the aerodynamic optimization of the different components characterizing an aeroengine is pushed up to a level that no noticeable improvement can be obtained anymore without introducing a significant technological breakthrough. As a consequence, the main industries and research centers investigate the possibility of improving the overall performance of the machine by introducing more complex but more accurate design methodologies. In particular, it is well known that a gas turbine is a very complex machine in which the different components heavily interact between each other. Despite that, the design process is usually organized in such a way that the compressor, combustor and turbine are designed separately, with little interaction between the different teams.
It is therefore interesting to investigate the possibility of including the mutual interactions between different components into the design process. From this point of view, the combustor-turbine interaction is the most critical one, as it directly influences the maximum temperature reached by the machine.

The aim of the current thesis is to investigate in detail the applicability of modern numerical methodologies to reproduce the mutual interaction between combustor and turbine. The flow field at the interface between combustor and turbine is very complex, being characterized by I) A very high turbulence level (up to 25%), II) a non uniform total temperature profile, characterized by the presence of hot streaks (HS) and cold streaks (CS) III) A swirling and highly unsteady velocity field.
Historically, the main limit in studying the flow in HPTs operating at realistic inlet conditions resides in the lack of test rigs and numerical investigations capable of modeling all these features at the same time; from the literature review it clearly emerges that the effect of the combustion chamber on the HPT is typically studied by investigating the effect of high swirl, temperature distortion and turbulence on the HPT stage separately, while only very few recent works try to investigate all these features at the same time. Moreover, theoretical temperature or velocity distributions are commonly considered at the turbine inlet, which are quite far from the distortions observed for real machines.
To conclude, it must be also pointed out that only two very recent papers discuss in more detail how the presence of the turbine downstream affects the flow field within the combustor [27, 62].

From the numerical standpoint, a complete and accurate study of the interaction between combustor and turbine copes with two main problematics:
First of all, it must be considered that the only way to correctly reproduce the mutual effect of combustor and turbine (i.e. taking into account the potential effect of the HPT on the combustor as well) is to simulate both components at the same time in an integrated framework. Nevertheless, it must be taken into account that the combined resolution of a low-Mach reactive flow (for the combustor) and a transonic flow with static and rotating components (for the turbine) with a unique solver is problematic and requires the development of ad-hoc codes, to guarantee the stability of the solution [23].
Secondly, classical test cases in use for the validation of CFD for turbomachinery normally consider axial and uniform flows with no more than 5% of turbulence at the inlet, which is about 1/5 of what is normally expected in recent engines. Therefore, the accuracy of RANS models in reproducing the complex and high turbulent flow field observed at the combustor-turbine interface has never been validated before.
In the last 10 years, LES demonstrated to be particularly suited to reproduce the formation and propagation of the HS within the combustor, thanks to its ability to directly solve the most energetic turbulent structures, which are responsible for the turbulent mixing. To compensate the lack of experimental test cases reproducing realistic conditions at the combustor-turbine interface, LES could therefore be applied to the study of the HS propagation in turbine, and used to validate less expensive RANS models applied to such a complex flow field.
The current thesis is divided in two parts, in which the aforementioned problematics are treated separately.

To solve the combustion chamber and the turbine at the same time by CFD, a "coupled approach" is employed: at this scope, the whole domain is divided in two subdomains (representing respectively combustor and HPT). The flow field within the subdomains is solved separately by two different solvers, which exchange information to each other several times during the simulation to get a common stabilized solution.
The exchange of information consists in mapping flow quantities from the subdomain downstream to the outlet upstream, and from the upstream solution to the downstream inlet. Considering the better quality of the solution in combustion chamber when unsteady approaches are used, coupling procedures are developed for URANS-URANS, LES-URANS and LES-LES applied to combustor and turbine respectively.
The methodologies were tested for academic test cases with increasing difficulty, focusing the attention on the continuity of the solution in space and time. The test cases are chosen to reproduce some typical unsteady flow features at the outlet of modern LBCs.

In terms of velocity and TKE, the upstream and downstream solutions show a satisfactory continuity at the interface between the subdomains when the URANS-URANS and the LES-URANS coupled procedures are applied. The pressure distribution depicts instead a discontinuity at the interface, albeit limited in amplitude. Such a discontinuity is due to the fact that non-reflecting conditions shall be used at the outlet of the subdomain upstream to avoid spurious distortons of the unsteady structures approaching the outlet patch.
A better pressure continuity can be enforced by decreasing the relaxation coeffcient for the non-reflecting condition or by imposing directly a Dirichlet pressure condition at the upstream outlet (the Dirichlet condition can be easily obtained by the information coming from the solution downstream). To avoid spurious reflections, these techniques can be implemented only if the interface between the subdomain is not interested by unsteady pressure distortions.
When the LES-LES procedure is applied, a very accurate continuity of all flow variables is achieved at the interface. To obtain this, the price to pay is that the LES-LES coupled procedure is "conditionally stable" , and strict requirements must be respected in terms of grid and time step for the two simulations.
For the LES-URANS coupling, the passage of information between the subdomain upstream to the one downstream is achieved by filtering out the turbulence crossing the interface (which is directly resolved by LES and modeled by URANS) while transferring the most energetic vortices. This is done by applying a time-marching filter to the variables exchanged from LES to URANS. To properly set-up the time interval in which the time-marching filter is applied, a procedure is developed in this work and validated for complex flow fields.

After the validation of the coupling methods for complex turbulent test cases, a real combustor-turbine configuration is studied by applying the URANS-URANS coupling technique. The configuration is designed to represent a realistic industrial Lean Burn combustor coupled to a high pressure stator.
During the coupled simulation, two subdomains representing respectively the combustion chamber and the turbine are analyzed by two different solvers based on the OpenFOAM platform. The convergence of the coupling is checked by monitoring the pressure at the interface between the subdomains. After 7 communications, the two simulations reach the same pressure level at the interface, indicating convergence of the coupled procedure.
Once the simulation is converged, the continuity of the solution is checked at the interface, appearing satisfactory all flow variables.
The coupled solution is investigated in detail to characterize the complex interaction between the hot streak, the swirl generated within the combustor and the secondary flows formed within the NGV. In particular, the hot

streak migration within the NGV is influenced by the residual swirl at the combustor outlet, while the cold streaks (which are generated by the cooling of the combustion chamber) interact with the secondary flows developed close to the endwalls. All these phenomena have a considerable impact on the aero-thermal field of the stator, leading to a very non uniform adiabatic blade temperature distribution.
Moreover, the test case is characterized a pronounced tangential migration of the swirl within the combustor, which affects the aerodynamic performance of the airfoil. Such migration, which is also coherent with the observations of Insinna et al. [70], is most likely due to the geometrical shape of the annular combustion chamber.
To conclude, it is pointed out that the presence of the NGV downstream causes a pressure distortion at the combustor outlet, which affects the flow field in the secondary zone of the combustion chamber. By employing the coupled approach, it is estimated that the potential effect of the HPT influences the flow field within the combustor up to $0.8C_{ax}$ upstream of the NGV blade.
The application of the zonal LES-URANS coupled procedure to the combustor-turbine test case is considered as a future development of the present activity.

In the second part of this work, two LES solvers available at VKI are validated for the first time on the external flow field of turbines. The final goal is to estabilish a robust and accurate LES-based solver to study the realistic aero-thermal field in 3D HPT profiles. The tool can be used in the future for a detailed characterization of the combustor-turbine interaction as well as to benchmark less expensive RANS models.
Before being able to apply LES to a complex 3D flow field, a well defined step-by-step validation procedure must be established by progressively increasing the complexity of the test cases.
As a first step, the WALE model implemented in the commercial solver Fine/Open is validated on a low pressure turbine profile, which is characterized by a relatively low Reynolds. Results clearly show that LES is much more accurate than RANS in reproducing the mean flow field. The large amount of unsteady data obtained during the simulation permitted to characterize in detail the laminar to turbulent transition observed for the separated shear layer.
Considering the future application to the the HS propagation in turbomachinery, the main drawback of Fine/Open is linked to the fact that non-reflecting conditions are not implemented.
To avoid the formation of spurious numerical fluctuations close to the boundaries, for the current case a numerical sponge layer was generated by coarsening the grid close to the inlet and outlet patches. This method demonstrated to be effective in damping the waves, but it prevents from a detailed reproduction of the turbulence transferred from the combustor to the turbine,

which can be included into the analysis only by refining the grid up to the HPT domain inlet.
Following these consideration, the second test case of the validation is investigated by using the open source code TUMDF, which is applied for the first time to LES for turbomachinery. The solver is validated on a HPT prismatic airfoil, obtaining a satisfactory comparison with the available experimental data both in terms of time averaged and fluctuating fields.
The results obtained are very encuraging and constitute a first successful application of LES to the external field of turbines at VKI. Nevertheless, before being applied to the combustor-turbine interaction, the two solvers require further development on the following points: (I) an advanced synthetic turbulence generator must be implemented and validated at the inlet. (II) The computational effort required for 3D LES in HPT shall be evaluated in detail, considering also the possibility of using less computationally expensive Detached Eddy Simulation (DES) techniques to further limit the grid requirements at wall.

To conclude, an assessment of the most common two-equation turbulence models is proposed by comparing RANS with LES for a test case representing a combustor simulator coupled to a turbine stage. For the current application, LES results are obtained at CERFACS in the framework of the FACTOR project [75].
The study clearly demonstrated that the application of classical two equations RANS models to a realistic high turbulence field is very critical. In particular, it emerges that the turbulence decay must be tuned with care to avoid a non-physical decay of the turbulence level immediately downstream from the inlet. Moreover, the $k-\omega$ Wilcox model reproduces a non-physical generation of turbulence in proximity to the blade leading edge, while the $k-\omega$ SST underestimates the HS diffusion with respect to the other models investigated.
The $k-\omega$ Wilcox and the $k-\epsilon$ models, for which the Bradshaw's assumption for accelerating boundary layers is not respected, also overestimate the effect of the turbulence on the blade load, which can be reproduced in a more realistic way only employing the $k-\omega$ SST.
To synthesize, the current work clearly evidences that the HPT flow field reproduced by RANS is highly affected by the imposition of realistic turbulence levels at the inlet, and in some cases clearly non-physical results are obtained.
Even though the comparison with LES permits to point out some of the main problematics linked to the application of RANS to realistic flow fields in HPTs, it is nowadays necessary to develop more sophisticated experimental facilities to reproduce the combustor-turbine interaction, which could be used for a complete validation of the CFD tools available at the state of the art.
This step is essential to get the adequate confidence in the numerical tools

before including the combustor-turbine interface into the common industrial design process.

Part III.

Appendix

Appendix A.

Advanced Methods for the Interaction Between Compressor and Inlet Ducts

In this chapter, which is distinct from the rest of this thesis, unsteady RANS computations are used to study the inception of rotating stall in a transonic centrifugal compressor interacting with the inlet duct of the machine. Realistic installation effects, as commonly found nowadays due to space limitations, are taken into account to evaluate the stability limit. To this end, the effect of ideal uniform inlet conditions (normally found for long straight inlet) is compared with inlet distortions generated by a bent pipe installed just in front of the impeller.
The numerical techniques that have to be applied to correctly represent the rotating stall are explained in detail: all simulations are done modeling the whole annulus of the radial machine, using high performance computing to represent the non-periodic phenomena leading to the stall inception. Moreover, stable boundary conditions are employed, with the aim to avoid the inception of large non-physical surge cycles.
When an uniform inlet flow to the compressor is considered, the formation of 8 blockage cells rotating in the same direction of the compressor is pointed out. On the other hand, when the elbow is installed in front of the impeller, the distorted flow suppresses the formation of a rotating stall pattern.

Results of the present chapter are also published in part in:

S.Vagnoli, T. Verstraete (2015) *URANS analysis of the effect of realistic inlet distortions on the stall inception of a centrifugal compressor*, Computers & Fluids,116,pp.192-204.

A.1. Introduction

Today the design of efficient and stable compression systems becomes increasingly more challenging considering that more compact solutions are required, resulting from strict limits on the encumbrance and weight. Because of this, bent pipes (elbows) are often installed in the proximity of the compressor inlet, forcing the impeller to operate with a nonuniform inlet

flow, which will affect the performance and the stall limit.
For centrifugal compressors, it is not as trivial to identify the occurrence of stall as in axial compressors. This is particularly due to the fact that in radial impellers the presence of rotating stall cells is often indicated by an increase of noise only, without an abrupt change of performance [143], since the centrifugal effect on compression is always predominant on the aerodynamic one [144].
For unshrouded transonic compressors, one of the most important initiators of rotating stall is the interaction between the tip clearance vortex and the main flow [145–147], which lead to the first inception of rotating disturbances within the machine [148, 149].
Because of the intrinsically time-dependent nature of the stall itself, it is not trivial to reproduce the rotating stall inception by means of CFD: an unsteady approach shall be used, and the whole annulus of the compressor shall be analyzed, to take into account the non-periodic time-dependent nature of the phenomenon. Such kind of approach is highly time consuming, and has become possible only in recent years, thanks to an increased computational power.
Few studies can be found in the literature with the aim to numerically reproduce the rotating stall, mainly related to axial compressors [145, 150–152] (this emphasizes a lack of similar studies applied to centrifugal compressor); Chen et al. [145] and Gourdain et al. [152] compare numerical results with experiments for axial compressors in stall. A close prevision of the operaton point at the stall inception limit between CFD and experiments is pointed out by both authors.
Focusing the attention on the mutual interactions between different components, it shall be stated that non-uniform inlet conditions to the impeller can be due to for example bent pipes installed close to the inlet, because of strict space constraints to be taken into account during the design of many applications. The non-uniformity of the flow entering the compressor could heavily influence the rotating stall inception process, even though a lack of works about inlet distortion effects can be pointed out in literature [153].
Ariga et al [154] experimentally studied the influence of different types of total pressure inlet distortions, comparing the performance of the impeller with distorted and undistorted inlet flow. The degradation of performance due to nonuniformities becomes more remarkable at high massflow, while little effect is noticed at lower mass flow, as also confirmed by other authors [155].
From a numerical point of view, Kim et al. [5] investigate three different bends with the aim to reduce the nonuniformity at the impeller inlet and to improve the performance of the machine. In this case, steady CFD is only used to design the inlet duct, but the effect on the radial compressor itself is not investigated.
Considering the lack of investigations on the effect of inlet distortions on the stall inception, the transition to stall of a transonic centrifugal compres-

sor is analyzed in detail through numerical simulations. Two configurations with respectively a straight inlet and an elbow are investigated by means of unsteady RANS simulations, reproducing the non-periodic nature of the rotating cells by full annulus models of the machine.

A.2. The Flow Solver and Numerical Model

A.2.1. Analyzed Geometry

The geometry employed for this investigation is shown in Fig.A.1-a. It is a transonic centrifugal compressor, whose shape has been optimized at the von Karman Institute for Fluid Dynamics. The geometry consists of an unshrouded impeller with 9 main and 9 splitter blades, and a vaneless diffuser. The main design parameters are shown in table 1.
Two different configurations for the flow at the inlet have been considered. In the first case, a straight pipe is modeled, whilst in the second case a 90° bent section is imposed upstream of the previous domain. Dimensions of the bent pipe are shown in Fig.A.1-b.
No experimental data are available for the geometry considered, therefore

Table A.1.: Design parameters for the centrifugal compressor in study.

PARAMETER	DESIGN VALUE
Design massflow	10.84 (kg/s)
π_{TT} design	3.87 (-)
η_{TT} design	0.845 (-)
Rotation velocity	24800 (RPM)
Ma_{tip} (based on ωr_{tip})	1.11 (-)
Number of main blades	9
Impeller exit radius	186.5 (mm)
Clearance (% of span at LE)	1%

the validation of the numerical approach was performed on the NASA rotor 37 [156]. This test case was chosen for two main reasons: (I) The NASA-37 is a transonic machine (II) The NASA-37 presents a very similar behavior to the one expected for the centrifugal impeller at near stall conditions (as it will be demonstrated later). The validation is presented in session A.3.

A.2.2. The Flow solver

In the present work, the commercial software FINE/TURBO has been used to solve both steady and unsteady compressible Reynolds-Averaged Navier-

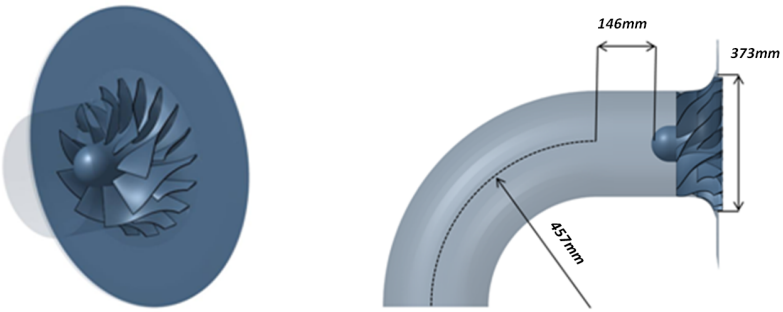

(a) (b)

Figure A.1.: (a) Geometry of the radial transonic compressor analyzed. (b) Dimensions of the bent pipe considered for the analysis.

Stokes (URANS) equations. This is a second order cell-centered finite volume solver for structured multiblock meshes. The code was already successfully employed in different circumstances to represent unsteady flow patterns of tip loaded transonic axial and radial compressors operating at near stall conditions [134, 157, 158].
For the Unsteady RANS simulations, 405 time steps are used to model one rotation of the compressor. The solution for every time step is obtained by means of 100 inner iterations, using the 4th order Jameson's scheme. A maximum Courant number of 2 is imposed for the inner iterations. The turbulence model employed is the Spalart-Allmaras one equation model.

A.2.3. Boundary Conditions for the Unsteady Analysis

To perform numerical simulations at near stall and stall conditions, the choice of proper boundary conditions at the outlet shall be discussed in detail.
To induce stall in the compressor, the machine must operate at low massflow. In this operating point, the system is also more prone to surge.
Surge is a dynamic resonance of the whole compression system (of which the compressor is only a part), leading to low frequency and high amplitude fluctuations of the massflow. Since the whole system is directly involved, surge can only be reproduced by directly including the resisting circuit in the numerical model, (i.e. meshing all volumes upstream and downstream the compressor) with a subsequent dramatic increase of the computational cost. Therefore, when the domain modeled includes the compressor only, the inception of surge must be avoided to prevent non-physical massflow

fluctuations.
Greitzer's theory [159] identifies two different limits for surge inception:

- **The static stability limit** according to which the system is unstable when the slope of the compressor curve (defined as $\delta\pi/\delta\dot{m}$) is lower than the one of the throttle.
- **The dynamic stability limit** which further decreases the limit when a storage volume is present at the compressor outlet.

By imposing a constant pressure at the domain outlet (as it is usually done for steady RANS simulations of turbomachines) the static stability condition cannot be satisfied when the compressor operates on the part of the characteristic curve with positive slope. This means that at low massflow a surge cycle will be initialized, and reliable CFD results cannot be obtained. A proper boundary condition to get stable rotating stall configurations without surge inception requires an increase of the static stability limit, and this can be achieved by using a relation between massflow and pressure with one degree of freedom, as shown in equation A.1.

$$p_{out} = p_0 + \kappa \cdot \dot{m}^2 \tag{A.1}$$

In this case, the equation represents the effect of an ideal valve installed at the compressor outlet. The parameter κ is the throttle setting, and an increase of this value corresponds to the closure of the throttle valve.
It is worthwhile to note that such a boundary condition does not introduce any further inertial effect on the outlet flow, representing a fully resistive outlet for the electrical analogy. This means that, according to Greitzer's analysis, the dynamic stability limit will be very close to the static one, since only the inertial effects of the compressor wheel volume will be present in the system.

A.3. Validation of the Numerical Approach: the NASA Rotor 37.

In order to make sure that the numerical set-up (boundary conditions, numerical schemes, grid quality, turbulence model etc.) is adequate to represent the main phenomena characterizing the near stall conditions, a preliminary analysis was performed for a geometry presenting a similar behavior to the compressor in study. For a transonic unshrouded compressor with axial inlet and pronounced tip gap in fact, the onset of unsteady disturbances at low massflow is likely to be generated at the leading edge of the inducer, by the breakdown of the tip leakage vortex interacting with the passage shock [160]. In some circumstances, this leads to a local increase of blockage, which

rotates within the annulus [148, 149].

Yamada et al. [149] numerically showed that the transonic NASA rotor

Table A.2.: Parameters of NASA rotor 37.

PARAMETER	DESIGN VALUE
Choke massflow	20.93 (kg/s)
Rotation velocity	17189 (RPM)
Matip (based on ωr_{tip})	1.31 (-)
Number of blades	36
Impeller radius (@ LE)	252 (mm)
Clearance (% of span at LE)	0.45%

37 [156], although an axial compressor, presents very similar features to the ones expected for the inducer of the centrifugal machine of the present study when operated close to stall. According to this observation, the NASA rotor 37 was chosen to validate the numerical approach, focusing the attention on the accuracy of the tip vortex reproduction close to stall. The specification for the NASA rotor 37 are listed in table A.2.

The computational domain employed for the analysis is shown in Fig. A.2.

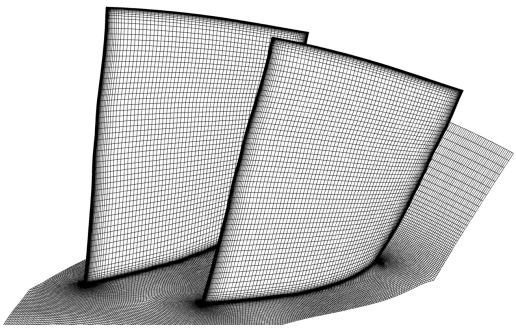

Figure A.2.: Detail of the mesh used to reproduce the NASA rotor 37.

The final grid is characterized by 1.45x10^6 elements, with 18 cells to represent the tip clearance. The compressor wis reproduced only by one blade passage, imposing periodic conditions in transversal direction. $Y+$ lower than 1 was kept at the wall. Steady RANS computations are performed using the Spalart-Allmaras turbulence model, and stable operating conditions at low massflow are obtained employing the outlet condition depicted by equation A.1.

Figure A.3 shows the pressure ratio evaluated in between the design condition and the stall limit. The agreement between the numerical and the experimental results is in this case excellent. The stability limit, which is

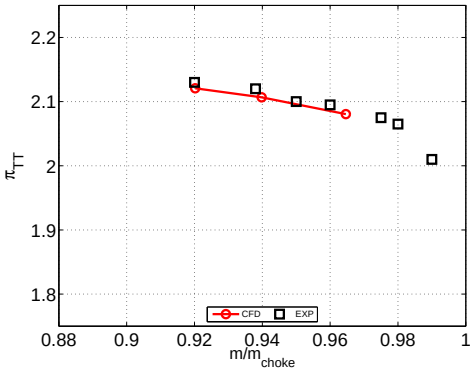

Figure A.3.: Experimental and numerical performance comparison for the NASA rotor 37.

defined in this case as the last operating point for which a stable RANS solution can be achieved, is correctly predicted at 92% of the chocked mass-flow.

To investigate in more detail the accuracy of CFD to reproduce the tip

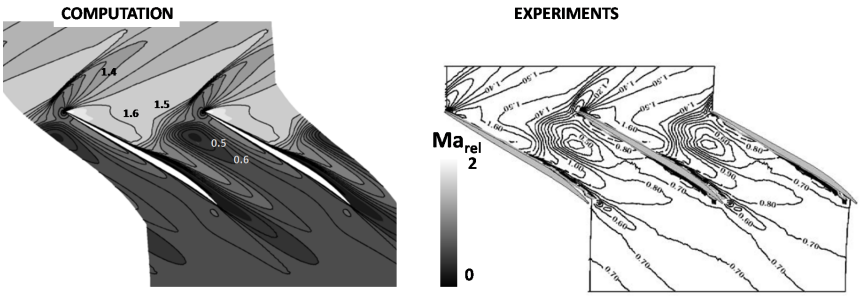

Figure A.4.: Experimental and numerical performance comparison for the NASA37 rotor: Mach isolines at 95% of span.

vortex behavior, experimental and numerical isolines of relative Mach number at 95% of span are compared in Fig. A.4. An area of blockage is present close to the leading edge of the blades, linked to the tip leakage vortex interacting with the shock. The position and the intensity of the low mach number region is accurately captured by the computation.

Fig. A.5 shows the axial velocity distribution at near stall conditions, plotted on a plane perpendicular to the rotor axis at 20% of the chord length within the passage. The presence of the already described low speed area is clearly evident close to the passage tip. The numerical results reproduce very accurately the velocity distribution obtained by the experiments as well as the position of the shock in the blade to blade direction.

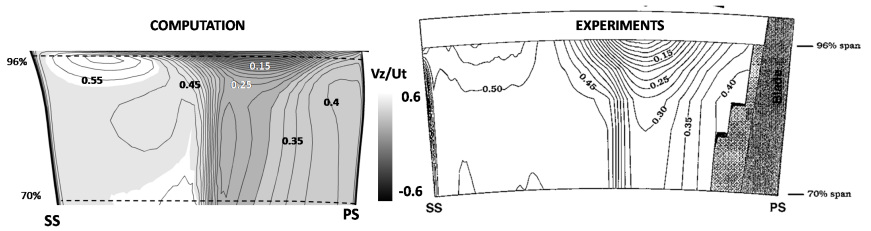

Figure A.5.: Experimental and numerical performance comparison for the NASA rotor 37: axial velocity distribution at x/c=0.2.

According to this preliminary analysis, it is expected that the numerical approach is able and mature enough to accurately reproduce the behavior of a transonic compressor operating close to stall, when the formation of stall cells is generated by a tip vortex instability.

A.4. Analysis of the Stability Limit for the Centrifugal Compressor with Straight and Bent Pipe at the Inlet

A.4.1. Numerical Setup

The final mesh representing the full annulus of the centrifugal compressor is composed by 25 x 10^6 nodes, including 16 elements in radial direction within the tip clearance. A mesh convergence analysis was performed, mainly focusing the attention on the blade pressure distribution close to the tip (where the stall inception is expected). To reduce the computational costs, $Y+$ at wall was maintained around 20 to apply wall functions. A detail for two blade passages is shown in Fig.A.6. The computational time required for the unsteady analyses is 4036 CPUhr per rotation on 48 processors of a SGI cluster. About 15 rotations for each operating point are simulated.

The imposition of wall functions is necessary to limit the dimension of the numerical domain when the full annulus is reproduced [152]. To quantify the effect of the wall functions in the accuracy of the tip flow representation, two steady computations are performed with two different grids for an operating point close to stall. In addition to the mesh already described (suited for the use of wall functions) another grid is obtained by refining the boundary layer to $Y+ < 1$, to allow a direct resolution.This finer mesh is characterized by 4.5x10^6 elements per blade passage, that is 40x10^6 elements to reproduce the whole machine.

Figure A.7 shows the main blade pressure distribution at 98% of span for

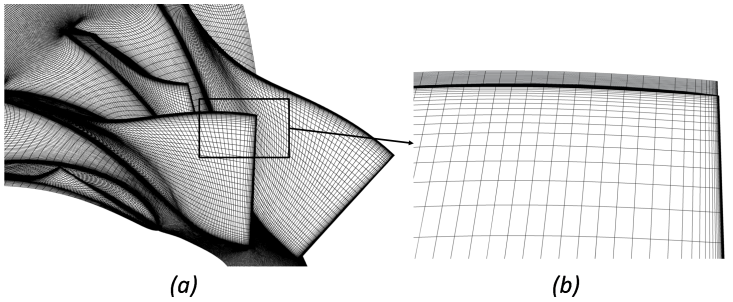

Figure A.6.: (a) Detail of the mesh for two blade passage. (b) Detail of the tip clearance mesh.

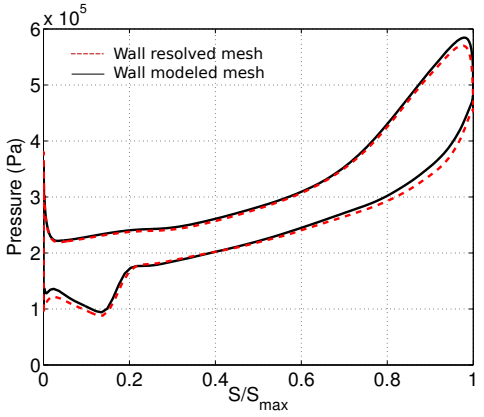

Figure A.7.: Pressure distribution on the main blades at near stall conditions at 98% of the span. Comparison between the mesh with wall models and with direct resolution of the boundary layer.

the two calculations. Results are in excellent agreement between each other, in particular for the first 60% of the chord. The radial part of the impeller is of lower interest since the stall inception is not expected to take place there. In particular, both domains reproduce the impact of the shock on the suction side at the same distance from the leading edge ($S/S_{max} = 20\%$).

A detail of the Mach distribution at 98% of span within the inducer is shown in Fig. A.8. Even in this case, the comparison between the two solutions is satisfactory. As expected, a low Mach area is reproduced close to the blade pressure side just upstream of the shock, representing the breakup of the tip leakage vortex. An analogous behavior of the suction side boundary layer is moreover predicted, pointing out an acceleration close to the leading edge and a separation induced by the shock.

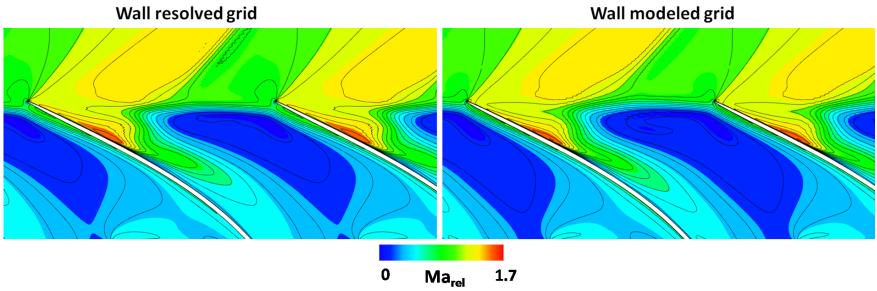

Figure A.8.: Mach number close to the tip at near stall conditions reproduced by the mesh with wall models and with direct resolution of the boundary layer. Picture at 98% of the span.

A.4.2. The Numerical Computations

Based on the previous discussion, the wall modeled full annulus grid composed by 25x10^6 elements is employed to analyze the stall inception. Stabilized operating points at low massflow are obtained using the outlet boundary condition defined by Eq. A.1. Values for κ are shown in table A.3 for the different cases analyzed, ranging from C0 to C6.

Table A.3.: Values of k for the different cases analyzed according to equation 1.

COMPRESSOR WITH STRAIGHT PIPE	COMPRESSOR WITH BENT PIPE
CASE 0 (C0) : k = 2800	CASE 4 (C4) : k = 3000
CASE 1 (C1) : k = 3100	CASE 5 (C5) : k = 3150
CASE 2 (C2) : k = 3250	CASE 6 (C6) : k = 3300
CASE 3 (C3) : k = 3400	Note: k is expressed in $s/(Kg \cdot m)$

A.4.3. Centrifugal Compressor With Straight Inlet

For the configuration with straight inlet, the characteristic curve close to stall is reproduced by steady RANS and Eq. A.1 for the outlet patch, progressively varying the value of κ. At a later stage, the operating points shown in Table A.3 are progressively analyzed with URANS. The unsteady simulations C0 and C1 are initialized from the last stable RANS solutions, considering about 10 rotations to stabilize the unsteadiness and 5 additional rotations to post process the results.

The global performance of the compressor over time is plotted in Fig. A.9.

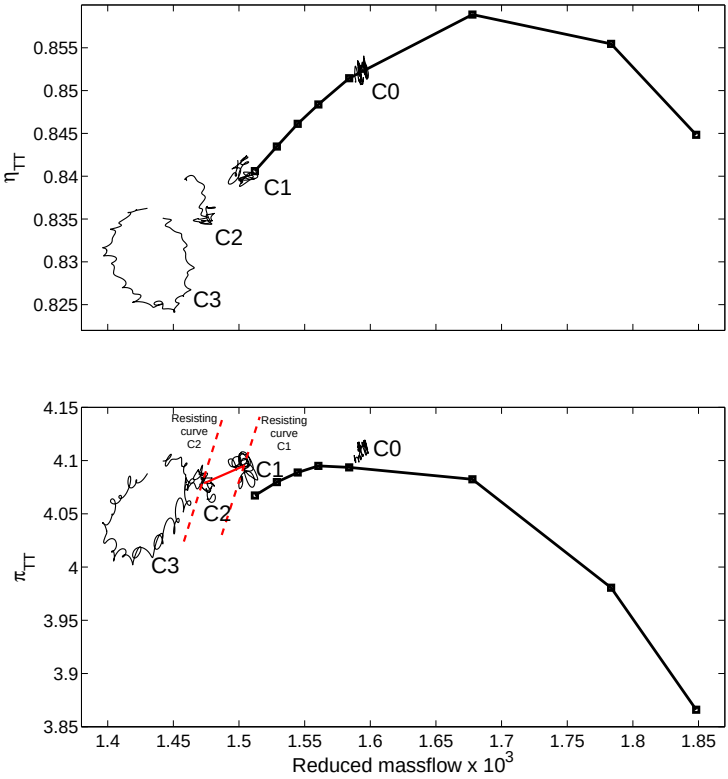

Figure A.9.: Overal performance of the compressor for cases 1, 2 and 3: total to total pressure ratio (lower part) and total to total efficiency (higher part) together with RANS results for operating points at higher massflow. The compressor curve (in red) respects the stability limit imposed by the resisting curves (in dashed red) for cases 1 and 2.

For the URANS simulations, data from the last 3 rotations are considered. At the last stable RANS operating condition the characteristic curve has a clear positive slope.
Cases 1 and 2 show an unsteady high frequency fluctuation of performance in time around a well defined average value, without showing the inception of a surge cycle.
The resisting throttle curves indicating the outlet boundary condition imposed for cases C1 and C2 are also represented in figure. Their shape can be directly calculated by equation 1 for the two different values of k. The intersection between the throttle and the compressor curve clearly shows that operating points C1 and C2 fulfil the stability limit, since the local tangent of the throttle curve is still considerably higher than the one of the

compressor. Therefore, considering that the dynamic stability limit is very close to the static one for such configuration, an inception of surge is not expected for these operating points. Case 3, on the other hand, shows a large periodic fluctuation. This is related to a cycle of hysteresis caused by surge of the analyzed configuration. Since a surge cycle cannot be accurately reproduced, this configuration will not be considered anymore.
From Fig. A.9 it is also clear that the time-averaged URANS performance prediction differs from the RANS one for cases C0, C1 and C2. In this part of the curve, the performance is strongly influenced by the unsteady interaction of tip vortex, main flow and shock at the tip, and the different values obtained by URANS can be related to the time-dependent reproduction of such phenomenon.
The unsteady tip vortex behavior can be depicted in Fig. A.10 where the

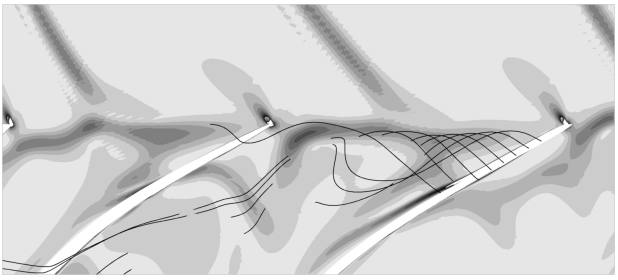

Figure A.10.: Schlieren picture of the flow field close to the tip for case C1 at 95% of the span. The clearance flow is indicated by red lines.

magnitude of the density gradient (corresponding to a schlieren picture of the flow) is represented for a blade to blade plane at 95% of span. For case C1, an instantaneous solution is shown. The tip clearance flow, pointed out by red lines over the central blade, interacts with the shock and breaks down within the passage, impinging on the blade to the left.
Figure A.11 shows an instantaneous snapshot of the entropy (figure a) and the Mach field (figure b) at 98% of span within 3 blade passages for the unsteady solution C1. For clarity, Mach number isolines are added to the plots, and the sonic isoline is pointed out in red.
The high entropy area within the inducer indicates losses due to the mixing between tip vortex (that breaks down) and main flow, leading to a local increase of blockage. It is interesting to observe that the solution is not uniform from one passage to another; this evidences that the tip behavior is unsteady and characterized by a different phase among the passages, indicating the possible presence of a rotating disturbance [160].
The presence of a rotating disturbance can be also deduced following the Vo criterion [146]. According to that, a stall inception of rotating type can be expected for tip loaded compressors when the tip vortex is aligned with the leading edge of the blades, as clearly shown in this case by the entropy

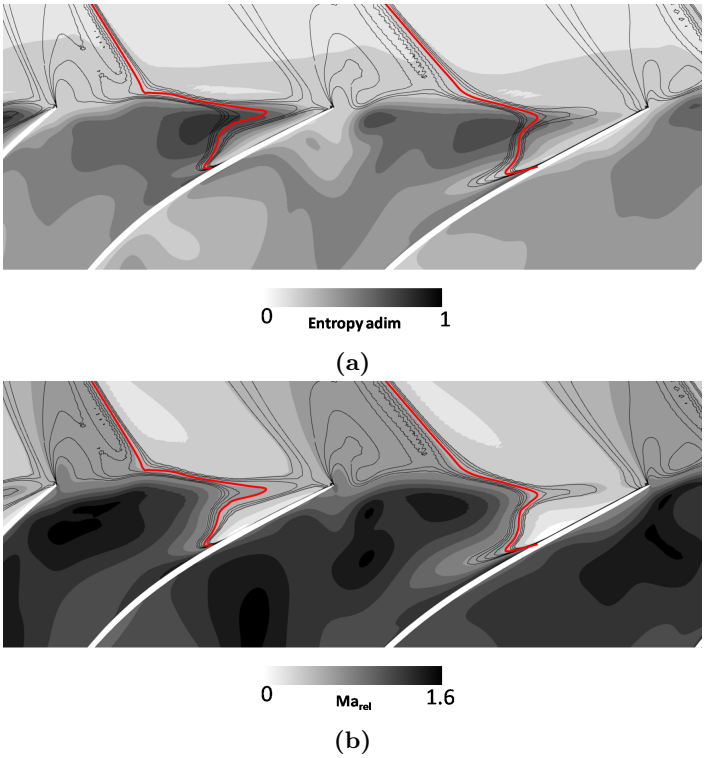

Figure A.11.: Instantaneous solution of entropy (a) and Mach (b) for case C1. Plane at 98% of span. The sonic line is depicted in red.

Table A.4.: Position of the probes used for the analysis.

Number of Probes	Z/Z_{chord}	r/r_{tip}	Frame of reference
9	0.25	0.98	Relative

peak position.
Observing Fig.A.11b, one can also state that the unsteady behavior of the clearance flow leads to an oscillation of the passage shock and of the flow separation taking place within the passage itself. In this case, in fact, a flow separation can be observed on the suction side of blades 2 and 3, pointed out by the low Mach area generated just downstream of the shock. The flow remains instead attached to the suction side of blade 1 along the inducer.

To better describe the tip unsteadiness observed for condition C1, 9 numerical pressure probes were imposed at the pressure side of each main blade, within the axial inducer. Pressure signals are registered in the rela-

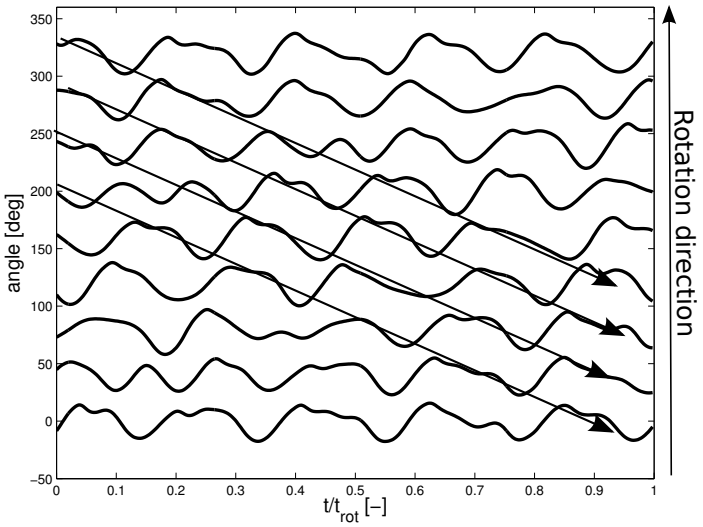

Figure A.12.: Pressure fluctuations over one rotation for the numerical probes imposed in the relative frame of reference. The propagation of the disturbances within the annulus is depicted by arrows.

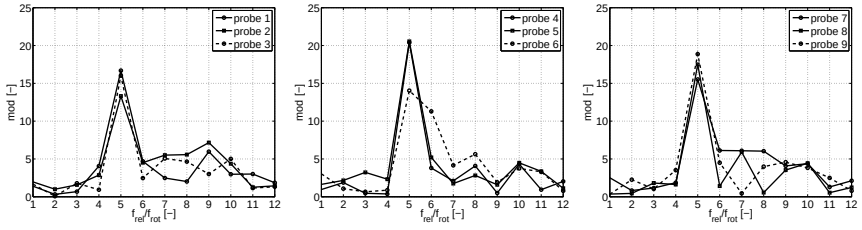

Figure A.13.: Fast fourier transform of the signals represented in Fig. A.12.

tive frame of reference to directly filter out the effect of the blade passage on the fluctuations. The position of the probes is shown in table A.4.
Fig.A.12 represents the non-dimensionalized pressure fluctuations registered by the 9 probes during one rotation of the compressor. Signals are shifted relatively to each other within the graph to represent the angular position of the probes.
A regular oscillating pressure pattern is clearly shown for all probes, with an averaged rms amplitude equal to 14% of the local averaged pressure value. The phase shift between the signals depends on the relative angular position of the probes; this is a clear indication that flow disturbances are rotating within the annulus. To better evidence this behavior, black arrows are also included in the graphs, representing the propagation of the distur-

bance among the probes. The disturbances are moving at a relative velocity equal to $\omega_{rel} = -64\%\omega_{rot}$ (that is $\omega_{abs} = 36\%\omega_{rot}$ in the absolute frame of reference).
Figure A.13 points out the averaged Fast Fourier Transform performed on all pressure signals. A detailed mapping in the frequency space cannot be forcedly achieved because of the small time window represented by one single rotation.
The results are strongly influenced by the aforementioned flow unsteadiness. A peak for pressure fluctuations at f_{rel}/f_{rot}= 5 is clearly present for all probes. Considering Eq. A.2 (where N_{cells} indicates the number rotating disturbances):

$$f_{rel}/f_{rot} = N_{cells} \cdot \omega_{rel}/\omega_{rot} \tag{A.2}$$

One can deduce the presence of 8 cells rotating within the annulus.

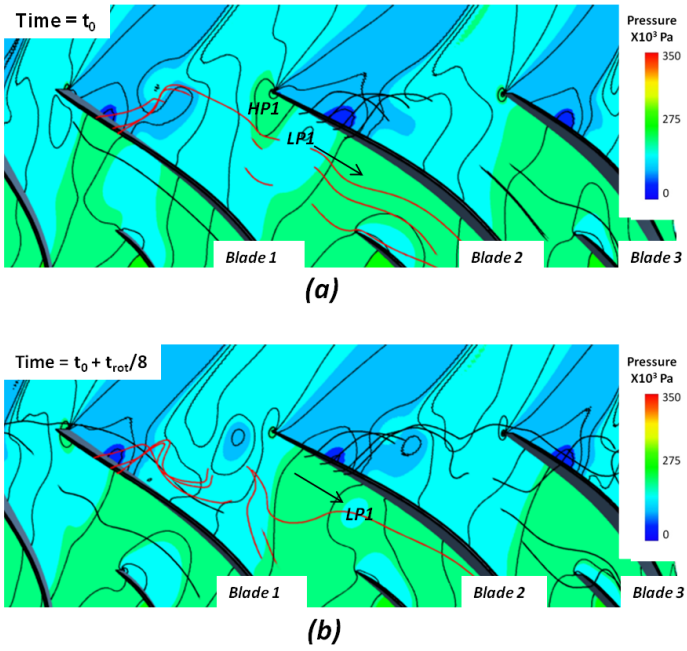

Figure A.14.: (a) Pressure field at 92% of span for case 1 at time = t_0 and (b) at time $t_0 + \tau_{rot}/8$. The tip flow streamlines of passage 1 are represented in black, while the one of passage 2 are represented in red.

To better understand how the disturbance propagates within the inducer, a detail of the pressure field at 92% of span for case 1 is shown in Fig.A.14-a for a reference time t_0, whilst the same field is shown in Fig. A.14-b at t_0

+ $\tau_{rot}/8$. The streamlines of the tip vortices for blades 1 and 2 are also depicted in red and in black respectively.
According to Fig.A.14-a, blade 1 is characterized by a strong over tip flow, which breaks down and interacts with the pressure side of blade 2. The mixing of tip vortex and main flow generates the low pressure area indicated as LP1. The low pressure area is preceded by a higher pressure section (HP1), which indicates blockage of the main flow entering within the passage.
The low pressure area on the pressure side decreases the blade tip load of blade 2 close to the leading edge, generating a weak clearance vortex above the blade itself which does not interact with blade 3.
The pressure field at time $t_0+\tau_{rot}/8$ in Fig.A.14-b shows a migration of LP1 downstream: this causes a lower blockage within the passage, restoring the correct blade load at the leading edge of blade 2. The clearance flow of blade 2 tends then to increase, interacting with the pressure side of blade 3 and leading to a variation of blade load (and consequently of tip flow intensity). Such unsteady tip vortex fluctuation is responsible of the rotating pressure disturbances depicted in Fig. A.12, and leads to a regular fluctuation of the tip shocks and consequently a fluctuation of the induced separation, observed in Fig. A.11b.
The generation of a rotating disturbance due to the tip flow unsteadiness was also experimentally observed by Mailach et al. [148] and numerically by Yamada et al. [149] for axial transonic compressors with relatively large tip clearance. For radial impellers, to the best of the author's knowledge, this is the first time that a direct observation and description of the phenomenon is given.
One can also point out an analogy between the rotating cells described and what Fringe and Van den Baenbussche [144] experimentally observed and defined as mild impeller rotating stall (MIRS). The mild impeller rotating stall is in fact characterized by an high number of cells with low rotation velocity and generates a relatively weak fluctuation of the pressure field. Due to the limited measurement capabilities of the time, little explanation of the phenomenon was given.
Despite the presence of the rotating blockage cells and of the separated flow downstream of the shock, a degradation of performance is not observed, because of the much higher isentropic contribution of the centrifugal force in the pressure rise with respect to the aerodynamic one.

A.4.4. Centrifugal Compressor With Bent Pipe

Ai it was done for the previous configuration, three different operating conditions are analyzed by URANS for the impeller with bent pipe placed in front. The outlet condition (defined in equation A.1) is applied with the κ values shown in Table A.3.

To describe the flow distortion at the impeller inlet, the viscous flow field

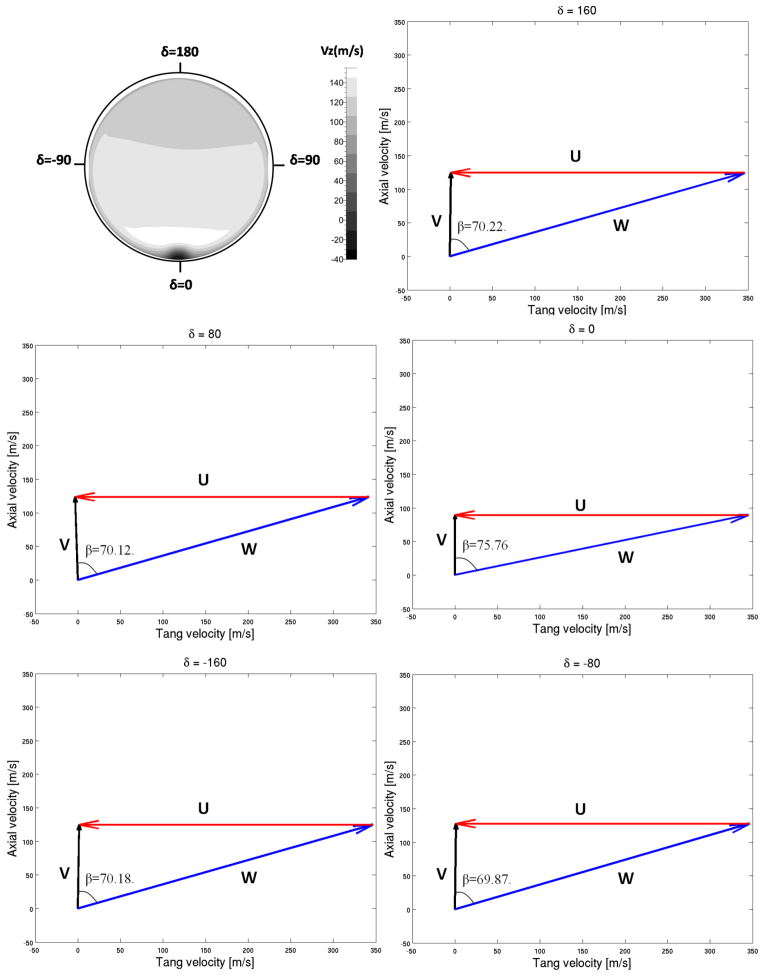

Figure A.15.: Incidence of the flow entering the compressor for the blade to blade plane at 92% of span. Vectors are averaged around 9 arcs representing the inlet of each passage and imposed at a distance z/c_{main} =-0.06 from the leading edge of blades.

at the outlet of the analyzed bent pipe is shown in Fig. A.15 for C5. In the same figure, the geometrical angle δ used in this chapter to describe the flow is also reported for later reference. At $\delta = 0°$, where a strong increase in axial velocity would be expected from potential flow theory, a low momentum zone is present indicating a separation. The typical secondary flow pattern in the elbow consists of two counter rotating vortices which are schematically represented by arrows in Fig.A.15. These vortices lead to

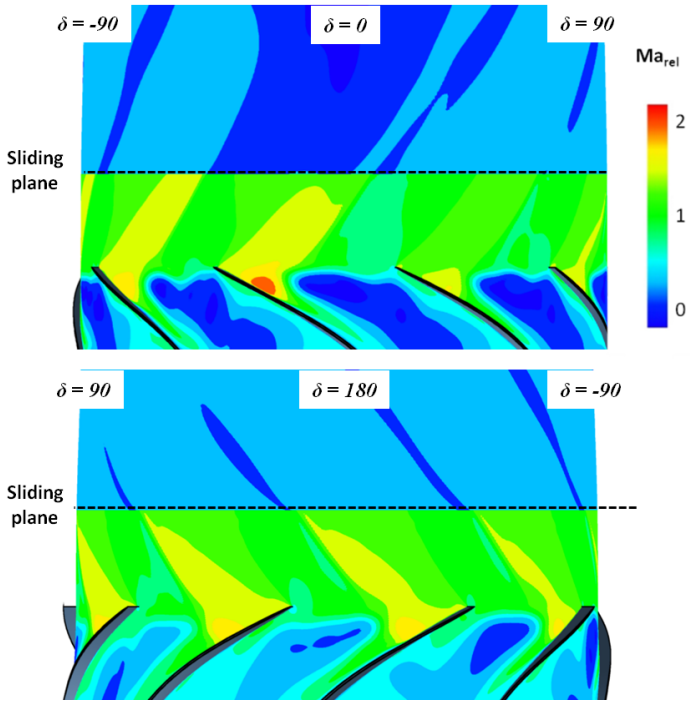

Figure A.16.: Relative Mach field along the annulus for C5.

positive incidence for the blades located at negative δ angles, and positive incidence for the blades located at positive δ.

Fig.A.15 shows also the instantaneous velocity triangles at the leading edge of five compressor blades at 92% of span for the same case C5. The velocity triangles are evaluated considering the circumference at the required radius at a distance z/c_{main}=-0.06 from the blades (where the subscript *main* differentiate the main blade from the splitters); the circumference is then divided in nine equal arcs (each one representing the flow interacting with a specific blade) and the incidence is computed by the spatially averaged velocity components along such sections.

When the bent pipe is installed in front of the compressor, the strongest effect on the incidence is linked to the presence of the recirculation zone at δ= 0°, which results in a large incidence on the profile at that position. The flow angle passes in fact to 75.7° from the average value of 70.1°, resulting in a 5.6° change in incidence. The effect of the secondary flows appears instead to be negligible.

Fig.A.16 represents the relative Mach field at 92% of span for case 5 along the whole annulus. The structure of the flow at the inducer tip is completely different with respect to the case with straight pipe (Fig.A.11b): the most

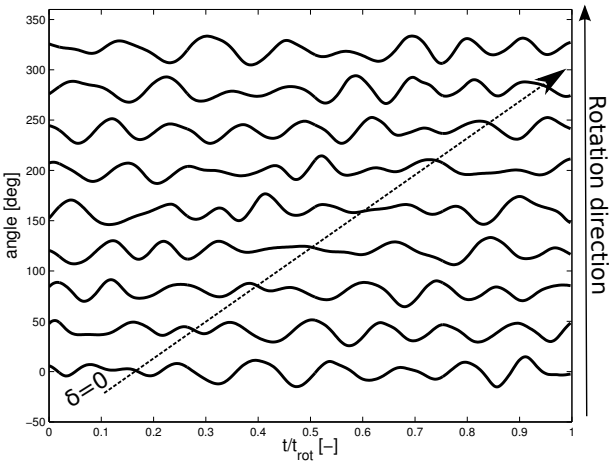

Figure A.17.: Pressure fluctuations over one rotation for the numerical probes imposed in the relative frame of reference. The effect of the recirculation at the pipe outlet is depicted by an arrow.

important influence on the unsteady flow field is due to the recirculating flow at the pipe outlet, which interacts with the blades in between $\delta = +45°$ and δ = -45°.

In the area around δ= 0°, the increasing blade load generates a strong tip

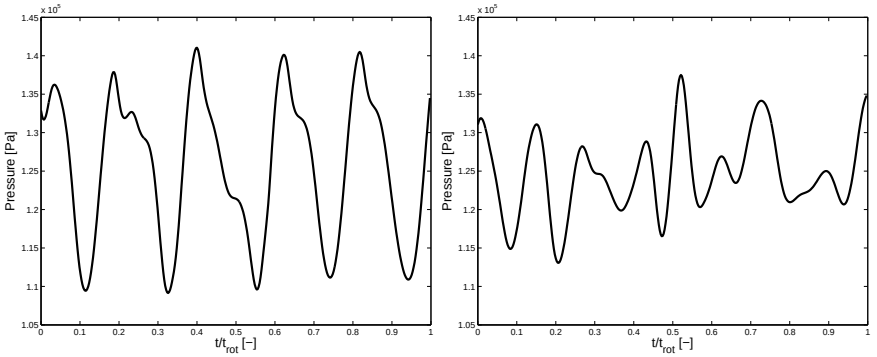

Figure A.18.: Pressure signal over one rotation one of the probes, case 5 (on the right) and case 1 (on the left).

vortex that breaks down and interacts with the following blade, increasing the flow blockage in a similar way to what happens for the configuration with straight pipe. On the other hand, in the upper part of the duct (closer to δ= 180°) the incidence decreases, leading to a lower blade load at the leading edge and a weaker tip vortex. The tip vortex mainly interacts with

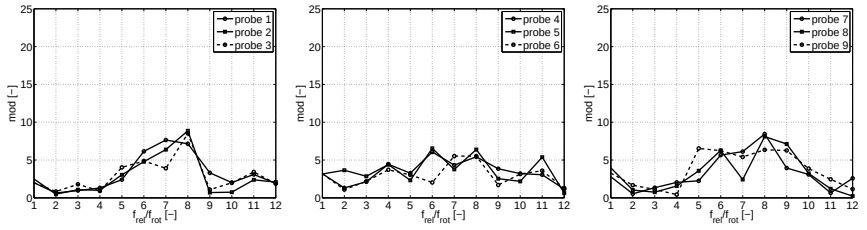

Figure A.19.: Fast fourier transform of the signals represented in Fig. A.17.

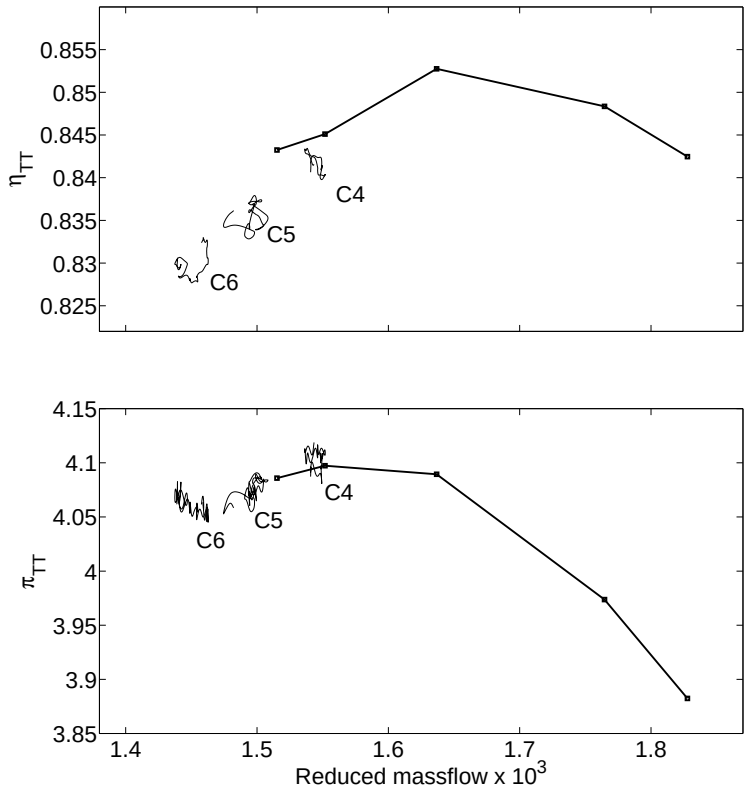

Figure A.20.: Overal performance of the compressor for cases 4, 5 and 6: total to total pressure ratio (lower part) and total to total efficiency (higher part) together with RANS results for higher massflow operating points.

the flow at the center of the channel, avoiding the propagation of the rotating disturbance among the different blades according to the mechanism previously explained.

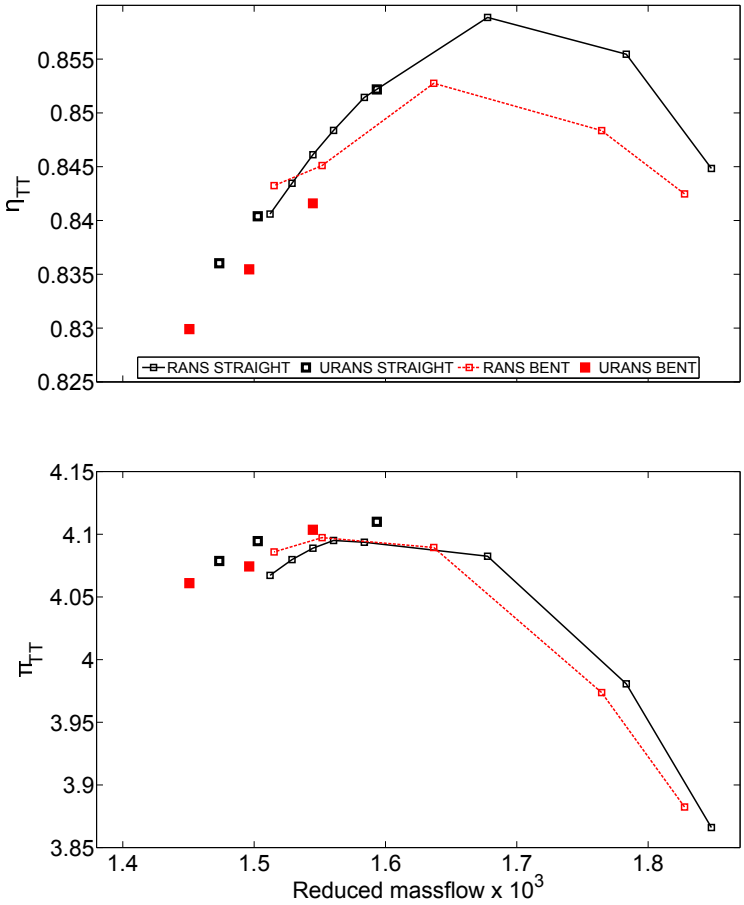

Figure A.21.: Comparison between averaged results for the straight and bent pipe in terms of total to total pressure ratio (lower part) and total to total efficiency (higher part).

This conclusion is confirmed by looking at the signal from the probes already used for the previous configuration, plotted in Fig. A.17. For the case discussed (case 5), the only disturbance propagating within the annulus is the one due to the recirculation at the pipe outlet. The average rms of the fluctuating amplitude of the signals in Fig. A.17 is equal to 8.5% of the mean pressure value, representing a reduction of 30% with respect to the configuration with straight pipe. A comparison for the two cases is given in Fig. A.18 for one of the probes as example.
The FFT of the nine signals, shown in Fig. A.19, points out that there is no frequency contribution that is clearly predominant on the others, as it was

for Fig. A.13. This is clearly representative of the fact that the mutual unsteady interaction between the passages, which determines the propagation of the mild stall cells for the configuration with straight inlet, is not present in this case.
One can thus conclude that the inlet distortion generated by the bent pipe has a crucial effect in avoiding the formation of the rotating blockage generated by the blade tip vortex for the operating points analyzed.
The presence of the one per revolution perturbation, due to the bent pipe, interacts with the higher natural frequency of the stall cells rotating within the annulus, preventing their formation. Since the external disturbance leads to a fluctuation in time of the blade load, an amplification of the rotating stall behavior can be expected when the fluctuating load frequency and phase coincide with one of the harmonics of the rotating stall itself. This effect is therefore unlikely to happen in real applications, and thus no further investigated in this work.
The performance is plotted in Fig. A.20 both for unsteady and steady RANS simulations. Features characterizing the inception of surge are not noticed for the three cases analyzed. The performance are then compared to the ones obtained with the straight pipe in Fig. A.21. To simplify the visualization, the time-averaged values is plotted for the URANS simulation.
As expected, the unsteady solutions for the bent pipe configuration show a lower time-averaged efficiency compared to the one obtained for the straight pipe, as it is affected by the flow separation in the elbow. Nevertheless, the time-averaged pressure ratio is similar, strengthening the consideration that the compressor in study is not significantly affected by different aerodynamic configurations of the flow field close to stal, because of the high contribution of the centrifugal forces to compression. On the other hand, stronger effect due to the bend is depicted by the steady results at higher massflow, confirming the experimental observations of Ariga et al. [154].

A.5. Final remarks

A numerical unsteady analysis of the flow field within a centrifugal compressor is discussed in this chapter, with the aim to study the influence of the inlet duct shape on the stall inception mechanisms. Two configurations of the inlet duct are considered, modeling a straight pipe and a 90 degree bent pipe. The latter is representative of typical configurations which can be found because of space limitations.
To correctly reproduce the stall pattern from the numerical point of view, care must be taken to avoid the imposition of non-physical periodicity, as well as the inception of surge cycles; at this scope, the full annulus of the machine is modeled and more stable outlet boundary conditions are employed with respect to the classical Dirichlet pressure conditions.

When the bent pipe is not present, the tip vortex interacts with the shock close to the leading edge and breaks down, interacting with the flow field inside the blade passage. The breackdown generates an unsteady blockage that rotates within the annulus. For this particular case, 8 cells rotating at 36% of the rotor speed are detected, mainly affecting the tip of the blades only. The rotating disturbances also influence the tip shock position and intensity, as well as the induced flow separation, generating a mild stall of the impeller.
When the bent pipe in front of the impeller is considered, the recirculating flow within the elbow causes blockage at the compressor inlet. Because of that, the incidence increases at the tip of blades interacting with the low-momentum flow, and decreases when the blades interact with higher momentum flow. The periodic variation of incidence clearly affects the tip vortex behavior, avoiding the formation of the rotating blockage pattern pointed out for the straight pipe case operating at the same massflow.
Despite the different flow field inside the machine, no noticeable difference is observed between the two configurations in terms of performance close the stability limit. This is due to the centrifugal effect on the compression, which is dominating the aerodynamic one. Conversely, the steady analysis with frozen rotor approach shows a higher influence of the pipe on the performance at higher massflow, with a pronounced reduction of pressure ratio and effectiveness for the configuration with bent inlet.

Appendix B.

Validation of the NSCBC implemented in OpenFOAM

The NSCBC implemented in the framework of this thesis is assessed on typical test cases with increasing difficulty;

- The shock tube, to test the interaction of the outlet anechoic boundary with a pressure waves.
- The Euler vortex, to test the interaction of the outlet anechoic boundary with a vorticity wave.
- The high-Reynolds vortex shedding, to test the interaction of the outlet anechoic boundary with the structures generated by a realistic High-Re case.

All simulations are performed by using the compressible p-based solver rhoPimpleFoam, modified to include the NSCBC treatment. A second order central scheme in space is employed for the convective terms (filteredLinear scheme in OpenFOAM), while the solution is advanced in time using an explicit Euler scheme.

B.1. The shock tube

The shock tube is a classical test to assess the capability of anechoic conditions to let a pressure wave cross the patches without spurious reflections. The test consists of a free flow initialized with discontinuous pressure and temperature fields.
At $t = 0$, the flow is characterized by a uniform velocity $U = 40m/s$. $T = 278.75K$ and $p = 95000Pa$ are imposed in the first half of the domain, while a uniform temperature and pressure $T = 348.423K$ and $p = 100000Pa$ are imposed in the second half.
From the numerical standpoint, a laminar computation is performed on a 1D domain discretized by 1000 elements. Fixed velocity and temperature are imposed at the inlet, while the outlet is treated with the NSCBC approach. The time step is chosen to keep $CFL < 1$ everywhere. Figure B.1 shows the pressure evolution in time along the domain. The time is nondimensionalized

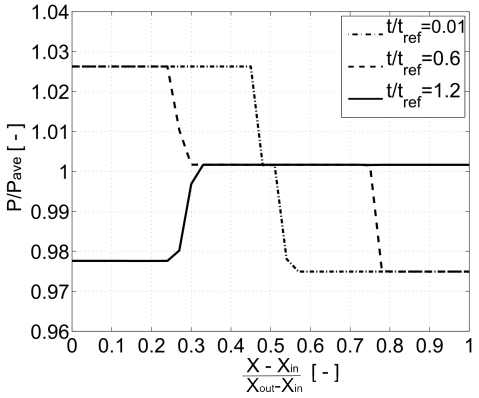

Figure B.1.: Evolution of the shock tube solution. NSCBC are used at outlet (X=1).

by $t_{ref} = L_{dom}/2c$ with L_{dom} indicating the domain length and $c = \sqrt{\gamma RT}$ the speed of sound computed for $T = 348.423K$. At $t = 0$ backwards and forward-moving pressure waves are generated. The wave propagating backwards is reflected by the Dirichlet boundary conditions imposed at the inlet, while a perfect transmission of the upstream-moving wave can be observed at the outlet. The reflection coefficient of the outlet patch is computed by using the 2-microphones method [161], resulting almost exactly zero.

B.2. Euler vortex convected across the outlet

The anechoic formulation of the NSCBC is tested on a two-dimensional inviscid compressible vortex (defined as Euler vortex) convected through the non-reflecting boundary.
The initial condition of the problem corresponds to a single vortex superimposed on a uniform flow field with a constant velocity U_0 aligned with x. The vortex can be described by the mathematical formulation in Eq. 3.23. The computational domain is represented by a square of $L_{dom} = 10R_v$, discretized by a 100x100 2D grid. The initial conditions are obtained by mapping the mathematical shape of the vortex at the domain center. Constant $T = T_0$ and $U = U_0$ are imposed at the inlet, while anechoic NSCBC are used at the outlet imposing $p_{Inf} = 100000Pa$, $\beta = 0.3$ and $\lambda_{Inf} = L_{dom}$. The set-up is such that the vortex will be convected towards the domain outlet in x direction starting from $t = 0$.
Two different conditions are considered, representing two vortices characterized by a different intensity.

- $C_v = 2.5m^2/s$, $R_v = 0.01$, $U_0 = 100m/s$, $T_0 = 1500K$, $p_0 = 100000Pa$
- $C_v = 0.2m^2/s$, $R_v = 0.01$,$U_0 = 100m/s$, $T_0 = 1500K$, $p_0 = 100000Pa$

Results in time will be presented with respect to $t_{ref} = L_{dom}/U_0$.
In Fig. B.2 three different snapshots of pressure and velocity fields are presented for the case at $C_v = 0.2m^2/s$. The pictures represent the vortex approaching the outlet ($t/t_{ref} = 0.375$), the center of the vortex crossing the outlet ($t/t_{ref} = 0.5$), and the vortex leaving the domain ($t/t_{ref} = 0.625$).

Close to the non-reflecting boundary, no noticeable deformations of the

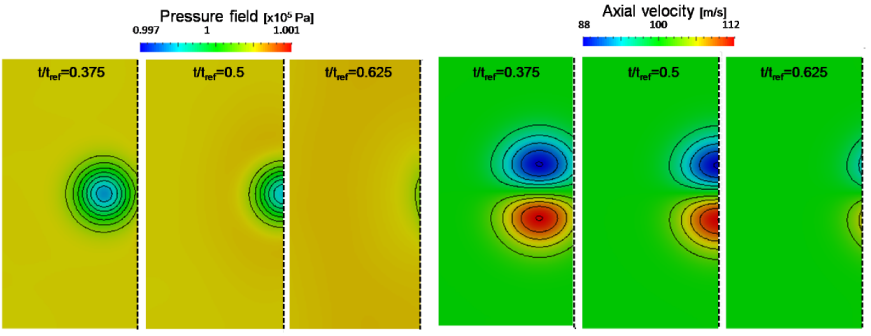

Figure B.2.: Validation of the NSCBC: vortex crossing the outlet. $C_v = 0.2m^2/s$.

velocity field are observed. The accuracy of the solution is satisfactory also in terms of pressure field, although one can notice the formation of a reflection wave moving upstream, which is limited in amplitude with respect to the local pressure value.
To quantify the error induced by the boundary condition implemented, $\epsilon_{\Delta p}$ is introduced:

$$\epsilon_{\Delta p} = \frac{p_{CFD} - p_{exact}}{p_{Inf} - p_{exact,r=0}} \tag{B.1}$$

Where p_{CFD} stands for the pressure value numerically calculated. The analythical solution p_{exact} of the vortex crossing the outlet can be obtained considering that a vortex convected can be described by the following equation:

$$\frac{\delta p}{\delta t}_{exact} + U_0 \frac{\delta p}{\delta x} = 0 \tag{B.2}$$

which can be used to integrate in time the initial solution of Eq. **??**.
In Fig. B.3, the evolution of the error is monitored at the outlet along y for the three time instants previously introduced ($t/t_{ref} = 0.375 - 0.5 - 0.625$). For both configurations studied, the maximum difference between the exact and the numerical solution is obtained for $t/t_{ref} = 0.5$ (i.e. when half of the vortex has crossed the outlet) and it remains always lower than 0.25%.

The positive error indicates that the low-pressure peak at the vortex center is underestimated with respect to the mathematical result, therefore the vortex crossing the outlet is attenuated. The amplitude of the attenuation is in line with the one obtained by other authors [83], therefore the NSCBC implemented can be considered successfully validated for the test case discussed.

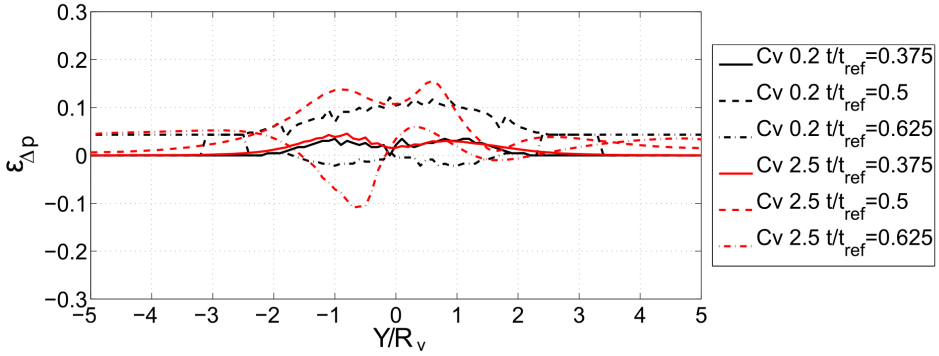

Figure B.3.: Error $\epsilon_{\Delta p}$ in function of y at the outlet.

B.3. High Reynolds vortex shedding test case

Before using the NSCBC for coupled simulations on industrial configurations, these shall be validated on a High-Reynolds flow. The High-Reynolds test case represents two cylinders in tandem, placed at a distance $L = 5.5d_{cyl}$ from each other, where d_{cyl} stands for the diameter of the cylinder. The two cylinders are centered on a rectangular domain whose dimensions are $\Delta x = 25.5d_{cyl}$ and $\Delta y = 20d_{cyl}$ in axial and transversal direction respectively. The velocity and temperature at the inlet are fixed to get $Re = 400000$ (based on the cylinder diameter) and $M = 0.3$ within the domain (as already discussed in chapter 4. At the outlet the Lodato's version of the NSCBC is used, imposing $p_{Inf} = 400000Pa$, $\beta = 0.3$ and $\lambda_{Inf} = 5 \cdot L_{dom}$.
The domain is discretized by the structured grid shown in Fig. B.4. $1.3 \cdot 10^6$ cells are used, keeping $Y+$ lower than 5 at walls, while $X+/Z+$ are limited to 150. The subgrid scales are modeled by the Smagorinsky model with the Van Driest formulation. A time step $dt = 10^{-8}s$ is employed to keep CFL¡1. The Pope criterion for the current simulation is shown in Fig. B.6. For the purpose of the study, a very accurate resolution close to the wall is not needed. The grid is instead more refined downstream to resolve the fluctuating wake interacting with the outlet patch.

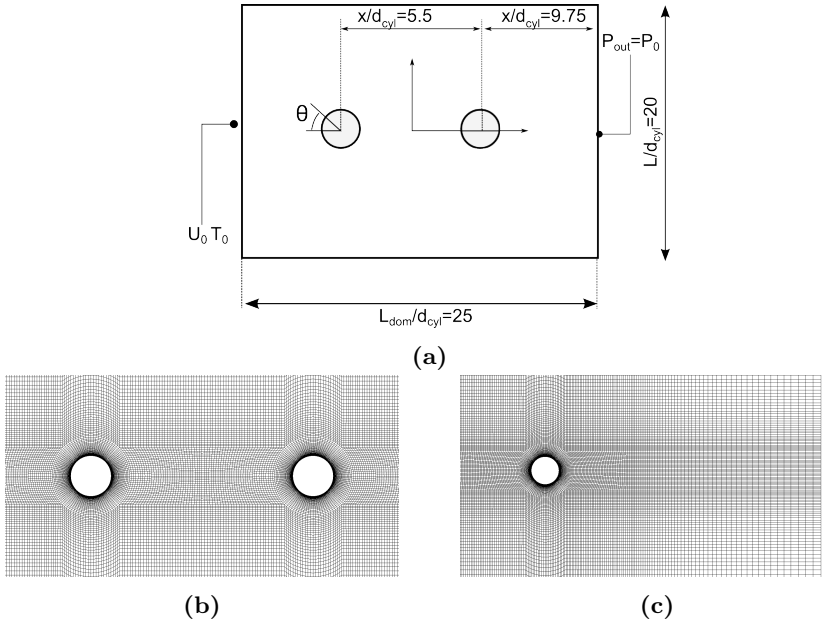

Figure B.4.: High-Reynolds vortex shedding test case: reference domain (a). Detail of the grid between the cylinder (b). Detail of the grid between the cylinder downstream and the outlet (c).

The results are depicted in Fig. B.5, where the coherent turbulent structures obtained with the Q criterion are shown together with the instantaneous velocity and pressure fields. Despite the fact that the domain is relatively short (the outlet is located at $\Delta x/d_{cyl}$=9.75 from the center of the cylinder downstream) both pressure and velocity fields appear smooth and the presence of the vortex shedding can be clearly depicted. The vortical and turbulent structures developed within the domain, visualized by the Q criterion, are convected across the outlet without observing numerical deformation.
The same simulation performed by using the standard convective outlet conditions (implemented as default in OpenFOAM) leads to strong non-physical oscillations of the pressure field, which compromises the quality of the solution. From this study, one can conclude that the simulation is not feasible with standard convective conditions, and the use of the NSCBC is necessary to stabilize the pressure field within the domain.
Considering the application of the NSCBC to coupled simulations, it is worthwhile to point out that the averaged pressure obtained at the outlet is 1.5% lower than p_{Inf}. Even though the error can be acceptable in several industrial applications, it leads to serious problem during the coupled computations; in this case, the transmission of the potential effect from

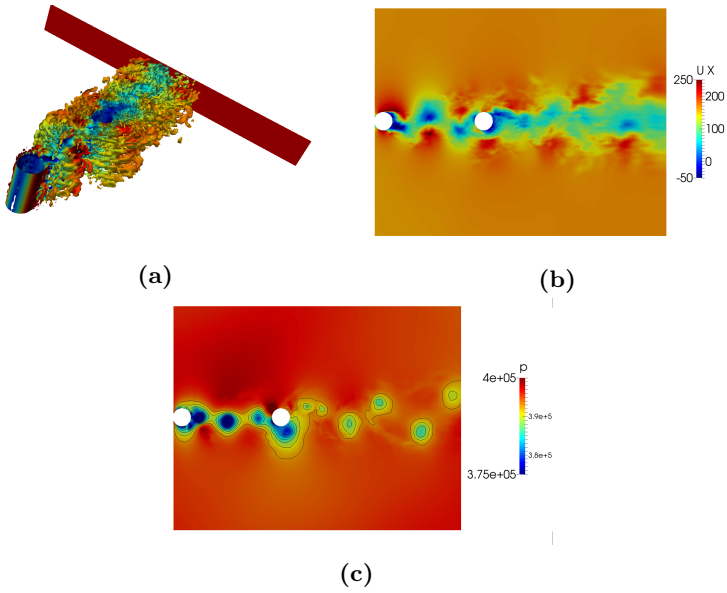

Figure B.5.: Solution obtained for the high Reynolds vortex shedding test case. 3D view of the turbulent structures (Q criterion) interacting with the outlet. The structure are colored in function of the local axial velocity value (a). Axial velocity field (b). pressure field (c).

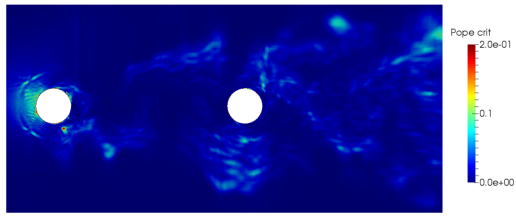

Figure B.6.: Pope criterion for the High-Reynolds vortex shedding test case.

the downstream to the upstream domain depends on an accurate imposition of $p_{out,ave} = p_{Inf}$. The possible techniques to impose more accurately p_{Inf} at the outlet are discussed in section 3.2.2.3.

List of Figures

1. Main components of a turboengine. 2
2. T-S diagram of the Brayton cycle. 2
3. Efficiency η_{TH} of the real Brayton cycle. 3
4. Turbulent scales resolved and modeled by each approach (elaborated from [9]. 5

2.1. Rich Quench Lean combustor scheme (a) and Dry Low NO_x combustor scheme (b). The fuel and air entering the primary zone are indicated in red, the diluition air in dark blue and the cooling flow in light blue. 12
2.2. Temperature field measured at the outlet of a military engine [31]. 13
2.3. The OTRF QinetiQ experimental facility (a) and the hot streak generator designed by Hall et al. [32] (b). Pictures from [32, 34]. 13
2.4. Experimental (a) and numerical visualization (b) of the flow field at the outlet of the QinetiQ test rig [34]. 14
2.5. Turbulence field at the QinetiQ test rig outlet obtained by URANS simulation [32]. 14
2.6. PIV of the velocity field measured at the center of the combustor simulator [36]. 15
2.7. Outlet temperature (a), swirl (b) and turbulence conditions (c) measured at the outlet of the FACTOR combustor simulator [36, 37]. 16
2.8. Nu distribution at 50% span of a NGV blade with and without HS imposed at the inlet (a) and schematization of the HS propagation for different clocking positions [31]. 17
2.9. Migration of the HS in a stator passage for different clocking configurations [40]. 18
2.10. Segregation effect for cold and hot streaks: scheme of the incidence variation elaborated from [46] (a). Experimental measurement of the relative inlet angle to the rotor of the MT1 stage, from Beard et al. [45]. 19
2.11. Secondary flows generated by the HS in the rotor passage [**?**]. 19
2.12. Temperature distribution calculated for the MT1 rotor blade [48]. 20
2.13. PIV visualization of the vortices formed downstream from a NGV passage with swiril imposed at the inlet [51]. 22
2.14. Swirl effect on the HS migration from Khanal et al. [53]. . . . 22

2.15. Turbulence level measure at the outlet of a RQL combustor operating in "cold" conditions [54]. 23
2.16. Total velocity isolines for low and high free-stream turbulence levels. Experimental investigation from Radomsky et al. [55]. 24
2.17. Experimental test rig used by Jenkins et al. [57, 58]. to investigate the interaction between HS and turbulence level (a). HS visualization on plane B for two different turbulence levels, results are shown for negative Z only (b). 25
2.18. Rotor blade surface heat fluxes. Solution of the HS-swirl combined case (left). Superimposed solution of two separated simulations (right) [53]. 26
2.19. Total temperature outlet at the high pressure NGV outlet computed with 2D inlet boundary conditions (left) and 1D inlet boundary conditions (right) [60]. 26
2.20. Potentiale effect of the NGV on the time averaged and rms temperature field within a combustion chamber from Roux et al. [24]: geometry investigated (a), time averaged (b) and RMS (c) temperature distribution. 28
2.21. Comparison of the velocity profile in different axial positions within a combustor: simulations with and without NGV downstream [23]. 28
2.22. Numerical decay of the inlet turbulence level upstream the NGV LE obtained by RANS. It clearly shows that for high inlet TU the turbulent decay must be tuned with care to avoid a quasi-laminar free-stream flow at the NGV LE. Results from Wang et al. [59]. 32
2.23. LES and RANS TU distribution resolved within the NGV passage, compared to experimental visualizations at the NGV outlet. Results from Cha et al. [54]. 33

3.1. Scheme of the two possible approaches in space for coupled simulations. The solver applied to the domain upstream (D_u) is coupled to the one for the domain downstream (D_d). . . . 41
3.2. Scheme of the two possible approaches in time for coupled simulations. The solver applied to the domain upstream (D_u) is coupled to the one for the domain downstream (D_d). . . . 42
3.3. Scheme of the upstream subdomain outlet with characteristic waves. 44
3.4. Frequency response of the time marching average filter. The time is defined in linear scale on the left, while it is defined in logaritmic scale on the right. 47
3.5. Filtering of the signal obtained along the wake of a cylinder at $X/d = 3.5$. The flow is solved by LES. $Re = 400000$. Time domain. 48

3.6. Filtering of the signal obtained along the wake of a cylinder at $X/d = 3.5$. The flow is solved by LES. $Re = 400000$. Frequency domain. 49
3.7. Frequency response of the time marching average filter (in black) compared to the simplified expression 3.15 (in red), to estimate the damping of f_c and $f_{t,LES}$. 51
3.8. Damping of the signal $m_{c,LES}$ (a) and $m_{t,LES}$ (b) in function of the sampling frequency. 52
3.9. Visualization of an ideal vortex approaching the outlet of the computational domain: $C_v = 2.5m^2/s$. 58
3.10. $\delta p/\delta t_{err}$ along y for different values of β (a). $\delta p/\delta t_{err}$ with respect to β at $y = \pm/R_v$ (b). 59
3.11. Evolution of the outlet pressure between two consecutive time instants for different values of β. $\beta = 0$ (a), $\beta = 0.3$ (b), $\beta = 0.6$ (c). $dt = 10^{-6}s$. At t_0 the LES outlet is at $x = 2.5R_v$. 59
3.12. Optimum β in function of the vortex intensity C_v (a) and of the freestream Mach number (b). 60
3.13. Vortex approaching the domain outlet. $C_v = 2.5m^2/s$. Effect of the parameter β. The z axis is directed as the vorticity vector. 61
3.14. Pouiseuille flow developing between two planar surfaces. $x_1 = x$ and $x_2 = y$. 62
3.15. Domain including one single cylinder (a). Cylinders in tandem simulated to reproduce the potential effect (b). 63
3.16. Pressure distribution obtained at $\Delta x/d_{cyl} = -1.5$ from the downstream cylinder. 64
3.17. $P_{out,ave}$ distribution at the anechoic outlet for different values of λ_{Inf}. 65
3.18. Surface averaged pressure fluctuations at the anechoic outlet for the computations performed to test the p_{Inf} imposition at the outlet. 65

4.1. Method 1: structure of the LES-LES coupling procedure in space (right) and synchronization in time (left). 70
4.2. Method 2: structure of the LES-URANS coupling procedure in space (right) and synchronization in time (left). 72
4.3. 76
4.4. Scheme of the backwards-moving shock wave test case. On the left: method 1. On the right: method 2. 76
4.5. Shock propagation between the domains. 76
4.6. 77
4.7. Scheme of the convected Euler vortex test case. On the left: method 1. On the right: method 2. 77
4.8. Error $\epsilon_{\Delta p}$ in function of the Y coordinate at the outlet for the two coupling procedures. 78

4.9. Vortex convection between the domains. Method 1 is applied. 79
4.10. Vortex convection between the domains. Method 2 is applied. 80
4.11. Wiggles generated at the inlet of the upstream domain when method 2 with strong coupling is applied. 81
4.12. The turbulent channel geometry with boundary conditions. . 82
4.13. Detail of the 2D grid used for the RANS simulations of the turbulent channel: passage center. 83
4.14. Velocity distribution close to the wall computed by CFD and compared to the results of Eckelmann [90]. 83
4.15. Friction coefficient computed by CFD and compared with the correlation of Dean [92]. 84
4.16. RMS velocity fluctuations computed by the experiments of Kreplin et al. [91] and the current simulation. 85
4.17. Upstream and downstream subdomains for the URANS-URANS coupled simulation of the cooling channel. 85
4.18. Convergence of the URANS-URANS coupling procedure: pressure evolution at the overlapping region center. 86
4.19. Axial velocity (a) and pressure (b) distribution in X direction for the URANS-URANS coupled solution. 86
4.20. Axial velocity (a) and TKE profile (b) in Y direction for the URANS-URANS coupled solution. Results at the overlapping region center. 87
4.21. Upstream and downstream subdomains for the LES-URANS coupled simulation of the cooling channel. 87
4.22. LES and URANS signals in correspondence of the URANS subdomain inlet section. The signal is monitored in the middle of the channel for two values of T_s 89
4.23. Velocity field close to the LES-URANS interface. 89
4.24. Axial velocity (a), TKE (b) and pressure profile (c) in Y direction for the LES-URANS coupled solution. Results in correspondence of the URANS subdomain inlet section. . . . 90
4.25. Scheme of the cylinders in tandem test case. 92
4.26. Mesh used for the coupled computation of the cylinders in tandem: general view of the mesh (a). Detail of the overlapping region (b). 93
4.27. Procedure to evaluate T_s considering the attenuation error of signal $m_{c,LES}$ (a) and the spurious propagation of the signal $m_{t,LES}$ (b). 94
4.28. FFT of u_x evaluated on the upstream and downstream solution in the position where the downstream inlet is located for two coupled simulations, including 20 (a) and 200 (b) LES snapshots for the average. 95
4.29. TKE field resolved by the coupled procedure with passage of TKE from LES to RANS (a), passage of TKE/3 from LES to RANS (b), full URANS (c). 97

4.30. Decay of the resolved velocity fluctuations by URANS. The coordinate x goes from the downstream cylinder wall to the domain outlet (x=1). 98
4.31. Vorticity field resolved by the coupled procedure (a), and full URANS (b). 99
4.32. Continuity of u_x (a), pressure (b) and TKE (c) in y direction at the overlapping center. 100
4.33. Time averaged field obtained by the coupled simulation: mean axial velocity (a) mean pressure field (b). 101
4.34. C_p distribution for the cylinder upstream (a) and downstream (b). Experimental data for the cylinder downstream are at lower Reynolds number than the one considered in this work, therefore it can be used as reference only. 102
4.35. Strouhal number evolution with respect to the Reynolds number: experimental values for single cylinders and present computations of two cylinders in tandem. 103
4.36. Interface of the non-coincident grid used for the LES-LES coupling. 103
4.37. Instantaneous pressure (a) and velocity (b) fields obtained for the coupled simulation. Isolines for the upstream computation are pointed out in black, the ones for the downstream are in white. 104
4.38. TKE spectrum for probes 1, placed at $x/d_{cyl} = 2.75$ from the upstream cylinder (a) and for probe 2, placed at $x/d_{cyl} = 2.75$ from the downstream cylinder (b). 105

5.1. 3D view (a) and sections of the airfoil at 15%, 50% and 85% of span (b) of the prismatic NGV designed to investigate the combustor-turbine interaction. 112
5.2. 3D view (a) and sketch (b) of the combustion chamber designed in the COPA-GT framework to investigate the combustor-turbine interaction. 114
5.3. Grid employed for the study of the LS89 2D profile. 116
5.4. Isentropic Mach number distribution for the LS89 profile. Conditions MUR 45 and MUR 47. Results are obtained with FINE/Turbo (a) and OpenFOAM (b) employing second order central schemes and the $k - \omega$ SST turbulence model. 116
5.5. Absolute Mach number flow field for the LS89 profile with MUR 47 obtained with FINE/Turbo (a) and OpenFOAM (b). Experimental schlieren picture of the LS89 flow at $M_{2,is} \sim 1.02$ (c). 118
5.6. Inlet conditions imposed for the mesh convergence study. . . 119
5.7. Mesh convergence study: convergence of the blade pressure distribution. 120

5.8. Mesh convergence study: convergence of $\Delta p/p_{tot,in}$ (a), Φ_T (b) and turbulence on P41 (c). 121
5.9. Snapshots of the grid used to reproduce the 3D NGV. General view (a) and blade to blade view (b). 122
5.10. Total temperature distribution within the passage for Mesh 0 (a), Mesh 1 (b) and Mesh 2 (c). 123
5.11. Axial vorticity distribution within the passage for Mesh 0 (a), Mesh 1 (b) and Mesh 2 (c). 124
5.12. Outlet total temperature distribution within the passage for Mesh 0 (a), Mesh 1 (b) and Mesh 2 (c). 124
5.13. Axial vorticity distribution at the outlet for Mesh 0 (a), Mesh 1 (b) and Mesh 2 (c). 125
5.14. Comparison of $T_{tot}/T_{tot,ave}$ and $RTDF$ obtained for the current geometries and for other modern geometries in literature. 126
5.15. Streamlines into the combustor colored by the total temperature. 127
5.16. Streamlines of the cooling and interaction with the hot streak generated by the combustion. 127
5.17. Comparison of $T_{tot}/T_{tot,ave}$, swirl and Turbulence obtained by FINE/Open and XiFOAM on Mesh 0. 129
5.18. Grid used for the to model the combustor during the analysis of the combusor-turbine interaction. 130
5.19. Isentropic Mach number distribution of the 3D NGV with uniform inlet conditions. 131
5.20. Coupled domain for the combustor-turbine simulation. The overlapping region is shown in detail. 131
5.21. Pressure fluctuations monitored by one of the probes in the overlapping region during the stabilization of the communication process. 132
5.22. Mach distribution at the interface between the domains. The distribution obtained for the turbine is pointed out by black isolines, while white isolines are used for the combustor. . . . 133
5.23. Total temperature development within the NGV passage. The swirl and the secondary flows are indicated by arrows. 134
5.24. Adiabatic wall temperature distribution on the NGV for the coupled case. 135
5.25. M_{is} at 15% of span (a) 50% of span (b) and 75% of span (c) with uniform inlet boundary conditions and for the coupled simulation. 136
5.26. Total temperature distribution and flow streamlines within the combustor. The swirl vortex migration is highlighted. . . 137
5.27. Scheme of the swirl migration inside the combustion chamber. 137
5.28. Pressure distribution at successive axial positions upstream from the blade leading edge. The distance from the blade LE at 50% span is indicated in the graph. 139

5.29. Axial momentum distribution at successive axial positions upstream from the blade leading edge. The distance from the blade LE at 50% span is indicated in the graph. 139
5.30. Total temperature distribution at successive axial positions upstream from the blade leading edge. The distance from the blade LE at 50% span is indicated in the graph. 140
5.31. Turbulence distribution at successive axial positions upstream from the blade leading edge. The distance from the blade LE at 50% span is indicated in the graph. 140
5.32. circumferentially-averaged profiles of pressure (a), axial momentum (b), total temperature (c) and turbulence (d) on a plane at $X = 55\%C_{ax}$ upstream from the blade leading edge. 142

6.1. Load distribution experimentally obtained for the T106-C. $Re = 80000$ (a), $Re = 140000$ (b), $Re = 250000$ (c). 149
6.2. General view of the grid (a). Zoom of the mesh close to the rear suction side (b). 150
6.3. Physical CFL field across the domain. 152
6.4. Blade load distribution at $Re = 80000$. LES, experimental and RANS distributions are compared. 153
6.5. Negative axial velocity profile in the rear suction side. 154
6.6. Losses (a) and outlet angle (b) variation with Reynolds. Experimental and numerical results are compared. 154
6.7. Total pressure profile at $x/C_{ax} = 0.465$ downstream from the blade TE. Y indicates the transversal direction. 155
6.8. Post processing planes used to visualized the wake profile. The entropy field in the blade to blade plane is shown. 155
6.9. Wake evolution on two planes at different distance from the blade TE. Y indicates the transversal direction. 156
6.10. FFT for the three probes listed in Tab. 6.4 157
6.11. Q criterion applied to the LES flow field. 158
6.12. Visualization of the vorticity field. 159

7.1. Schematic evolution of base pressure in function of downstream pressure. 163
7.2. Cascade and view of the blade with rotatable trailing edge cylinder. 164
7.3. Effect of downstream Mach number on trailing edge pressure distribution. 165
7.4. On the left: 2D view of the final mesh around the blade. On the right: detail of the mesh at trailing edge. 167
7.5. Blade Mach number distribution. 168
7.6. Boundary layer profiles close to the trailing edge: pressure side left suction side right. 168

7.7. Time averaged pressure distribution along the trailing edge. RANS and URANS results are from Leonard et al. [133]. . . 169
7.8. Angular distribution along the trailing edge of the phase-lock averaged amplitude of pressure fluctuations. 169
7.9. Snapshots of the instantaneous static pressure distribution along the trailing edge. 170
7.10. Schlieren visualization of the flow field at $M_{2,is}$=0.79. 171
7.11. Blade suction side unsteady pressure fluctuations: experimental-left [130]; numerical-right. 172
7.12. Comparison of trailing edge base pressure variation at transonic outlet conditions. 173
7.13. Wake density gradients and vorticity for $M_{2,is}$=0.97 (a) and $M_{2,is}$=1.05 (b). 174
7.14. Unsteady pressure fluctuations for $M_{2,is}$=0.97. 175
7.15. Unsteady pressure fluctuations for $M_{2,is}$=1.05. 176
7.16. Angular distribution along the trailing edge of the phase-lock averaged amplitude of pressure fluctuations for all cases investigated. 176
7.17. Strouhal number for different outlet conditions obtained with CFD and experiments. 177

8.1. Sketch of the test rig designed within the European project FACTOR. Dimensions are referred to the axial chord of the NGV. 180
8.2. Configurations reproduced by LES: clocking PA (a) and clocking LE (b). 182
8.3. Detail of the mesh used for the RANS analysis. 184
8.4. TKE decay measured between the domain inlet and one plane placed 0.2 $C_{ax,s}$ downstream from P40. RANS results are obtained employing the SST model with different μ_T/μ at the inlet. 186
8.5. Effect of the turbulence model on the TKE distribution within the NGV passage. 188
8.6. Evolution of turbulent kinetic energy within the HPT stage-mid span evolution. 189
8.7. Total temperature distribution on P405 and P41 for RANS and LES. 190
8.8. Radial distributions of Φ evaluated for RANS and LES on P40, P41 and P42. 191
8.9. F_2 distribution (a) and μ_T/μ definition (b) activated for the SST model within the channel for different turbulent decays imposed at the inlet. 193
8.10. M_{is} distribution at 50% of span for NGV 1 for different turbulence models. 194

8.11. T_{tot} distribution within the passage and visualization of the HS and CS propagation. 196
8.12. Adiabatic wall temperature distribution on the vanes. Clocking PA case. 197
8.13. Adiabatic wall temperature distribution on the vanes. Clocking LE case. 197
8.14. Difference in temperature distribution on the NGV surfaces: the effect of μ_T/μ is investigated by plotting $T_{ad,w}^{case2} - T_{ad,w}^{case4}$ along the blade, adimensionalized by $T_{tot,P40}$. 198
8.15. Adiabatic temperature distribution on the rotor surface for the clocking PA and clocking LE cases. The SST model with μ_T/μ=1513 at the inlet is compared to the result with μ_T/μ=17 as well. 198
8.16. Blade load distribution for the case with uniform inlet conditions and for the clocking PA configuration at 30%, 50% and 70% of span. 199
8.17. Effect of the clocking on the aerodynamic load of the NGVs, 30% and 70% of span. 201
8.18. Scheme of the FFTB algorithm used for the CHT simulation. 202
8.19. Convergence history for the CHT simulation performed considering the blade in Torolon. 204
8.20. Blade in Torolon: Wall temperature distribution on the rotor blades for the CHT computation (a). Difference between CHT and adiabatic results (b). 204
8.21. Blade in metal: Wall temperature distribution on the rotor blades for the CHT computation (a). Difference between CHT and adiabatic results (b). 205

A.1. (a) Geometry of the radial transonic compressor analyzed. (b) Dimensions of the bent pipe considered for the analysis. . 220
A.2. Detail of the mesh used to reproduce the NASA rotor 37. . . 222
A.3. Experimental and numerical performance comparison for the NASA rotor 37. 223
A.4. Experimental and numerical performance comparison for the NASA37 rotor: Mach isolines at 95% of span. 223
A.5. Experimental and numerical performance comparison for the NASA rotor 37: axial velocity distribution at x/c=0.2. 224
A.6. (a) Detail of the mesh for two blade passage. (b) Detail of the tip clearance mesh. 225
A.7. Pressure distribution on the main blades at near stall conditions at 98% of the span. Comparison between the mesh with wall models and with direct resolution of the boundary layer. 225
A.8. Mach number close to the tip at near stall conditions reproduced by the mesh with wall models and with direct resolution of the boundary layer. Picture at 98% of the span. . . . 226

A.9. Overal performance of the compressor for cases 1, 2 and 3: total to total pressure ratio (lower part) and total to total efficiency (higher part) together with RANS results for operating points at higher massflow. The compressor curve (in red) respects the stability limit imposed by the resisting curves (in dashed red) for cases 1 and 2. 227
A.10. Schlieren picture of the flow field close to the tip for case C1 at 95% of the span. The clearance flow is indicated by red lines. 228
A.11. Instantaneous solution of entropy (a) and Mach (b) for case C1. Plane at 98% of span. The sonic line is depicted in red. . 229
A.12. Pressure fluctuations over one rotation for the numerical probes imposed in the relative frame of reference. The propagation of the disturbances within the annulus is depicted by arrows. 230
A.13. Fast fourier transform of the signals represented in Fig. A.12. 230
A.14. (a) Pressure field at 92% of span for case 1 at time = t_0 and (b) at time $t_0 + \tau_{rot}/8$. The tip flow streamlines of passage 1 are represented in black, while the one of passage 2 are represented in red. 231
A.15. Incidence of the flow entering the compressor for the blade to blade plane at 92% of span. Vectors are averaged around 9 arcs representing the inlet of each passage and imposed at a distance z/c_{main} =-0.06 from the leading edge of blades. . . . 233
A.16. Relative Mach field along the annulus for C5. 234
A.17. Pressure fluctuations over one rotation for the numerical probes imposed in the relative frame of reference. The effect of the recirculation at the pipe outlet is depicted by an arrow. . . . 235
A.18. Pressure signal over one rotation one of the probes, case 5 (on the right) and case 1 (on the left). 235
A.19. Fast fourier transform of the signals represented in Fig. A.17. 236
A.20. Overal performance of the compressor for cases 4, 5 and 6: total to total pressure ratio (lower part) and total to total efficiency (higher part) together with RANS results for higher massflow operating points. 236
A.21. Comparison between averaged results for the straight and bent pipe in terms of total to total pressure ratio (lower part) and total to total efficiency (higher part). 237

B.1. Evolution of the shock tube solution. NSCBC are used at outlet (X=1). 242
B.2. Validation of the NSCBC: vortex crossing the outlet. $C_v = 0.2m^2/s$. 243
B.3. Error $\epsilon_{\Delta p}$ in function of y at the outlet. 244

B.4. High-Reynolds vortex shedding test case: reference domain (a). Detail of the grid between the cylinder (b). Detail of the grid between the cylinder downstream and the outlet (c). . . 245
B.5. Solution obtained for the high Reynolds vortex shedding test case. 3D view of the turbulent structures (Q criterion) interacting with the outlet. The structure are colored in function of the local axial velocity value (a). Axial velocity field (b). pressure field (c). 246
B.6. Pope criterion for the High-Reynolds vortex shedding test case. 246

List of Tables

4.1. Range of applicability of the two coupling methods developed. 73
4.2. List of test cases presented in this chapter. 74
4.3. Continuity error at the interface for the LES-URANS coupling. High Reynolds cylinders in tandem. 102
4.4. Strouhal number evaluated by the simulations performed. . . 103

5.1. Boundary conditions for the design of the combustor-NGV test case. 110
5.2. Data of the combustion chamber. 114
5.3. Grids used for the convergence study. 117
5.4. Grids used for the convergence study of the combustor simulation. 123
5.5. Continuity error at the interface for the URANS-URANS coupling. Combustor-turbine interaction. 132
5.6. Surface averaged values of $T_0/T_{0,mean}$. 135

6.1. Details of the T106-C turbine blade in cascade configuration. 149
6.2. Details of the T106-C LES computation. 151
6.3. Results in terms of profile losses and outlet angle for $Re = 80000$. 153
6.4. Location of the numerical probes imposed for the unsteady analysis of the LES results. 156

7.1. Details of the blade investigated for the trailing edge flow field. The gauging angle is defined as $arcsin(l_{th}/g)$, with l_{th} the throat. 164
7.2. Features of the mesh. 167

8.1. Details of the boundary conditions and dimensions of the blades. 183
8.2. Cases run for the sensitivity analysis to μ_T/μ and to the turbulence model. 185
8.3. Total to total effectiveness calculated with different turbulence models with low and high inlet turbulent decay. 194
8.4. Effect of the non-uniform flow on the aerodynamic losses. . . 200

A.1. Design parameters for the centrifugal compressor in study. . . 219
A.2. Parameters of NASA rotor 37. 222
A.3. Values of k for the different cases analyzed according to equation 1. 226

A.4. Position of the probes used for the analysis. 229

Bibliography

[1] Rolls Royce Plc. *The Jet Engine. 5th edition.* Rolls Royce Technical Publications, 2005. 2

[2] M. P Boyce. *Gas Turbine Engineering Handbook.* Elsevier, London, UK, 2011. 3

[3] Shahpar, S., Caloni, S. Aerodynamic Optimisation of High Pressure Turbines for Lean-burn Combustion System. In *Proceedings of ASME Turbo Expo 2012. Paper N. GT2012-69228*, Copenhagen, Denmark, June 11-15 2012. 3, 26

[4] Sheoran, Y., Bouldin, B., Murali Krishnan, P. Compressor Performance and Operability in Swirl Distortion. *ASME Journal of Turbomachinery*, 134(4), 2001. 3

[5] Kim, Y., Engeda, A., Aungier, R., Direnzi, G. The Influence of Inlet Flow Distortion on the Performance of a Centrifugal Compressor and the Development of an Improved Inlet using Numerical Simulations. *Journal of Power and Energy*, 215:1–16, 2001. 3, 218

[6] Barker, A. G., Carrotte, J. F. Influence of Compressor Exit Conditions on Combustor Annular Diffusers, Part I: Diffuser Performance. *ASME Journal of Propulsion and Power*, 2001. 4

[7] Barker, A. G., Carrotte, J. F. Influence of Compressor Exit Conditions on Combustor Annular Diffusers, Part II: Flow Redistribution. *ASME Journal of Propulsion and Power*, 2001.

[8] Duncan Walker, A., Carrotte, J. F., McGuirk, J. Compressor/Diffuser/Combustor Aerodynamic Interactions in Lean Module Combustors. *Journal of Engineering for Gas Turbines and Power*, 2008. 4

[9] S. B. Pope. *Turbulent Flows.* Cambridge University Press, UK, 2000. 5, 6, 247

[10] J. D Anderson. *Computational Fluid Dynamics: The Basics with Applications.* McGrawhill Inc, NJ, USA, 1995. 5

[11] Moin, P., Mahesh, K. Direct Numerical Simulation: A Tool in Turbulence Research. *Annual Review of Fluid Mechanics*, 1998. 5

[12] Choi, H., Moin, P. Grid-Point Requirements for Large Eddy Simulation: Chapman's Estimate Revisited. *Physics of Fluids*, 2012. 5, 6

[13] Piomelli, U. . Large-eddy and Direct Simulation of Turbulent Flows. In *VKI Lecture Notes*, 1997. 5, 50, 88

[14] Chapman, D. R. Computational Aerodynamics Development and Outlook. *AIAA Journal*, 1979. 6

[15] Mahesh, K.,Constantinescu, G., Apte, S., Iaccarino, G., Moin, P. . Large-eddy simulation of gas turbine combustors. *Annual Research Briefs. Center for Turbulence Research, NASA Ames/Stanford Univ*, 2001. 6

[16] Gicquel, L. Y. M., Staffelbach, G., Poinsot, T. . Large Eddy Simulations of gaseous flames in gas turbine combustion chambers. *Progress in Energy and Combustion Science*, 2012.

[17] di Mare, F., Jones, W. P. , Menzies, K. R. . Large eddy simulation of a model gas turbine combustor. *Combustion and Flame*, 2004. 6

[18] Collado Morata, E., Gourdain, N., Duchaine, F., Gicquel, L. Y. M. Effects of Free-stream Turbulence on High Pressure Turbine Blade Heat Transfer Predicted by Structured and Unstructured LES. *Heat and Mass Transfer*, 55:5754–5768, 2012. 6, 44

[19] Wang, G., Papadogiannis, F., Duchaine, F., Gourdain, N., Gicquel, L. . Towards Massively Parallel Large Eddy Simulation of Turbine Stages. In *Proceedings of ASME Turbo Expo 2013: power for land, sea and air. Paper N. GT2013-94852*, San Antonio, USA, June 3-7 2013. 41

[20] Vagnoli, S., Verstraete, T., Mateos, B., Sieverding, C. H. Prediction of the Unsteady Turbine Trailing Edge Wake Flow Characteristics and Comparison with Experimental Data. *Proceedings of the Institution of Mechanical Engineers, Part A: Journal of Power and Energy*, 229 (5):487–497, 2015. 75, 164

[21] Tyacke, J. C., Tucker, P. G. Future Use of Large Eddy Simulation in Aero-engines. *ASME Journal of Turbomachinery*, 2015. 6, 145, 178

[22] Peric M. Ferziger, J. H. *Computational Methods for Fluid Dynamics.* Springer Science and Business Media, Dordrecht, the Netherlands, 2012. 6

[23] Klapdor, Elena Verena. *Simulation of Combustor - Turbine Interaction in a Jet Engine.* PhD thesis, Technischen Universit 2011. 6, 27, 28, 30, 210, 248

[24] Cazalens M. Poinsot T. Roux, S. Outlet-boundary-condition influence for large eddy simulation of combustion instabilities in gas turbines. *Journal of Propulsion and Power*, 24(3):541–546, 2008. 6, 27, 28, 248

[25] Lefebvre, M., Arts, T. Prediction of Laminar/Turbulent Flows in a Two-Dimensional High Pressure Turbine Linear Cascade. In *2nd European Conference on Turbomachinery,Fluid Dynamics and Thermodynamics*, Antwerpen, BE, March 5-7 1997. 7, 192

[26] Baughn, J. W., Butler, R. J., Byerley, A. R., Rivir, R. B. An Experimental Investigation of Heat Transfer, Transition and Separation on Turbine Blades at Low Reynolds Number and High Turbulence Intensity. In *ASME paper 95-WA/HT-25.* 7

[27] Koupper, C., Bonneau, G., Gicquel, L., Duchaine, F. Large Eddy Simulation of the Combustor-Turbine Interface: Study of the Potential and Clocking Effects. In *Proceedings of ASME Turbo Expo 2016: power for land, sea and air. Paper N. GT2016-56443*, Seoul, South-Korea, July 2016. 8, 145, 181, 182, 209

[28] Warren J Whitney, Roy G Stabe, and Thomas P Moffitt. Description of the warm core turbine facility and the warm annular cascade facility recently installed at nasa lewis research center. Technical report, SAE Technical Paper, 1980. 11

[29] Tonghuo Shang. *Influence of inlet temperature distortion on turbine heat transfer*. PhD thesis, Massachusetts Institute of Technology, 1995. 11

[30] Ballal D. Lefebvre, A. *Gas Turbine Combustion* . Hoboken CRC Press, NJ, USA, 2010. 12, 15, 42, 112, 113

[31] T Povey, KS Chana, TV Jones, and J Hurrion. The effect of hot-streaks on hp vane surface and endwall heat transfer: An experimental and numerical study. *Journal of Turbomachinery*, 129(1):32–43, 2007. 12, 13, 16, 17, 18, 247

[32] K. S. Povey T. Hall, B. F. Chana. Design of a nonreacting combustor simulator with swirl and temperature distortion with experimental validation. *Journal of Engineering for Gas Turbines and Power*, 136 (8):081501, 2014. 12, 13, 14, 114, 126, 247

[33] T Povey and I Qureshi. A hot-streak (combustor) simulator suited to aerodynamic performance measurements. *Proceedings of the Institution of Mechanical Engineers, Part G: Journal of Aerospace Engineering*, 222(6):705–720, 2008. 12

[34] Povey T. Hall, B. F. Experimental study of non-reacting low nox combustor simulator for scaled turbine experiments. In *ASME Turbo Expo 2015: Turbine Technical Conference and Exposition*, pages V04BT04A040–V04BT04A040. American Society of Mechanical Engineers, 2015. 13, 14, 16, 247

[35] Koupper, C., Caciolli, G., Gicquel, L., Duchaine, F., Bonneau, G., Tarchi, L., Facchini, B. . Development of an Engine representative Combustor Simulator Dedicated to Hot Streak Generation. *ASME Journal of Turbomachinery*, 136(11):111007, 2014. 14, 29, 67, 181

[36] Caciolli G. Facchini B. Tarchi L. Koupper C. Bacci, T. and J.-L. Champion. Flowfield and temperature profiles measurements on a combustor simulator dedicated to hot streaks generation. In *ASME Turbo Expo 2015: Turbine Technical Conference and Exposition*, pages V05CT17A001–V05CT17A001. American Society of Mechanical Engineers, 2015. 15, 16, 247

[37] Caciolli G. Facchini B. Tarchi L. Koupper C. Bacci, T. and J.-L. Champion. Turbulence field measurements at the exit of a combustor simulator dedicated to hot streaks generation. In *ASME Turbo Expo 2015: Turbine Technical Conference and Exposition*. American Society of Mechanical Engineers, 2015. 16, 247

[38] L. Duchaine F. Bacci T. Facchini B. Picchi A. Tarchi L. Bonneau G. Koupper, C. Gicquel. Experimental and numerical calculation of turbulent timescales at the exit of an engine representative combustor simulator. *Journal of Engineering for Gas Turbines and Power*, 138 (2):021503, 2016. 15

[39] Montomoli F. Martelli F. Chana K. S. Qureshi I. Povey T. Salvadori, S. Analysis on the effect of a nonuniform inlet profile on heat transfer and fluid flow in turbine stages. *Journal of Turbomachinery*, 134(1): 011012, 2012. 16, 20

[40] An, B.T., Liu, J, Jiang, H.D. Numerical Investigation on Unsteady Effects of Hot Streak on Flow and Heat Transfer in a Turbine Stage. *ASME Journal of Turbomachinery*, 131(3):031015, 2009. 17, 18, 247

[41] MD Barringer, KA Thole, MD Polanka, JP Clark, and PJ Koch. Migration of combustor exit profiles through high pressure turbine vanes. *Journal of Turbomachinery*, 131(2):021010, 2009. 18

[42] Jack L Kerrebrock and AA Mikolajczak. Intra-stator transport of rotor wakes and its effect on compressor performance. *Journal of Engineering for Gas Turbines and Power*, 92(4):359–368, 1970. 18

[43] Daniel J Dorney, Roger L Davis, David E Edwards, and Nateri K Madavan. Unsteady analysis of hot streak migration in a turbine stage. *Journal of Propulsion and Power*, 8(2):520–529, 1992. 18

[44] Miller R. J. Ong, J. Hot streak and vane coolant migration in a downstream rotor. *Journal of Turbomachinery*, 134(5):051002, 2012. 18

[45] Beard, P., Smith, A., Povey, T. Impact of Severe Temperature Distortion on Turbine Efficiency. *ASME Journal of Turbomachinery*, 135 (1):011018–1–12, 2013. 18, 19, 126, 247

[46] Adami P. Salvadori S. Chana K. S. Martelli, F. and L. Castillon. Aerothermal study of the unsteady flow field in a transonic gas turbine with inlet temperature distortions. In *ASME Turbo Expo 2008: Power for Land, Sea, and Air*, pages 1735–1747. American Society of Mechanical Engineers, 2008. 18, 19, 247

[47] TL Butler, OP Sharma, HD Joslyn, and RP Dring. Redistribution of an inlet temperature distortion in an axial flow turbine stage. *Journal of Propulsion and Power*, 5(1):64–71, 1989. 18

[48] Smith A. D. Chana K. S. Povey T. Qureshi, I. Effect of temperature nonuniformity on heat transfer in an unshrouded transonic hp turbine: an experimental and computational investigation. *Journal of Turbomachinery*, 134(1):011005–1–12, 2012. 19, 20, 247

[49] Jones T. V. Chana, K. S. An investigation on turbine tip and shroud heat transfer. *Journal of turbomachinery*, 125(3):513–520, 2003. 20

[50] Menshikova V. Haller B. He, L. Influence of hot streak circumferential length-scale in transonic turbine stage. *ASME Paper No. GT2004-53370*, 2004. 20

[51] Lucas Giller and Heinz-Peter Schiffer. Interactions between the combustor swirl and the high pressure stator of a turbine. In *ASME Turbo Expo 2012: Turbine Technical Conference and Exposition*, pages 1401–1415. American Society of Mechanical Engineers, 2012. 21, 22, 247

[52] Gregor Schmid and Heinz-Peter Schiffer. Numerical investigation of inlet swirl in a turbine cascade. In *ASME Turbo Expo 2012: Turbine Technical Conference and Exposition*, pages 543–552. American Society of Mechanical Engineers, 2012. 21

[53] Khanal, B., He, L., Northall, J., Adami, P. Analysis of Radial Migration of Hot-Streak in Swirling Flow Through High-Pressure Turbine Stage. *ASME Journal of Turbomachinery*, 135(4):041005, 2013. 21, 22, 25, 26, 135, 247, 248

[54] Cha, C., Ireland, P., Denman, P., Savarianandam, V. Turbulence Levels are High at the Combustor-Turbine Interface. In *Proceedings of ASME Turbo Expo 2013: power for land, sea and air. Paper N. GT2012-69130*, Copenhagen, Denmark, June 11-15 2012. 23, 33, 126, 145, 179, 248

[55] Thole K. A. Radomsky, R. W. Flowfield measurements for a highly turbulent flow in a stator vane passage. *Journal of turbomachinery*, 122(2):255–262, 2000. 23, 24, 248

[56] Lambert M. Rutheford A. W. Arts, T. *Aerothermal Investigation of a Highly Loaded Transonic Linear Turbine Guide Vane Cascade*. VKI, 1990. 24, 111, 115

[57] Varadarajan K.m Bogard D. G. Jenkins, S. The effect of high mainstream turbulence and turbine vane film cooling on the dispersion of a simulated hot streak. *Journal of Turbomachinery*, 126(1):203–211, 2004. 24, 25, 248

[58] Bogard D. G. Jenkins, S. The effects of the vane and mainstream turbulence level on hot streak attenuation. *Journal of Turbomachinery*, 127(1):215–221, 2005. 24, 25, 248

[59] Zhiduo Wang, Zhaofang Liu, and Zhenping Feng. Influence of mainstream turbulence intensity on heat transfer characteristics of a hp turbine stage with inlet hot streak. In *ASME Turbo Expo 2015: Turbine Technical Conference and Exposition*, pages V05BT13A010–V05BT13A010. American Society of Mechanical Engineers, 2015. 24, 32, 248

[60] Dyson, T. E., Helmer, D.B., Tallman, J.A. Large-Scale Simulation of the Clocking Impact of 2D Combustor Profile on a Two Stage High Pressure Turbine. In *Proceedings of ASME Turbo Expo 2014: power for land, sea and air. Paper N. GT2014-25883*, Dusseldorf, Germany, June 16-20 2014. 26, 32, 248

[61] Klapdor, E. V., Pyliouras, S., Eggels, R. L., Janicka, J. Towards Investigation of Combustor Turbine Interaction in an Integrated Simulation. In *Proceedings of ASME Turbo Expo 2010: power for land, sea and air. Paper N. GT2010-22933*, Glasgow, U.K., June 14-18 2010. 27, 30

[62] Raynaud, F., Eggels, R., Staufer, M., Sadiki, A., Janicka, J. Towards Unsteady Simulation of Combustor-Turbine Interaction in an Integrated Simulation. In *Proceedings of ASME Turbo Expo 2015: power for land, sea and air. Paper N. GT2015-42110*, Montreal, Canada, June 15-19 2015. 27, 30, 209

[63] Tyacke, J. C., Tucker, P. G., Loveday, R. J., Nagabushana, R. V., Watson, R., Iftekhar, N., Xiaoyu, Y. Large Eddy Simulations for Turbines: Methodologies, Cost and Future Outlooks. *ASME Journal of Turbomachinery*, 2015. 30, 147

[64] Wu X. Kim S. Alonso J. Pitsch H. Schlüter, J. Coupled rans-les computation of a compressor and combustor in a gas turbine engine. In *40 th AIAA/ASME/SAE/ASEE Joint Propulsion Conference and Exhibit*, 2004. 30, 31

[65] Pitsch H. Moin P. Schlüter, J. Large-eddy simulation inflow conditions for coupling with reynolds-averaged flow solvers. *AIAA journal*, 42(3): 478–484, 2004.

[66] X. Kim S. Shankaran S. Alonso J. Pitsch H. Schlüter, J. Wu. A framework for coupling reynolds-averaged with large-eddy simulations for gas turbine applications. *Journal of Fluids Engineering*, 127(4): 806–815, 2005. 31

[67] Pitsch H. Moin P. Schlüter, J. Outflow conditions for intregrated large eddy simulation/reynolds-averaged navier-stokes simulations. *AIAA journal*, 43(1):156–164, 2005. 31, 40

[68] Fröhlich J. Von Terzi, D. Coupling conditions for les with downstream rans for the prediction of incompressible turbulent flows. *Turbulence and Shear Flow Phenomena TSFP–5, Munich, Germany*, 2007. 31

[69] Collado Morata, Elena. *Impact of the Unsteady Aerothermal Environment on the Turbine Blades Temperature*. PhD thesis, Institut National Polytechnique de Toulouse, 2012. 31, 40, 78

[70] Insinna, S., Salvadori, S., Martelli, F. . Simulation of Combustor-NGV Interaction using RANS Solvers: Validation and Application to a Realistic Test Case. In *Proceedings of ASME Turbo Expo 2014: power for land, sea and air. Paper N. GT2014-25433*, Dusseldorf, Germany, June 16-20 2014. 31, 40, 44, 125, 126, 136, 212

[71] Insinna, Massimiliano. *Investigation of the Aero-Thermal Aspects of Combustor/Turbine Interaction in Gas Turbines*. PhD thesis, University of Florence, 2015. 31

[72] Menter, F. R. . Influence of Freestream Values on k-omega Turbulence Model Predictions. *AIAA Journal*, 30(6):1657–1659, 1992. 32, 187

[73] Menter, F. R. . Zonal Two Equation k-omega Turbulence Models for Aerodynamic Flows. *AIAA paper*, 30(6):1657–1659, 1993. 32, 185, 191

[74] PG Tucker. Trends in turbomachinery turbulence treatments. *Progress in Aerospace Sciences*, 63:1–32, 2013. 33

[75] Koupper, Charlie. *Unsteady Multi-component Simulations Dedicated to the Impact of the Combustion Chamber on the Turbine of Aeronautical Gas Turbines.* PhD thesis, Institut National Polytechnique de Toulouse, 2015. 33, 139, 145, 179, 181, 213

[76] Schoenfeld, T., Rudgyard, M. . Steady and Unsteady Flow Simulations Using the Hybrid Flow Solver AVBP. *AIAA Journal*, 37(11):1378–1385, 1999. 33, 145, 182

[77] Mattsson, K., Iourokina, I., Ham, F. Towards a Stable and Accurate Coupling of Compressible and Incompressible Flow Solvers . *Center For Turbulent Research, Annual Research Briefs*, pages 31–41, 2005. 40

[78] Von Terzi, D., Mary, I., Frohlich, J. Segregated LES/RANS Coupling COnditions for the Simulation of Complex Turbulent Flows. *Numerical Simulation of Turbulent Flows and Noise Generation*, 104:231–252, 2005. 40

[79] Francois B., Costes, M. Comparison of Chimera and Sliding Mesh Techniques for Unsteady Simulation of Counter Rotating Open-Rotors. In *ISABE Conference*, 2011. 41

[80] Duchaine, F., Mendez, S., Nicoud, F., Corpron, A., Moureau, V., Poinsot, T. Coupling Heat Transfer Solvers and Large Eddy Simuations for Combustion Applications. *Center For Turbulent Research, Annual Research Briefs*, pages 113–126, 2005. 41, 75

[81] Papadogiannis, Dimitrios. *Coupled LES of Combustion Chamber-Turbine Interactions.* PhD thesis, Institut National Polytechnique de Toulouse, 2015. 42

[82] Thompson, K. W. Time Dependent Boundary Conditions for Hyperbolic Systems. *Journal of Computational Physics*, 127(4):1–24, 1987. 44, 53, 55

[83] Poinsot, T. J., Lele, S. K. Boundary Conditions for Direct Simulations of Compressible Viscous Flows. *Journal of Computational Physics*, 101 (1):104–129, 1992. 44, 53, 54, 61, 68, 77, 151, 160, 244

[84] S. W. Smith. *The Scientist and Engineer's Guide to Digital Signal Processing* . California Technical Publishing, US, 1997. 47

[85] Lodato, G., Domingo, P., Vervisch, L. Three-dimensional Boundary Conditions for Direct and Large-Eddy Simulation of Compressible Viscous Flows. *Journal of Computational Physics*, 227:5105–5143, 2008. 53, 55, 56, 60, 75

[86] Rudy, D. H., Strikwerda, J. Boundary Conditions for Direct Simulations of Compressible Viscous FLows. *Journal of Computational Physics*, 36(55), 1981. 56

[87] Bianchini, Cosimo. *Assessment of Boundary Conditions for Heat Transfer and Aeroacoustic Analysis.* PhD thesis, University of Florence, 2011. 56

[88] Piscaglia, F., Montorfano, A., Onorati, A. Development of a Non-Reflecting Boundary Condition for Multidimensional Nonlinear Duct Acoustic Computation. *Journal of Sound and Vibration*, 332(4):992–935, 2013. 56

[89] Kim, J., Moin, P., Moser, R. Turbulence Statistics in Fully Developed Channel Flow at Low Reynolds Number. *Journal of Fluid Mechanics*, 177:133–166, 1987. 81

[90] Eckelmann, H. The Structure of the Viscous Sublayer and the Adjacent Wall Region in a Turbulent Channel Flow. *Journal of Fluid Mechanics*, 64, 1974. 82, 83, 250

[91] Kreplin, H., Eckelmann, H. Behavior of the Three Fluctuating Velocity Components in the Wall Region of a Turbulent Channel Flow. *Physics of Fluids*, 22, 1979. 82, 84, 85, 250

[92] Dean, R. B. Reynolds Number Dependence of Skin Friction and Other Bulk Flow Variables in Two-Dimensional Rectangular Duct Flow. *ASME Journal of Fluids Engineering*, 100, 1978. 84, 250

[93] Farell, C., Blessmann, J. On Critical Flow Around Smooth Circular Cylinders . *Journal of Fluid Mechanics*, 136:375–391, 1983. 91, 99

[94] Roshko, A. Experiments on the Flow Past a Circular Cylinder at Very High Reynolds Number. *Journal of Fluid Mechanics*, 10(3):345–356, 1961. 91

[95] Jenkins, L., Khorrami, M. R., Meelan, M., Choudhari, M. M., McGinley, C. B. Characterization of Unsteady Flow Structures Around Tandem Cylinders for Component Interaction Studies in Airframe Noise. In *26th AIAA Aeroacoustics Conference. Paper N. AIAA2005-2812*, Monterey, California, May 23-25 2005. 91, 99

[96] Okajima, A. Flows Around Two Tandem Circular Cylinders at Very High Reynolds Numbers. *Bulleting of the JSME*, 22(116):504–511, 1979. 91

[97] Mahir, N., Zekeriya, A. Numerical Investigation of Convective Heat Transfer in Unsteady Flow Past Two Cylinders in Tandem Arrangements. *Int. Journal of Heat and Fluid Flow*, 29(5):1309–1318, 2008. 102

[98] Siemens AG. *Industrial Gas Turbines The comprehensive product range from 5 to 50 megawatt.* 2015. 110, 112

[99] Chigier N. A. Beer, J. M. *Combustion Aerodynamics.* Hasted Press Division, Wiley, 1972. 113

[100] Numeca International. *NUMECAs flow integrated environment for turbomachinery and internal flows. User Manual.* Numeca Int., Bruxelles, BE, 2000. 115, 184, 185

[101] Zimont, V., Polifke, W., Bettelini, M., Weisenstein, W. An Efficient Computational Model for Premixed Turbulent Combustion at High Reynolds Numbers Based on a Turbulent Flame Speed Closure. *ASME Journal of Engineering for Gas Turbines and Power*, 120(3):526–532, 1998. 122

[102] G´ulder, ´O. Correlations of Laminar Combustion Data for Alternative S.I. Engine Fuels. *SAE Technical Paper 841000*, 1984. 122

[103] Weller, H. The Development of a New Flame Area Combustion Model Using Conditional Averaging. *Thermo-fluids section report TF 9307*, 1993. 128

[104] Hodson, H. P., Howell, R. J. . The Role of Transition in High-lift Low-pressure Turbines for Aeroengines. *Progress in Aerospace Sciences*, 2005. 147

[105] Mayle, R. E. . The Role of Laminar-Turbulent transition in Gas Turbine Engines. *ASME Journal of Turbomachinery*, 1991. 148

[106] Malkiel, E., Mayle, R. E. Transition in a Separation Bubble. In *ASME 1995 International Gas Turbine and Aeroengine Congress and Exposition*, Houston, Texas, June 5-8 1995. 148

[107] Menter, F. R., Langtry, R. B., Likki, S. R., Suzen, Y. B. . A correlation based transition model using local variablesPart I: model formulation. *ASME Journal of Turbomachinery*, 2006. 148

[108] Langtry, R. B., Menter, F. R., Likki, S. R., Suzen, Y. B. . A correlation based transition model using local variablesPart II: test cases and industrial applications. *ASME Journal of Turbomachinery*, 2006. 148

[109] Babajee, J., Arts, T. . 148

[110] Pacciani, R., Marconcini, R., Arnone, A., Bertini, F. . 148

[111] Michalek, J., Monaldi, M., Arts, T. . Aerodynamic Performance of a Very High Lift Low Pressure Turbine Airfoil (T106C) at Low Reynolds and High Mach Number With Effect of Free Stream Turbulence Intensity. *ASME Journal of Turbomachinery*, 2012. 148, 149

[112] Ducros, F., Comte, P., Lesieur, M. Large-eddy simulation of transition to turbulence in a boundary layer developing spatially over a flat plate. *Journal of Fluid Mechanics*, 1996. 149

[113] Marty, J. Numerical Investigations of Separation-Induced Transition on High-lift Low-pressure Turbine Using RANS and LES Methods. *Proceedings of the Institution of Mechanical Engineers, Part A: Journal of Power and Energy*, 228(8):924–952, 2014. 150, 151, 157

[114] Raverdy, B, Mary, I., Sagaut, P., Liamis, N. High-Resolution Large-Eddy Simulation of Flow Around Low-Pressure Turbine Blade. *AIAA Journal*, 41(3):390–397, 2003.

[115] Funazaki, K., Yamada, K., Tanaka, N., Chiba, Y. Detailed Studies on Separated Boundary Layers over Low-Pressure Turbine Airfoils under Several High Lift Conditions: Effect of Freesteam Turbulence. In *Proceedings of ASME Turbo Expo 2009. Paper N. GT2009-59813*, Orlando, USA, June 8-12 2009.

[116] Sarkar, S., Voke, P. R. Large-eddy simulation of Unsteady Surface Pressure Over a Low Pressure Turbine Blade Due to Interactions of Passing Wakes and Inflexional Boundary Layer. *ASME Journal of Turbomachinery*, 128(2):221–231, 2006. 150

[117] Jameson, A., Schmidt, W., Turkel, E. Numerical Solutions of the Euler Equations by Finite Volume Methods Using Runge-Kutta Time-stepping Schemes. *AIAA paper N. 1259*, 1981. 150

[118] Jameson, A. Time Dependent Calculations Using Multigrid, with Applications to Unsteady Flows Past Airfoils and Wings. *AIAA paper N. 1596*, 1991. 150

[119] Choi, H., Moin, P. Effects of the Computational Time Step on Numerical Solutions of Turbulent Flow. *Journal of Computational Physics*, 1994. 150, 152

[120] Michelassi, V., Chen, L., Pichler, R., Sandberg, R. Compressible Direct Numerical Simulation of Low-Pressure Turbines: Part II - Effect of Inflow Disturbance. *ASME Journal of Turbomachinery*, 2015. 151

[121] Bigoni, Fabio. *Numerical investigation of high-lift low pressure turbine blade profiles for aeronautical applications and comparison with the experiments", year =*. PhD thesis. 152

[122] Simoni, D., Ubaldi, M., Zunino, P., Lengani, D. An experimental investigation of the separated-flow transition under high-lift turbine blade pressure gradients. *Flow, Turbulence and Combustion*, 2012. 157

[123] Daniel J Bodony. Analysis of sponge zones for computational fluid mechanics. *Journal of Computational Physics*, 212(2):681–702, 2006. 160

[124] Sieverding, C. H. *Advanced Course on Turbines*. VKI, 1990. 162

[125] Sieverding, C. H., Stanislas, C., Snoeck, J. The Base Pressure Problem in Transonic Turbine Blades. *ASME Journal of Engineering for Power*, 102:711–718, 1980. 162

[126] Lawazceck, O., Heinemann, H. von karman vortex sheet in the wake of subsonic and transonic cascades. *ADARD CP 177 on Unsteady phenomena in Turbomachines*, 1976. 162

[127] Heinemann, H., Butefisch, K.A. Determination of the vortex shedding frequency of cascades with different trailing edges. *AGARD CP227*, 1977.

[128] Carscallen,W.E., Gostelow, J.P. Observations of vortex shedding in the wake from a transonic turbine nozzle Vanes. In *Proceedings of IRROMAC-5*, Kaanapali, HI, 1994. 162

[129] Cicatelli, G., Sieverding, C. H. The Effect of Vortex Shedding on the Unsteady Pressure Distribution Around the Trailing Edge of a Turbine Blade. *ASME Journal of Turbomachinery*, 1997. 162

[130] Sieverding, C. H., Richard, H., Desse, J. M. Turbine Blade Trailing Edge Flow Characteristics at High Subsonic Outlet Mach Number. *ASME Journal of Turbomachinery*, 2003. 163, 164, 166, 171, 172, 254

[131] Sieverding, C., Ottolia, D., Bagnera, C., Comadoro, A., Brouckaert, J. F., Desse,J. M. Unsteady Turbine Blade Wake Characteristics. *ASME Journal of Turbomachinery*, 2004. 163

[132] Kopriva, J., Laskowsky, G. M., Reza, H., Sheikhi, H. Assessment of High Pressure Cooled and Uncooled Turbine Blade Wakes via RANS and URANS at Engine Scale Conditions. In *Proceedings of ASME Turbo Expo 2013: power for land, sea and air. Paper N. GT2013-94285*, San Antonio, USA, June 3-7 2013. 163

[133] Leonard, T., Duchaine, F., Gourdain, N., and Gicquel, L. Steady/Unsteady Reynolds Averaged Navier-Stokes and Large Eddy Simulation of a Turbine Blade at High Subsonic Outlet Mach Number. In *Proceedings of ASME Turbo Expo 2010: power for land, sea and air. Paper N. GT2010-22469*, Glasgow, UK, June 14-18 2010. 163, 164, 166, 169, 171, 254

[134] Borm, O., Kau, H.P. Unsteady Aerodynamics of a Centrifugal Compressor Stage - Validation of Two Different CFD Solvers. In *Proceedings of ASME Turbo Expo 2012*, Copenhagen, Denmark, June 2012. 166, 220

[135] Sandberg, R., Pichler, R., Chen, L., Johnstone, R., Michelassi, V. Compressible Direct Numerical Simulation of Low-Pressure Turbines: Part I - Methodology. *ASME Journal of Turbomachinery*, 2015. 172

[136] Sieverding,C. H., Heinemann, H. The influence of boundary layer state on vortex shedding from flat plates and turbine blades. *ASME Journal of Turbomachinery*, 1990. 177

[137] Jouini, D. B. M., Sjolander, S. A., Moustapha, S. H. Aerodynamic Performance of a Transonic Turbine Cascade at Off-Design Conditions. In *Proceedings of ASME Turbo Expo 2000: power for land, sea and air. Paper N. 2000-GT-0482*, Munich, GE, May 8-11 2000. 177

[138] Menter, F. R., Kuntz, M., Langtry, R. . Ten Years of Industrial Experience with the SST Turbulence Model. *Heat and Mass Transfer*, 4 (1), 2003. 185, 191, 192

[139] Bode, C., Aufderheide, T., Kozulovic, D., Friedrichs, J. . The Effects of Turbulence Length Scale on Turbulence and Transition Prediction in Turbomachinery Flows. In *Proceedings of ASME Turbo Expo 2014: power for land, sea and air. Paper N. GT2014-27026*, Dusseldorf, Germany, June 16-20 2014. 185

[140] Cambier, L., Veuillot, J. P. . Status of the elsA Software for Flow Simulation and Multi-Disciplinary Applications. In *46th AIAA Aerospace Sciences Meeting and Exibit*, Reno, Nevada, January 7-10 2008. 185, 202

[141] Menter, F. R. . Performance of Popular Turbulence Model for Attached and Separated Adverse Pressure Gradient Flows. *AIAA Journal*, 30(8):2066–2072, 1992. 192

[142] Verstraete, Tom. *Heat Transfer and Multi Disciplinary Optimization Applied on Micro-gasturbines.* PhD thesis, Universiteit Gent, 2008. 202, 203

[143] N.A. Cumpsty. *Compressor Aerodynamics.* Longman, Essex, U.K, 1989. 218

[144] Frigne, P., Van den Braenbussche, R. A. Distinction between Types of Impeller and Diffuser Rotating Stall in Centrifugal Compressors with Vaneless Diffuser. *ASME Journal of Engineering for Gas Turbines and Power*, 106:468–474, 1984. 218, 232

[145] Chen, J. P., Hathaway, M. D., Herrick, G. P. Prestall Behavior of a Transonic Axial Compressor Stage via Time-Accurate Numerical Simulations. *ASME Journal of Turbomachinery*, 130(4):041014.1–041014.12, 2008. 218

[146] Vo, H. D. *Role of Tip Clearance Flow on Axial Compressor Stability*. PhD thesis, Massachusetts Institute of Technology, 2001. 228

[147] Hah, C., Rabe, D. C., Wadia, A.R. Role of Tip-Leakage Vortices and Passage Shock in Stall Inception in a Swept Transonic Compressor Rotor. In *Proceedings of ASME Turbo Expo 2004: power for land, sea and air* , Wien, Austria, June 2004. 218

[148] Mailach, R., Lehmann, I., and Vogeler, K. Rotating Instabilities in an Axial Compressor Originating From the Fluctuating Blade Tip Vortex. *ASME Journal of Turbomachinery*, 123:453–460, 2001. 218, 222, 232

[149] Yamada, K., Funazaki, K., Sazaki, H. Numerical Investigation on Relation Between Unsteady Behavior of Tip Leakage Vortex and Rotating Disturbance in a Transonic Axial Compressor Rotor. In *Proceedings of ASME Turbo Expo 2008: power for land, sea and air*, Berlin, Germany, June 2008. 218, 222, 232

[150] Niazi, S. *Numerical Simulation of Rotating Stall and Surge Alleviation in Axial Compressors*. PhD thesis, Georgia Institute of Technology, 2000. 218

[151] Hathaway, M. D., Herrick, G., Chen, J., Webster, R. A Time Accurate Unsteady Simulation of the Stall Inception Process in the Compression System of a US Army Helicopter Gas Turbine Engine. In *Proceedings of the DoD Users Group Conference* , Washington, DC, USA, June 2004.

[152] Gourdain, N., Burguburu, S., Leboeuf, F., Michon, G.J. Simulation of Rotating Stall in a Whole Stage of an Axial Compressor. *Journal of Computers and Fluids*, 39:1644–1655, 2010. 218, 224

[153] Engeda, A., Kim, Y. , Aungier, R., Direnzi, G. The Inlet Flow Structure of a Centrifugal Compressor Stage and Its Influence on the Compressor Performance. *ASME Journal of Fluids Engineering*, 125:779–785, 2003. 218

[154] Ariga, I., Masuda, S., Ookita, A. Inducer Stall in a Centrifugal Compressor with Inlet Distortion. *ASME Journal of Turbomachinery*, 109: 27–35, 1987. 218, 238

[155] Leilei, W., Ce, Y., Ben, Z., Dazhong, L, Chaochen, M., Du L. The change of the inlet geometry of a centrifugal compressor stage and its

influence on the compressor performance. *Journal of Thermal Science*, 22(3):197–208, 2013. 218

[156] L. Reid and R. D. Moore. *NASA Technical Paper 1337*. NASA, Lewis research center, Cleveland, Ohio, 1978. 219, 222

[157] Biesinger, T., Cornelius, C., Nurnberg, C., Rube, C. Speed Line Computation of a Transonic Compressor Stage with Unsteady CFD Methods. In *Proceedings of ASME Turbo Expo 2012*, Copenhagen, Denmark, June 2012. 220

[158] Zhang, Y., Xingen, L., Chu, W., Zhu, J. . Numerical Investigation of Unsteady Tip Leakage Flow and Rotating Stall Inception in a Transonic Compressor . *Journal of Thermal Science*, 19:310–317, 2010. 220

[159] Greitzer, E.M. The Stability of Pumping Systems The 1980 Freeman Scholar Lecture. *Journal of Fluid Engineering*, 103:193–235, 1981. 221

[160] Yamada, K., Funazaki, K., Furukawa, M. The Behavior of Tip Clearance Flow at Near-Stall Condition in a Transonic Axial Compressor Rotor. In *Proceedings of ASME Turbo Expo 2007: power for land, sea and air*, Monreal, Canada, May 2007. 221, 228

[161] Seybert, A. F., Ross, D. F. Experimental determination of acoustic properties using a twomicrophone randomexcitation technique. *Journal of the Acoustical Society of America*, 61:992–935, 1977. 242